The Pennsylvania State University

The Graduate School

Department of Aerospace Engineering

MODEL FOLLOWING AND HIGH ORDER AUGMENTATION FOR ROTORCRAFT CONTROL, APPLIED VIA PARTIAL AUTHORITY

A Dissertation in

Aerospace Engineering

by

James Michael Spires

Submitted in Partial Fulfillment
of the Requirements
for the Degree of

Doctor of Philosophy

June 2017

The dissertation of James Michael Spires was reviewed and approved* by the following:

Joseph Horn
Professor of Aerospace Engineering
Dissertation Advisor
Chair of Committee

Edward Smith
Professor of Aerospace Engineering

Jacob Langelaan
Associate Professor of Aerospace Engineering

Christopher Rahn
Professor of Mechanical Engineering

Philip J. Morris
Professor of Aerospace Engineering
Head of the Department of Aerospace Engineering

*Signatures are on file in the Graduate School

ABSTRACT

This dissertation consists of two main studies, a few small studies, and design documentation, all aimed at improving rotorcraft control by employing multi-input multi-output (MIMO) command-model-following control as a baseline, together with a selectable (and de-selectable) MIMO high order compensator that augments the baseline.

Two methods of MIMO command-model-following control design are compared for rotorcraft flight control. The first, Explicit Model Following (EMF), employs SISO inverse plants with a dynamic decoupling matrix, which is a purely feed-forward approach to inverting the plant. The second is Dynamic Inversion (DI), which involves both feed-forward and feedback path elements to invert the plant. The EMF design is purely linear, while the DI design has some nonlinear elements in vertical rate control. For each of these methods, an architecture is presented that provides angular rate model-following with selectable vertical rate model-following. Implementation challenges of both EMF and DI are covered, and methods of dealing with them are presented. These two MIMO model-following approaches are evaluated regarding (1) fidelity to the command model, and (2) turbulence rejection. Both are found to provide good tracking of commands and reduction of cross coupling.

Next, an architecture and design methodology for high order compensator (HOC) augmentation of a baseline controller for rotorcraft is presented. With this architecture, the HOC compensator is selectable and can easily be authority-limited, which might ease certification. Also, the plant for this augmentative MIMO compensator design is a stabilized helicopter system, so good flight test data could be safely gathered for more accurate plant identification. The design methodology is carried out twice on an example helicopter model, once with turbulence rejection as the objective, and once with the additional objective of closely following pilot commands. The turbulence rejection HOC is feedback only (HOC_FB), while the combined objective HOC has both feedback and feedforward elements (HOC_FBFF). The HOC_FB was found to be better at improving turbulence rejection but generally degrades the following of pilot commands. The HOC_FBFF improves turbulence rejection relative to the

Baseline controller, but not by as much as HOC_FB. However, HOC_FBFF also generally improves the following of pilot commands.

Future work is suggested and facilitated in the areas of DI, MIMO EMF, and HOC augmentation. High frequency dynamics, neglected in the DI design, unexpectedly change the low frequency behavior of the DI-plant system, in addition to the expected change in high frequency dynamics. This dissertation shows why, and suggests a technique for designing a pseudo-command pre-filter that at least partially restores the intended DI-plant dynamics. For EMF, a procedure is presented that avoids use of a reduced-order model, and instead uses a full-order model or even frequency-domain flight test data. With HOC augmentation, future research might investigate the utility of adding an H_∞ constraint to the design objective, which is known as an equal-weighting mixed-norm H_2/H_∞ design. Because all the formulas in the published literature either require solution of three coupled Riccati Equations (for which there is no readily available tool), or make assumptions that do not fit the present problem, appropriate equal-weighting H_2/H_∞ design formulas are derived which involve two de-coupled Riccati Equations.

TABLE OF CONTENTS

LIST OF FIGURES

LIST OF TABLES

NOMENCLATURE

$\mathbf{A}$	matrix of the effect of $\Delta\mathbf{x}$ on $\Delta\dot{\mathbf{x}}$
A	see Equations (5-3) and (5-16)
A_*	a state matrix
$A_{\hat{P}}, B_{\hat{P}}, C_{\hat{P}}$	knowns in the regulator Riccati equation
A_Q, B_Q, C_Q	knowns in the estimator Riccati equation
$A_{\dot{x}_\mathrm{a},\ x_\mathrm{b}}$	effect of state b on state derivative a
$A_{\dot{x},\ x}$	diag. element of $\mathbf{A}$, effect of a state on its deriv.
$a^{\mathrm{b}}_{\mathrm{i},y}$	inertial acceleration in the body-right axis
$a^{\mathrm{b}}_{\mathrm{meas},y}$	measured acceleration in the body-right axis
$a_{y,\mathrm{tgt}}$	target measured acceleration in the body-right axis, in g's
$\mathbf{B}$	matrix of the effect of $\Delta\mathbf{u}$ on $\Delta\dot{\mathbf{x}}$
$\mathbf{B_1}$	matrix of the effect of $\Delta\mathbf{u}_3$ on $\Delta\dot{\mathbf{x}}$
$\mathbf{B}_2$	matrix of the effect of Δu_{col} on $\Delta\dot{\mathbf{x}}$
B_*	an input matrix
B_1, B_2	see Equations (5-3) and (5-17)
$B_{\dot{x},*}$	effect of control u_* on the state derivative
Col, col	abbreviation for collective inceptor
$\mathbf{C}$	matrix that converts $\Delta\mathbf{x}$ to $\mathbf{y}$
$\mathbf{C}_{pqr}$	matrix that extracts *p*, *q*, and *r* from $\Delta\mathbf{x}$
C_*	an output matrix
C_1, C_2	see Equations (5-3) and (5-18)

D_*	a direct input to output matrix
$D_{11}, D_{12}, D_{21}, D_{22}$	see Equations (5-3) and (5-19)
$\tilde{D}_{12\perp}$, $\tilde{D}_{21\perp}$	see Equation (5-43)
d	$\lfloor d_{\text{lat}} \quad d_{\text{lng}} \quad d_{\text{ped}} \quad d_{\text{col}} \rfloor^{\text{T}}$
$\mathbf{d}_3$	$\lfloor d_{\text{lat}} \quad d_{\text{lng}} \quad d_{\text{ped}} \rfloor^{\text{T}}$
d	SISO disturbance, or MIMO disturbance after weighting
d_*	inputs to the decoupled plant, in EMF
d_{lat}/p , d_{lng}/q , d_{ped}/r , $d_{\text{col}}/w^{\text{ned}}$	inverses of the decoupled dynamics, in EMF
Err, err	abbreviation for error
$G_e(s)$	transfer function matrix for the existing system
g	magnitude of gravitational acceleration
I , **I**	identity matrix
K_{P}^*	proportional gain on error, $*\rightarrow$ EMF or DI
K_I	integral gain on error, SISO
K_{I}^*	integral gain on error, $*\rightarrow$ EMF or DI
k_{p} , k_{ip}	SISO 1st order gain for: (actual) plant, identified plant
$k_{\text{P}}^{\text{EMF}}$, $k_{\text{I}}^{\text{EMF}}$	adjustments from DI gains to those for EMF
Lat, lat	abbreviation for lateral inceptor
Lng, lng	abbreviation for longitudinal inceptor
$\mathbf{M}_{1x3}$	mixing matrix that decouples vertical rate
$\mathbf{M}_{3x4}$	mixing matrix that decouples angular rates
$\mathbf{N}(s)$	matrix of plant transfer function numerators
N_*^*	a plant transfer function numerator

n	noise after weighting
Ped, ped	abbreviation for pedal inceptor
$\mathbf{P}(s)$	matrix of plant transfer functions
P_*^*	a plant transfer function
$\hat{P}$	unknown in the regulator Riccati equation
p, q, r	body frame angular rates (roll, pitch, yaw)
Q	unknown in the estimator Riccati equation
$r_{\text{tgt,tc}}$	yaw rate target contribution for coordinated turning
s	Laplace domain variable
${}^{\text{h}}T^{\text{b}}$	transformation matrix, body to heading frame
Tgt	abbreviation for target, the input to a command model
Δt	simulation time step: 0.01 sec
turb	abbreviation for air turbulence
u_*	a flight dynamics input, upstream of the boost actuators
$\mathbf{u}$	$\lfloor u_{\text{lat}} \quad u_{\text{lng}} \quad u_{\text{ped}} \quad u_{\text{col}} \rfloor^{\text{T}}$
$\mathbf{u}_3$	$\lfloor u_{\text{lat}} \quad u_{\text{lng}} \quad u_{\text{ped}} \rfloor^{\text{T}}$
u_*/d_*	mixing transfer func., angular rate decoupling
u_*/u_{col}	mixing transfer func., angular rate decoupling
u_{col}/d_*	mixing transfer func., vertical rate decoupling
u, v, w	translational rates in body axes (fwd, right, dwn)
U_* , V_*	unitary matrices of a Singular Value Decomposition
V	true airspeed
W_{A}	actuation weighting matrix

W_{D}	disturbance weighting matrix
W_{N}	noise weighting matrix
W_{n_*}	axis-specific noise weight on an error or target
W_{P}	performance weighting matrix
W_{p_*}	axis-specific performance weight on an error
w^{ned}, w^{h}, or wh	translational rate down
$\mathbf{x}$	state vector, usually $\lfloor v \quad w \quad p \quad q \quad r \rfloor^{\mathrm{T}}$
x	state vector of the augmented plant
x_*	a subset of x
$\mathbf{y}$	MIMO output vector
y	SISO output, or MIMO output (sensed angular rates vector)
y_{cmd}, $\mathbf{y}_{\mathrm{cmd}}$	SISO command, MIMO command
y_{fb}	angular rate errors
y_{fbi}	integral of angular rate errors
y_{ff}	angular rate targets
y_{HOC}	input to the HOC
y_{n}	y_{HOC} with noise
z	closed-loop output of the augmented plant
z_a, z_{p}	actuator and performance outputs of the augmented plant
γ	H_∞ performance bound
Δ	prefix meaning deviation from trim
δ_*	a bare airframe input
$\boldsymbol{\delta}$	$\lfloor \delta_{\mathrm{lat}} \quad \delta_{\mathrm{lng}} \quad \delta_{\mathrm{ped}} \quad \delta_{\mathrm{col}} \rfloor^{\mathrm{T}}$
$\boldsymbol{\delta}_*$	a bare airframe input vector

ζ	damping ratio of a transfer function pole
θ	pitch attitude
λ	system pole
ξ	closed-loop input vector to the augmented plant
ξ_d, ξ_n	disturbance and noise input vectors to the augmented plant
Σ_*	singular values matrix of a Singular Value Decomposition
$\boldsymbol{\sigma}$	$\lfloor \dot{w}^{\mathrm{h}}_{\mathrm{cmd}} \quad \dot{p}_{\mathrm{cmd}} \quad \dot{q}_{\mathrm{cmd}} \quad \dot{r}_{\mathrm{cmd}} \rfloor^{\mathrm{T}}$, DI pseudo-command
$\boldsymbol{\sigma}_3$	$\lfloor \dot{p}_{\mathrm{cmd}} \quad \dot{q}_{\mathrm{cmd}} \quad \dot{r}_{\mathrm{cmd}} \rfloor^{\mathrm{T}}$, DI pseudo-command
$\tau_{\mathrm{p}}, \tau_{\mathrm{ip}}$	SISO 1st order time const.: (actual) plant, identified plant
υ, υ_{HOC}	TITO control input, HOC output (which is also a TITO control input)
ϕ	roll attitude
ω	frequency variable
$\square_{\mathrm{a}}$	associated with actuation
$\square_{\mathrm{CL}}$	associated with the HOC closed-loop
$\square_{\mathrm{c}}$	a state-space parameter of the HOC
$\square_{\mathrm{cmd}}$	command value; comes from a command model
$\square_{\mathrm{cld}}$	command value, lagged; comes from a command model
$\square_{d}$	associated with disturbance
$\square_{\mathrm{d}}$	associated with the design model
$\square_{\mathrm{e}}$	associated with the existing system: helicopter with Baseline Rate Mode active
$\square_{\mathrm{est}}$	estimated value
$\square_{\mathrm{err}}$	error value

$\square_{\mathrm{ff}}$	feedforward term
$\square_{\mathrm{fb}}$	feedback term
$\square_{\mathrm{i}}$	associated with angular rate error integrator
$\square_{m,n}$	matrix element specified by row *m*, column *n*
$\square_{n}$	associated with noise
$\square_{p}$	associated with performance
$\square_{\mathrm{trm}}$	trim value
$\square^{(2)}$	change of variables used in Section 5.5.1
$\square^{\mathrm{h}}$	heading frame value
$\square^{\mathrm{ned}}$	north-east-down frame value
$\square^{\mathrm{T}}$	matrix transpose
$\{\ \}$	column vector
$\lfloor\ \rfloor$	row vector
$\lvert\ \rvert$	determinant
$[\ ]_{\phi\theta}$	matrix that depends upon ϕ and θ
$[\ ]_{\dot{w}^{\mathrm{ned}},\,\phi\theta}$	row of $[\ ]_{\phi\theta}$ associated with $\dot{w}^{\mathrm{ned}}$
$\dot{\square}$	derivative with respect to time
$\tilde{\square}$	plant matrix corresponding to the Ref. [36] formulation

ACKNOWLEDGEMENTS

I am most grateful to Dr. Joseph F. Horn for giving me a funded initial topic, for advancing my understanding of MIMO helicopter control system design and analysis, and for providing strategic advice on the planning of trade studies. When I got stuck, Dr. Horn knew the way forward. I thank Bell Helicopter for funding more than two years of this research, through contract XWORX-SOW-0053 and through fellowship awards, and for their reviews of our research reports which made me more aware of certain practical design considerations for manned rotorcraft. I also appreciate my advisory committee, Dr. Edward Smith, Dr. Jacob Langelaan, and Dr. Christopher Rahn, for their constructive criticism and suggestions, which improved the quality of this dissertation. Finally, I thank my fellow graduate student Mark DeAngelo for being an outstanding study partner for the Ph.D. Candidacy Exam.

Chapter 1

Introduction

1.1 Motivation

Although traditional helicopters are Multi-Input Multi-Output (MIMO) systems with significant cross coupling, classical Single-Input Single-Output (SISO) control design methods continue to dominate within the manned helicopter industry. Compared against modern MIMO control design, SISO design methods are well understood and more intuitive, and have a long certification history within regulatory agencies. Still, MIMO design seems to have potential to improve helicopter dynamic performance, by accounting for cross coupling, and by higher order dynamic compensation.

A way to combine the simplicity and intuition of SISO design with the benefits of MIMO design is to employ a MIMO technique for decoupling and inversion, combined with SISO explicit command-model-following and error control, then augmented with high order compensation (HOC) for further error reduction. The overarching objective of the present research is to advance this form of rotorcraft model-following control. The attractiveness of explicit command-model-following is explained next.

With model-following control, the control law is designed to make the plant response match the response of a reference model, also known as a command model. The input to a command model is called the target, and the output is called the command. Command models can generally be defined such that if the response of the vehicle matches the model, piloted handling qualities requirements are satisfied. As examples, bandwidth and damping for a particular response-axis/input pair can be set using a second-order command model, response quickness versus amplitude can be specified using a non-linear element within the command model, and decoupling is specified by using SISO command models for all response-axis/input pairs. Command models respond to pilot inputs, not disturbances, so model following also implies disturbance rejection. Therefore, command-model-following is an intuitive architecture.

With explicit model following control, there is feed forward control from the command model to the decoupled input that ideally causes the rotorcraft to follow the command with no error control, so that response quickness is not strongly dependent upon the aggressiveness of the feedback control, which eases the task of satisfying both quickness and stability margin specifications. Also, command models provide commands that actually represent the desired response, so that errors terms are a measure of deviation from desired behavior, which facilitates application of a high order regulator (the HOC) to draw the response closer to that which is desired.

A high-level diagram of the system architecture of the present work is shown in Figure 1-1 below. The architecture of the rate command models is shown in Figure 1-2.

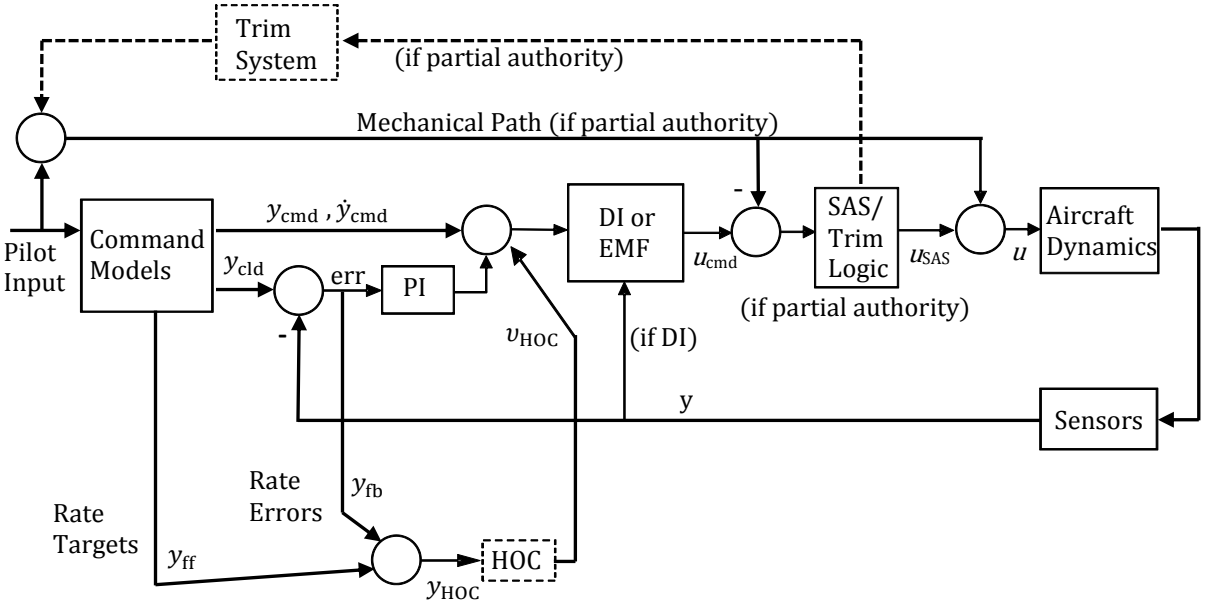

Figure 1-1. Schematic of PSU Control Architecture with HOC Augmentation

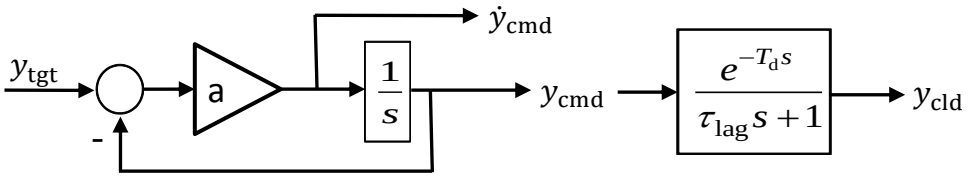

Figure 1-2. Rate Command Model Architecture

The practicality of the control architecture and design process presented in this work is enhanced by the following aspects. Command model following is an intuitive approach to handling qualities. There

is a clear separation of channels, using the familiar successive-loop-closure method for Baseline feedback design. The full range of channelized response types can be implemented, from angular/vertical rate command to position hold. Highly accurate system identification should be possible from flight test for the Baseline-stabilized rotorcraft, which is the plant utilized in the HOC design; therefore, the complex HOC can be designed with greater confidence than if one must rely upon simulation dynamics. The HOC is selectable and de-selectable, which should ease certification. Finally, the control law can be implemented as a partial authority system.

1.2 Literature Review

Two general approaches for reduction of cross coupling are dynamic crossfeeds in the forward path, and a state-feedback technique known as Dynamic Inversion (Ref. [1]). Catapang, et al., in 1994 (Ref [2]) present a design method for dynamic crossfeeds between the lateral and longitudinal controls of a rotorcraft. With cross coupling made small, the resulting on-axis dynamics can be inverted, producing Explicit Model Following. Horn and his students have made extensive use of Dynamic Inversion for rotorcraft control (eg. Refs. [3] and [4]). Dynamic Inversion accomplishes both decoupling and inversion.

Two common high order MIMO design methods are H_2 (Linear Quadratic Gaussian) and H_∞. Both are output feedback approaches that effectively include two components: a state estimator, and estimated-state feedback. For plants that are detectable and stabilizable, both methods yield stabilizing controllers for the plant used in the design. With H_2 design, the system input is taken to be uncorrelated zero-mean Gaussian white noise, and the mean-square of the resulting output is minimized. With H_∞ design, the maximum gain from input to output, over all frequencies, is limited by a chosen scalar. The H_2 measure is generally viewed as a good measure of control performance, while the H_∞ measure relates to control robustness against uncertainty in the plant. H_2 and H_∞ control synthesis can be accomplished via Matrix Algebraic Riccati Equations (Doyle, et al., Ref. [5]) or Linear Matrix Inequalities (Boyd, et al., Ref. [6]). Likewise, mixed-norm H_2/H_∞ control synthesis can be accomplished via Matrix Algebraic

Riccati Equations (Haddad and Bernstein, Ref. [7]) or Linear Matrix Inequalities (Khargonekar and Rotea, Ref. [8]).

MIMO design methods have been applied to manned helicopters in simulation studies and one real flight test program, to improve handling qualities and robustness. The 1990's saw a flurry of activity in this field. Manness and Murray-Smith, Ref. [9], used eigenstructure assignment to meet handling quality criteria. Takahashi, Ref. ,[10] used H_2 design to synthesize a rate-command control law for hovering, which was implemented on the NASA Ames vertical motion simulator. This H_2 controller produced good decoupling and quick response, but also a mild tendency toward pilot induced oscillation in roll. Foster, et al., Ref. [11], and Spurgeon, et al., Ref. [12], applied model reference sliding mode control to rotorcraft simulation models. A team of researchers in the United Kingdom and Canada developed H_∞ controllers for two full authority fly-by-wire manned helicopters: an experimental Bell 205 (Postlethwaite, et al., Ref. [13]) and a simulation model of a fly-by-wire Westland Lynx MK7 (Postlethwaite, et al., Ref. [14]). They selected control design architectures that produced implicit model following with an H_∞ controller having feed forward and feedback elements. Both helicopter control designs were evaluated through piloted simulation, and generally showed Level 1 handling qualities. The Bell 205 controller was also flight tested, but in flight test showed only Level 2 handling qualities. The difference between simulation and flight test outcomes was likely due to inaccuracies in the bare-airframe plant used in the control synthesis.

More recently, model predictive, neural, and adaptive control methodologies have been applied to the helicopter control problem. Wan and Bogdanov, Ref. [15], and Bogdanov, et al., Ref. [16], developed a control scheme that uses model predictive control for a feed forward component, combined with state-dependent Riccati equation and neural network feedback. Adaptive controllers have been developed for helicopters (Refs. [17], [18],[19], and [20]. These learning controllers have excellent performance, but are expected to be very difficult to certify for manned vehicles. Bichlmeier, et al., 2013, Ref. [21], presented adaptive augmentation of a helicopter baseline controller. This adaptive control operates at the angular rate control level, and the controllers are intended to be certifiable.

Horn and Bridges, 2007, Ref. [4], introduced the idea of augmenting a model-following baseline controller with a MIMO compensator that acts on angular rate error. The objective of that study was gust

rejection during shipboard operations, so the MIMO compensator was designed to minimize the H_2 response to turbulence having a known spectral composition, using feedback control. The time traces showed reduced pilot workload during operation within the simulated ship airwake. Then, Hayes, et al., 2012, Ref. [22], showed that, for a given phase margin, an augmentative H_2 compensator produced better hands-off rate and attitude tracking performance in turbulence, than increasing the baseline gains. Most recently, Rigsby, et al., 2013, Ref. [23], employed this augmentative H_2 compensator approach to reduce the swinging of an external load during low speed operations, which improves handling qualities and the precision of external load handling.

1.3 Research Contributions and Reader's Guide

The present research makes advancements that can be placed into three categories: (1) command models, (2) decoupling and inversion, and (3) high order compensation. Each contribution is now introduced and located within the structure of this dissertation. At the end of this section is a summary of the contributions, Table 1-1.

The first group of advancements deals with the command models. A command model architecture is presented in Section 3.3.1, called parallel rate-command loops, that implements smooth switching between attitude and rate command modes, with proper feed-forward signals. In the yaw axis, at high speed, this architecture is modified to implement lateral acceleration and rate modes (see Section 3.3.2.2). An alternative architecture is also presented (in Section 3.3.4), called single rate-command loop, that meets the same requirements as the first. The two command model architectures are compared in terms of resulting gain and phase margins when feedback control is included. The final advancement in command models is to put an arctangent limiter on the rate target (Section 3.3.5) to follow the ADS-33 Level 1 quickness versus amplitude specification (Ref. [24]).

The second group of advancements deals with the decoupling and inversion portion of a MIMO command-model-following control system. The present work extends the dynamic decoupling in Ref. [2] by increasing the dimensions from 2x2 to 3x4, adds selectable climb rate decoupling, and derives inverse

models for all axes, resulting in a complete Explicit Model Following (EMF) architecture for rotorcraft (Section 4.2). Rotorcraft applications of Dynamic Inversion (DI) are extended by developing non-linear selectable vertical rate model following (Section 4.3.2). EMF and DI are compared; mathematically for the SISO case (Section 4.1.3), and by application to an example helicopter for the MIMO case (Section 4.6). EMF and DI, applied to a first order SISO system, are shown to be equivalent in the presence of modeling errors.

Groundwork is laid for further refining EMF and DI. While the present EMF is developed using a reduced order model of the rotorcraft, Section 4.8.1 explains how EMF could be derived using a full order model or flight test data. With DI, the effects of neglected dynamics are considered, and methods for reducing these effects are proposed (Section 4.8.2).

The command models, decoupling, and inversion are combined with feedback error control to form the Baseline control system. The final advancement is with augmentation of the Baseline control through high order compensation (HOC), to reduce errors between the ideal and actual response (Chapter 5). HOC is state-space output feedback control that employs dynamic state estimation; examples are H_2, H_∞, and H_2/H_∞. While a previous study (Ref. [22]) showed the turbulence rejection benefits of H_2 HOC that acts upon angular rate errors, the present study shows that if angular rate targets (the inputs to the angular rate command models) are also inputs for the H_2 HOC, then the HOC can be made to improve both turbulence rejection and the following of pilot-induced commands (Section 5.3). The HOC is shown to have little effect upon control system robustness (Section 5.3.3). Future work in HOC might consider adding H_∞ constraint as a design knob for improving robustness, so H_2/H_∞ formulas are derived that are appropriate for the present application (Section 5.5.1).

In this final study, the control laws are implemented via 10% partial authority. This means the control laws can modify the raw inceptor-based bare-airframe actuator positions by up to 10% of full throw, which is typical of non-fly-by-wire rotorcraft. By limiting control law authority, the pilot is able to overcome a run-away control law input, and therefore less redundancy and fault detection/accommodation are required, reducing cost and weight. However, partial authority often limits the effectiveness of the

control laws during large-amplitude maneuvers due to saturation of the control-law actuation at a level significantly below overall control authority.

Table 1-1. Dissertation Contributions

Category	**Contributions**
Command Models	• Two command model architectures that implement smooth switching between attitude and rate modes, with proper feed-forward signals. • For the yaw axis, a command model architecture that implements smooth switching between lateral acceleration and rate modes, with proper feed-forward signals. • An arctangent limiter on rate target to follow ADS-33 Level 1 quickness versus amplitude.
Decoupling and Inversion	• Dynamic decoupling matrix from 4 inceptor inputs to 3 angular rate responses. • Combined dynamic decoupling with SISO inverse plants to create a form of Explicit Model Following (EMF). • With EMF, easily selectable, and de-selectable, vertical rate model following. • With Dynamic Inversion, easily selectable, and de-selectable, nonlinear vertical rate model following. • Showed the effects of neglected actuation and measurement dynamics upon SISO DI, and what can be done to at least partially restore performance. • Proposed a method for reducing the effects of neglected dynamics upon MIMO DI.
High Order Compensation	• Showed that by utilizing angular rate targets as inputs to HOC, in addition to angular rate errors, the HOC can be made to improve both turbulence rejection and the following of pilot-induced commands. • Derivation of equal-weighting H_2/H_∞ Compensator with $B_1D_{21}^T \neq 0$ and $C_1^TD_{12} \neq 0$ (see Equation (5-37)), which is noted to match a published pure H_∞ solution.

Chapter 2

Simulation Models and Design Environment

The airframe dynamics and control laws were derived, implemented, and evaluated in MATLAB-Simulink R2012a. The airframe dynamics consist of bare airframe dynamics plus actuator and sensor dynamics. The source for all bare airframe models is the GENHEL-PSU UH-60, a nonlinear blade-element helicopter flight dynamics model, written in FORTRAN 90. This flight dynamics model is derived from code obtained from Sikorsky Helicopters and documented by Howlett in Ref. [25]. The boost actuators are second order with natural frequency 4.7 Hz and damping ratio 0.7, rate limited to full throw in 0.1 second.

2.1 Linear Bare Airframe

Linear bare airframe dynamic models were extracted from the GENHEL-PSU UH-60 model, in all the configurations and at all the trim speeds considered. These models were utilized by MATLAB scripts and implemented in Simulink models, together with the control laws, for design and evaluation.

As extracted from GENHEL-PSU, the linear models have the following states and inputs. All linear model states and inputs are deviations from trim, which in notated with a Δ in front of the name. For those states that are zero in trim, the Δ notation is not applied.

GENHEL-PSU UH-60 states:

$\Delta u, \Delta v, \Delta w$ } body-frame translational rates, i.e. velocity forward, right, and down

p, q, r } body-frame angular rates, i.e. roll rate, pitch rate, and yaw rate

$\Delta\varphi, \Delta\theta, \Delta\psi$ } body frame attitude in Euler angles, i.e. roll, pitch, and heading

$\Delta\beta_0$, $\dot{\beta}_0$ } main rotor coning angle and coning angle rate

$\Delta\beta_{1c}$, $\dot{\beta}_{1c}$ } main rotor longitudinal flapping and rate thereof

$\Delta\beta_{1s}$, $\dot{\beta}_{1s}$ } main rotor lateral flapping and rate thereof

$\Delta\zeta_0, \dot{\zeta}_0, \Delta\zeta_{1c}, \dot{\zeta}_{1c}, \Delta\zeta_{1s}, \dot{\zeta}_{1s}$ } main rotor lead-lag terms and rates thereof

$\Delta\lambda_0$, $\Delta\lambda_{1c}$, $\Delta\lambda_{1s}$ } main rotor inflow up to the first harmonic

$\Delta\Omega$ } main rotor speed

plus four engine states.

GENHEL-PSU UH-60 inputs:

$\Delta\delta_{lat}$ } lateral input (to the mechanical mixer)

$\Delta\delta_{lng}$ } longitudinal input (to the mechanical mixer)

$\Delta\delta_{col}$ } collective input (to the mechanical mixer)

$\Delta\delta_{ped}$ } pedals input (to the mechanical mixer)

$\Delta\delta_{tht}$ } engine throttle

Throughout the present work main rotor speed is taken to be constant, meaning the following states and inputs are always truncated: Ω and the four engine states, and δ_{tht}. This means the high fidelity linear models used in this work have 24 states and 4 inputs. State truncation is achieved by removing from the state and input matrices the rows and columns associated with the state, and removing the state from the state vector. Input truncation is achieved by removing from the input matrices the column associated with the input, and removing the input from the input vector. In math notation, the truncation process is shown by Equations (2-1) and (2-2) below. The states and inputs to keep are the vectors $\mathbf{x}_k$ and $\boldsymbol{\delta}_k$, and the states and inputs to truncate are the vectors $\mathbf{x}_t$ and $\boldsymbol{\delta}_t$.

$$\begin{Bmatrix}\dot{\mathbf{x}}_k\\ \dot{\mathbf{x}}_t\end{Bmatrix}=\begin{bmatrix}\mathbf{A}_{k,k} & \mathbf{A}_{k,t}\\ \mathbf{A}_{t,k} & \mathbf{A}_{t,t}\end{bmatrix}\begin{Bmatrix}\mathbf{x}_k\\ \mathbf{x}_t\end{Bmatrix}+\begin{bmatrix}\mathbf{B}_{k,k} & \mathbf{B}_{k,t}\\ \mathbf{B}_{t,k} & \mathbf{B}_{t,t}\end{bmatrix}\begin{Bmatrix}\boldsymbol{\delta}_k\\ \boldsymbol{\delta}_t\end{Bmatrix}$$
$$\mathbf{y}=\begin{bmatrix}\mathbf{C}_k & \mathbf{C}_t\end{bmatrix}\begin{Bmatrix}\mathbf{x}_k\\ \mathbf{x}_t\end{Bmatrix}+\begin{bmatrix}\mathbf{D}_k & \mathbf{D}_t\end{bmatrix}\begin{Bmatrix}\boldsymbol{\delta}_k\\ \boldsymbol{\delta}_t\end{Bmatrix} \tag{2-1}$$

$$\begin{aligned}\dot{\mathbf{x}}_k &= \mathbf{A}_{k,k}\mathbf{x}_k+\mathbf{B}_k\boldsymbol{\delta}_k\\ \mathbf{y} &= \mathbf{C}_k\mathbf{x}_k+\mathbf{D}_k\boldsymbol{\delta}_k\end{aligned} \tag{2-2}$$

2.2 Stitched Full Flight Envelope Bare Airframe Model

All results presented here were obtained using a full flight envelope flight dynamics model, formed by stitching (Zivan and Tischler, Ref. [26]) the 24-state linear models of the GENHEL-PSU UH-60 and adding actuator and sensor dynamics. The model stitching approach of Zivan and Tischler moves the 6-DOF propagation from the linear model to the Newton-Euler nonlinear formulas, in addition to interpolating between linear models based on (in the present work) forward speed.

2.3 Reduced Order Linear Bare Airframe Models

For the purpose of designing the Dynamic Inversion and Explicit Model Following elements, low order models are derived from the high fidelity linear models. The model order reduction was achieved through a combination of residualization and truncation.

States associated with fast dynamics are removed via residualization. Those states are treated as though they instantly reach their steady-state values, as follows. The states to keep are the vector $\mathbf{x}_k$, and the states to residualize are the vector $\mathbf{x}_r$.

$$\begin{Bmatrix} \dot{\mathbf{x}}_k \\ \dot{\mathbf{x}}_r = 0 \end{Bmatrix} = \begin{bmatrix} \mathbf{A}_{k,k} & \mathbf{A}_{k,r} \\ \mathbf{A}_{r,k} & \mathbf{A}_{r,r} \end{bmatrix} \begin{Bmatrix} \mathbf{x}_k \\ \mathbf{x}_r \end{Bmatrix} + \begin{bmatrix} \mathbf{B}_k \\ \mathbf{B}_r \end{bmatrix} \boldsymbol{\delta}$$
$$\mathbf{y} = \begin{bmatrix} \mathbf{C}_k & \mathbf{C}_r \end{bmatrix} \begin{Bmatrix} \mathbf{x}_k \\ \mathbf{x}_r \end{Bmatrix} + \mathbf{D}\boldsymbol{\delta} \tag{2-3}$$

Next solve for the quasi-steady $\mathbf{x}_r$.

$$0 = \begin{bmatrix} \mathbf{A}_{r,k} & \mathbf{A}_{r,r} \end{bmatrix} \begin{Bmatrix} \mathbf{x}_k \\ \mathbf{x}_r \end{Bmatrix} + \mathbf{B}_r \boldsymbol{\delta}$$
$$\mathbf{x}_r = -\mathbf{A}_{r,r}^{-1} \left(\mathbf{A}_{r,k} \mathbf{x}_k + \mathbf{B}_r \boldsymbol{\delta} \right) \tag{2-4}$$

Substitute this result into the kept dynamics and into the output formula.

$$\begin{aligned}\dot{\mathbf{x}}_k &= \begin{bmatrix}\mathbf{A}_{k,k} & \mathbf{A}_{k,r}\end{bmatrix}\begin{Bmatrix}\mathbf{x}_k \\ -\mathbf{A}_{r,r}^{-1}\left(\mathbf{A}_{r,k}\mathbf{x}_k + \mathbf{B}_r\boldsymbol{\delta}\right)\end{Bmatrix} + \mathbf{B}_k\boldsymbol{\delta} \\ &= \mathbf{A}_{k,k}\mathbf{x}_k - \mathbf{A}_{k,r}\mathbf{A}_{r,r}^{-1}\left(\mathbf{A}_{r,k}\mathbf{x}_k + \mathbf{B}_r\boldsymbol{\delta}\right) + \mathbf{B}_k\boldsymbol{\delta} \\ \mathbf{y} &= \begin{bmatrix}\mathbf{C}_k & \mathbf{C}_r\end{bmatrix}\begin{Bmatrix}\mathbf{x}_k \\ -\mathbf{A}_{r,r}^{-1}\left(\mathbf{A}_{r,k}\mathbf{x}_k + \mathbf{B}_r\boldsymbol{\delta}\right)\end{Bmatrix} + \mathbf{D}\boldsymbol{\delta} \\ &= \mathbf{C}_k\mathbf{x}_k - \mathbf{C}_r\mathbf{A}_{r,r}^{-1}\left(\mathbf{A}_{r,k}\mathbf{x}_k + \mathbf{B}_r\boldsymbol{\delta}\right) + \mathbf{D}\boldsymbol{\delta}\end{aligned} \tag{2-5}$$

Finally, rearrange into standard form.

$$\begin{aligned}\dot{\mathbf{x}}_k &= \left(\mathbf{A}_{k,k} - \mathbf{A}_{k,r}\mathbf{A}_{r,r}^{-1}\mathbf{A}_{r,k}\right)\mathbf{x}_k + \left(\mathbf{B}_k - \mathbf{A}_{k,r}\mathbf{A}_{r,r}^{-1}\mathbf{B}_r\right)\boldsymbol{\delta} \\ \mathbf{y} &= \left(\mathbf{C}_k - \mathbf{C}_r\mathbf{A}_{r,r}^{-1}\mathbf{A}_{r,k}\right)\mathbf{x}_k + \left(\mathbf{D} - \mathbf{C}_r\mathbf{A}_{r,r}^{-1}\mathbf{B}_r\right)\boldsymbol{\delta}\end{aligned} \tag{2-6}$$

For the DI and EMF design models, starting with a high fidelity 24 state model, as described in Section 2.1 , main rotor blade dynamics (flapping and lagging) and inflow dynamics are residualized. Other states are truncated, as described next. For Dynamic Inversion (Section 4.3), and for EMF for Angular Rates (Section 4.2.1), truncated states are forward speed (Δu), and the attitudes ($\Delta\varphi$, $\Delta\theta$, $\Delta\psi$). For EMF for Vertical Rate (Section 4.2.2), pitch attitude ($\Delta\theta$) is not truncated, as it is used to form the vertical rate output. The following equations show the state truncation operation. The states to keep are the vector $\mathbf{x}_k$, and the states to truncate are the vector $\mathbf{x}_t$.

$$\begin{aligned}\begin{Bmatrix}\dot{\mathbf{x}}_k \\ \dot{\mathbf{x}}_t = 0\end{Bmatrix} &= \begin{bmatrix}\mathbf{A}_{k,k} & \mathbf{A}_{k,t} \\ \mathbf{A}_{t,k} & \mathbf{A}_{t,t}\end{bmatrix}\begin{Bmatrix}\mathbf{x}_k \\ \mathbf{x}_t = 0\end{Bmatrix} + \begin{bmatrix}\mathbf{B}_k \\ \mathbf{B}_t\end{bmatrix}\boldsymbol{\delta} \\ \mathbf{y} &= \begin{bmatrix}\mathbf{C}_k & \mathbf{C}_t\end{bmatrix}\begin{Bmatrix}\mathbf{x}_k \\ \mathbf{x}_t = 0\end{Bmatrix} + \mathbf{D}\boldsymbol{\delta}\end{aligned} \tag{2-7}$$

$$\begin{aligned}\dot{\mathbf{x}}_k &= \mathbf{A}_{k,k}\mathbf{x}_k + \mathbf{B}_k\boldsymbol{\delta} \\ \mathbf{y} &= \mathbf{C}_k\mathbf{x}_k + \mathbf{D}\boldsymbol{\delta}\end{aligned} \tag{2-8}$$

Actuation dynamics are not included in the reduced order linear airframe models used to derive EMF and DI control laws. Therefore, in the formulas above, **u** could have been used in the place of $\boldsymbol{\delta}$.

Chapter 3

Baseline Control Features

The Baseline Control consists of low-order Dynamic Inversion, command models with feed-forward compensation, and proportional-lag (PL) or proportional-integral (PI) feedback control. Together, these provide command-model-following and enhanced stability across the flight envelope. The dynamic inversion reduces cross-coupling and is speed-scheduled, so the plant to be controlled by the remainder of the control system is more diagonally dominant and more consistent across the speed range. The Baseline control has an architecture that accommodates degraded modes with sensor failures. Specifically it can revert to Rate Mode to operate with only angular rate and climb rate sensors.

The next chapter deals with the comparison of two methods for MIMO dynamic inversion. The remaining sub-sections of this chapter present aspects of the Baseline Control that are independent of the dynamic inversion method.

3.1 Partial Authority with Trim Follow-Up for the Chapter 5 Study

For the Chapter 5 study, "High Order Compensator Augmentation of a Baseline Partial Authority Controller", the pitch, roll, and yaw control are implemented through partial authority SAS actuators with trim follow-up to relieve SAS bias. There is nothing novel presented in this sub-section; it is just documentation of the partial authority implementation.

The SAS actuators are second order with natural frequency 5 Hz and damping ratio 0.8. Position limits are ±10%, and rate limits depend upon the control axis; pitch: 20%/s, roll: 40%/s, yaw: 25%/s.

The trim follow-up functional diagram is shown by Figure 3-1. Trim follow-up is at the rate of 5%/second, with a first order filter to smooth the starting and stopping, and is only active when the associated inceptor is in detent. The trim follow-up logic incorporates a ±2% deadband, to prevent constant trim motor activity, and time delay to give the pilot time to react, in the event of a run-away SAS actuator, prior to the trim follow-up exacerbating the situation. The trim filter frequency is set so that

when the SAS bias enters the deadband with the trim rate at full, the trim motion will continue such that the SAS is approximately centered. The formula is freq = rate/deadband, which in this case is freq = 5/2 = 2.5 rad/second.

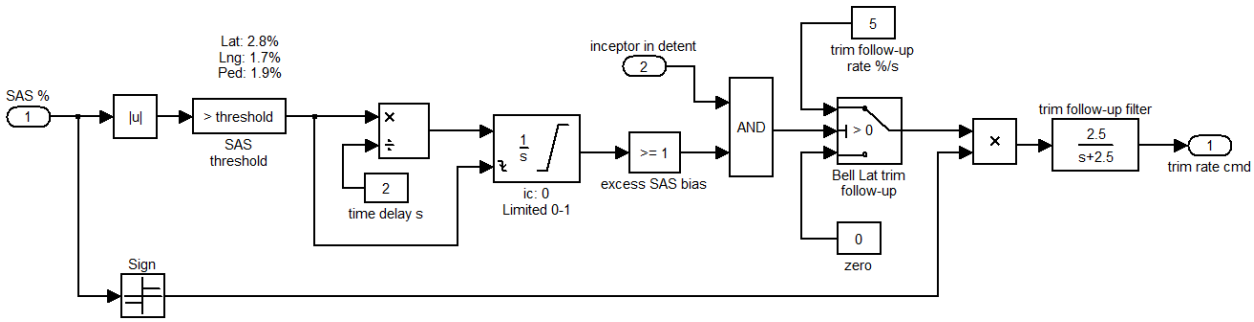

Figure 3-1: Trim Follow-Up

In vertical, control is implemented through full authority trim alone (no SAS actuator). All trim motors are rate-limited to 5%/second.

3.2 Response Types

The active Baseline control mode in each axis depends upon the mode number that is selected and the helicopter speed, as detailed in Figure 3-2 through Figure 3-5. The abbreviations in those figures are defined below.

Init	Initialization.
Manual	Manual. Direct stick-to-head functionality.
RC	Rate Command.
ACAH	Attitude Command Attitude Hold.
RCAH	Rate Command Attitude Hold.
TRC	Translational Rate Command
PH	Position Hold
+HH	Heading Hold added to the active roll mode.
ACSH	Attitude Command Speed Hold.
RCHH	Rate Command Heading Hold.

LatAccel	Lateral Acceleration Command and Hold.
+TC	Turn Coordination added to the active directional mode.
CR	Climb Rate Hold
Alt	Altitude Hold

	Horz Spd			Fwd & Side Spd		Fwd Spd		
AP Mode		PH spd tolerance		TRC max spd		Lat ACAH max spd		HdgHld selected & Fwd Spd > 40 kts
-2	Init							
-1	Manual							
0	RC							
1	ACAH					↔	RCAH	+HH
2	TRC			↔	ACAH	↔	RCAH	+HH
3	PH	↔	TRC	↔	ACAH	↔	RCAH	+HH

Figure 3-2: Lateral Axis Modes

	Horz Spd			Fwd & Side Spd		Fwd Spd	
AP Mode		PH spd tolerance		TRC max spd		Lng ACAH max spd	
-2	Init						
-1	Manual						
0	RC						
1	ACAH					↔	ACSH
2	TRC			↔	ACAH	↔	ACSH
3	PH	↔	TRC	↔	ACAH	↔	ACSH

Figure 3-3: Longitudinal Axis Modes

The values for the transition speeds above are:

Position Hold Speed Tolerance = 2 knots

Translational Rate Command Max Speed = 6 knots

Lateral Attitude Command Attitude Hold Max Speed = 50 knots

Longitudinal Attitude Command Attitude Hold Max Speed = 50 knots

		Forward Speed			
			Blending for Fwd Spd 40-60		AP Mode 1 or higher & Fwd Spd > 40 kts
AP Mode	-2	Init			
	-1	Manual			
HdgHld & APmode >= 1	false	RC	↔	LatAccel	+TC
	true	RCHH	↔	LatAccel	+TC

Figure 3-4: Directional Axis Modes

AP Mode Vert	
-1	Manual
0	CR
1	Alt

Figure 3-5: Vertical Axis Modes

3.3 Command Models

3.3.1 **Pitch and Roll**

The Pitch and Roll command models have the same structure, so they will be discussed together. The primary objective is command-model-following in both rate and attitude modes, meaning there is a feed-forward signal that will theoretically produce the commanded response with no feedback correction. A secondary objective is that the rate mode remain active as a loop inside the attitude mode, facilitating smooth transitions between rate and attitude modes. These objectives are accomplished with the architecture shown by Figure 3-6 and Figure 3-7.

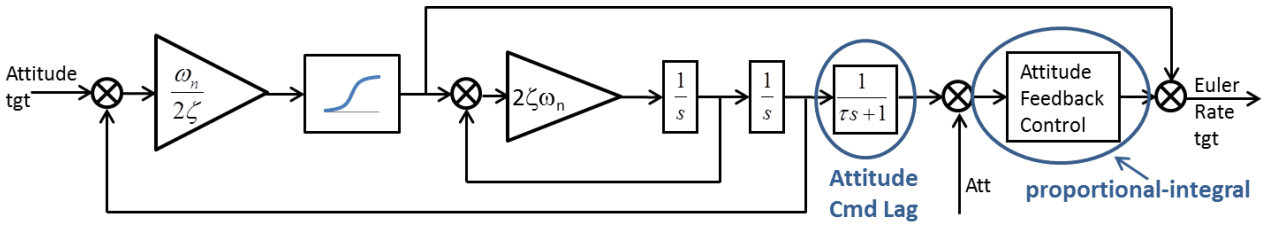

Figure 3-6: Attitude Command Model

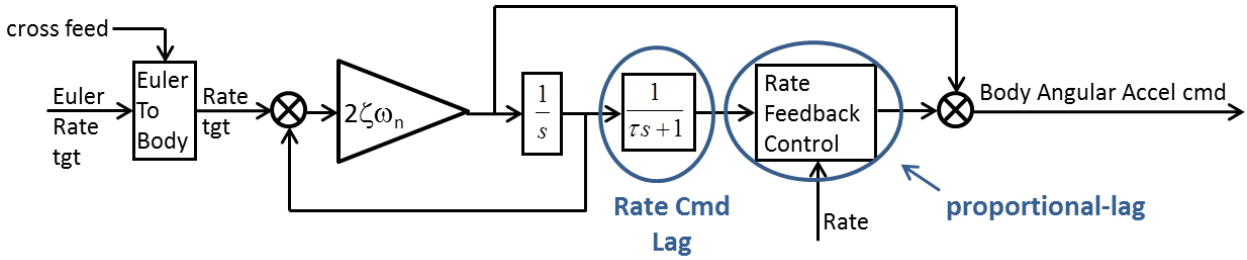

Figure 3-7: Angular Rate Command Model

When in rate mode, the command model is first-order, with time-constant $1/2\zeta\omega_n$. When in attitude mode, the command model is second-order and includes a duplication of the rate command model. Proper initialization combined with the attitude command model feed-forward causes the rate command model to approximately match the rate-loop within the attitude command model. The rate command model feed-forward is an acceleration command, and with proper initialization of the rate command, if this acceleration command is met, the vehicle will follow the command model. So, this parallel rate loops architecture, together with the dynamic inversion, provides command-model-following.

3.3.2 **Yaw**

Yaw rate control has the same rate command model and feedback architecture as pitch and roll (Figure 3-7), but without the Euler-To-Body conversion, as the body-frame yaw rate is the one used throughout the yaw control law. At low speed, yaw rate target is set to a fixed angular rate per % pedal. At high speed, yaw rate target is derived from the lateral acceleration target, which in turn is set to a fixed acceleration per % pedal. Also at high speed, if in attitude mode, the yaw rate necessary for coordinated turning is added to the yaw rate target so that pedal input is not needed:

$$r_{\text{tgt,tc}} = \frac{g}{V}\sin(\phi)\cos(\theta) \tag{3-1}$$

where g is magnitude of gravitational acceleration, V is true airspeed, ϕ is roll attitude, and θ is pitch attitude. Low speed is less than 40kts; high speed is greater than 60kts. At speeds between 40 and 60 kts, the the low-speed and high-speed yaw rate targets are blended.

In the two major studies, presented in Chapter 4 and Chapter 5 , the way differs by which yaw rate target is derived from lateral acceleration target at high speed. Basically, a more advanced approach was developed for the Chapter 5 study, as will be seen by comparison of the next two sub-sections.

3.3.2.1 Yaw Rate Target from Lateral Acceleration Target, for Chapter 4

For the Chapter 4 study, MIMO Model Following Control Design Methods for Rotorcraft, the conversion from lateral acceleration target to yaw rate target is based on the steady-state yaw rate associated with the lateral acceleration:

$$r_{\text{tgt}} = \frac{g}{V} a_{y,\text{tgt}} + r_{\text{tgt,tc}} \tag{3-2}$$

3.3.2.2 Yaw Rate Target from Lateral Acceleration Target, for Chapter 5

For the Chapter 5 study, High Order Compensator Augmentation of a Baseline Partial Authority Controller, the conversion from lateral acceleration target to yaw rate target involves a lateral acceleration command model. Yaw rate target is set by the lateral acceleration command model and lateral acceleration error proportional feedback. The lateral acceleration command model is diagramed in Figure 3-8, together with how it interacts with lateral acceleration feedback control and turn coordination to produce the yaw rate target.

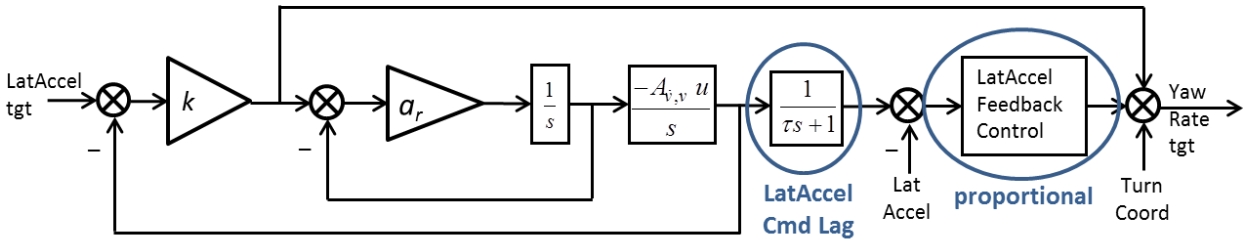

Figure 3-8: Lateral Acceleration Command Model and Feedback Control

The gain *k* is calculated on the fly using

$$k = \frac{a_r}{4\zeta^2\left(-A_{\dot{v},v}u\right)} \tag{3-3}$$

where $\zeta = 0.7$ is the desired damping ratio, u is forward airspeed, v is sideward airspeed, a_r is the corner frequency of the yaw rate command model, and $A_{\dot{v},v}$ is the stability derivative that relates $\dot{v}$ to v .

3.3.3 **Vertical**

The vertical control command model architecture is very similar to pitch and roll. The differences are: (1) altitude replaces attitude, and (2) there is no conversion between altitude rate command and vertical rate command.

Vertical control works as follows. When the collective is pushed out of detent or the collective Force Trim Release (FTR) button is pressed, the detent is frozen and vertical control is not active. Vertical control is reactivated

a) Upon return to detent

b) Upon release of collective trigger (FTR button)

When vertical control is reactivated, a fixed vertical control target is captured. In climb rate mode, vertical control captures current climb rate as the fixed climb rate target. If the captured climbrate is less than 200 ft/min, climb rate target is set to zero. In altitude mode, vertical control captures a fixed altitude target based on a second order command model, such that the initial climb rate target approximately matches the climb rate. Figure 3-9 through Figure 3-12 show examples of rate and altitude capture upon return to detent.

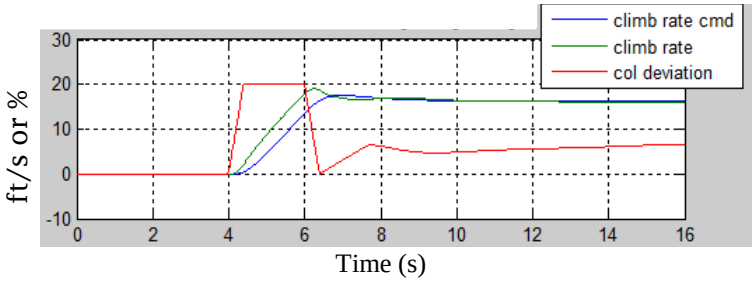

Figure 3-9: Vertical Rate Capture – 10 knots

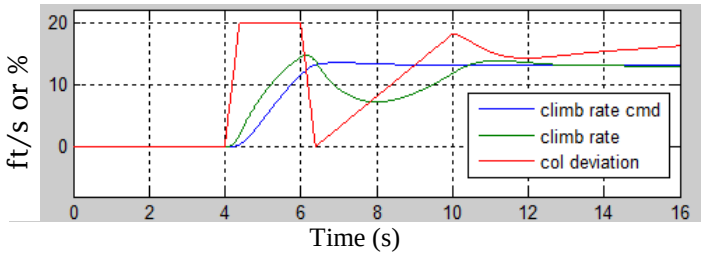

Figure 3-10: Vertical Rate Capture – 120 knots

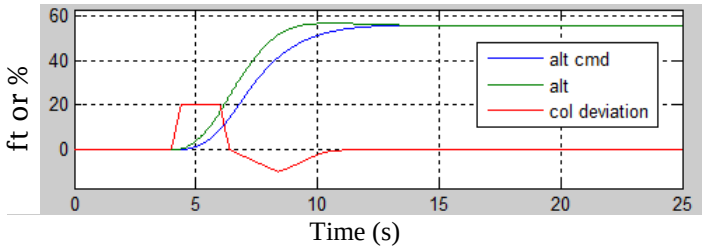

Figure 3-11: Altitude Capture – 10 knots

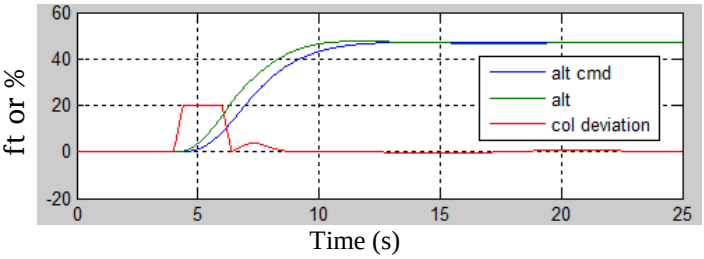

Figure 3-12: Altitude Capture – 120 knots

3.3.4 **Command Lag Study**

Note that, in a command model following architecture, the commands are truth, while feedback must be based on measured. Therefore, prior to comparing commands against the measured values, the commands pass through a lag that approximates the measurement lag. In most command-model-following control laws, these command lags have no effect on loop stability margins since they are part of the feed forward only. However, with the parallel rate loops architecture, in attitude mode the rate command lag is within the attitude feedback loop, so it affects attitude mode gain and phase margins. Two alternatives were considered: 1) eliminating the rate command lags in the parallel-rate-command-loops architecture when in attitude mode, and 2) a different architecture that puts the rate command lag outside of the attitude feedback loop. Figure 3-13 shows this architecture.

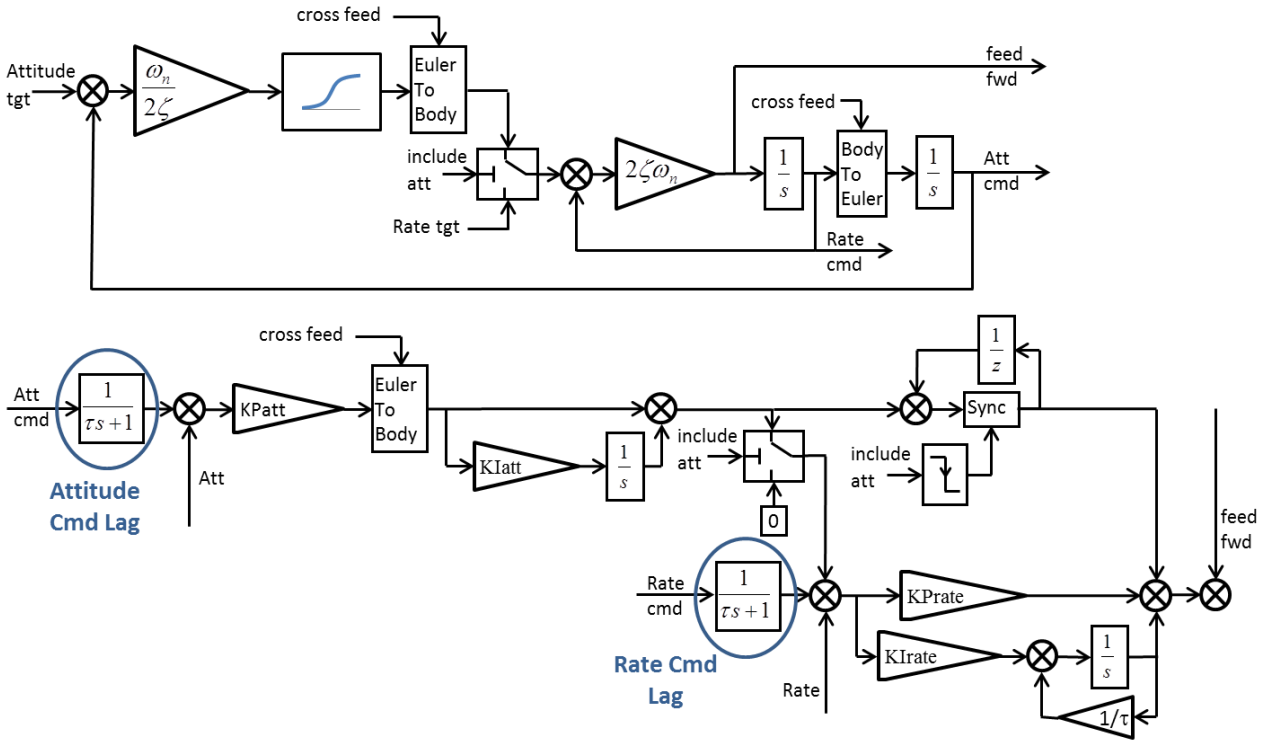

Figure 3-13: Single Rate Command Loop Command Model (not selected)

In the present application, there appears to be no net benefit from either effort to avoid rate command lag within the attitude feedback loop, as shown by Table 3-1. In this table, the results from the two alternative architectures are color-coded: yellow for noticeably worse, and green for noticeably better.

Table 3-1. Effects of Removing Rate Command Lag within Attitude Feedback Loop

		Margins in Attitude/Altitude Mode					
		Rate Error Proportional-Lag Control (similar to Proportional-Integral)					
		With Rate Cmd Lags		Without Rate Cmd Lags		Single Rate Command Loop	
Axis	Speed [kts]	Gain Margin [dB]	Phase Margin [deg]	Gain Margin [dB]	Phase Margin [deg]	Gain Margin [dB]	Phase Margin [deg]
Lat	10	9.19	45.1	7.30	48.2	7.01	46.6
	120	6.04	52.2	5.16	54.0	5.11	52.4
Lng	10	6.66	45.0	6.45	42.3	6.27	40.4
	120	16.20	45.2	15.90	49.0	15.90	53.9
Col	10	17.80	45.3	17.70	40.7	17.60	37.5
	120	9.22	55.7	9.03	48.6	8.75	43.8
Ped	10	10.30	55.3	10.20	55.5	10.20	55.5
	120	11.00	45.9	10.90	45.9	10.90	45.8
		gains tuned with rate cmd lags		same gain, bypassed the lags		same gain, single rate cmd loop	

3.3.5 **Controlling Attitude Command Model Quickness versus Amplitude**

The pitch and roll attitude command models should be designed to meet the ADS-33 Level 1 quickness specification (Ref. [24]). By applying a step change to the attitude target, one finds that an arctangent limiter on the rate target (see Figure 3-6) produces quickness versus amplitude that followes the trend in the ADS-33 specification. Without any limiter the command model dynamics would be linear, so quickness would be the same regardless of amplitude. Other command model variations evaluated for quickness versus amplitude were (a) a simple limiter on the rate target, and (b) a rate limiter with no other dynamics. The results are shown in Figure 3-14. The advantage to following the contour of the Level 1 boundary, on the side of Level 1, is that Level 1 handling qualities are achieved but with less stress on the rotorcraft components compared against a control law that is more aggressive than necessary.

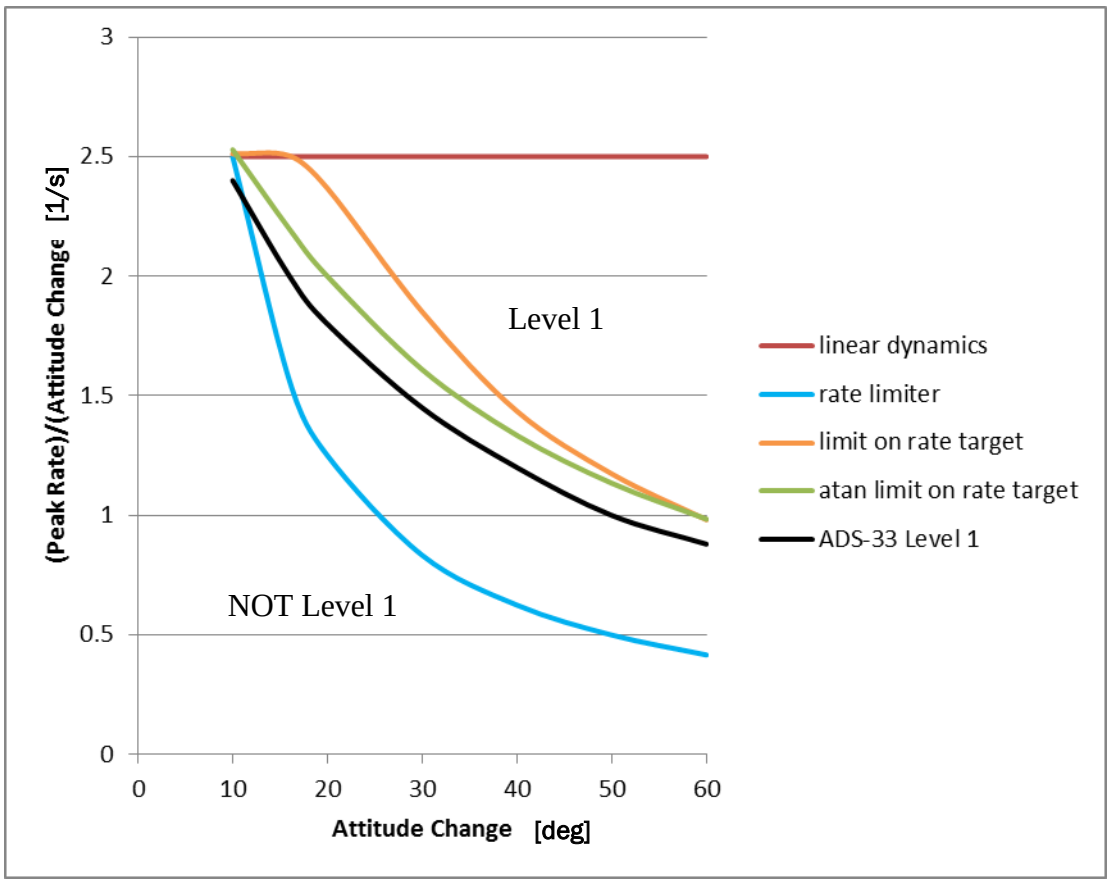

Figure 3-14: Attitude Command Model Quickness Comparison

Chapter 4

MIMO Model Following Control Design Methods

The present chapter presents and compares two multi-input multi-output (MIMO) model-following control design methods for rotorcraft. The first combines single-input single-output (SISO) inverse plants (Refs. [27], [28], and [29]) with a dynamic decoupling matrix (Refs. [2] and [30]). This purely feed-forward approach to inverting the plant is called Explicit Model Following (EMF) in this dissertation. The second is Dynamic Inversion (DI), which involves both feed-forward and feedback path elements to invert the plant (Refs. [1], [31], [32], and [33]). The EMF design is purely linear, while the DI design has some nonlinear elements in vertical rate control to account for roll and pitch attitude.

For each of these methods, an architecture is presented that provides angular rate model-following with selectable vertical rate model-following, such that the angular rate control always accounts for the vertical inputs, and when the vertical rate model-following is active it accounts for the angular inputs. Both approaches are based on reduced order models, and are speed-scheduled. The same command model is utilized with both approaches, and feedback control is applied to the error between the command model and measured responses.

These two MIMO model-following approaches are evaluated by coupling them with a full flight envelope flight dynamics model, described in Section Chapter 2. Evaluation criteria are (1) fidelity to the command model, analyzed in both frequency and time domains, and (2) turbulence rejection measured in root-mean-square (RMS) of the responses.

4.1 EMF and DI with SISO 1st Order Plant

Comparison between EMF and DI begins by considering the simplest case: controlling a 1st order SISO plant. In the following analysis perfect plant inversion is not assumed; the inverse plant is based on an identified plant, which differs from the actual plant. Parameters associated with the plant are given the subscript ‘p’, and those associated with the identified plant have subscript ‘ip’. No command model is

necessary for this comparison, although one would be necessary for implementation to provide the command (y_{cmd}) and its derivative. Feedback control is included to compensate for modeling errors, and the response transfer functions are derived for command and disturbance inputs.

4.1.1 **SISO Explicit Model Following**

The SISO Inverse Plant approach is shown clearly by Harding, et al., (Ref. [27]). Figure 4-1 diagrams the simplest implementation for a 1st order system. The plant inversion components are inside the dashed box.

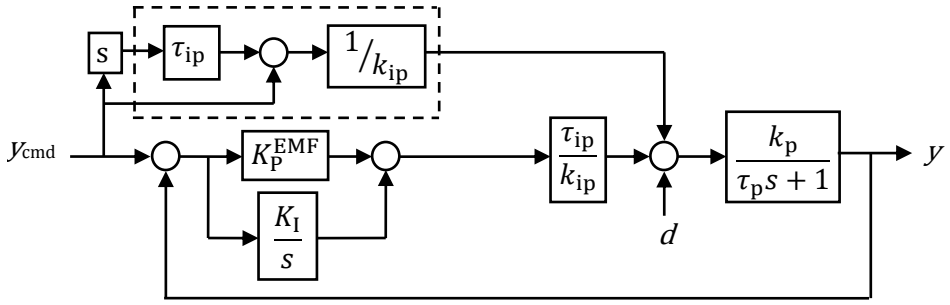

Figure 4-1. SISO Explicit Model Following diagram.

4.1.2 **SISO Dynamic Inversion**

The Dynamic Inversion approach is state-space, so inherently MIMO, as shown in Stevens and Lewis (Ref. [1]). But when simplified for a 1st order SISO plant, it takes the form shown in Figure 4-2. The plant inversion components are inside the dashed box.

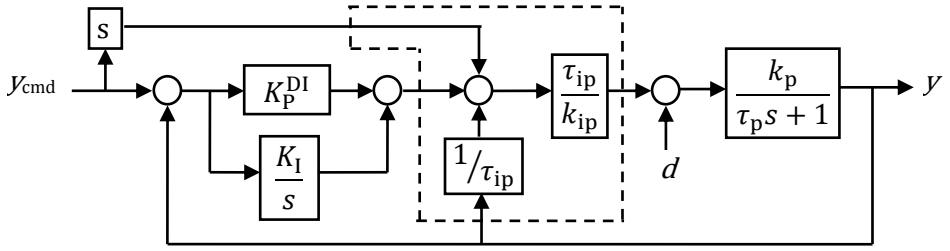

Figure 4-2. SISO Dynamic Inversion diagram.

4.1.3 **Comparison: EMF and DI with SISO 1st order plant**

Performing the block algebra reveals that the two approaches yield identical transfer functions when

$$K_{\mathrm{P}}^{\mathrm{EMF}} = K_{\mathrm{P}}^{\mathrm{DI}} - 1/\tau_{\mathrm{ip}} \tag{4-1}$$

(see Table 4-1). The simplicity of this substitution is due to the $\tau_{\mathrm{ip}} / k_{\mathrm{ip}}$ term placed in the EMF feedback control path.

Table 4-1. SISO Transfer Functions of EMF and DI

	SISO EMF and DI
$\left(\frac{y}{y_{\mathrm{cmd}}}\right)$	$\frac{\frac{k_{\mathrm{p}}}{k_{\mathrm{ip}}}\frac{\tau_{\mathrm{ip}}}{\tau_{\mathrm{p}}}\left[s^2 + K_{\mathrm{P}}^{\mathrm{DI}} s + K_{\mathrm{I}}\right]}{s^2 + \left(\frac{k_{\mathrm{p}}}{k_{\mathrm{ip}}}\frac{\tau_{\mathrm{ip}}}{\tau_{\mathrm{p}}}K_{\mathrm{P}}^{\mathrm{DI}} + \left(1 - \frac{k_{\mathrm{p}}}{k_{\mathrm{ip}}}\right)\frac{1}{\tau_{\mathrm{p}}}\right)s + \frac{k_{\mathrm{p}}}{k_{\mathrm{ip}}}\frac{\tau_{\mathrm{ip}}}{\tau_{\mathrm{p}}}K_{\mathrm{I}}}$
$\left(\frac{y}{d}\right)$	$\frac{\frac{k_{\mathrm{p}}}{\tau_{\mathrm{p}}}s}{s^2 + \left(\frac{k_{\mathrm{p}}}{k_{\mathrm{ip}}}\frac{\tau_{\mathrm{ip}}}{\tau_{\mathrm{p}}}K_{\mathrm{P}}^{\mathrm{DI}} + \left(1 - \frac{k_{\mathrm{p}}}{k_{\mathrm{ip}}}\right)\frac{1}{\tau_{\mathrm{p}}}\right)s + \frac{k_{\mathrm{p}}}{k_{\mathrm{ip}}}\frac{\tau_{\mathrm{ip}}}{\tau_{\mathrm{p}}}K_{\mathrm{I}}}$

This SISO analysis gave us guidance on design of the MIMO EMF feedback paths, and a starting point for EMF feedback gain selection, based on the DI feedback gains. Note that if the plant is perfectly identified, the (speed scheduled) DI transforms the plant into an integrator from the perspective of the feedforward and feedback control signals. Therefore, the feedback gains do not need to be scheduled with speed. The EMF proportional feedback gain does need to be speed scheduled. Taking Equation (4-1) as the scheduling law, where $K_{\mathrm{P}}^{\mathrm{DI}}$ is constant and $1/\tau_{\mathrm{ip}}$ is a function of forward speed, yields EMF closed-loop transfer functions that are identical to DI in the SISO case.

4.2 MIMO EMF

The MIMO EMF design, developed here, combines the SISO inverse plant feedforward approach presented in Harding, et al. (Ref. [27]) with extensions of the dynamic decoupling approach presented in

Catapang et al. (Ref. 27). Extensions to the dynamic decoupling in Ref. [2] are increasing the dimensions from 2x2 to 3x4, and including selectable climb rate decoupling. Figure 4-3 is a diagram of this architecture; the notation therein is defined in the following sub-sections.

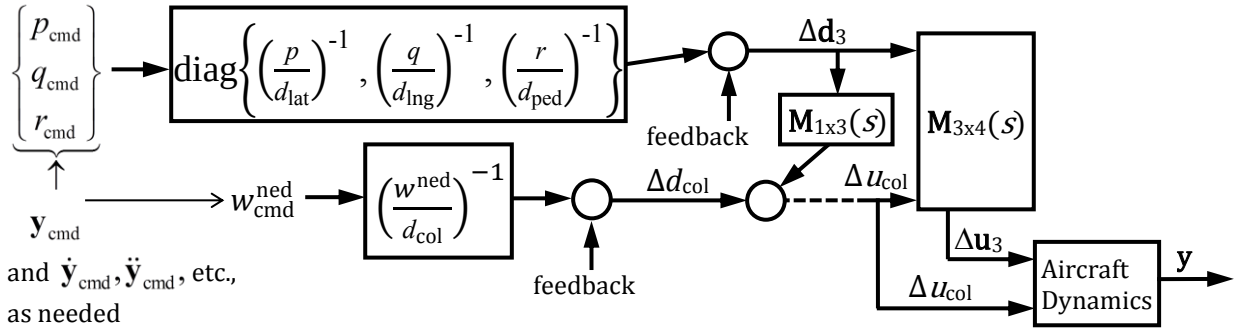

Figure 4-3. MIMO EMF diagram.

The transfer functions of the dynamic mixing matrices, and the inverses of the decoupled plants, can be high-order and unstable. For example, if the decoupled dynamics have a right-half-plane zero, the associated inverse plant is unstable. Because an unstable decoupling matrix or inverse plant is unacceptable, and high order is undesirable, the theoretically exact transfer functions are replaced with stable low-order approximations through frequency-domain fitting over the range $1 \text{ rad/sec} \le \omega \le 10 \text{ rad/sec}$ (Ref. [2] did the same over 2 to 10 rad/sec). Specifically, all poles λ of the plant inverses and mixing elements are forced to have damping ratio $\zeta \ge 0.3$ and $\text{Re}(\lambda) \le -0.2$. To ensure numerical stability, a limit on the magnitude of the poles is also enforced: $|\lambda| \le (2\,\Delta t)^{-1}$. Good to excellent frequency matching was obtained with the following transfer function order specifications (numerator order / denominator order): mixing elements (2/2), d_{lat}/p (1/0), d_{lng}/q (2/1), d_{ped}/r (2/1), d_{col}/w^{ned} (1/0).

4.2.1 **MIMO EMF for Angular Rates**

All the EMF and DI designs evaluated in this work are based on reduced-order linear models at specific forward trim speeds. For MIMO EMF for Angular Rates, the reduced-order model has input, state, and output vectors:

$$\Delta\mathbf{u} = \begin{bmatrix} \begin{bmatrix} \Delta u_{\text{lat}} & \Delta u_{\text{lng}} & \Delta u_{\text{ped}} \end{bmatrix} \triangleq \Delta\mathbf{u}_3^{\text{T}} & \Delta u_{\text{col}} \end{bmatrix}^{\text{T}} \tag{4-2}$$

$$\Delta\mathbf{x} = \begin{bmatrix} \Delta v & \Delta w & p & q & r \end{bmatrix}^{T} \tag{4-3}$$

$$\mathbf{y} = \begin{bmatrix} p & q & r \end{bmatrix}^{\text{T}} \tag{4-4}$$

Because actuation dynamics are neglected, the bare airframe input $\boldsymbol{\delta} = \mathbf{u}$. For states and inputs that are normally trimmed to non-zero, the Δ notation is applied. In standard form, this design model is:

$$\begin{aligned} \Delta\dot{\mathbf{x}} &= \mathbf{A}\Delta\mathbf{x} + \mathbf{B}\Delta\mathbf{u} \\ \mathbf{y} &= \mathbf{C}_{pqr}\Delta\mathbf{x}\ , \quad \text{where } \mathbf{C}_{pqr} = \begin{bmatrix} \mathbf{0}_{3x2} & \mathbf{I}_3 \end{bmatrix} \end{aligned} \tag{4-5}$$

This state-space linear system is converted to a plant transfer function matrix:

$$\mathbf{P}(s) = \frac{\mathbf{y}}{\mathbf{u}}(s) = \mathbf{C}_{pqr}\left[s\mathbf{I} - \mathbf{A}\right]^{-1}\mathbf{B} = \mathbf{C}_{pqr}\frac{\text{Adj}\left(s\mathbf{I} - \mathbf{A}\right)}{\left|s\mathbf{I} - \mathbf{A}\right|}\mathbf{B} \tag{4-6}$$

The denominator of $\mathbf{P}(s)$ is a scalar, and the numerator is

$$\mathbf{N}(s) = \mathbf{C}_{pqr}\left[\text{Adj}\left(s\mathbf{I} - \mathbf{A}\right)\right]\mathbf{B} \tag{4-7}$$

The EMF approach utilizes the method of invariant dynamic decoupling (Refs. [2] and [30]) to diagonalize the system, as shown in Equation (4-8).

$$\begin{Bmatrix} p \\ q \\ r \end{Bmatrix} = \underbrace{\begin{bmatrix} \frac{p}{u_{\text{lat}}} & \frac{p}{u_{\text{lng}}} & \frac{p}{u_{\text{ped}}} & \frac{p}{u_{\text{col}}} \\ \frac{q}{u_{\text{lat}}} & \frac{q}{u_{\text{lng}}} & \frac{q}{u_{\text{ped}}} & \frac{q}{u_{\text{col}}} \\ \frac{r}{u_{\text{lat}}} & \frac{r}{u_{\text{lng}}} & \frac{r}{u_{\text{ped}}} & \frac{r}{u_{\text{col}}} \end{bmatrix}}_{\mathbf{P}(s)} \begin{bmatrix} 1 & \frac{u_{\text{lat}}}{d_{\text{lng}}} & \frac{u_{\text{lat}}}{d_{\text{ped}}} & \frac{u_{\text{lat}}}{u_{\text{col}}} \\ \frac{u_{\text{lng}}}{d_{\text{lat}}} & 1 & \frac{u_{\text{lng}}}{d_{\text{ped}}} & \frac{u_{\text{lng}}}{u_{\text{col}}} \\ \frac{u_{\text{ped}}}{d_{\text{lat}}} & \frac{u_{\text{ped}}}{d_{\text{lng}}} & 1 & \frac{u_{\text{ped}}}{u_{\text{col}}} \\ 0 & 0 & 0 & 1 \end{bmatrix} \triangleq \mathbf{M}_{3x4} \begin{Bmatrix} \overbrace{\begin{Bmatrix} \Delta d_{\text{lat}} \\ \Delta d_{\text{lng}} \\ \Delta d_{\text{ped}} \end{Bmatrix}}^{\triangleq \Delta\mathbf{d}_3} \\ \Delta u_{\text{col}} \end{Bmatrix} = \begin{bmatrix} \frac{p}{d_{\text{lat}}} & 0 & 0 & 0 \\ 0 & \frac{q}{d_{\text{lng}}} & 0 & 0 \\ 0 & 0 & \frac{r}{d_{\text{ped}}} & 0 \end{bmatrix} \begin{Bmatrix} \Delta\mathbf{d}_3 \\ \Delta u_{\text{col}} \end{Bmatrix} \tag{4-8}$$

Each of the elements of the mixing matrix $\mathbf{M}_{3x4}$ are solved in terms of the elements of $\mathbf{N}(s)$, as shown in Appendix A. The decoupled dynamics are then:

$$\frac{p}{d_{\text{lat}}} = \frac{p}{u_{\text{lat}}} + \frac{p}{u_{\text{lng}}}\frac{u_{\text{lng}}}{d_{\text{lat}}} + \frac{p}{u_{\text{ped}}}\frac{u_{\text{ped}}}{d_{\text{lat}}} \tag{4-9}$$

$$\frac{q}{d_{\text{lng}}} = \frac{q}{u_{\text{lng}}} + \frac{q}{u_{\text{lat}}}\frac{u_{\text{lat}}}{d_{\text{lng}}} + \frac{q}{u_{\text{ped}}}\frac{u_{\text{ped}}}{d_{\text{lng}}} \tag{4-10}$$

$$\frac{r}{d_{\text{ped}}} = \frac{r}{u_{\text{ped}}} + \frac{r}{u_{\text{lat}}}\frac{u_{\text{lat}}}{d_{\text{ped}}} + \frac{r}{u_{\text{lng}}}\frac{u_{\text{lng}}}{d_{\text{ped}}} \tag{4-11}$$

The inverse plants, to be used in combination with command models, are the reciprocals of the decoupled dynamics. Given a 5-state plant, these inverse plants appear to be 13th order over 12th order. In the cases considered, the actual highest order was 3rd over 2nd after pole-zero cancellations with tolerance 0.01 rad/sec. For implementation, these "exact" transfer functions were replaced with stable approximations having highest order 2nd over 1st , as mentioned previously.

4.2.2 **MIMO EMF for Vertical Rate**

To include vertical rate as an output, pitch attitude is added as a state to the plant used in the previous section. Descent rate is then given by $w^{\text{ned}} = \Delta w - u_{\text{trm}}\Delta\theta$, where u_{trm} is body-frame forward speed in trim. When vertical rate regulation is selected, the collective actuator motion is computed using equation (4-12),

$$\Delta u_{\text{col}} = \left[\begin{bmatrix} \frac{u_{\text{col}}}{d_{\text{lat}}} & \frac{u_{\text{col}}}{d_{\text{lng}}} & \frac{u_{\text{col}}}{d_{\text{ped}}} \end{bmatrix} \triangleq \mathbf{M}_{1x3} \quad 1\right] \begin{Bmatrix} \Delta d_{\text{lat}} \\ \Delta d_{\text{lng}} \\ \Delta d_{\text{ped}} \\ \Delta d_{\text{col}} \end{Bmatrix} \tag{4-12}$$

where the elements of this row vector are designed such that only Δd_{col} produces a vertical rate response. Each of the elements of the mixing matrix $\mathbf{M}_{1x3}$ are solved in terms of the elements of $\mathbf{N}(s)$, as shown in Appendix B. The decoupled angular rate dynamics, and therefore the angular rate inverse plants, are unchanged by the specification of Δu_{col} from $\Delta\mathbf{d}$. The transfer function for the decoupled vertical dynamics, which is inverted for EMF feedforward, is given by:

$$\frac{w^{\text{ned}}}{d_{\text{col}}} = \frac{w^{\text{ned}}}{u_{\text{lat}}}\frac{u_{\text{lat}}}{u_{\text{col}}} + \frac{w^{\text{ned}}}{u_{\text{lng}}}\frac{u_{\text{lng}}}{u_{\text{col}}} + \frac{w^{\text{ned}}}{u_{\text{ped}}}\frac{u_{\text{ped}}}{u_{\text{col}}} + \frac{w^{\text{ned}}}{u_{\text{col}}} \tag{4-13}$$

Given a 6-state angular-vertical rate plant, the inverse plant appears to be 18th order over 17th order. For the cases considered, the actual highest order was 1st over 0th after pole-zero cancellations with tolerance 0.01 rad/sec.

4.3 MIMO DI

The MIMO DI design comes from Stevens and Lewis (Ref. [1]), which has been applied to helicopters by Horn et. al (e.g. Refs. [31], [32], and [33]). This approach requires feedback of all the states in the design (reduced-order) model, but the design model employed in this dissertation includes Δv and Δw, which are rarely if ever directly measured on a production rotorcraft. Therefore, for these states, estimation algorithms were developed (see Appendix C) and implemented. The previous work in helicopter DI is also extended by adding non-linear selectable vertical rate control.

4.3.1 **MIMO DI for Angular Rates**

For angular rate control, the MIMO DI design is based on the same reduced-order linear models as the corresponding MIMO EMF control system, but the collective control effect is separated from the other plant inputs:

$$\Delta\dot{\mathbf{x}} = \mathbf{A}\Delta\mathbf{x} + \mathbf{B_1}\Delta\mathbf{u}_3 + \mathbf{B_2}\Delta u_{\text{col}} \tag{4-14}$$

The first derivative of the output should follow the DI input ($\boldsymbol{\sigma}_3$), known as the pseudo-command.

$$\dot{\mathbf{y}} = \boldsymbol{\sigma}_3 \triangleq \lfloor\, \dot{p}_{\text{cmd}} \quad \dot{q}_{\text{cmd}} \quad \dot{r}_{\text{cmd}} \,\rfloor^{\text{T}} \tag{4-15}$$

Let the plant input be

$$\Delta\mathbf{u}_3 = \left[\mathbf{C}_{pqr}\mathbf{B}_1\right]^{-1}\left\{\boldsymbol{\sigma}_3 - \mathbf{C}_{pqr}\mathbf{A}\Delta\mathbf{x} - \mathbf{C}_{pqr}\mathbf{B}_2\Delta u_{\text{col}}\right\} \tag{4-16}$$

Then

$$\begin{aligned}\dot{\mathbf{y}} = \mathbf{C}_{pqr}\dot{\mathbf{x}} &= \mathbf{C}_{pqr}\mathbf{A}\mathbf{x} \;+\; \mathbf{C}_{pqr}\mathbf{B}_1\left[\mathbf{C}_{pqr}\mathbf{B}_1\right]^{-1}\left\{\boldsymbol{\sigma}_3 - \mathbf{C}_{pqr}\mathbf{A}\mathbf{x} - \mathbf{C}_{pqr}\mathbf{B}_2\Delta u_{\text{col}}\right\} \;+\; \mathbf{C}_{pqr}\mathbf{B}_2\Delta u_{\text{col}} \\ &= \boldsymbol{\sigma}_3\end{aligned} \tag{4-17}$$

So, with this design the transfer function matrix from $\boldsymbol{\sigma}_3$ to **y** is the diagonal matrix of single integrators. Schematically, this MIMO DI for Angular Rates is shown in Figure 4-4. This simple form of DI depends upon [$\mathbf{C}_{pqr}\mathbf{B}_1$] being nonsingular, which is generally the case for aircraft. A DI implementation also fails if the zero dynamics are unstable. The zero dynamics are the system modes, after DI has been applied, that are not observable through **y**, and the number of these modes is the

difference between the number of states **x** and outputs **y**. See Ref. [1] for a more extensive discussion of these DI issues. In the present work, the zero dynamics have always been stable.

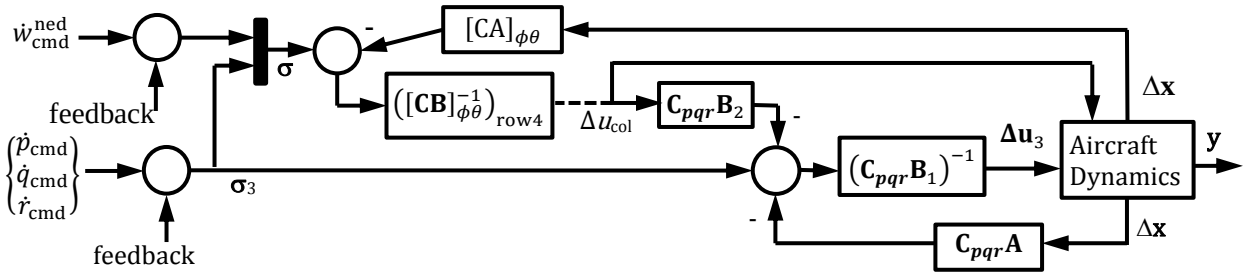

Figure 4-4. MIMO DI diagram

4.3.2 **MIMO DI for Vertical Rate**

The MIMO DI that includes vertical rate control is based on the same reduced-order linear state equations as the angular rate controllers. As a reminder, $\Delta\mathbf{x} = \begin{Bmatrix}\Delta v & \Delta w & p & q & r\end{Bmatrix}^T$ and $\Delta\mathbf{u} = \begin{Bmatrix}\Delta u_{\text{lat}} & \Delta u_{\text{lng}} & \Delta u_{\text{ped}} & \Delta u_{\text{col}}\end{Bmatrix}$. The outputs are now

$$\mathbf{y} = \begin{bmatrix} w^{\text{ned}} & p & q & r \end{bmatrix}^T \tag{4-18}$$

Next, the derivatives of the outputs are expressed in terms of the state equation matrices. The derivative of $\begin{Bmatrix}p & q & r\end{Bmatrix}^T$ is

$$\begin{bmatrix} \dot{p} & \dot{q} & \dot{r} \end{bmatrix}^T = \mathbf{C}_{pqr}\mathbf{A}\Delta\mathbf{x} + \mathbf{C}_{pqr}\mathbf{B}\Delta\mathbf{u} \tag{4-19}$$

An approximation for $\dot{w}^{\text{ned}}$ (descent acceleration) is derived in Appendix D. Combining this result, Equation (D-6), for $\dot{w}^{\text{ned}}$ with Equation (4-19), the complete expression for the output derivatives is given by Equation (4-20) .

$$\begin{aligned}\begin{Bmatrix}\dot{w}^{\text{ned}}\\ \dot{p}\\ \dot{q}\\ \dot{r}\end{Bmatrix} &= \begin{bmatrix}[\mathbf{CA}]_{\dot{w}^{\text{ned}},\phi\theta}\\ \mathbf{C}_{pqr}\mathbf{A}\end{bmatrix}\Delta\mathbf{x} + \begin{bmatrix}[\mathbf{CB}]_{\dot{w}^{\text{ned}},\phi\theta}\\ \mathbf{C}_{pqr}\mathbf{B}\end{bmatrix}\Delta\mathbf{u} \\ &= [\mathbf{CA}]_{\phi\theta}\Delta\mathbf{x} + [\mathbf{CB}]_{\phi\theta}\Delta\mathbf{u}\end{aligned} \tag{4-20}$$

The state-dependent matrices in this relation are labeled $[\mathbf{CA}]_{\phi\theta}$ and $[\mathbf{CB}]_{\phi\theta}$ to show their correspondence with linear dynamic inversion. Let the system input be

$$\Delta\mathbf{u} = [\mathbf{CB}]_{\phi\theta}^{-1}\left(\boldsymbol{\sigma} - [\mathbf{CA}]_{\phi\theta}\Delta\mathbf{x}\right) \tag{4-21}$$

where

$$\boldsymbol{\sigma} \triangleq \begin{bmatrix} \dot{w}_{\text{cmd}}^{\text{ned}} & \dot{p}_{\text{cmd}} & \dot{q}_{\text{cmd}} & \dot{r}_{\text{cmd}} \end{bmatrix}^{\text{T}} \tag{4-22}$$

is the pseudo-command. Then

$$\begin{aligned} \dot{\mathbf{y}} &= [\mathbf{CA}]_{\phi\theta}\Delta\mathbf{x} + [\mathbf{CB}]_{\phi\theta}\Delta\mathbf{u} \\ &= [\mathbf{CA}]_{\phi\theta}\Delta\mathbf{x} + [\mathbf{CB}]_{\phi\theta}[\mathbf{CB}]_{\phi\theta}^{-1}\left(\boldsymbol{\sigma} - [\mathbf{CA}]_{\phi\theta}\Delta\mathbf{x}\right) = \boldsymbol{\sigma} \end{aligned} \tag{4-23}$$

From this inversion, only use the result for Δu_{col}:

$$\Delta u_{\text{col}} = \left([\mathbf{CB}]_{\phi\theta}^{-1}\right)_{\text{row4}}\left(\boldsymbol{\sigma} - [\mathbf{CA}]_{\phi\theta}\Delta\mathbf{x}\right) \tag{4-24}$$

This is the collective motion required to achieve $\dot{w}_{\text{cmd}}^{\text{ned}}$ when the other plant inputs are acting to achieve $\{\dot{p}_{\text{cmd}} \quad \dot{q}_{\text{cmd}} \quad \dot{r}_{\text{cmd}}\}^T$, which is exactly what the DI for Angular Rates is doing.

Because the $[\mathbf{CA}]_{\phi\theta}$ and $[\mathbf{CB}]_{\phi\theta}^{-1}$ matrices depend upon roll and pitch attitudes, they must be computed in real time. However, both can be expressed as trigonometric functions of roll and pitch attitude combined with speed-scheduled matrices and vectors, which is shown in Appendix E.

4.4 Command Models Specifications

Command models receive target values from pilot inceptors, and output all commands and command derivatives needed for the inversions and for feedback control. The same command models are used for EMF and DI. The pitch and roll attitude command models are second-order, and constructed such that the inner loop of each is the corresponding first-order rate command model. Yaw rate and vertical rate command models are first order. The attitude commands natural frequencies (rad/sec) and damping

ratios are: pitch (ω_n=1.73, ζ=0.9), roll (ω_n=4.15, ζ=0.95). The rate command corner frequencies (rad/sec) are: pitch (3.11), roll (7.88), yaw (2.5), vertical (1.26).

4.5 Error Feedback Control

Rate error ($\mathbf{y}_{err}$) feedback was designed for both DI and EMF such that rate loop gain and phase margins are approximately the same for both control methods, as shown in Table 4-2.

Table 4-2. Rate Mode Gain(dB) and Phase(deg) Margins

		Lateral		Longitudinal		Pedal		Vertical	
		Gain	Phase	Gain	Phase	Gain	Phase	Gain	Phase
10 kts	EMF	12.6	87.7	14.3	54.6	15.3	51.9	10.3	68.2
	DI	14.3	77.6	16.9	55.3	11.5	52.0	10.2	67.9
120 kts	EMF	9.4	68.7	22.2	118	16.4	57.8	12.9	69.4
	DI	9.1	72.0	15.4	117	14.0	61.9	12.8	65.2

The stability margin analysis was performed using the high order stitched model, and gains adjusted until the margin requirements were satisfied. No speed scheduling was used for the DI error feedback gains (no scheduling is required in the DI method as discussed earlier). No speed scheduling was used for the EMF error feedback beyond the $1/\tau_{ip}$ term mentioned in the SISO section. The angular rate error channels employ proportional-lag (PL) control, and the vertical rate error channel uses proportional-integral (PI) control. The DI rate error proportional gain is limited to

$$K_{\mathrm{P}}^{\mathrm{DI}} \geq -A_{\dot{x},\, x} \tag{4-25}$$

to ensure that the specified rate damping is no less than the natural value identified from the design model. The EMF rate error proportional gain is formed as

$$K_{\mathrm{P}}^{\mathrm{EMF}} = \left(K_{\mathrm{P}}^{\mathrm{DI}} + A_{\dot{x},\, x} \right) k_{\mathrm{P}}^{\mathrm{EMF}} \tag{4-26}$$

where $A_{\dot{x},\, x}$ is the MIMO version of $-\tau_{\mathrm{ip}}^{-1}$, and $k_{\mathrm{P}}^{\mathrm{EMF}}$ is an adjustment used to match stability margins between DI and EMF. Similarly, for rate error lag gain or integral gain:

$$K_{\mathrm{I}}^{\mathrm{EMF}} = K_{\mathrm{I}}^{\mathrm{DI}} k_{\mathrm{I}}^{\mathrm{EMF}} \tag{4-27}$$

In MIMO control, the τ_{ip}/k_{ip} term in Figure 4-1 is interpreted to be the gain of the MIMO EMF inverse plant, when that inverse plant is expressed in the zeros-poles-gain form.

The command modes can be set to rate or attitude mode for the roll and pitch channels, rate or altitude for vertical, while the yaw channel is always rate mode. Turn coordination is active at high forward speeds via a yaw rate target contribution based on roll and pitch attitudes and airspeed (see Ref. [33]). Attitude and altitude modes operate as loops around the corresponding rate modes. Pitch and roll attitude feedback is PI, while altitude feedback is proportional (P).

In the formation of error signals, commands are conditioned through a first order lag, and sometimes a time delay, prior to differencing with the sensed value. This is to account for dynamics that were not considered in the inversions, such as actuation, rotor flapping, and sensors. The degree of command lagging is treated as a design variable and set experimentally. EMF and DI were found to prefer different degrees of rate command conditioning, while a single attitude command conditioning works well for both. Command conditioning for EMF rate errors, and for attitude errors, is set such that the conditioned commands approximately match their corresponding sensed response in the initial portion of the response to an on-axis input. DI was found to work better with less rate command lag/delay in the present application. For ease of implementation, the rate command lag time constants were set to get good DI response, and the follow-on time delays were set according to the strategy mentioned above, to get good EMF response.

4.6 Results

All results presented here were obtained using the high-order stitched bare airframe model discussed in Section Chapter 2, while reduced order bare airframe models were used to design DI and EMF, as detailed in Section 2.3 .

4.6.1 **Frequency Domain**

In the following matrices of frequency domain plots, plots on the diagonal reveal fidelity to the command model (cmdMdl), and off-diagonal plots show the cross-coupling. All input units are percent, climb rate (cr) is in feet/second, angular rates are in degrees/second, and the frequency unit is radians/second. Results from the high-order bare airframe alone are labeled "bareAFmdl". The rate mode frequency response magnitudes due to pilot inputs are shown, at low speed by Figure 4-5, and at high speed by Figure 4-6.

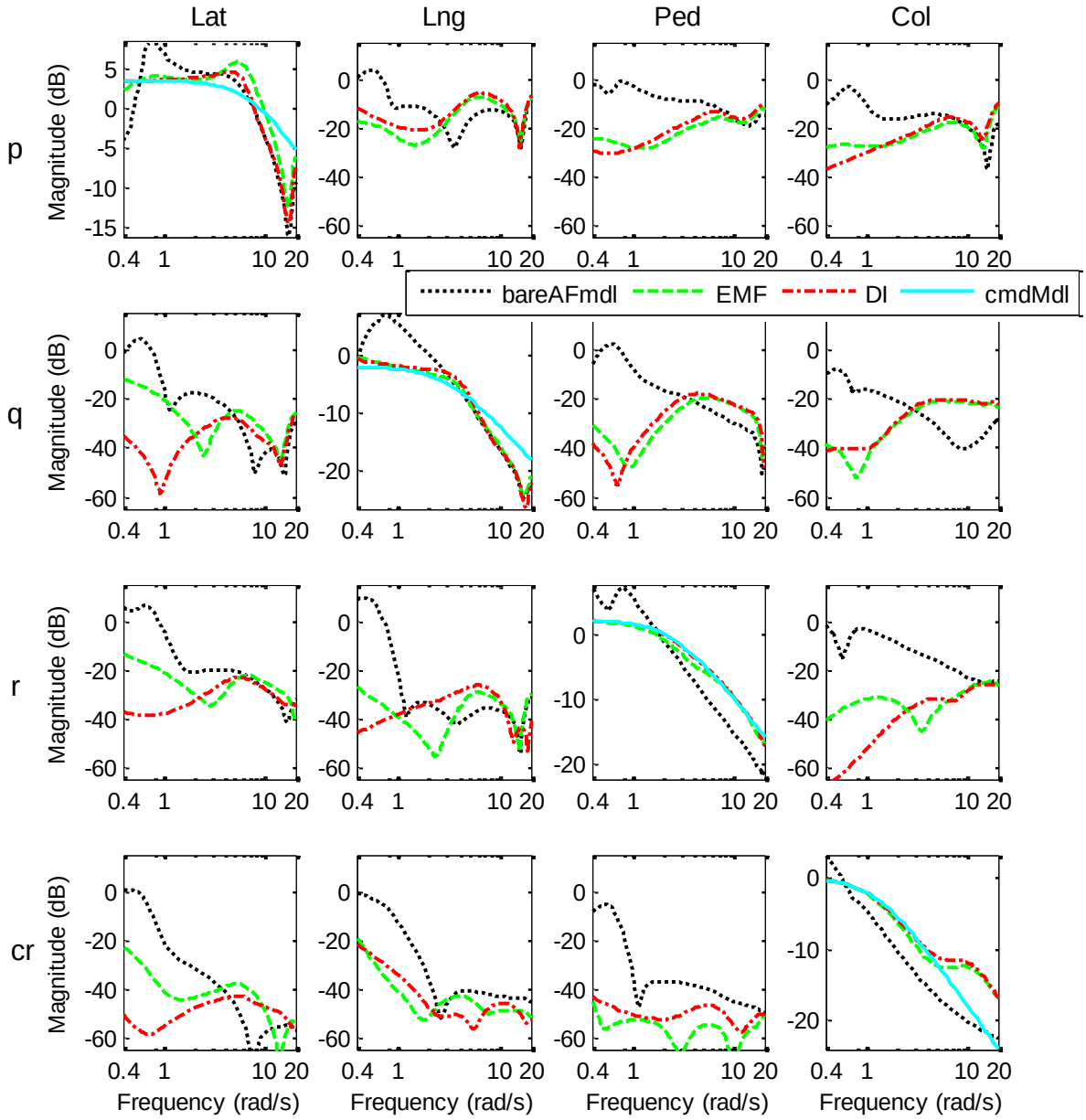

Figure 4-5. Frequency Response, Rate Mode, 10 knots

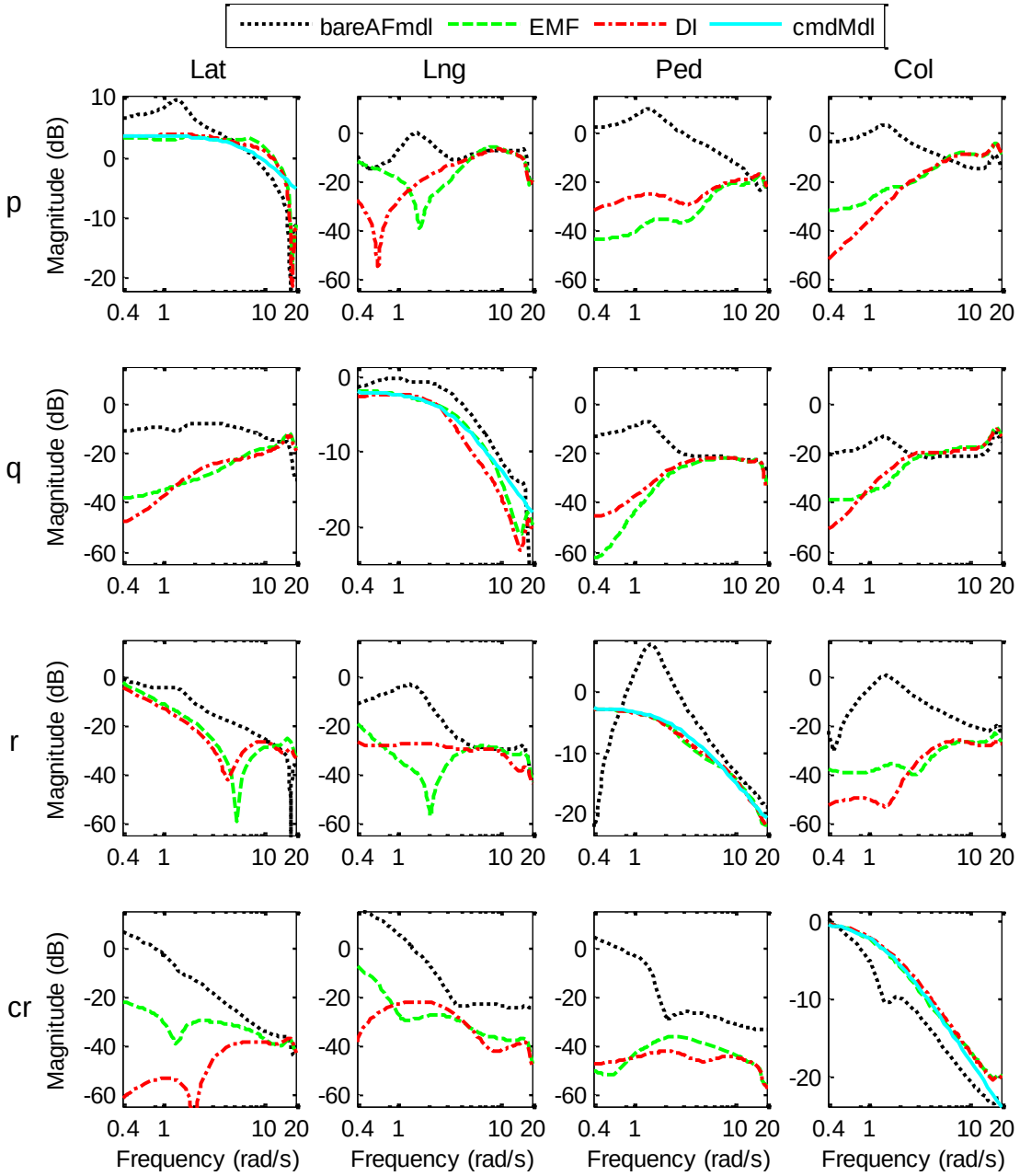

Figure 4-6. Frequency Response, Rate Mode, 120 knots

The on-axis responses (see the plots on the diagonals) are on top of the command models at lower frequencies, and at higher frequencies the responses usually deviate in some way from the command models. EMF and DI deviate similarly, and while there are a few places where a distinction between the two can be seen, they are much more similar than they are different.

Both EMF and DI reduce cross-coupling relative to the bare airframe where the bare airframe coupling is most significant. The only off-axis response that might not be helped by the rate mode control

laws is low speed Longitudinal (Lng) to roll rate (p), but this coupling is not significantly different between EMF and DI.

4.6.2 **Time Domain**

The plots below compare EMF and DI in time domain for fidelity to the command model and for decoupling. Overall, they show that the two approaches give very similar results, especially on-axis.

4.6.2.1 Angular Rate and Vertical Rate Mode

With a collective step at low speed, DI exhibits tighter control of off-axis responses (Figure 4-7). With a collective step at high speed, DI is slightly tighter in all axes (Figure 4-8).

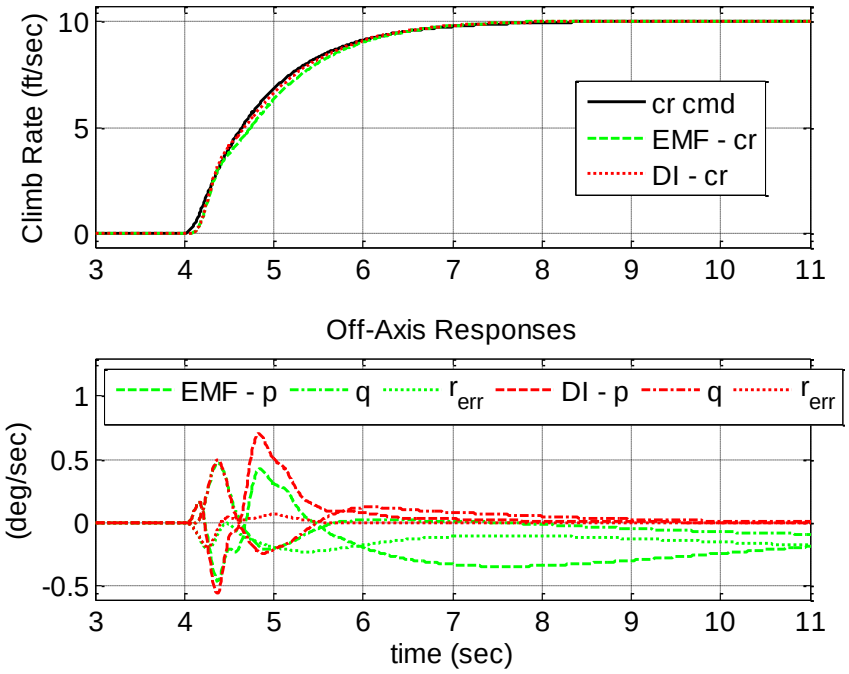

Figure 4-7. Rate Mode, Collective Step, 10 knots

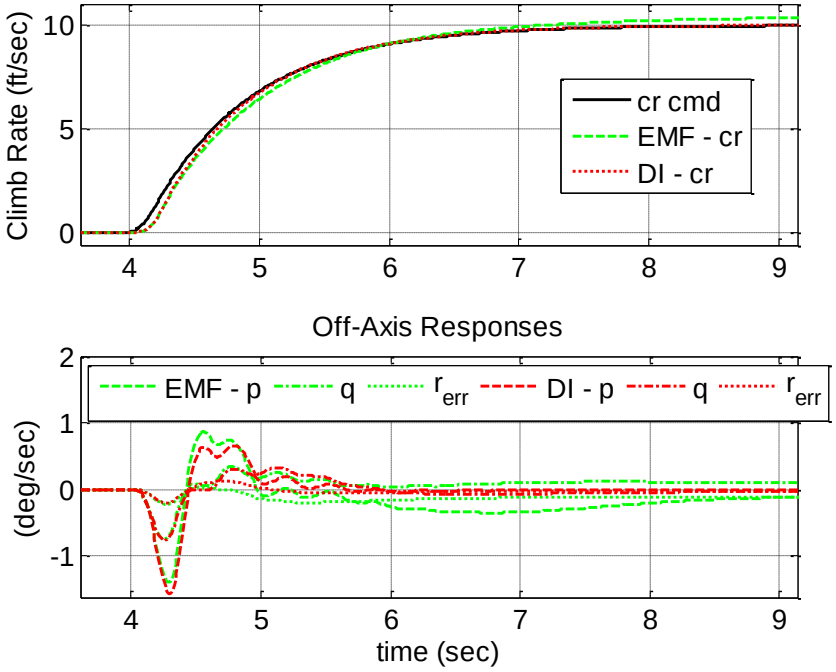

Figure 4-8. Rate Mode, Collective Step, 120 kts

The lateral pulse responses in rate mode (Figure 4-9 and Figure 4-10) show that DI is slightly better at maintaining commanded yaw rate and considerably better at suppressing off-axis response.

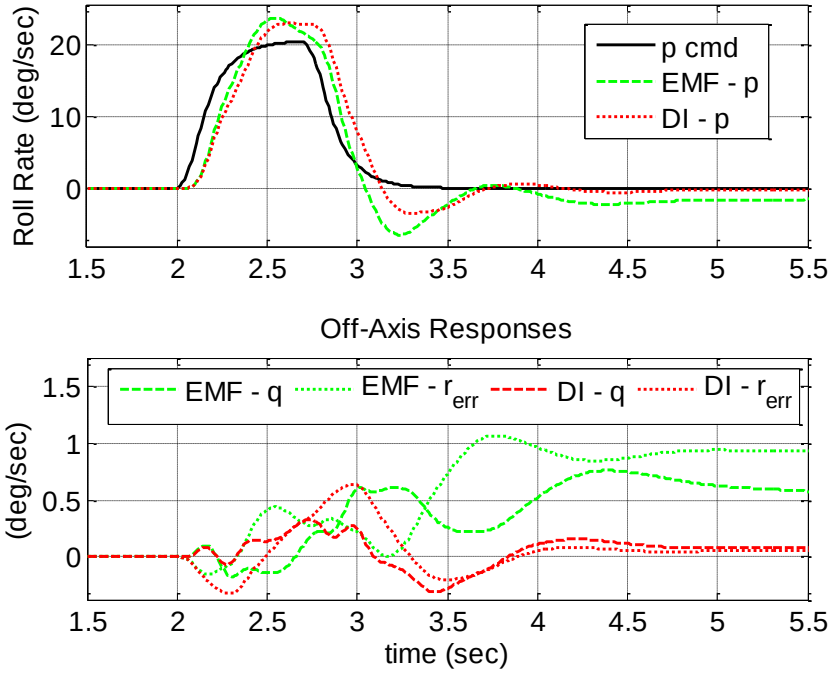

Figure 4-9. Rate Mode, Lateral Pulse, 10 kts

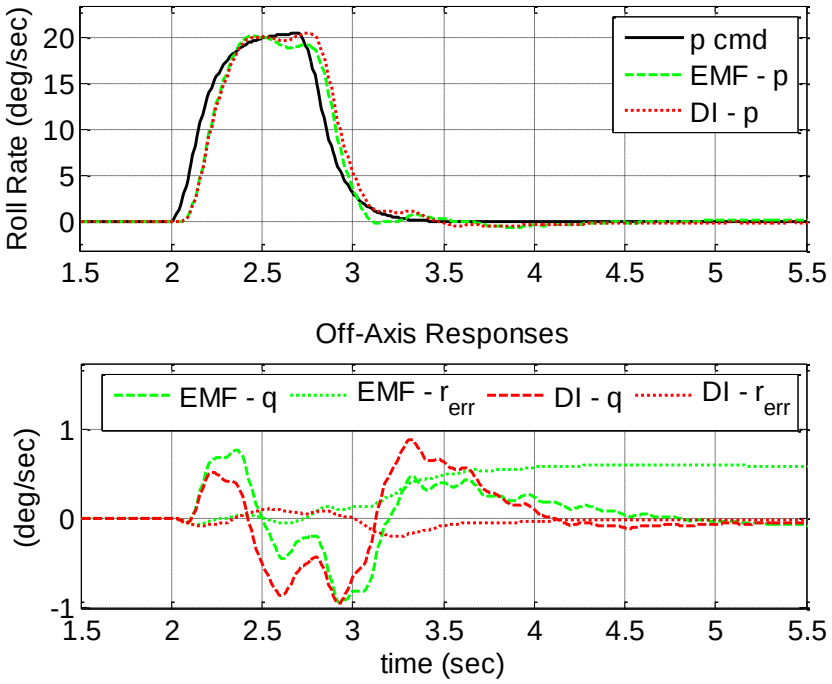

Figure 4-10. Rate Mode, Lateral Pulse, 120 kts

During the longitudinal pulse in rate mode at low speed (Figure 4-11), roll rate stabilizes well off of zero (the command) with DI, while with EMF roll rate trends toward zero. This may be because the DI *v* feedback takes out the natural speed stability.

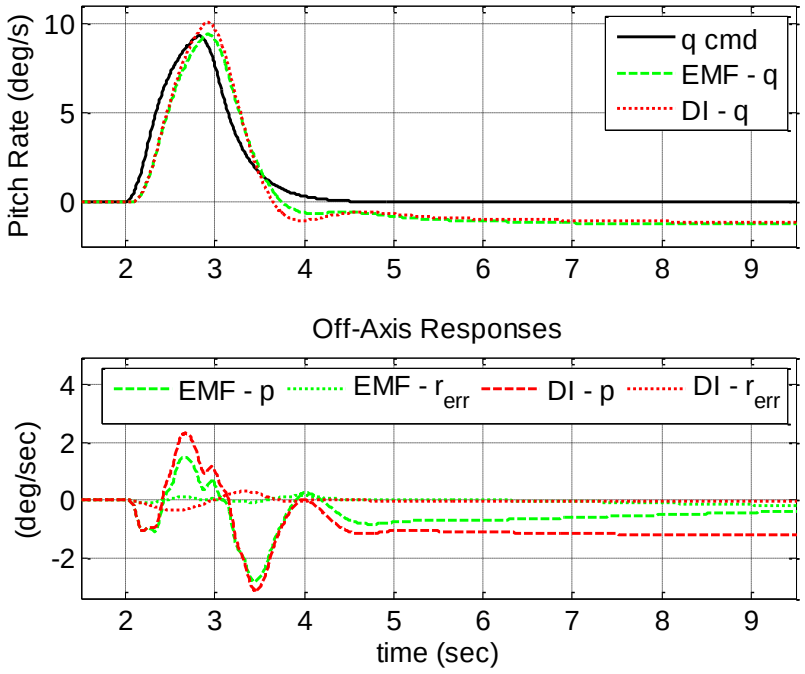

Figure 4-11. Rate Mode, Longitudinal Pulse, 10 kts

Figure 4-12 shows that the EMF pitch rate response more tightly follows the command during a longitudinal pulse in rate mode at high speed.

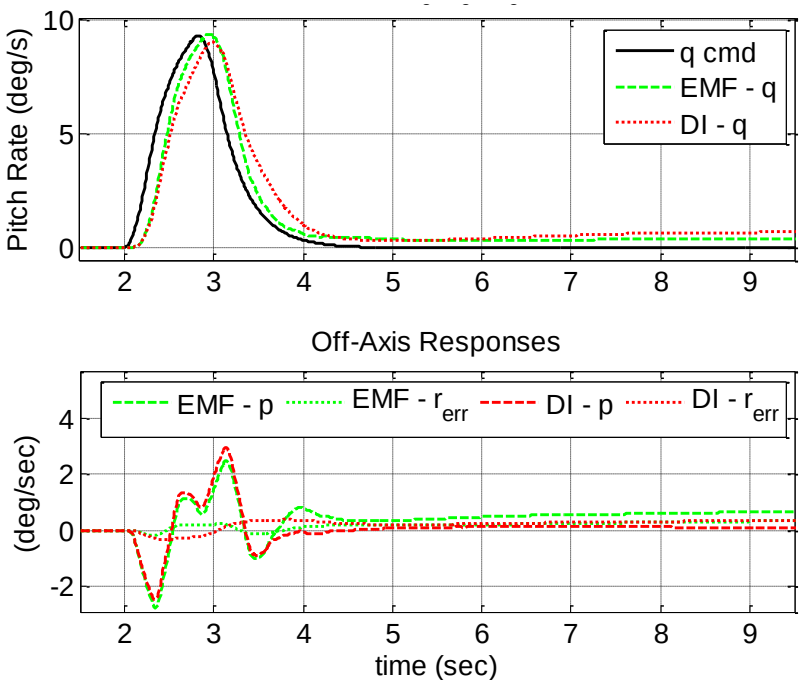

Figure 4-12. Rate Mode, Longitudinal Pulse, 120 kts

4.6.2.2 Attitude and Vertical Rate Mode

In the roll attitude response, near hover, EMF takes longer to achieve the target (Figure 4-13). This is probably due to sideslip, produced by a change in roll angle, for which EMF does not compensate. The sideslip produces an opposite direction roll moment, which the attitude feedback (PI) is eventually able to overcome. The reason the EMF does not compensate for sideslip produced by a roll angle change is two-fold. Roll attitude is not included as a state of the design model. Also, even if roll attitude were included in the design model, the constraint on the poles of the inverse plants would likely diminish the near-integrator type feedforward input that is required to compensate for roll-induced sideslip. DI compensates for lateral speed through the feedback of the estimated side speed state. This is also why DI maintains yaw rate near zero (the command), while EMF does not.

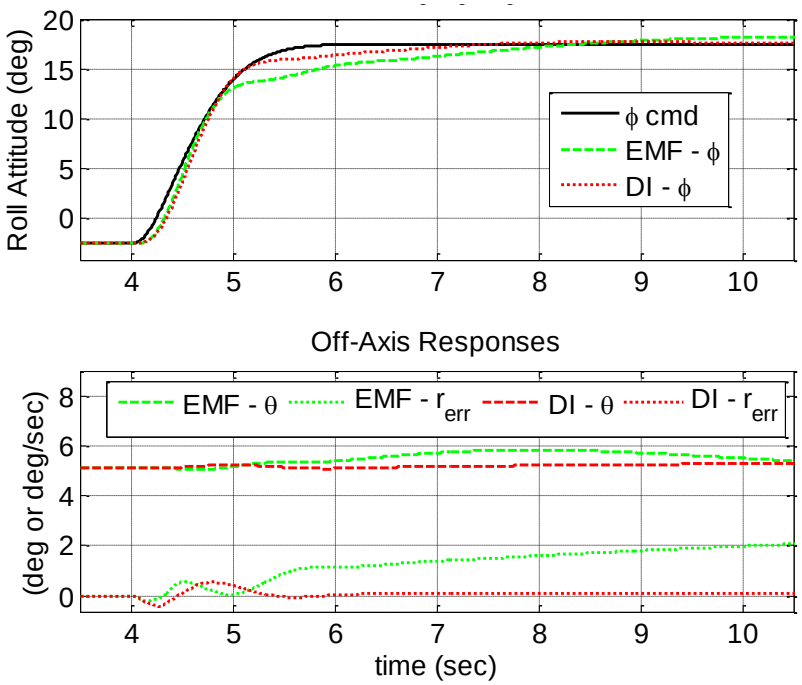

Figure 4-13. Attitude Mode, Lateral Step, 10 kts

In the roll attitude response test at high speed (Figure 4-14) DI is better at maintaining the off-axis commands (the starting values).

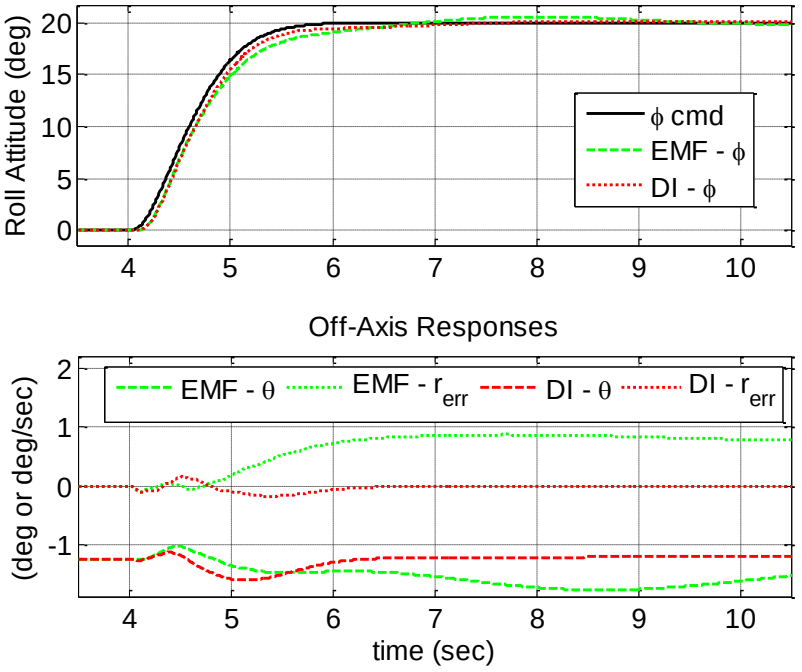

Figure 4-14. Attitude Mode, Lateral Step, 120 kts

In the low speed pitch attitude response (Figure 4-15), pitch stabilizes short of the command using either inversion strategy. This is due to uncompensated speed stability. The bare airframe inputs from the

control laws are the sum of two components, $\Delta\mathbf{u}$ and $\mathbf{u}_{trm}$. Due to the assumption that airspeed cannot be measured near hover, $\mathbf{u}_{trm}$ is static, while at higher forward speed $\mathbf{u}_{trm}$ is a function of airspeed which effectively neutralizes speed stability.

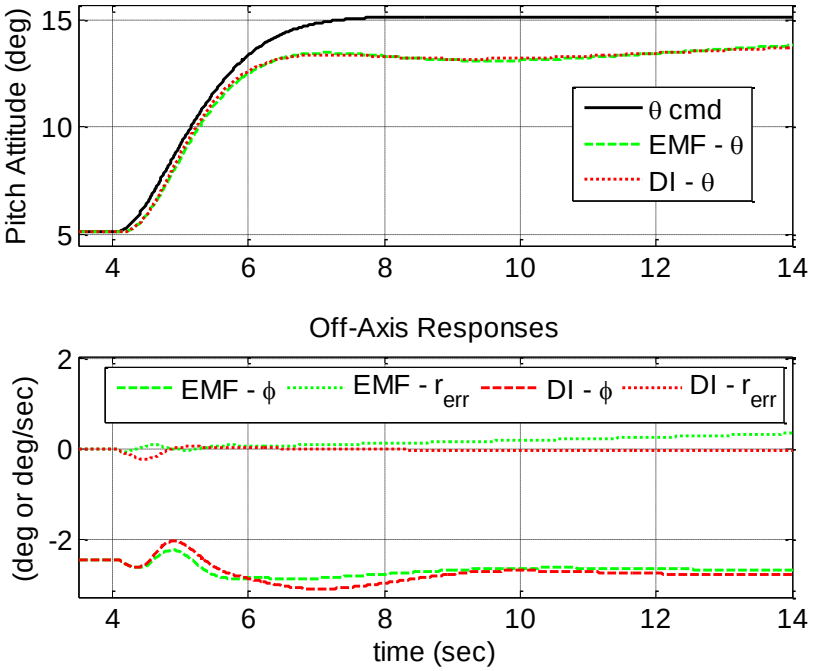

Figure 4-15. Attitude Mode, Longitudinal Step, 10 kts

In the pitch attitude response at high speed, yaw rate error is worse with DI than with EMF (Figure 4-16), but all off-axis responses are small. The pitch attitude command does not approach a constant value because the pitch attitude target is a constant deviation from trim attitude, but trim attitude is changing with forward speed.

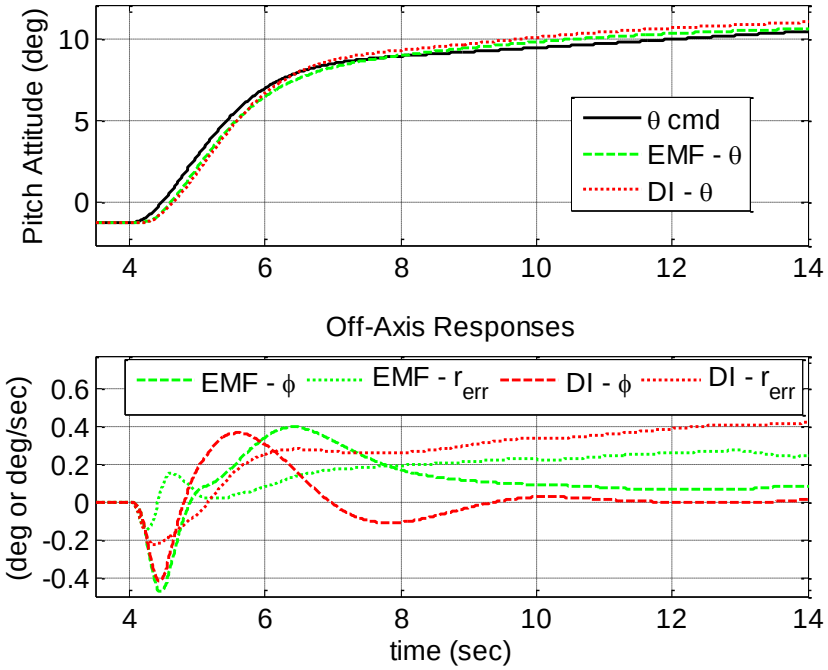

Figure 4-16. Attitude Mode, Longitudinal Step, 120 kts

In the attitude mode pedal pulse tests, DI is better at roll control at low speed (Figure 4-17), while EMF and DI have nearly equal performance at high speed (Figure 4-18).

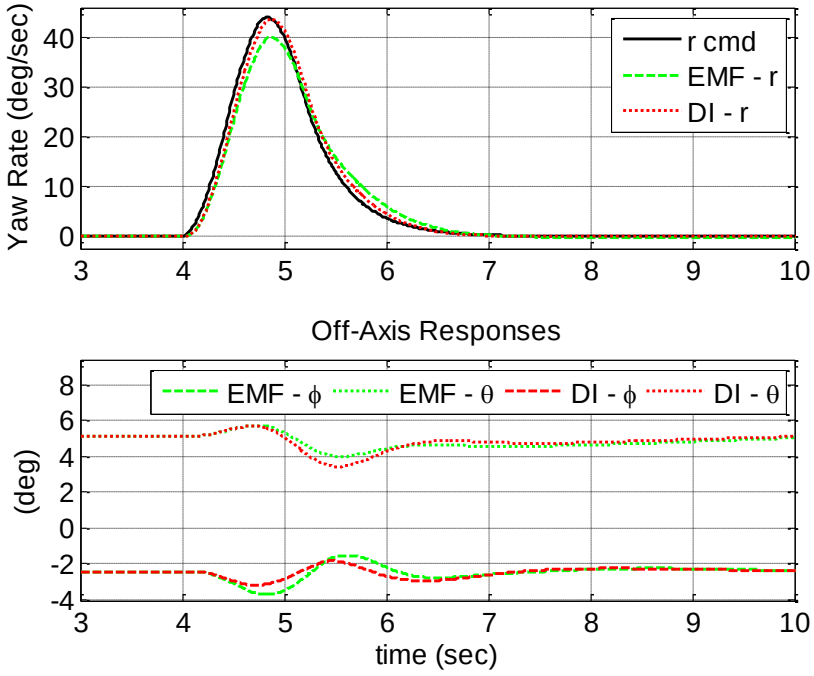

Figure 4-17. Attitude Mode, Pedal Pulse, 10 kts

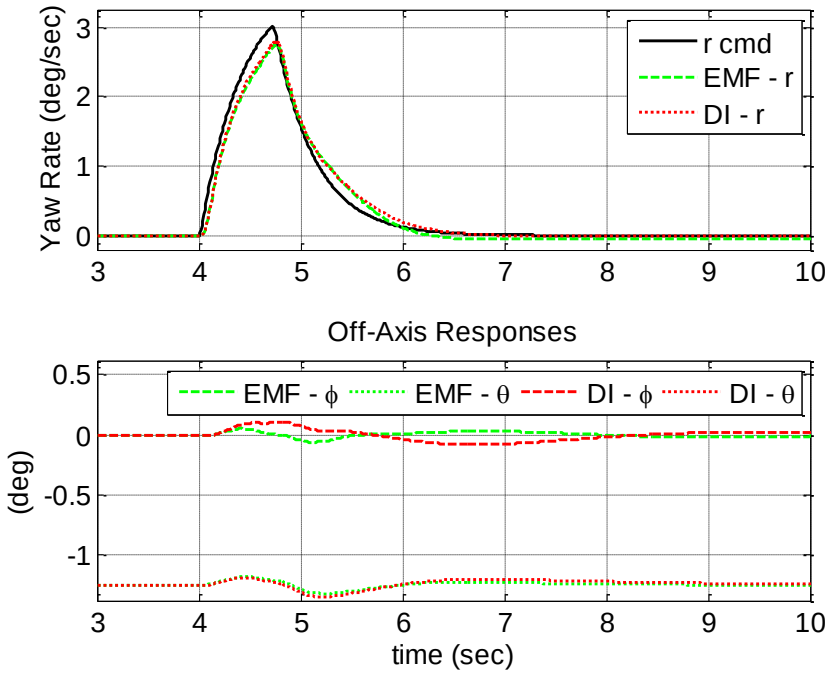

Figure 4-18. Attitude Mode, Pedal Pulse, 120 kts

During the attitude mode pedal step at low speed, DI provides slightly tighter yaw rate control than EMF (Figure 4-19). An attitude mode pedal step at high speed (Figure 4-20) shows DI gradually exceeding the yaw rate command and EMF remaining short of the command.

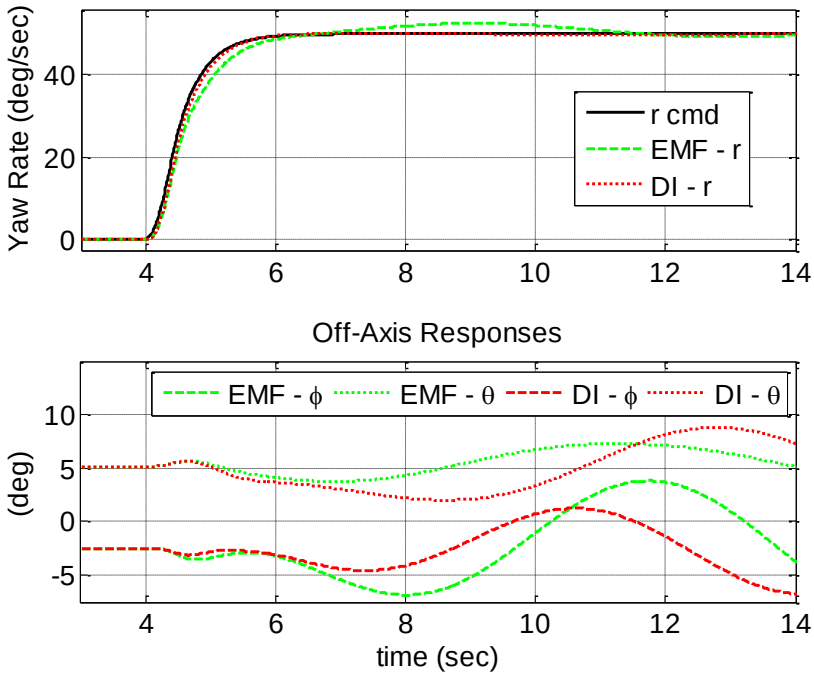

Figure 4-19. Attitude Mode, Pedal Step, 10 kts

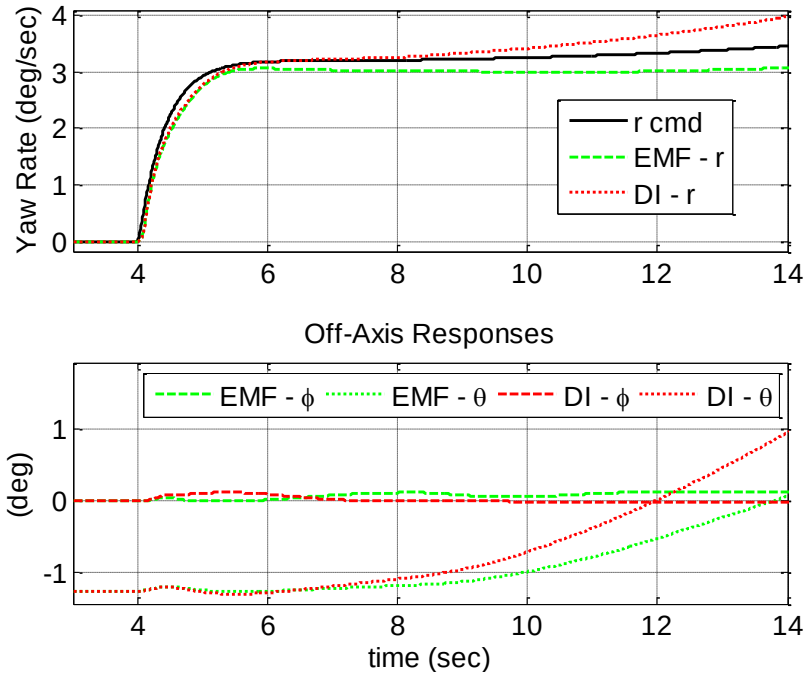

Figure 4-20. Attitude Mode, Pedal Step, 120 kts

4.6.3 **Turbulence**

For turbulence response evaluation the simulation is stimulated with the turbulence model developed by Lusardi, et al. (Ref. [34]), with parameters set to a moderate condition: mean wind speed = 41.3, wind vertical std dev = 6.5, wind lateral std dev = 8.5, all units ft/sec. The control system is in Attitude / Altitude mode. Turbulence response is measured in RMS of the rate responses. The results are shown in Figure 4-21.

Near hover, DI is somewhat better at suppressing the roll response to turbulence, but otherwise DI and EMF show almost no difference. At high speed, DI is much better at suppressing vertical rate, and somewhat better at roll and yaw rates, while EMF is somewhat better at suppressing pitch rate.

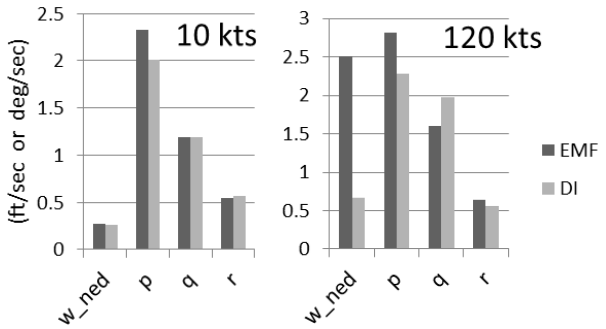

Figure 4-21. RMS Response in Turbulence

4.6.4 **Robustness Analysis**

The following robustness analysis shows the effects of perturbing bare airframe parameters upon stability and performance. The control laws are in Attitude / Altitude mode, except longitudinal pilot input performance at high speed is assessed in Attitude / Climb Rate mode. The perturbed bare airframe parameters are: weight, fuselage station center of gravity (fscg, +aft), main rotor blade density (bld den), and lag damper effectiveness (lag damp). The magnitudes of the perturbations are

weight: 92% and 109% of design

fscg: 5 inches forward and aft of design

bld den: 90% and 110% of design

lag damp: 80% of design

EMF results are in black. DI results are in green. EMF results with the design-plant are indicated by a black square, while DI results with the design-plant are indicated by a green diamond. Perturbed plant results are indicated by triangles: left-pointing means the parameter is reduced, right-pointing means the parameter is increased. Greater robustness is indicated by less separation between the triangles and their associated design-plant results.

The conclusion from these robustness results is that neither model-following method has an overall advantage over the other. Specific advantages are noted, per axis, per perturbation, and per speed regime, in the following sub-sections.

4.6.4.1 Stability Robustness

In this Chapter, stability robustness is assessed through gain and phase margin changes. Results are presented next.

In the vertical axis, at low speed, all margin sensitivities are low (Figure 4-22). In the vertical axis, at high speed, DI generally has less stability robustness than EMF (Figure 4-23).

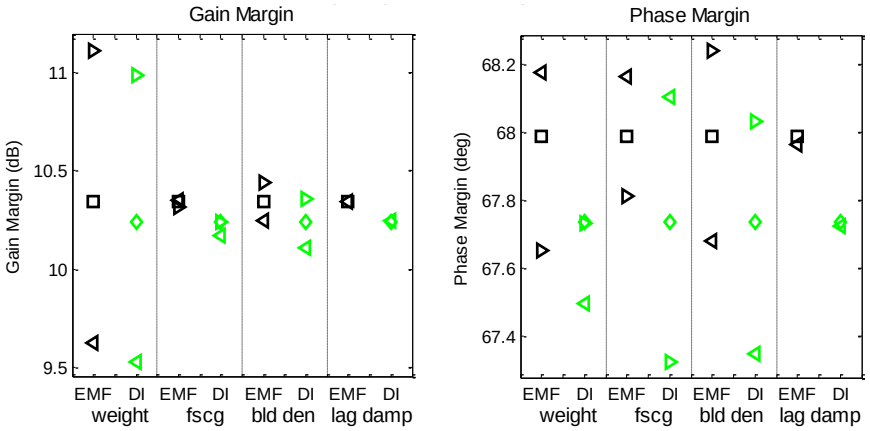

Figure 4-22. EMF vs DI, Stability Robustness, Vertical Axis – 10 knots

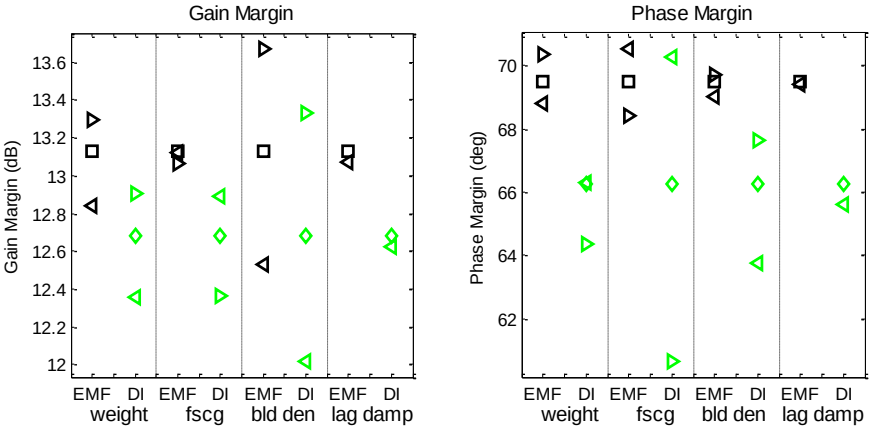

Figure 4-23. EMF vs DI, Stability Robustness, Vertical Axis – 120 knots

In the lateral axis at low speed (Figure 4-24), DI gain margin is less robust to fscg, but it starts with much more gain margin. DI phase margin is slightly more robust to blade density. In the lateral axis at high speed, there is little difference in stability robustness between DI and EMF (Figure 4-25).

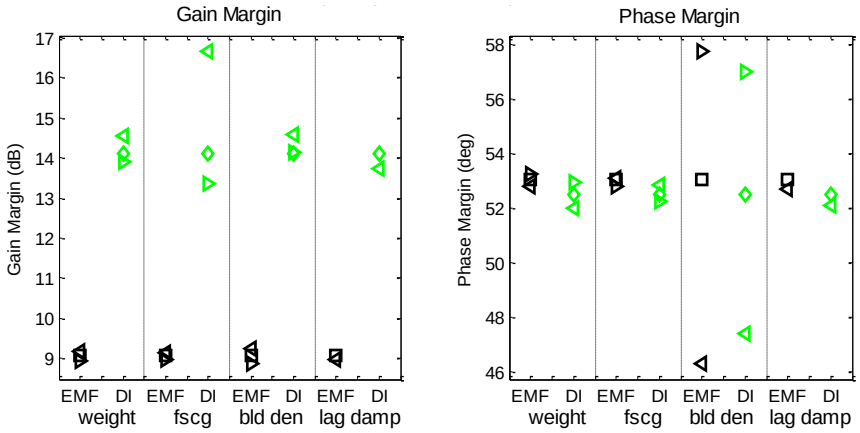

Figure 4-24. EMF vs DI, Stability Robustness, Lateral Axis – 10 knots

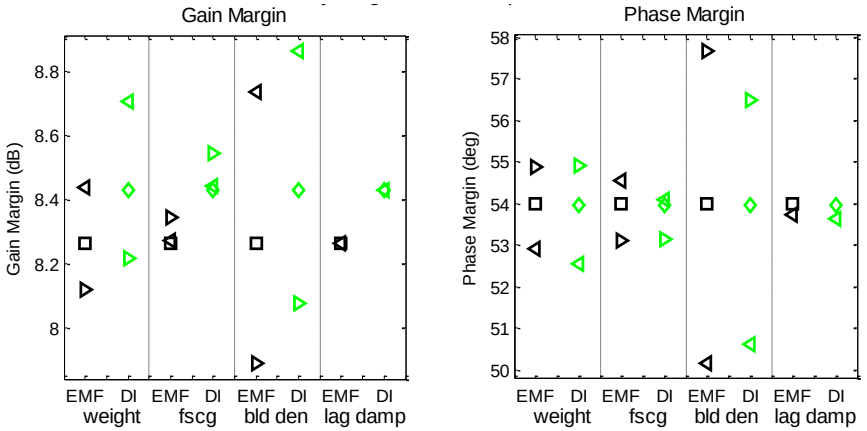

Figure 4-25. EMF vs DI, Stability Robustness, Lateral Axis – 120 knots

In the longitudinal axis at low speed (Figure 4-26), DI gain margin is more robust to weight and less robust to fscg. DI phase margin is less robust to weight and blade density, but all phase margin sensitivities are low.

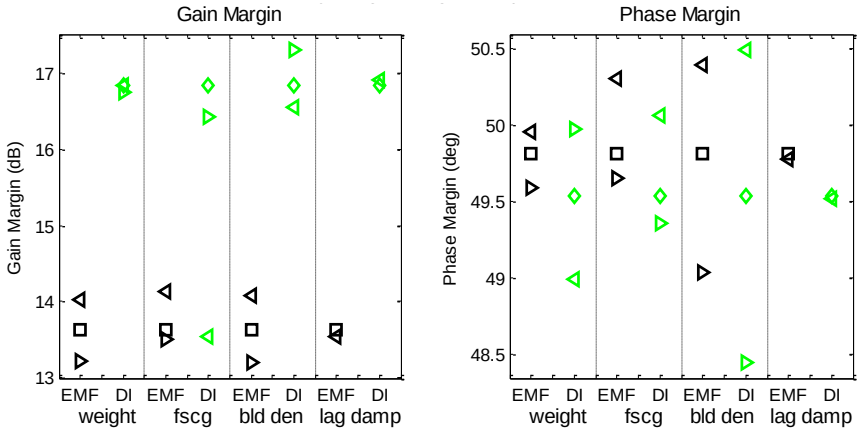

Figure 4-26. EMF vs DI, Stability Robustness, Longitudinal Axis – 10 knots

In the longitudinal axis at high speed (Figure 4-27), EMF gain margin is less robust, but it starts with much more gain margin. DI phase margin is less robust to weight and fscg, and more robust to blade density.

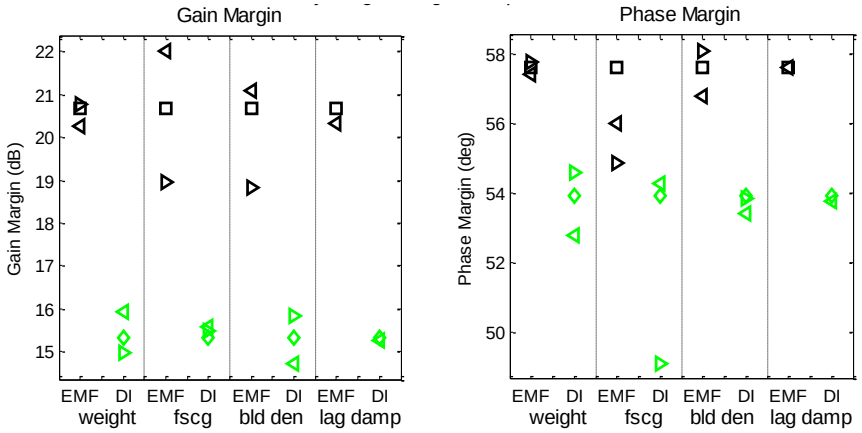

Figure 4-27. EMF vs DI, Stability Robustness, Longitudinal Axis – 120 knots

In the yaw axis at low speed (Figure 4-28), DI gain margin is less robust to fscg. DI phase margin is less robust to weight and blade density.

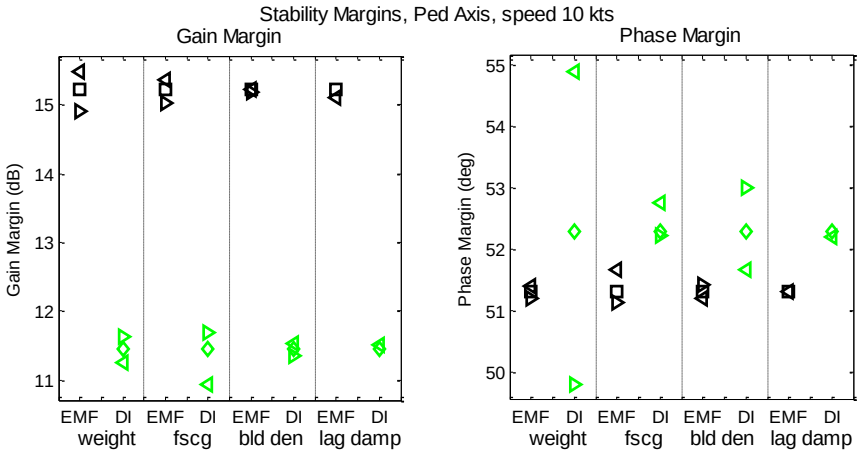

Figure 4-28. EMF vs DI, Stability Robustness, Yaw Axis – 10 knots

In the yaw axis at high speed (Figure 4-29), all gain margins are high, with low sensitivity. DI phase margin is less robust to weight.

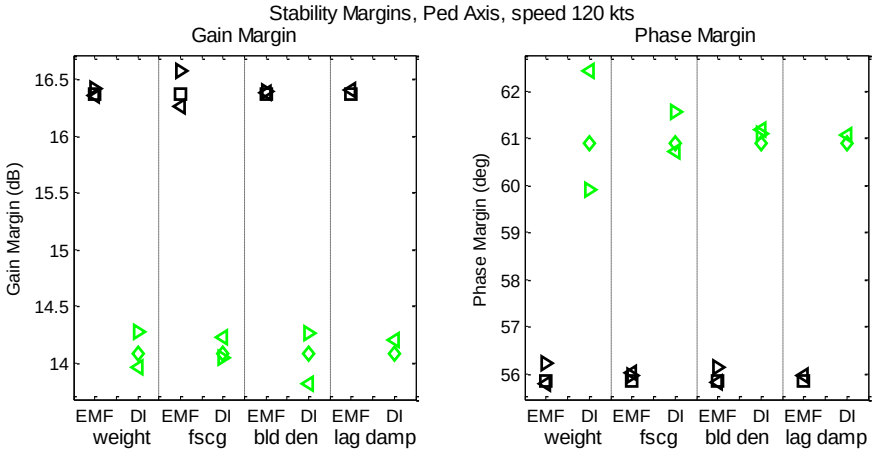

Figure 4-29. EMF vs DI, Stability Robustness, Yaw Axis – 120 knots

4.6.4.2 Performance Robustness

Turbulence performance robustness is assessed through changes in the root-mean-square of rates. In turbulence, at low speed (Figure 4-30), performance with either method (EMF or DI) is mostly insensitive to the bare airframe parameters considered. Roll rate is somewhat sensitive to blade density, but DI and EMF robustness are closely matched.

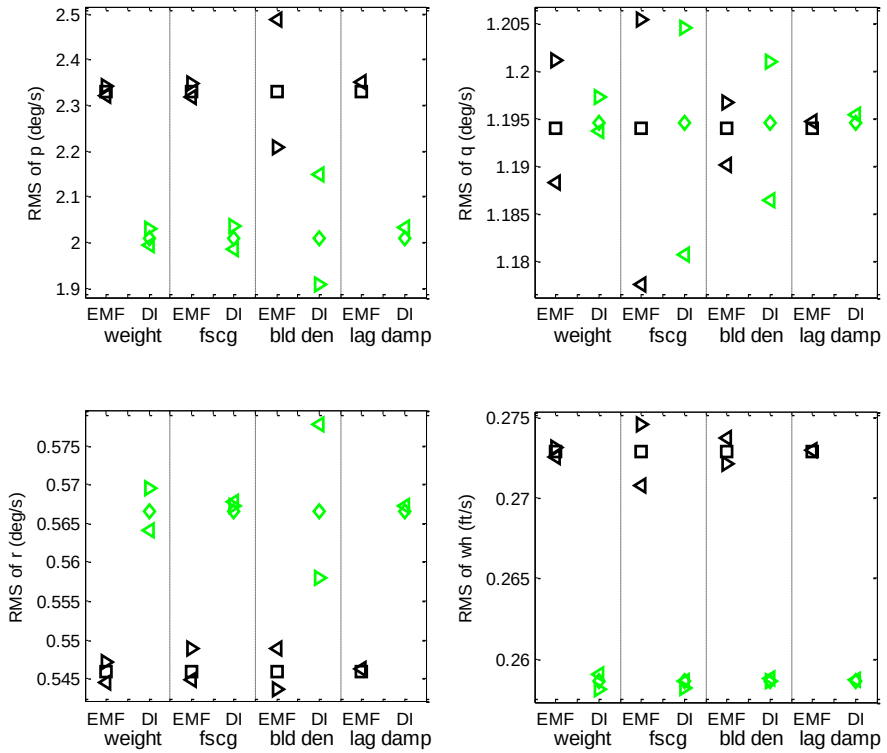

Figure 4-30. EMF vs DI, Performance Robustness, Turbulence – 10 knots

In turbulence, at high speed (Figure 4-31), DI is slightly more robust than EMF in a few combinations of perturbed parameter and response axis.

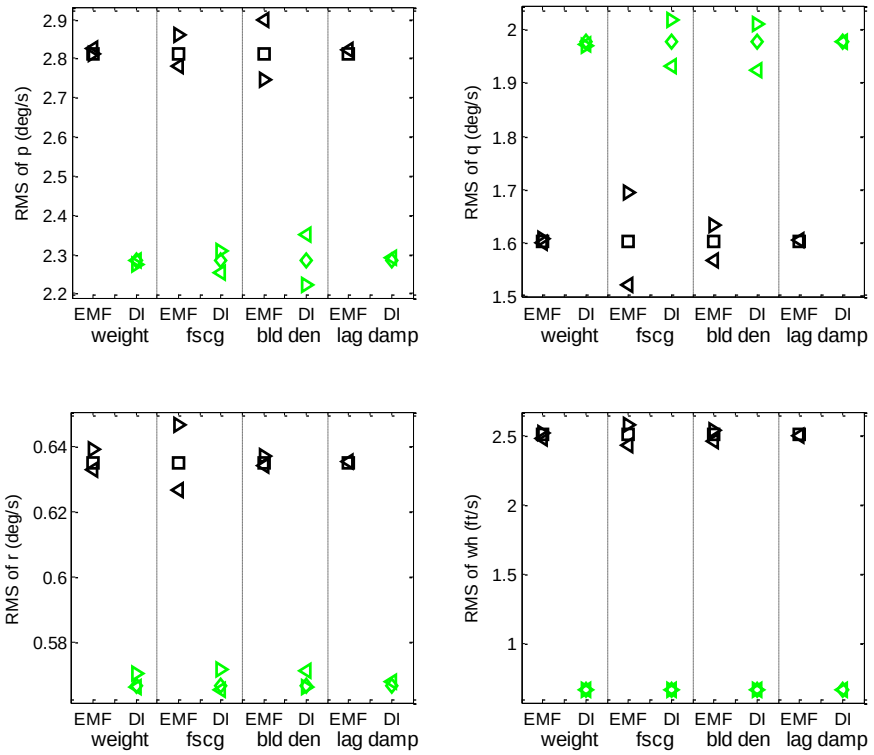

Figure 4-31. EMF vs DI, Performance Robustness, Turbulence – 120 knots

Command-following performance robustness is assessed through changes in the root-mean-square of rate errors during random band-limited (9 rad/s corner) pilot input, one inceptor at a time. These rate errors are the difference between lagged commands and measured response. Note that the on-axis rate errors (the upper left plot in each figure for inceptor-excited responses) are generally greater for DI than EMF. This is largely due to the way the command lags were intentionally designed, as mentioned in Section 4.5 : "Command conditioning for EMF rate errors . . . is set such that the conditioned commands approximately match their corresponding sensed response in the initial portion of the response to an on-axis input. DI was found to work better with less rate command lag/delay in the present application." The command-following performance robustness results are now covered in detail.

For pilot lateral input at low speed (Figure 4-32), EMF roll rate (p) error is more robust to blade density. EMF pitch rate (q) error is more robust to weight and blade density. EMF yaw rate (r) error is more robust to blade density. For pilot lateral input at high speed (Figure 4-33), DI robustness matches or

is better than EMF robustness, except for pitch rate error due to blade density and yaw rate error due to fscg or blade density.

For pilot longitudinal input at low speed (Figure 4-34), EMF is better than or equal to DI in robustness (vertical rate responses too insignificant to consider). For pilot longitudinal input at high speed (Figure 4-35), DI vertical rate (wh) error and yaw rate (r) error are generally more robust

For pilot pedal input at low speed (Figure 4-36), DI yaw rate (r) error is slightly more robust to fscg. Otherwise, EMF equals or betters the robustness of DI. For pilot pedal input at high speed (Figure 4-37), DI is more robust: in yaw rate (r) error to fscg, in vertical rate (wh) error to weight, and in pitch rate (q) error to weight. EMF is more robust: in roll rate (p) error to blade density, and in pitch rate (q) error to fscg and blade density.

For pilot collective input at low speed (Figure 4-38), all significant rate errors have about equal sensitivity, between EMF and DI, to bare airframe parameter perturbations. For pilot collective input at high speed (Figure 4-39), DI vertical rate (wh) error is more robust to weight and fscg. DI roll rate (p) error is more robust to weight and blade density. EMF pitch rate (q) error is generally slightly more robust. EMF yaw rate (r) error is more robust, but in all cases the yaw rate errors are much smaller than roll and pitch rate errors.

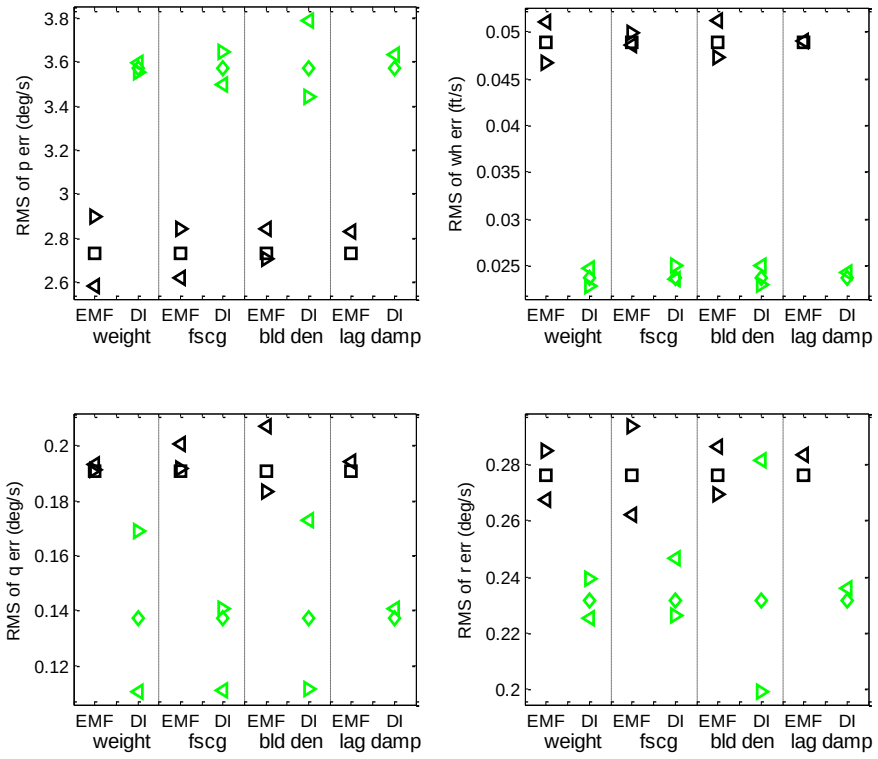

Figure 4-32. EMF vs DI, Performance Robustness, Pilot Lateral – 10 knots

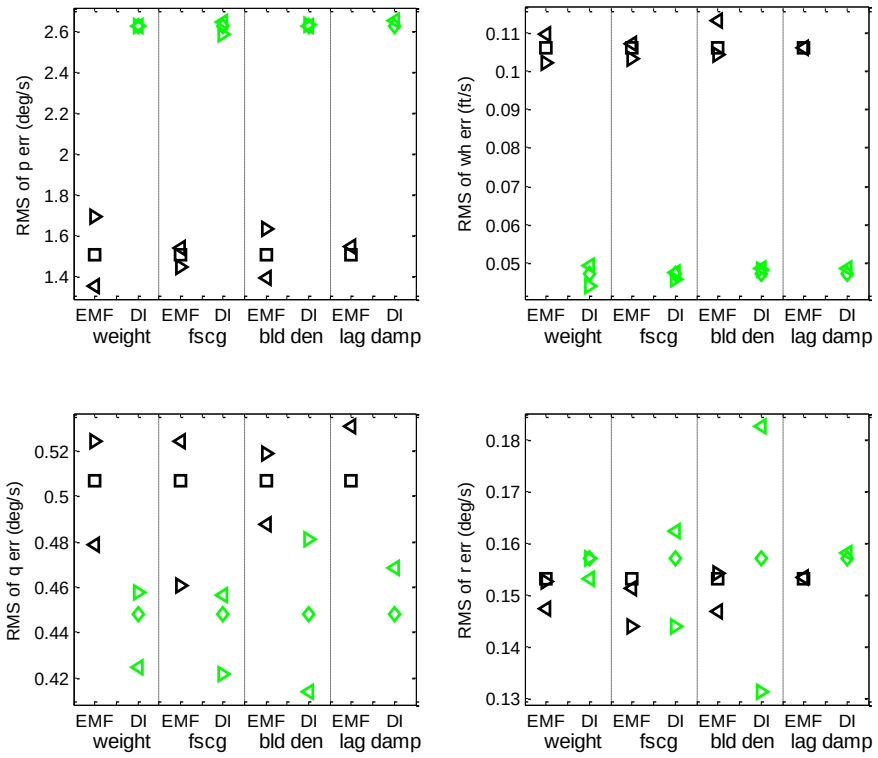

Figure 4-33. EMF vs DI, Performance Robustness, Pilot Lateral – 120 knots

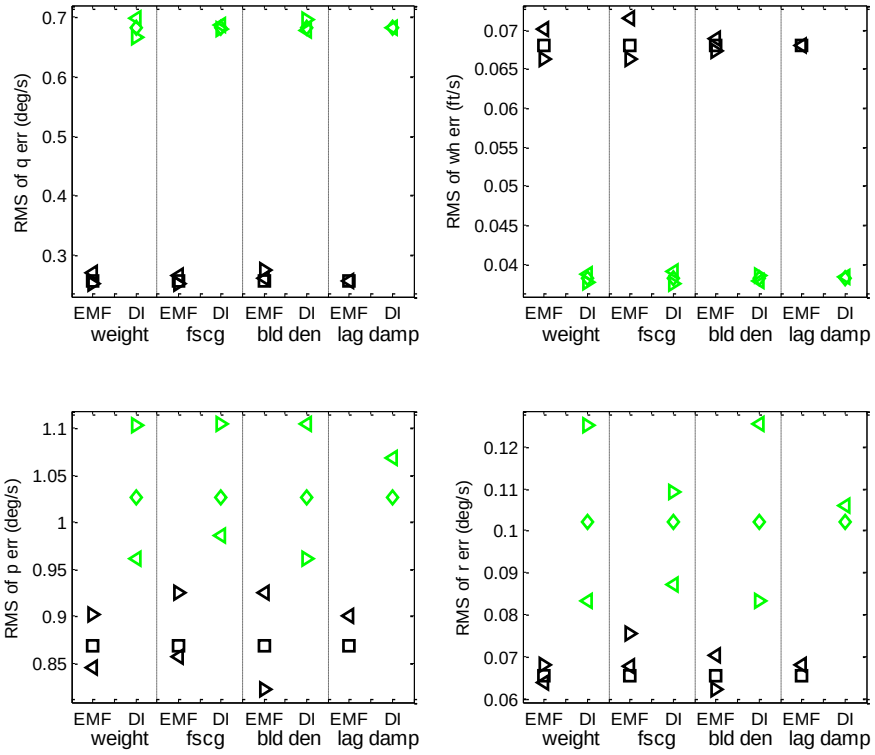

Figure 4-34. EMF vs DI, Performance Robustness, Pilot Longitudinal – 10 knots

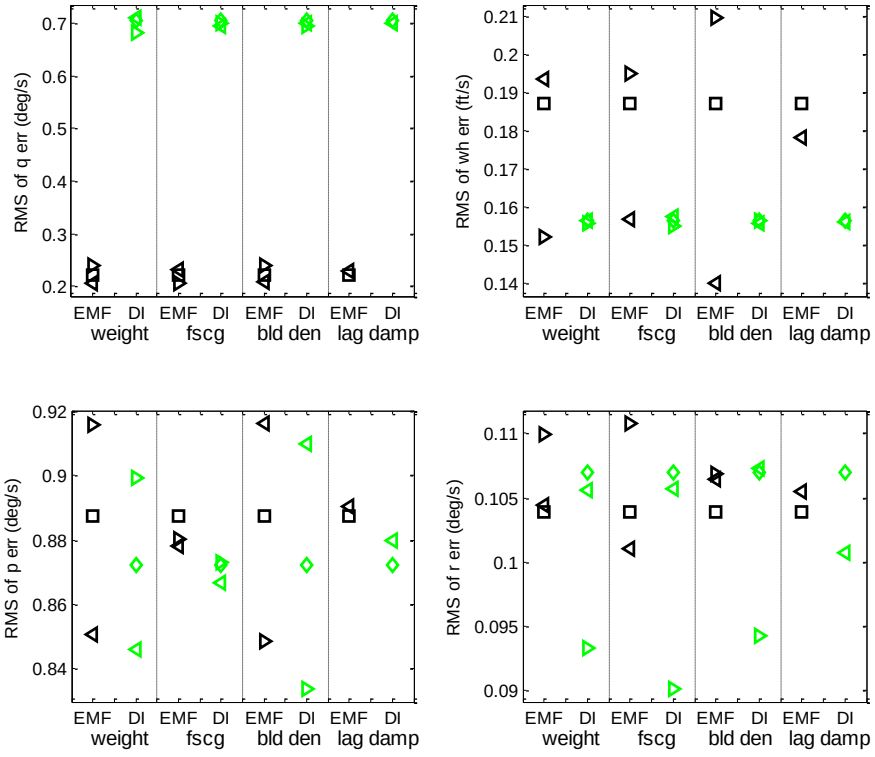

Figure 4-35. EMF vs DI, Performance Robustness, Pilot Longitudinal – 120 knots

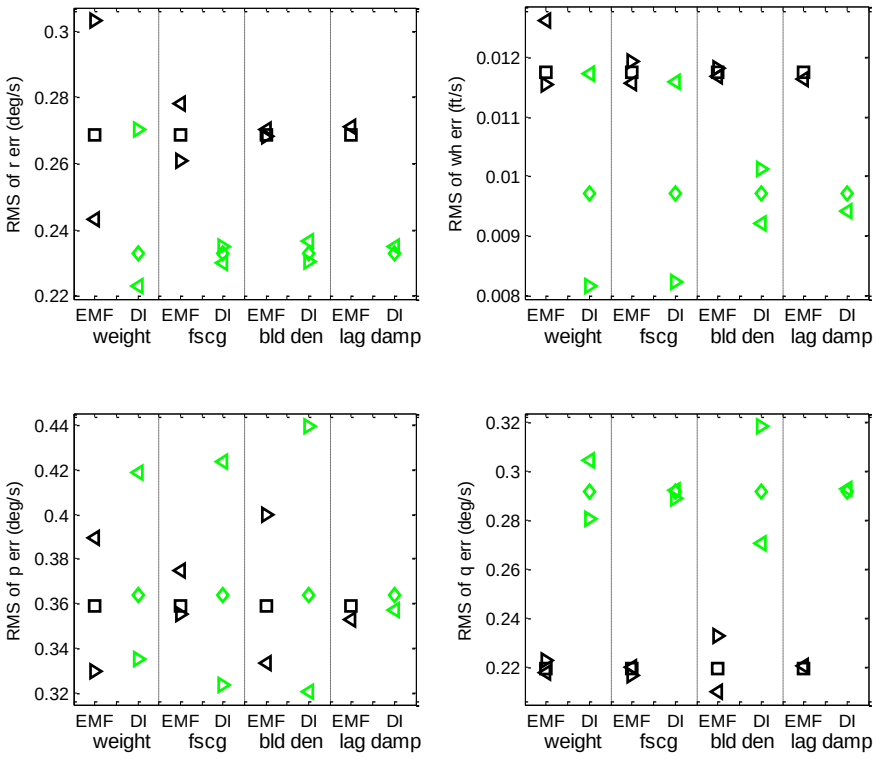

Figure 4-36. EMF vs DI, Performance Robustness, Pilot Pedal – 10 knots

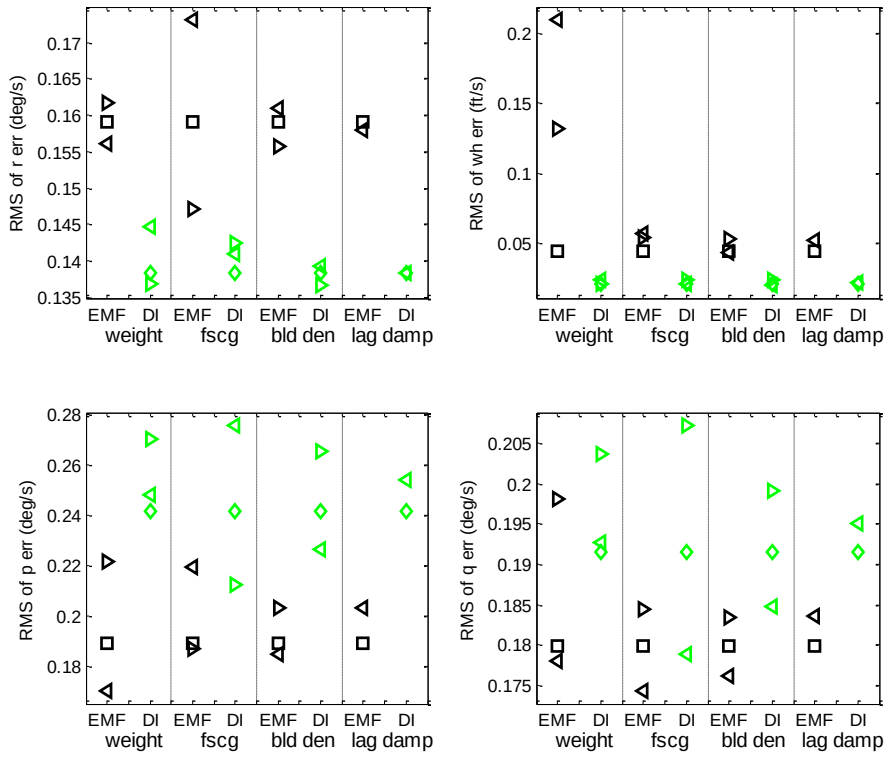

Figure 4-37. EMF vs DI, Performance Robustness, Pilot Pedal – 120 knots

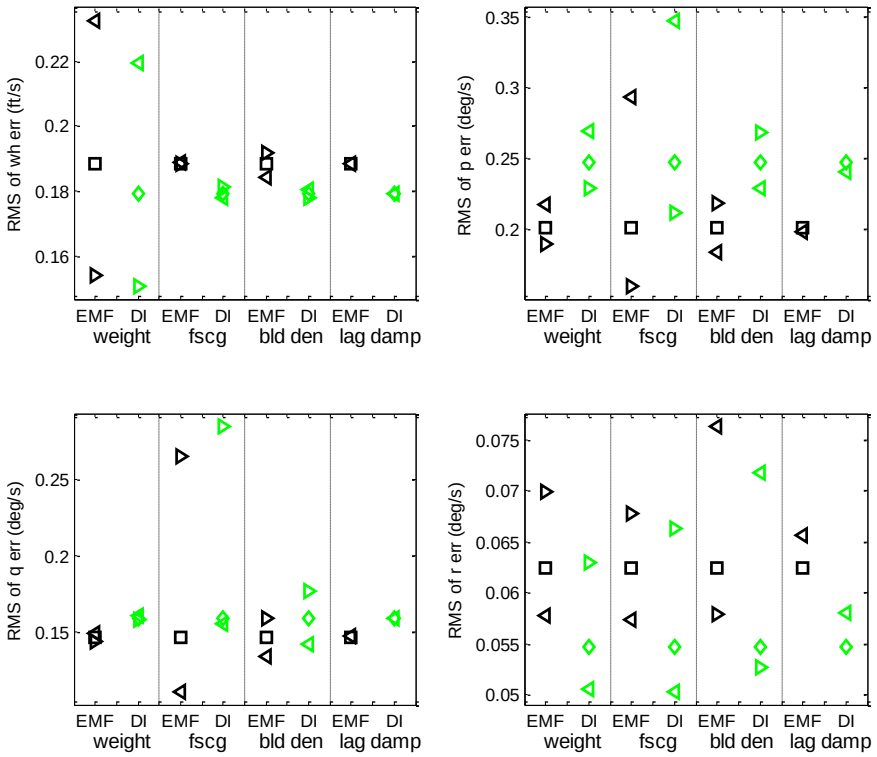

Figure 4-38. EMF vs DI, Performance Robustness, Pilot Collective – 10 knots

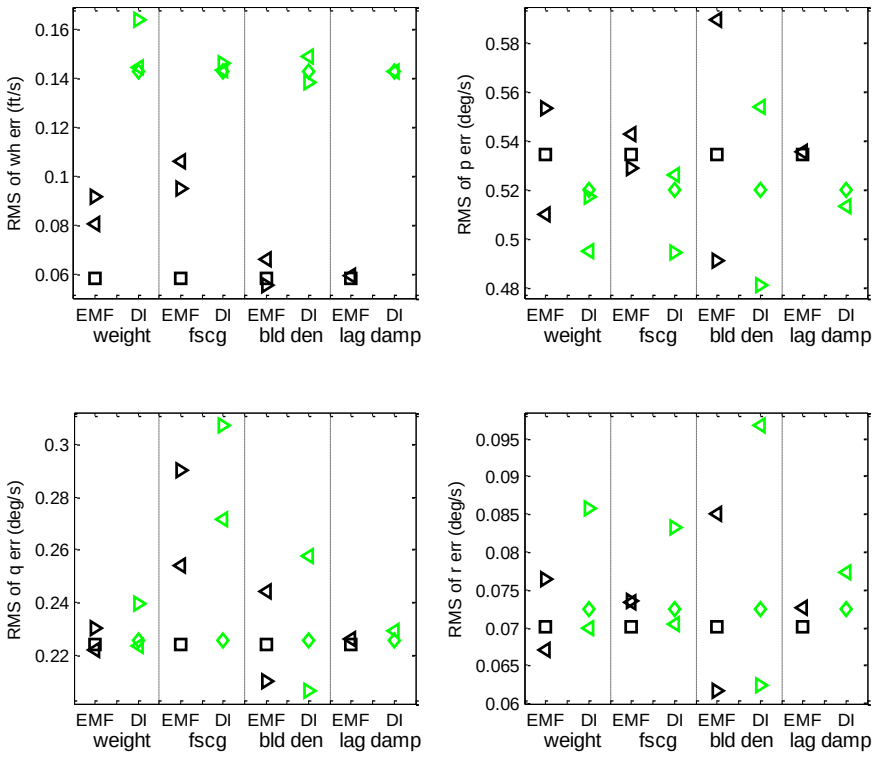

Figure 4-39. EMF vs DI, Performance Robustness, Pilot Collective – 120 knots

4.7 Conclusions regarding MIMO Model Following Control Design Methods

1) Two methods were presented for MIMO model-following control of rotorcraft, along with techniques to overcome implementation challenges. Each method was developed in a way that provides angular rate following, including compensation for collective activity, plus selectable vertical rate model following.

2) The MIMO EMF dynamic elements can be high order and unstable. Therefore the exact elements are generally replaced with approximate low-order stable transfer functions (Ref. [2]). However, an analysis showed that there are a large number of pole-zero cancellations within the exact elements. These cancellations, and the absence of very unstable poles, resulted in good approximations. The extensive pole-zero cancellation is probably not coincidental, and a state-space analysis, such as that presented by Blankinship (Ref. [35]), might reveal the true maximum order for the EMF elements.

3) MIMO EMF is complex to design. It involves many transfer function multiplications and summations, which can be tricky to implement in software. The low-order approximations need to be checked for anomalies that might need to be manually corrected. The pole locations of the EMF elements must be restricted.

4) MIMO EMF is complex to implement. In the example design, it includes 16 transfer functions (26 states) having 72 coefficients that need to be speed-scheduled. For second order polynomials, the frequency and damping should probably be scheduled rather than the coefficients.

5) With DI, if the designer wants to include states in the design model that are not directly sensed, a state estimator is needed, which can be imprecise. In the present work, the body side velocity state was included so that DI could compensate for weathervaning, yaw-roll coupling, and side-speed stability. Also, the body-down velocity state was included to facilitate vertical rate decoupling and inversion. EMF does not require state estimation for the inversion since it is done with feedforward compensation alone.

6) DI is easy to design. While the method can have problems, namely [**CB**] can be singular and the zero dynamics can be unstable, these potential problems have not arisen in the present application.

7) DI has no states, and the parameter scheduling is simple, with the exception of the add-on vertical control. The DI vertical control presented here is somewhat complicated because it includes nonlinearities and avoids real-time numerical matrix inversion. The EMF controller implemented in this work only uses linear compensation.

8) Both EMF and DI provide good tracking of commands and reduction of cross coupling. The biggest difference found between their performance, in the present work, is that DI vertical speed response to turbulence at high speed is much less than EMF.

9) Although MIMO EMF is a viable design tool for control law development, DI is easier to design and implement. Further, DI can include nonlinear compensation. DI's main drawback is the need for full design model state feedback, which must be provided by sensors or estimation.

4.8 Future Work

4.8.1 **Explicit Model Following Future Work**

The MIMO EMF derived and utilized in this dissertation is based on symbolic manipulation of a low-order design model, followed by fitting stable low-order transfer functions to the symbolic "exact" results. In future research, one might try skipping the low-order design model, and instead work numerically with the full-order linear model of the system or with flight test data, as described next.

Start with the frequency-domain representation of the bare-airframe.

$$\begin{Bmatrix} p \\ q \\ r \\ w^{\text{ned}} \end{Bmatrix} = \underbrace{\begin{bmatrix} \frac{p}{u_{\text{lat}}} & \frac{p}{u_{\text{lng}}} & \frac{p}{u_{\text{ped}}} & \frac{p}{u_{\text{col}}} \\ \frac{q}{u_{\text{lat}}} & \frac{q}{u_{\text{lng}}} & \frac{q}{u_{\text{ped}}} & \frac{q}{u_{\text{col}}} \\ \frac{r}{u_{\text{lat}}} & \frac{r}{u_{\text{lng}}} & \frac{r}{u_{\text{ped}}} & \frac{r}{u_{\text{col}}} \\ \frac{w^{\text{ned}}}{u_{\text{lat}}} & \frac{w^{\text{ned}}}{u_{\text{lng}}} & \frac{w^{\text{ned}}}{u_{\text{ped}}} & \frac{w^{\text{ned}}}{u_{\text{col}}} \end{bmatrix}}_{\mathbf{P}(s)} \begin{Bmatrix} \Delta u_{\text{lat}} \\ \Delta u_{\text{lng}} \\ \Delta u_{\text{ped}} \\ \Delta u_{\text{col}} \end{Bmatrix} \tag{4-28}$$

At a series of discrete frequencies that span the frequency range of interest, which for piloted rotorcraft is about 1-10 rad/s, calculate the elements of the mixing matrices as shown in the following formulas. These formulas are the same as derived in Appendix A and Appendix B, with the exception that here the full plant transfer functions are kept, rather than canceling out common denominators. The elements of $\mathbf{M}_{3x4}$ are

$$\begin{Bmatrix} \frac{u_{\text{lng}}}{d_{\text{lat}}} \\ \frac{u_{\text{ped}}}{d_{\text{lat}}} \end{Bmatrix} = -\begin{bmatrix} P^q_{\text{lng}} & P^q_{\text{ped}} \\ P^r_{\text{lng}} & P^r_{\text{ped}} \end{bmatrix}^{-1} \begin{Bmatrix} P^q_{\text{lat}} \\ P^r_{\text{lat}} \end{Bmatrix} \quad ; \quad \begin{Bmatrix} \frac{u_{\text{lat}}}{d_{\text{lng}}} \\ \frac{u_{\text{ped}}}{d_{\text{lng}}} \end{Bmatrix} = -\begin{bmatrix} P^p_{\text{lat}} & P^p_{\text{ped}} \\ P^r_{\text{lat}} & P^r_{\text{ped}} \end{bmatrix}^{-1} \begin{Bmatrix} P^p_{\text{lng}} \\ P^r_{\text{lng}} \end{Bmatrix}$$

$$\begin{Bmatrix} \frac{u_{\text{lat}}}{d_{\text{ped}}} \\ \frac{u_{\text{lng}}}{d_{\text{ped}}} \end{Bmatrix} = -\begin{bmatrix} P^p_{\text{lat}} & P^p_{\text{lng}} \\ P^q_{\text{lat}} & P^q_{\text{lng}} \end{bmatrix}^{-1} \begin{Bmatrix} P^p_{\text{ped}} \\ P^q_{\text{ped}} \end{Bmatrix} \quad ; \quad \begin{Bmatrix} \frac{u_{\text{lat}}}{u_{\text{col}}} \\ \frac{u_{\text{lng}}}{u_{\text{col}}} \\ \frac{u_{\text{ped}}}{u_{\text{col}}} \end{Bmatrix} = -\begin{bmatrix} P^p_{\text{lat}} & P^p_{\text{lng}} & P^p_{\text{ped}} \\ P^q_{\text{lat}} & P^q_{\text{lng}} & P^q_{\text{ped}} \\ P^r_{\text{lat}} & P^r_{\text{lng}} & P^r_{\text{ped}} \end{bmatrix}^{-1} \begin{Bmatrix} P^p_{\text{col}} \\ P^q_{\text{col}} \\ P^r_{\text{col}} \end{Bmatrix} \tag{4-29}$$

The elements of $\mathbf{M}_{1x3}$ are

$$\begin{aligned} \frac{u_{\text{col}}}{d_{\text{lat}}} &= \left(P^{w^{\text{ned}}}_{\text{lat}} \frac{u_{\text{lat}}}{u_{\text{col}}} + P^{w^{\text{ned}}}_{\text{lng}} \frac{u_{\text{lng}}}{u_{\text{col}}} + P^{w^{\text{ned}}}_{\text{ped}} \frac{u_{\text{ped}}}{u_{\text{col}}} + P^{w^{\text{ned}}}_{\text{col}} \right)^{-1} \left(-P^{w^{\text{ned}}}_{\text{lat}} - P^{w^{\text{ned}}}_{\text{lng}} \frac{u_{\text{lng}}}{d_{\text{lat}}} - P^{w^{\text{ned}}}_{\text{ped}} \frac{u_{\text{ped}}}{d_{\text{lat}}} \right) \\ \frac{u_{\text{col}}}{d_{\text{lng}}} &= \left(P^{w^{\text{ned}}}_{\text{lat}} \frac{u_{\text{lat}}}{u_{\text{col}}} + P^{w^{\text{ned}}}_{\text{lng}} \frac{u_{\text{lng}}}{u_{\text{col}}} + P^{w^{\text{ned}}}_{\text{ped}} \frac{u_{\text{ped}}}{u_{\text{col}}} + P^{w^{\text{ned}}}_{\text{col}} \right)^{-1} \left(-P^{w^{\text{ned}}}_{\text{lat}} \frac{u_{\text{lat}}}{d_{\text{lng}}} - P^{w^{\text{ned}}}_{\text{lng}} - P^{w^{\text{ned}}}_{\text{ped}} \frac{u_{\text{ped}}}{d_{\text{lng}}} \right) \\ \frac{u_{\text{col}}}{d_{\text{ped}}} &= \left(P^{w^{\text{ned}}}_{\text{lat}} \frac{u_{\text{lat}}}{u_{\text{col}}} + P^{w^{\text{ned}}}_{\text{lng}} \frac{u_{\text{lng}}}{u_{\text{col}}} + P^{w^{\text{ned}}}_{\text{ped}} \frac{u_{\text{ped}}}{u_{\text{col}}} + P^{w^{\text{ned}}}_{\text{col}} \right)^{-1} \left(-P^{w^{\text{ned}}}_{\text{lat}} \frac{u_{\text{lat}}}{d_{\text{ped}}} - P^{w^{\text{ned}}}_{\text{lng}} \frac{u_{\text{lng}}}{d_{\text{ped}}} - P^{w^{\text{ned}}}_{\text{ped}} \right) \end{aligned} \tag{4-30}$$

The decoupled frequency responses are then computed, at each discrete frequency, using Equations (4-9), (4-10), (4-11), and (4-13). The inverse plant frequency responses are the reciprocals of these decoupled frequency responses. The final step is to fit all these discrete frequency responses with stable low-order transfer function approximations.

4.8.2 **Dynamic Inversion Future Work**

It is interesting to examine the transfer function matrix between pseudo-commands and the first derivative of outputs using the plant's design model and no error feedback. In this case, the DI system is acting on the plant for which it was designed, so the transfer function matrix will be the identity matrix if the DI design and implementation are correct. If actuation dynamics are added, intuitively, one may expect the transfer function matrix to be very close to the identity matrix at low frequencies, with on-diagonal gain and phase roll-off at higher frequency in a manner similar to the actuator dynamics. Testing with the example plants of the present work showed diagonal-element high-frequency roll-offs as expected, but the low-frequency gain leveled a bit below 0 dB (gain of 1) in all axes. Removing the actuator dynamics resulted in the expected identity transfer matrix, which confirmed the DI derivation and implementation. The studies of the present work proceeded with no attempt to correct for the actuator effect. Future work might explore correction of DI for dynamics that are not included in the DI design model.

The present sub-section analyses the effect upon DI of dynamics that were not included in the DI design model, and derives a correction methodology to make DI closer to ideal. Future work might use an example helicopter to compare this method of correcting DI against including actuator (or sensor) dynamics in the design model, as shown by Stevens and Lewis (Ref. [1]). One complication of including more dynamics in the DI design model is that for each additional integration involved between input and output in the design model, the order of the DI will increase. For example, adding first order actuators to the DI design model used in this dissertation will cause the pseudo-commands to be the second derivative of the angular and vertical rates, and the ideal transfer functions between the pseudo-commands and the outputs will be double integrators, meaning for a stable system the feedback error control will need to operate on both the output and the derivative of the output.

SISO Dynamic Inversion with Measurement Lag

Consider SISO DI (Figure 4-2) applied to the model for which it was designed, but with the addition of a first order measurement lag (see Figure 4-40).

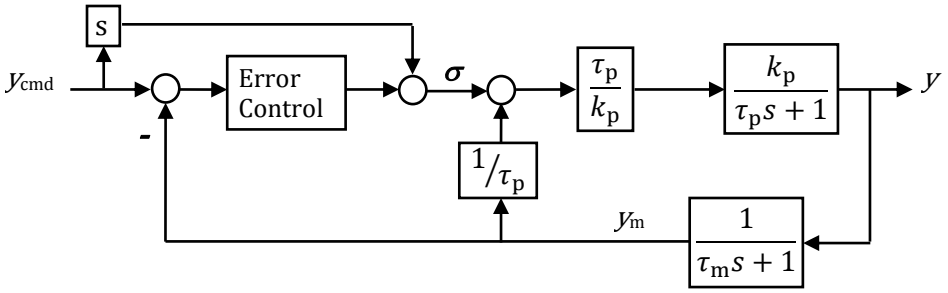

Figure 4-40. SISO Dynamic Inversion with Measurement Lag.

Reduce the DI loop to a transfer function.

$$\frac{y}{\sigma}=\frac{\frac{\tau_p}{\tau_p s+1}}{1-\frac{1/\tau_p}{\tau_m s+1}\frac{\tau_p}{\tau_p s+1}}=\frac{(\tau_m s+1)\tau_p}{(\tau_m s+1)(\tau_p s+1)-1}$$

$$=\frac{(\tau_m s+1)\tau_p}{\tau_m\tau_p s^2+(\tau_m+\tau_p)s}=\frac{\tau_p}{\tau_m+\tau_p}\frac{\tau_m s+1}{\underbrace{\left(\frac{\tau_m}{\frac{\tau_m}{\tau_p}+1}\right)}_{\tau_{eff}}s+1}\frac{1}{s} \tag{4-31}$$

In block diagram form, this result is shown in Figure 4-41.

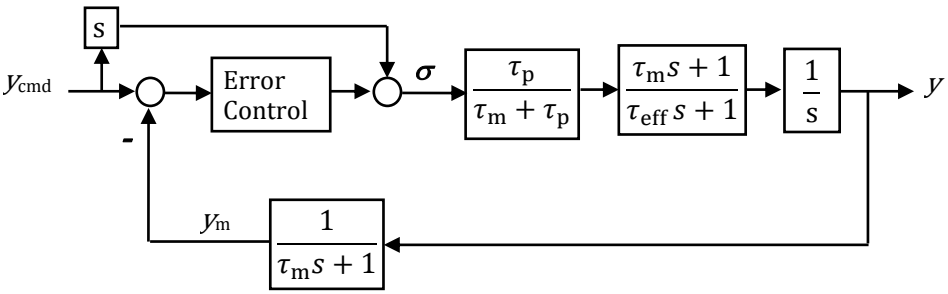

Figure 4-41. SISO DI with Measurement Lag, DI Loop Reduced to Transfer Function.

The $\sigma \to y$ transfer function was designed to be 1/s. The DI control law can be corrected to restore this result by pre-compensating the pseudo-command with the inverse of the non-ideal components. Also, in forming the error for feedback control, apply the measurement lag to the command before subtracting the measured output, so that when the true output follows the command, the error will be zero. These adjustments are shown by Figure 4-42 .

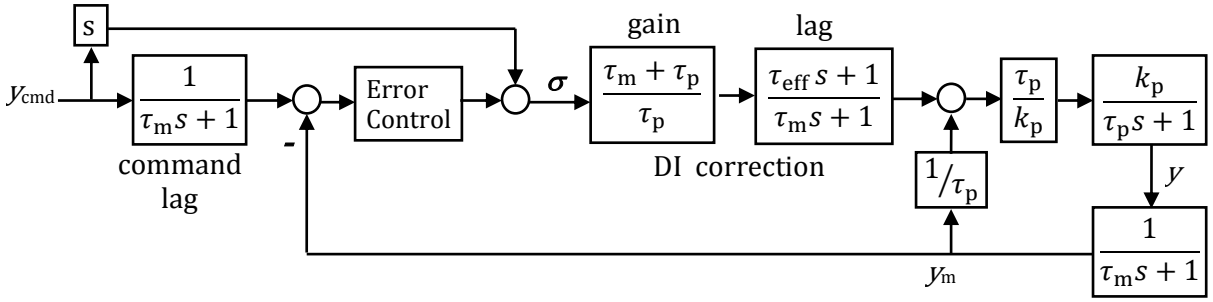

Figure 4-42. SISO DI, with Corrections for Measurement Lag Effects

SISO Dynamic Inversion with Actuation Dynamics

Consider SISO DI (Figure 4-2) applied to the model for which it was designed, but with the addition of a first order actuation lag (see Figure 4-43).

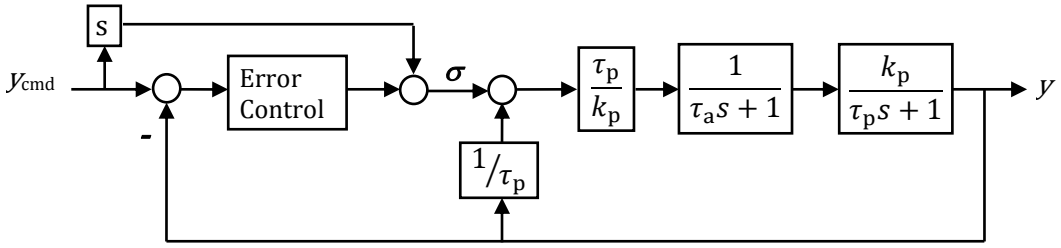

Figure 4-43. SISO Dynamic Inversion with Actuation Lag.

Reduce the DI loop to a transfer function.

$$\frac{y}{\sigma}=\frac{\tau_p}{\tau_a+\tau_p}\ \frac{1}{\underbrace{\left(\frac{\tau_a}{\frac{\tau_a}{\tau_p}+1}\right)}_{\tau_{eff}}s+1}\ \frac{1}{s} \tag{4-32}$$

In block diagram form, this result is shown in Figure 4-44.

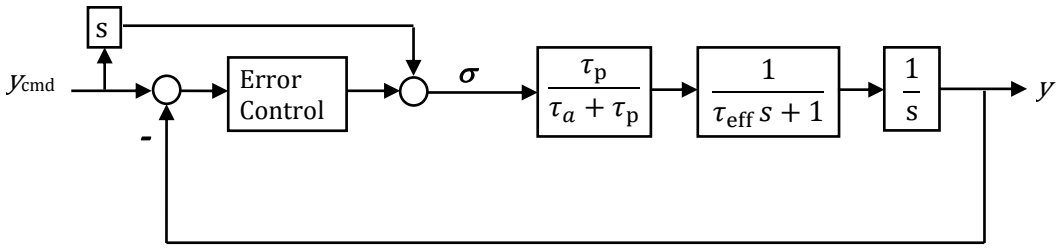

Figure 4-44. SISO DI with Actuation Lag, DI Loop Reduced to Transfer Function.

The $\sigma \to y$ transfer function was designed to be 1/s. The effect of actuation lag cannot be corrected to restore this result because the inverse of one of the non-ideal components is non-realizable.

Instead, treat the effective lag (having time constant τ_{eff}) as an acceptable modification to the ideal relationship between y_{cmd} and y.

$$\begin{aligned} y &= y_{\text{cmd}} \quad \text{(ideal)} \\ y &= \frac{1}{\tau_{\text{eff}}\, s+1}\, y_{\text{cmd}} \quad \text{(acceptable)} \end{aligned} \tag{4-33}$$

This means the DI control law is improved by pre-compensating the pseudo-command with the inverse of the non-ideal gain only. Also, in forming the error for feedback control, apply the effective lag to the command before subtracting the output, so that when the output follows the acceptable dynamics, the error will be zero. These adjustments are shown by Figure 4-45.

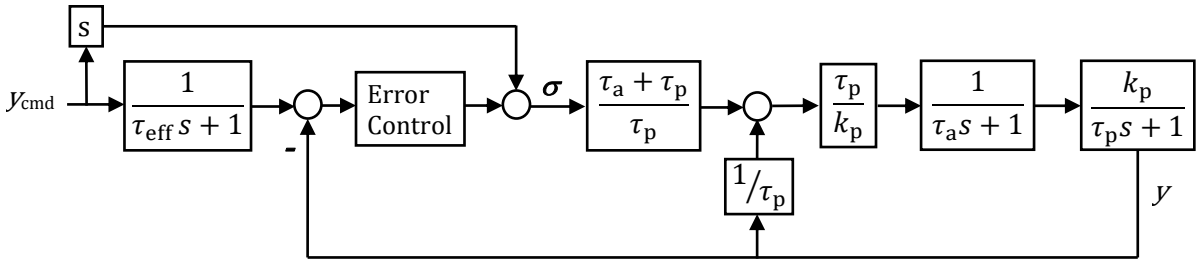

Figure 4-45. SISO DI, with Corrections for Actuation Lag Effects

Note that, for a stable plant, $\tau_{\text{eff}} < \tau_{\text{a}}$. This may explain why DI was found to work better with less rate command lag/delay compared with Explicit Model Following (as mentioned in Section 4.5).

MIMO Dynamic Inversion Applied to a Higher Order Model

Finally, consider MIMO DI applied to a high order model having more states than the design model. The notation for the design model is

$$\text{Design Model:} \quad \begin{aligned} \dot{\mathbf{x}}_{\text{d}} &= \mathbf{A}_{\text{d}}\mathbf{x}_{\text{d}} + \mathbf{B}_{\text{d}}\mathbf{u} \\ \mathbf{y} &= \mathbf{C}_{\text{d}}\mathbf{x}_{\text{d}} \end{aligned} \tag{4-34}$$

The notation for the high order model is

$$\text{High Order Model:} \quad \begin{aligned} \dot{\mathbf{x}} &= \mathbf{A}\mathbf{x} + \mathbf{B}\mathbf{u} \\ \mathbf{y} &= \mathbf{C}\mathbf{x} \end{aligned} \tag{4-35}$$

The Dynamic Inversion control law is

$$\mathbf{u} = \left(\mathbf{C}_{\text{d}}\mathbf{B}_{\text{d}}\right)^{-1}\left\{\boldsymbol{\sigma} - \mathbf{C}_{\text{d}}\mathbf{A}_{\text{d}}\mathbf{x}_{\text{d}}\right\} \tag{4-36}$$

When the DI control law is applied to the high order system, the design states $\mathbf{x}_d$ are replaced with sensed design states $\mathbf{x}_{ds}$.

$$\begin{aligned}\dot{\mathbf{x}} &= \mathbf{A}\mathbf{x} + \mathbf{B}\left(\mathbf{C}_d\mathbf{B}_d\right)^{-1}\left\{\boldsymbol{\sigma} - \mathbf{C}_d\mathbf{A}_d\mathbf{x}_{ds}\right\} \\ \dot{\mathbf{y}} &= \mathbf{C}\dot{\mathbf{x}} = \mathbf{C}\mathbf{A}\mathbf{x} + \mathbf{C}\mathbf{B}\left(\mathbf{C}_d\mathbf{B}_d\right)^{-1}\left\{\boldsymbol{\sigma} - \mathbf{C}_d\mathbf{A}_d\mathbf{x}_{ds}\right\} \\ \mathbf{x}_{ds} &= \mathbf{C}_s\mathbf{x}\end{aligned} \tag{4-37}$$

Expressing the sensed design states in terms of the high order model states ($\mathbf{x}_{ds} \rightarrow \mathbf{C}_s\mathbf{x}$) gives

$$\begin{aligned}\dot{\mathbf{x}} &= \left[\mathbf{A} - \mathbf{B}\left(\mathbf{C}_d\mathbf{B}_d\right)^{-1}\mathbf{C}_d\mathbf{A}_d\mathbf{C}_s\right]\mathbf{x} + \mathbf{B}\left(\mathbf{C}_d\mathbf{B}_d\right)^{-1}\boldsymbol{\sigma} \\ \dot{\mathbf{y}} &= \left[\mathbf{C}\mathbf{A} - \mathbf{C}\mathbf{B}\left(\mathbf{C}_d\mathbf{B}_d\right)^{-1}\mathbf{C}_d\mathbf{A}_d\mathbf{C}_s\right]\mathbf{x} + \mathbf{C}\mathbf{B}\left(\mathbf{C}_d\mathbf{B}_d\right)^{-1}\boldsymbol{\sigma}\end{aligned} \tag{4-38}$$

To observe the effect of the higher order dynamics, convert the above system to a matrix of transfer functions, **H**, and analyze the $\boldsymbol{\sigma} \rightarrow \dot{\mathbf{y}}$ relationship in frequency domain, which ideally would be the identity matrix.

To improve MIMO DI, define a desired transfer function matrix, **D**,

$$\dot{\mathbf{y}} = \mathbf{D}\boldsymbol{\sigma} \tag{4-39}$$

and calculate a pre-compensation matrix, **M**.

$$\begin{aligned}\mathbf{H}\mathbf{M} &= \mathbf{D} \\ \mathbf{M} &= \mathbf{H}^{-1}\mathbf{D}\end{aligned} \tag{4-40}$$

The pre-compensation matrix is added to the MIMO DI controller as shown by Figure 4-46 .

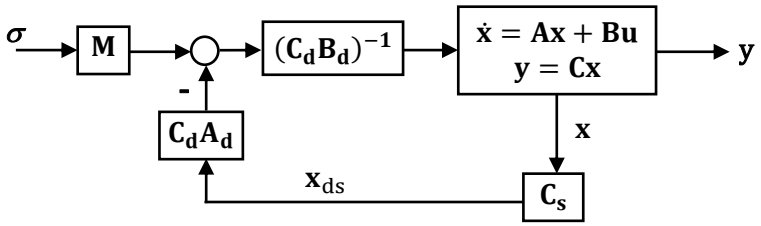

Figure 4-46. MIMO DI, with Corrections for Higher Order Effects

The desired transfer function matrix should be 0 for all off-diagonal elements. The diagonal elements should be defined by fitting a simple (0-order numerator) stable low order transfer function to the diagonal elements of **H**, and then modifying the numerators of those transfer functions to have low frequency gain equal to 1. The solution for **M** (Equation (4-40)) is obtained at a series of discrete frequencies that span

the frequency range of interest, which for piloted rotorcraft is about 1-12 rad/s. The **M** matrix so calculated will be complex, so one must decide how to convert **M** to a realizable form. In a preliminary investigation, **M** was forced to be constant and real by averaging each element over the frequencies and then taking the real part. In future research, one might allow the off-diagonal elements of **M** to be dynamic by fitting them with low order stable transfer functions.

Chapter 5

High Order Compensator Augmentation of a Partial Authority Controller

Chapter 3 reported upon the development and evaluation of practical MIMO model following control methods for a helicopter, as part of an otherwise classically designed Baseline control system. In the present chapter, the Dynamic Inversion method from that study is applied to the same helicopter but in the form of a partial authority (+-10%) system. This dissertation then presents a MIMO H_2 angular rate compensation architecture and design procedure to augment the partial-authority Baseline controller, providing improvement over Dynamic Inversion with classical feedback control alone. The control architecture being considered is shown in Figure 5-1 below. The MIMO compensator is represented by the block labeled HOC for High Order Compensator.

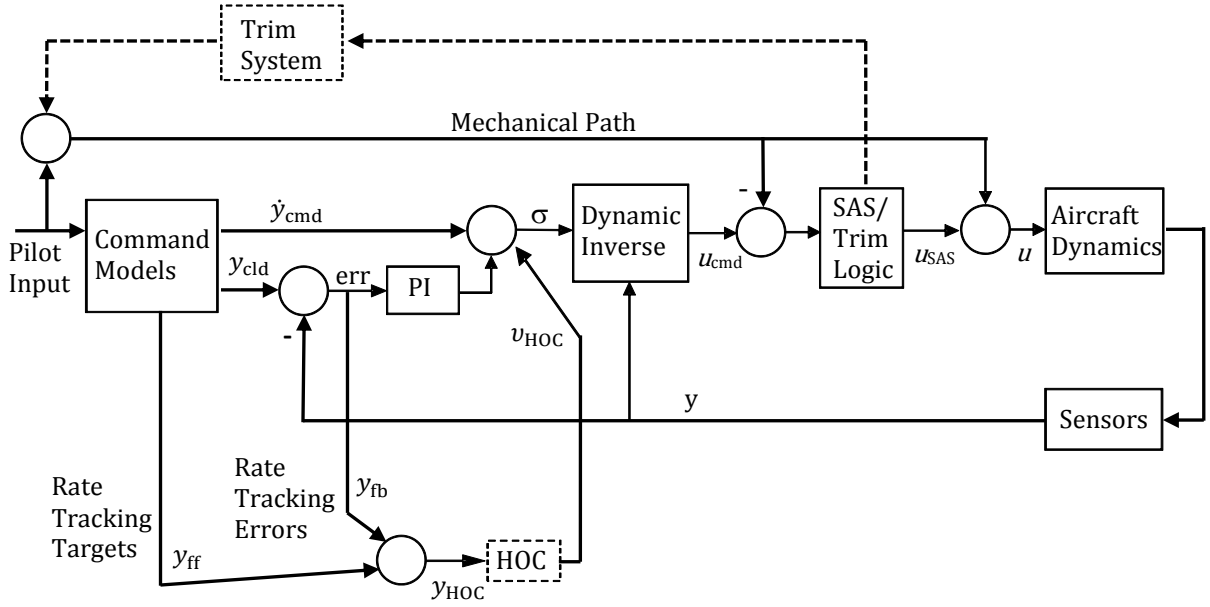

Figure 5-1. Schematic of PSU Partial Authority Control Architecture with HOC Augmentation

Because the proposed augmentative MIMO compensator acts at the rate control level, the same design is used in Rate Mode and all higher modes. Improvement to the Baseline (Dynamic Inversion with classical feedback alone) is evaluated in terms of: (1) root-mean-square (RMS) of rate error during random pilot input and air turbulence, and (2) qualitative evaluation of responses to pilot pulse and step inputs.

The augmentation design approach is to minimize standard deviation (H_2) of rate error, in rate mode, when the helicopter is subjected to pilot and turbulence disturbances. The plant used for HOC design is shown in Figure 5-2 below. $G_e(s)$ is the helicopter flight dynamics with the Baseline rate loops closed. The *W* blocks are weightings, which can include variation with frequency. The vector *d* is the disturbance, which can include pilot inceptors and air turbulence, and *n* is the vector of measurement noise. The vector υ_{HOC} is the input to the Baseline control from the HOC, y_{HOC} is the output vector used by the HOC, ξ is the closed-loop input vector consisting of disturbance and noise inputs, and *z* is the closed-loop output vector consisting of performance and actuation measures. The HOC is always designed to use the feedback outputs of angular rate error, labeled y_{fb}, and the design architecture allows for integral of angular rate error as a measurement for feedback. There is also the option of including the angular rate targets, labeled y_{ff}, in *y*; this generates a feed forward component within the MIMO augmentation, since the "disturbance" of the pilot inceptor movement is measured by the Baseline control and converted to the rate target in Rate Mode.

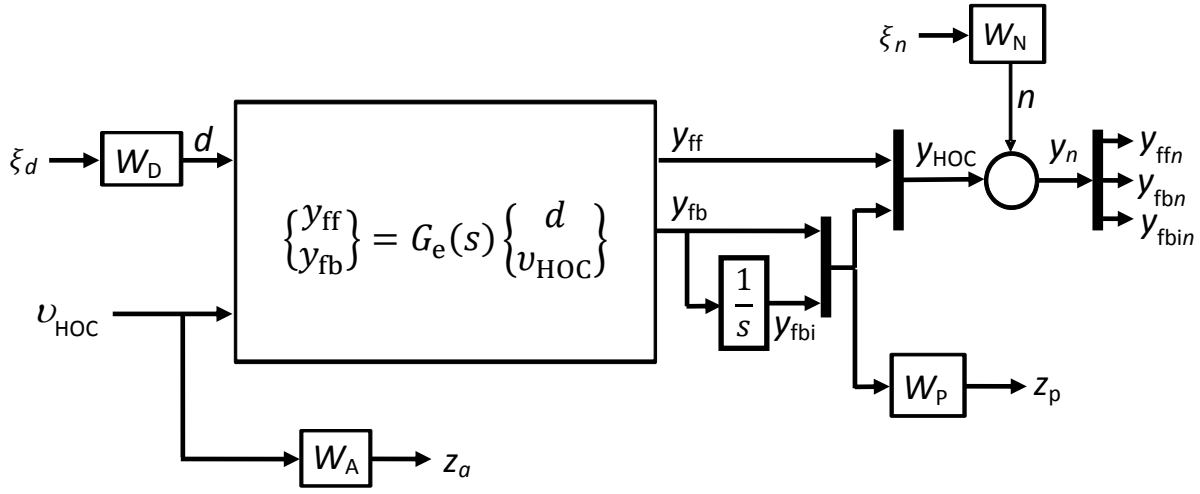

Figure 5-2. Schematic of Augmented Plant Model for HOC Design

Some benefits of this approach are that the HOC is selectable and can easily be authority-limited, which might ease certification. Also, because the plant for this augmentative MIMO compensator design is a stabilized helicopter system (the rate loops are closed), good flight test data could be safely gathered for more accurate plant identification.

5.1 Baseline Controller Adjustments Relative to Chapter 4

The Dynamic Inversion controller from the Chapter 4 study is applied to the same helicopter but in the form of a partial authority (+-10%) system. This means the control loops operate through additional actuators, the SAS actuators. The SAS actuators are second order with natural frequency 5 Hz and damping ratio 0.8. This caused loss of stability margins, so feedback gains had to be reduced slightly to return stability margins to the objectives for the Baseline Controller: greater than 50 deg phase margins, greater than 6 dB gain margins. The following adjustments to the DI gains were also found to be beneficial.

The effect of Δv upon $\dot{p}$ in the DI feedback is reduced.

$$\left[\mathbf{C}_{pqr}\mathbf{A}\right]_{1,1} \text{implemented} = 0.6 * \left[\mathbf{C}_{pqr}\mathbf{A}\right]_{1,1} \text{from design model} \tag{5-1}$$

This DI feedback neutralizes the natural dihedral effect. By reducing this feedback, some of the dihedral effect remains.

The effect of Δw upon $\dot{q}$ in the DI feedback is reduced.

$$\left[\mathbf{C}_{pqr}\mathbf{A}\right]_{2,2} \text{implemented} = 0.6 * \left[\mathbf{C}_{pqr}\mathbf{A}\right]_{2,2} \text{from design model} \tag{5-2}$$

At high speed, in Rate Mode, this reduces the rate of pitch divergence. It also improves pitch attitude phase margin by 7 degrees, and improves speed control margins by 0.25 dB and 7 degrees.

5.2 High Order Compensator Design

5.2.1 **Overview of High Order Compensator (HOC) Design**

The HOC is designed using linear optimal MIMO control theory, which requires that the plant be defined as a linear "Two Input / Two Output" (TITO) system. In this context, the two inputs consist of the closed-loop input *vector* (ξ) and the control *vector* (v_{HOC}), and the two outputs consist of the closed-loop output *vector* (z) and the sensor output *vector* (y_n). The vectors can have any dimension so it constitutes a general linear MIMO design problem. The notation for this TITO plant is shown by the equation

$$\begin{Bmatrix} \dot{x} \\ z \\ y_n \end{Bmatrix} = \begin{bmatrix} A & B_1 & B_2 \\ C_1 & D_{11}=0 & D_{12} \\ C_2 & D_{21} & D_{22} \end{bmatrix} \begin{Bmatrix} x \\ \xi \\ \upsilon_{\mathrm{HOC}} \end{Bmatrix} \tag{5-3}$$

In this application, from the perspective of the HOC, the "plant" consists of the existing plant (the aircraft with the Baseline control law active in Rate Mode), plus an option for integral action, combined with weightings applied to the closed-loop inputs and outputs. This plant used for HOC design, diagramed in Figure 5-2, is called the Augmented Plant Model. The state-space form of the Augmented Plant Model is derived in the next Section.

The general linear state-space representation of a dynamic compensator is

$$\begin{aligned} \dot{x}_c &= A_c x_c + B_c y_n \\ &= A_c x_c + B_c \left(C_2 x + D_{21}\xi + D_{22}\upsilon_{\mathrm{HOC}} \right) \\ \upsilon_{\mathrm{HOC}} &= C_c x_c + D_c y_n \\ &= C_c x_c + D_c \left(C_2 x + D_{21}\xi + D_{22}\upsilon_{\mathrm{HOC}} \right) \end{aligned} \tag{5-4}$$

For H_2 compensators, $D_c = 0$, so the closed-loop system is

$$\begin{gathered} \dot{x} = Ax + B_1\xi + B_2 C_c x_c \\ \dot{x}_c = B_c C_2 x + A_c x_c + B_c D_{21}\xi + B_c D_{22} C_c x_c \\ z = C_1 x + D_{12} C_c x_c \end{gathered} \tag{5-5}$$

In matrix form this is

$$\begin{gathered} \begin{Bmatrix} \dot{x} \\ \dot{x}_c \end{Bmatrix} = \begin{bmatrix} A & B_2 C_c \\ B_c C_2 & A_c + B_c D_{22} C_c \end{bmatrix} \begin{Bmatrix} x \\ x_c \end{Bmatrix} + \begin{bmatrix} B_1 \\ B_c D_{21} \end{bmatrix} \xi \\ z = \begin{bmatrix} C_1 & D_{12} C_c \end{bmatrix} \begin{Bmatrix} x \\ x_c \end{Bmatrix} \end{gathered} \tag{5-6}$$

and the closed-loop state-space matrices are

$$\begin{gathered} A_{CL} = \begin{bmatrix} A & B_2 C_c \\ B_c C_2 & A_c + B_c D_{22} C_c \end{bmatrix}, \quad B_{CL} = \begin{bmatrix} B_1 \\ B_c D_{21} \end{bmatrix} \\ C_{CL} = \begin{bmatrix} C_1 & D_{12} C_c \end{bmatrix}, \quad D_{CL} = [0] \end{gathered} \tag{5-7}$$

The HOC always operates on angular rate tracking errors (y_{fb}), and can optionally operate on angular rate tracking targets (y_{ff}) and integral of angular rate tracking errors (y_{fbi}). The injection point of the HOC control (υ_{HOC}) is the designer's choice, and the choice used for the present work is to inject the

HOC control signals at the pseudo-commands of the dynamic inversion. The closed-loop inputs (ξ) consist of signals that pass through weighting functions to become: pilot inceptor movement and air turbulence (disturbances *d*), and sensor noise (*n*). The closed-loop outputs (*z*) are rate tracking error, integral of tracking error (optionally), and the control activity of the HOC (υ_{HOC}), after these have been acted upon by weighting functions *W*. The weighting functions are linear time-invariant systems, which allows for both constant and frequency-dependent weightings that determine relative magnitude/importance.

5.2.2 **Augmented Plant Model in State-Space Form**

The state-space form of the Augmented Plant model will now be derived. The following subscripts are used in this derivation.

e: the existing system, i.e. the helicopter with Baseline Rate Mode active

d: disturbance

n: sensor noise

p: performance

a: actuation

i: integrator

In state-space form, the algebraically coupled equations are:

$$\begin{aligned} \dot{x}_{\mathrm{e}} &= A_{\mathrm{e}}x_{\mathrm{e}} + B_{\mathrm{e}d}d + B_{\mathrm{e}u}\upsilon_{\mathrm{HOC}} \\ y_{\mathrm{fb}} &= C_{\mathrm{fbe}}x_{\mathrm{e}} + D_{\mathrm{fb}d}d + D_{\mathrm{fb}u}\upsilon_{\mathrm{HOC}} \\ y_{\mathrm{ff}} &= C_{\mathrm{ffe}}x_{\mathrm{e}} + D_{\mathrm{ff}d}d + D_{\mathrm{ff}u}\upsilon_{\mathrm{HOC}} \end{aligned} \tag{5-8}$$

$$\dot{x}_d = A_d x_d + B_d \xi_d \,;\; d = C_d x_d + D_d \xi_d \tag{5-9}$$

$$\dot{x}_n = A_n x_n + B_n \xi_n \,;\; \begin{Bmatrix} n_{\mathrm{ff}} \\ n_{\mathrm{fb}} \end{Bmatrix} = \begin{bmatrix} C_{n\mathrm{ff}} \\ C_{n\mathrm{fb}} \end{bmatrix} x_n + \begin{bmatrix} D_{n\mathrm{ff}} \\ D_{n\mathrm{fb}} \end{bmatrix} \xi_n \tag{5-10}$$

$$\dot{x}_{\mathrm{p}} = A_{\mathrm{p}}x_{\mathrm{p}} + B_{\mathrm{p}} \begin{Bmatrix} y_{\mathrm{fb}} \\ y_{\mathrm{fbi}} \end{Bmatrix} ;\; z_{\mathrm{p}} = C_{\mathrm{p}}x_{\mathrm{p}} + D_{\mathrm{p}} \begin{Bmatrix} y_{\mathrm{fb}} \\ y_{\mathrm{fbi}} \end{Bmatrix} \tag{5-11}$$

$$\dot{x}_a = A_a x_a + B_a \upsilon_{\mathrm{HOC}} \; ; \; z_a = C_a x_a + D_a \upsilon_{\mathrm{HOC}} \tag{5-12}$$

$$\dot{x}_{\mathrm{i}} = y_{\mathrm{fb}} \; ; y_{\mathrm{fbi}} = x_{\mathrm{i}} \tag{5-13}$$

$$y_n = \begin{Bmatrix} y_{\mathrm{ff}n} \\ \{y_{\mathrm{fb}n}\} \\ \{y_{\mathrm{fbi}n}\} \end{Bmatrix} = \begin{Bmatrix} y_{\mathrm{ff}} \\ \{y_{\mathrm{fb}}\} \\ \{y_{\mathrm{fbi}}\} \end{Bmatrix} + \begin{Bmatrix} n_{\mathrm{ff}} \\ \{n_{\mathrm{fb}}\} \end{Bmatrix} \tag{5-14}$$

Making the algebraic substitutions, the augmented plant equation is

$$\begin{Bmatrix} \dot{x} \\ z \\ y = \begin{Bmatrix} y_{\mathrm{ff}n} \\ \{y_{\mathrm{fb}n}\} \\ \{y_{\mathrm{fbi}n}\} \end{Bmatrix} \end{Bmatrix} = \begin{bmatrix} A & B_1 & B_2 \\ C_1 & D_{11} = 0 & D_{12} \\ C_2 & D_{21} & D_{22} \end{bmatrix} \begin{Bmatrix} x \\ \xi \\ \upsilon_{\mathrm{HOC}} \end{Bmatrix} \tag{5-15}$$

$$\xi = \begin{Bmatrix} \xi_d \\ \xi_n \end{Bmatrix}, \qquad z = \begin{Bmatrix} z_{\mathrm{p}} \\ z_a \end{Bmatrix}$$

where

$$A = \begin{bmatrix} A_{\mathrm{e}} & B_{\mathrm{e}d} C_d & 0 & 0 & 0 & 0 \\ 0 & A_d & 0 & 0 & 0 & 0 \\ 0 & 0 & A_n & 0 & 0 & 0 \\ B_{\mathrm{p}} \begin{bmatrix} C_{\mathrm{fbe}} \\ 0 \end{bmatrix} & B_{\mathrm{p}} \begin{bmatrix} D_{\mathrm{fb}d} C_d \\ 0 \end{bmatrix} & 0 & A_{\mathrm{p}} & 0 & B_{\mathrm{p}} \begin{bmatrix} 0 \\ I \end{bmatrix} \\ 0 & 0 & 0 & 0 & A_a & 0 \\ C_{\mathrm{fbe}} & D_{\mathrm{fb}d} C_d & 0 & 0 & 0 & 0 \end{bmatrix} \tag{5-16}$$

$$B_1 = \begin{bmatrix} B_{\mathrm{e}d} D_d & 0 \\ B_d & 0 \\ 0 & B_n \\ B_{\mathrm{p}} \begin{bmatrix} D_{\mathrm{fb}d} D_d \\ 0 \end{bmatrix} & 0 \\ 0 & 0 \\ D_{\mathrm{fb}d} D_d & 0 \end{bmatrix}; \; B_2 = \begin{bmatrix} B_{\mathrm{e}u} \\ 0 \\ 0 \\ B_{\mathrm{p}} \begin{bmatrix} D_{\mathrm{fb}u} \\ 0 \end{bmatrix} \\ B_a \\ D_{\mathrm{fb}u} \end{bmatrix} \tag{5-17}$$

$$C_1 = \begin{bmatrix} D_{\mathrm{p}} \begin{bmatrix} C_{\mathrm{fbe}} \\ 0 \end{bmatrix} & D_{\mathrm{p}} \begin{bmatrix} D_{\mathrm{fb}d} C_d \\ 0 \end{bmatrix} & 0 & C_{\mathrm{p}} & 0 & D_{\mathrm{p}} \begin{bmatrix} 0 \\ I \end{bmatrix} \\ 0 & 0 & 0 & 0 & C_a & 0 \end{bmatrix}$$

$$C_2 = \begin{bmatrix} C_{\mathrm{ffe}} & D_{\mathrm{ff}d} C_d & C_{n\mathrm{ff}} & 0 & 0 & 0 \\ \begin{bmatrix} C_{\mathrm{fbe}} \\ 0 \end{bmatrix} & \begin{bmatrix} D_{\mathrm{fb}d} C_d \\ 0 \end{bmatrix} & C_{n\mathrm{fb}} & 0 & 0 & \begin{bmatrix} 0 \\ I \end{bmatrix} \end{bmatrix} \tag{5-18}$$

$$D_{11} = \begin{bmatrix} D_{\mathrm{p}} \begin{bmatrix} D_{\mathrm{fb}d} D_d \\ 0 \end{bmatrix} & \begin{matrix} 0 \\ 0 \end{matrix} \\ 0 & 0 \end{bmatrix};\ D_{12} = \begin{bmatrix} D_{\mathrm{p}} \begin{bmatrix} D_{\mathrm{fb}u} \\ 0 \end{bmatrix} \\ D_a \end{bmatrix}$$
$$D_{21} = \begin{bmatrix} D_{\mathrm{ff}d} D_d & D_{n\mathrm{ff}} \\ \begin{bmatrix} D_{\mathrm{fb}d} D_d \\ 0 \end{bmatrix} & D_{n\mathrm{fb}} \end{bmatrix};\ D_{22} = \begin{bmatrix} D_{\mathrm{ff}u} \\ \begin{bmatrix} D_{\mathrm{fb}u} \\ 0 \end{bmatrix} \end{bmatrix} \quad (5\text{-}19)$$

Note the requirement that the matrix product $D_{\mathrm{p}} D_{\mathrm{fb}d} D_d$ be zero so that $D_{11} = 0$. Otherwise H_2 performance would be fixed at infinity.

The order of this system can be relatively high as it includes all the states of the aircraft, sensors / actuators, Baseline control law, plus any additional states due to frequency shaped weighting functions or integral control. It is often helpful to reduce the order of the augmented plant through selective elimination of certain states, which will be elaborated upon later.

5.2.3 **High Order Compensator H_2 Design Formulas**

The present research employs a High Order Compensator synthesis method that minimizes H_2 performance. For H_2 performance, the inputs ξ are taken to be uncorrelated Gaussian white noise of unit intensity, and the performance measure is the mean-square of the closed-loop response

$$\left\| G_{CL} \right\|_2^2 = \lim_{t \to \infty} \mathbf{E}\left[z^T(t) z(t) \right] \leftarrow \text{minimize} \quad (5\text{-}20)$$

The HOC is designed by solving the standard algebraic Riccati equations (AREs), Equations (5-21) and (5-22) , which are constructed from the augmented plant model state space matrices, with the assumption that $D_{22} = 0$.

$$A_{\hat{P}}^T \hat{P} + \hat{P} A_{\hat{P}} - \hat{P} B_{\hat{P}} \hat{P} + C_{\hat{P}} = 0 \quad (5\text{-}21)$$

and

$$A_Q Q + Q A_Q^T - Q B_Q Q + C_Q = 0 \quad (5\text{-}22)$$

where

$$A_{\hat{P}} = A - B_2 \left(D_{12}^T D_{12} \right)^{-1} D_{12}^T C_1$$

$$B_{\hat{P}} = B_2 \left(D_{12}^T D_{12} \right)^{-1} B_2^T \tag{5-23}$$

$$C_{\hat{P}} = C_1^T C_1 - C_1^T D_{12} \left(D_{12}^T D_{12} \right)^{-1} D_{12}^T C_1$$

$$A_Q = A - B_1 D_{21}^T \left(D_{21} D_{21}^T \right)^{-1} C_2$$

$$B_Q = C_2^T \left(D_{21} D_{21}^T \right)^{-1} C_2 \tag{5-24}$$

$$C_Q = B_1 B_1^T - B_1 D_{21}^T \left(D_{21} D_{21}^T \right)^{-1} D_{21} B_1^T$$

The AREs can be solved using the solver in MATLAB or other mathematics utilities. Valid solutions for $\hat{P}$ and Q must be positive semi-definite, although in some cases they will have slightly negative eigenvalues due to numerical error. The HOC is then given by the following:

$$\begin{aligned} B_c &= \left(QC_2^T + B_1 D_{21}^T \right) \left(D_{21} D_{21}^T \right)^{-1} \\ C_c &= -\left(D_{12}^T D_{12} \right)^{-1} \left(B_2^T \hat{P} + D_{12}^T C_1 \right) \\ A_c &= A - B_c C_2 + B_2 C_c \end{aligned} \tag{5-25}$$

$$\dot{x}_c = A_c x_c + B_c y_{\text{HOC}} \quad , \quad \upsilon_{\text{HOC}} = C_c x_c \tag{5-26}$$

Note that the D_{11} and D_{22} matrices are assumed to be zeros (i.e. no direct throughput of controls to output or disturbances to performance variables). If D_{11} is not zero, H_2 performance is infinity. D_{22} will naturally be zero for real systems. In addition, D_{12} must be full column rank and D_{21} must be full row rank.

To improve the likelihood of good control synthesis, the augmented plant should not include uncontrollable or unobservable modes. Therefore, states that have little or no involvement in the input-output relationship are removed. It is also necessary to remove states associated with motion that is not expected to be asymptotically stabilized with an angular rate compensator, such as attitudes and translational rates. This model order reduction is accomplished via truncation, because, to schedule the

compensators (with speed, usually), it is necessary to avoid state transformations so that the state space structure remains consistent.

When active, the HOC operates on the rate tracking targets and errors (y_{HOC}) and adds the control signal v_{HOC} to the pseudo command ($\boldsymbol{\sigma}_3$). The integral of rate tracking errors, if used, can be considered to be inside the HOC block in Figure 5-1.

Note that much of the Baseline control law is not retained in the plant model used for HOC design. The states associated with any component not involved in an input-output path in Baseline Rate Mode or not active during small perturbations (e.g. the trim actuators) should not appear in the linearized model used in HOC design. If using MATLAB, these states are often removed automatically, but they may need to be removed manually using *modred*.

5.2.4 **High Order Compensator Design Steps**

The following is a step-by-step process for the HOC design.

5.2.4.1 Select measurements, and input injection point

The HOC augmentation method should always operate on rate tracking error, i.e. the difference between a commanded state and actual measured state, and can also operate on rate tracking target. This generally requires the Baseline control architecture to include some kind of command model. The input to the rate command model is called a rate target and the output is a rate command that follows an ideal dynamic response that meets handling qualities specifications. It is best if the HOC does *not* operate on measured rate (as opposed to measured rate *error*) because it would tend to fight the pilot input. The HOC input injection point can be directly at the actuator command or at some point earlier in the Baseline control, such as the pseudo-command within the dynamic inversion architecture.

The HOC design presented here operates on tracking targets and errors for roll, pitch, and yaw angular rates. The HOC does not operate in the vertical axis since the collective axis in this design has no SAS actuator, and the trim actuator has low bandwidth and small rate limit. The injection point is at the

"pseudo command", i.e. the commanded angular accelerations in the roll, pitch, and yaw axes, which then get converted to actuator commands in the inversion part of the control law.

5.2.4.2 Select disturbance and noise inputs

The HOC design requires external disturbances and sensor noise as the closed-loop inputs. Note that these disturbances and noises may or may not be implemented during a simulation, but they are used in the control synthesis process. Either pilot or turbulence disturbances must be incorporated, and both may be. If rate targets are included in the Augmented-Plant measurements (in addition to rate errors) then pilot disturbance must be included. The HOC design trials only included pilot disturbance when the rate targets were included as measurements (HOC with feed-forward control).

All augmented-plant measurements (y_{HOC}), to include tracking targets, tracking errors, and integrals of tracking errors (whatever is included in the chosen Augmented Plant), must include linearly independent direct feed through of closed-loop input. That is, the $\begin{bmatrix} D_{n\mathrm{ff}} \\ D_{n\mathrm{fb}} \end{bmatrix}$ matrix must have full row rank. To satisfy this requirement, a separate noise input was assigned to each measurement, and the "D" matrix of the noise filter was defined to be diagonal with all diagonal elements non-zero.

5.2.4.3 Generate linear plant model

SIMULINK linearization features were used to generate linearized models of the combined aircraft and Baseline Control (set to Rate Mode) in a trimmed condition at a range of forward speeds, which constitutes the Existing System ($G_{\mathrm{e}}(s)$ in Figure 5-2). With this SIMULINK mechanism, all Existing System inputs and outputs must be top level ports. It is helpful if the Simulink model is set up so that the resulting LTI object produced by the linearization scheme has well-labeled states, inputs, and outputs. In particular, having easily identified state names is useful for the model order reduction process discussed below. For most of the design process, a low speed (10 kts) and a high speed (120 kts) were selected for the evaluations.

Relatively high order linear models of the aircraft are used in the SIMULINK model. The model includes rotor flapping, lagging, and inflow dynamics represented in multi-blade coordinates. The Baseline Control adds a number of additional states due to actuators, sensor dynamics, and other dynamic components. Note that some of these states are eliminated in the model reduction process, covered next.

5.2.4.4 Model order reduction

It is helpful to remove states from the Existing System that (1) are weakly coupled to the inputs or outputs; (2) are associated with motion that is not expected to be asymptotically stabilized with an angular rate compensator, or (3) are not important for the frequency range over which the HOC is designed to operate. This model order reduction is accomplished via truncation, because to schedule the compensators (with speed, usually) it is necessary to avoid state transformations in order to maintain a consistent state space structure. In the model reductions, the *minreal* or *balreal* commands are avoided, because they result in state transformations that change the model structure each time the model is linearized at a particular operating point. This can present difficulties in scheduling of the HOC. Model truncation is accurate when removing de-coupled or slowly varying states, and it results in consistent HOC state space structure for the Riccati solutions at each operating point. This allows the use of linear interpolation of the HOC state space matrices with operating condition (typically airspeed is the interpolating variable).

In this application, the HOC is designed to compensate angular rates and higher order dynamics. It mainly operates to improve response in the 0.5 to 5 rad/sec frequency range (or sometimes at higher frequencies). Thus lower frequency dynamics associated with translational rates are eliminated. Attitudes cannot be expected to be asymptotically stabilized with an angular rate compensator, so they are also truncated from the Augmented Plant model used in HOC design. All states associated with sensors that measure velocities and attitude are removed, and all states associated with the vertical axis are removed since the HOC does not seek to augment vertical motion control. Since the trim follow up logic does not act continuously (there is a deadband), trim actuator states should not appear in the linear model either.

5.2.4.5 Select Weighting Functions

Turbulence Disturbance Weighting

For simulation of turbulence, the flight model is stimulated with the Control Equivalent Turbulence Input (CETI) model, which was developed by Lusardi, et al. (Ref. [34]) based on UH-60 flight test data. The turbulence intensity parameters are set to a moderate level: mean wind speed = 41.3 ft/sec, wind vertical std dev = 6.5 ft/sec, wind lateral std dev = 8.5 ft/sec. The CETI model treats turbulence as equivalent control inputs, driven by filtered white-noise. Therefore, these filters were chosen as the turbulence disturbance weighting functions, shown by Equation (5-27).

$$d_{\text{turb}} = \underbrace{\begin{bmatrix} \dfrac{114}{s^3+29.3\,s^2+428\,s+399} & 0 & 0 \\ 0 & \dfrac{126}{s^3+29.3\,s^2+428\,s+399} & 0 \\ 0 & 0 & \dfrac{45.0}{s^3+28.8\,s^2+414.5\,s+205.7} \end{bmatrix}}_{W_{\text{D,turb}}} \begin{Bmatrix} \xi_{\text{turb,lat}} \\ \xi_{\text{turb,lng}} \\ \xi_{\text{turb,ped}} \end{Bmatrix} \quad (5\text{-}27)$$

Turbulence inputs to the flight dynamics model, d_{turb}, are in equivalent inches of UH-60 inceptors.

Pilot Disturbance Weighting

For pilot disturbance weighting, identical low-pass filters were selected for each axis, with corner frequency 9 rad/sec and zero-frequency gain 5% of full throw of the Baseline Control inceptors.

$$d_{\text{pilot}} = \underbrace{\begin{bmatrix} 5\dfrac{9}{s+9} & 0 & 0 \\ 0 & 5\dfrac{9}{s+9} & 0 \\ 0 & 0 & 5\dfrac{9}{s+9} \end{bmatrix}}_{W_{\text{D,pilot}}} \begin{Bmatrix} \xi_{\text{pilot,lat}} \\ \xi_{\text{pilot,lng}} \\ \xi_{\text{pilot,ped}} \end{Bmatrix} \quad (5\text{-}28)$$

Noise Weighting

The noise weighting was made to be a direct feed-through diagonal matrix having no dynamics, as shown by Equation (5-29). The noise weights are varied as part of the HOC tuning process. In this work, the output *n* has unit deg/sec.

$$n = diag\underbrace{\begin{pmatrix} W_{n\_p\mathrm{Tgt}} \\ W_{n\_q\mathrm{Tgt}} \\ W_{n\_r\mathrm{Tgt}} \\ W_{n\_p\mathrm{Err}} \\ W_{n\_q\mathrm{Err}} \\ W_{n\_r\mathrm{Err}} \end{pmatrix}}_{W_{\mathrm{N}}} \begin{Bmatrix} \xi_{pTgt} \\ \xi_{qTgt} \\ \xi_{rTgt} \\ \xi_{p} \\ \xi_{q} \\ \xi_{r} \end{Bmatrix} \tag{5-29}$$

Significance of Disturbance and Noise Weightings

The disturbance weighting indicates the uncertainty in the plant model, while the noise weighting indicates the uncertainty in the measurements. The magnitude of the disturbance weighting relative to the sensor noise weighting determines how quickly the state-estimator portion of the HOC ($\dot{x}_c = A_c x_c + B_c y$) responds to changing measurements. If the poles of the HOC are too fast, the noise weighting should be increased relative to the disturbance weighting.

Actuator Weighting

The actuator weighting was scaled so that 10% inputs from the HOC resulted in an actuation measure of 1 at low frequency (below 5 rad/sec). The weight for each axis is frequency dependent such that the weighting increases by a factor of 10 as frequencies increase between 5 and 50 rad/sec. In transfer function form this is shown by Equation (5-30), where each axis has a scaling factor (*SF*) that converts the pseudo command ($\boldsymbol{\sigma}_3$) to equivalent flight dynamics input ($\mathbf{u}_3$) in percent.

$$z_a = \underbrace{\begin{bmatrix} 0.1\dfrac{0.2\ s+1}{0.02\ s+1}SF_{\dot{p}} & 0 & 0 \\ 0 & 0.1\dfrac{0.2\ s+1}{0.02\ s+1}SF_{\dot{q}} & 0 \\ 0 & 0 & 0.1\dfrac{0.2\ s+1}{0.02\ s+1}SF_{\dot{r}} \end{bmatrix}}_{W_A} \begin{Bmatrix} \upsilon_{\mathrm{HOC},\dot{p}} \\ \upsilon_{\mathrm{HOC},\dot{q}} \\ \upsilon_{\mathrm{HOC},\dot{r}} \end{Bmatrix} \tag{5-30}$$

The scale factors above are computed as follows. Start with the linear design model for angular rate EMF, Equation (4-5), but with **u** in %.

$$\begin{gathered} \Delta\dot{\mathbf{x}} = \mathbf{A}\Delta\mathbf{x} + \mathbf{B}\Delta\mathbf{u} \ \text{, } \mathbf{u} \text{ is in \%} \\ \mathbf{y} = \lfloor p \quad q \quad r \rfloor^T = \mathbf{C}_{pqr}\Delta\mathbf{x}\,, \quad \text{where } \mathbf{C}_{pqr} = \left[\mathbf{0}_{3x2} \quad \mathbf{I}_3\right] \\ \dot{\mathbf{y}} = \lfloor \dot{p} \quad \dot{q} \quad \dot{r} \rfloor^T = \mathbf{C}_{pqr}\left[\mathbf{A}\Delta\mathbf{x} + \mathbf{B}\Delta\mathbf{u}\right] = \mathbf{C}_{pqr}\mathbf{A}\Delta\mathbf{x} + \mathbf{C}_{pqr}\mathbf{B}\Delta\mathbf{u} \end{gathered} \tag{5-31}$$

The angular acceleration magnitudes associated with 1% control input are

$$\begin{aligned} \dot{p}_{1\%} &= \left[\mathbf{C}_{pqr}\mathbf{B}\right]_{\mathrm{row1}} \frac{\left\{\left[\mathbf{C}_{pqr}\mathbf{B}\right]_{\mathrm{row1}}\right\}^T}{\left\| \left[\mathbf{C}_{pqr}\mathbf{B}\right]_{\mathrm{row1}}\right\|_2} \\ \dot{q}_{1\%} &= \left[\mathbf{C}_{pqr}\mathbf{B}\right]_{\mathrm{row2}} \frac{\left\{\left[\mathbf{C}_{pqr}\mathbf{B}\right]_{\mathrm{row2}}\right\}^T}{\left\| \left[\mathbf{C}_{pqr}\mathbf{B}\right]_{\mathrm{row2}}\right\|_2} \\ \dot{r}_{1\%} &= \left[\mathbf{C}_{pqr}\mathbf{B}\right]_{\mathrm{row3}} \frac{\left\{\left[\mathbf{C}_{pqr}\mathbf{B}\right]_{\mathrm{row3}}\right\}^T}{\left\| \left[\mathbf{C}_{pqr}\mathbf{B}\right]_{\mathrm{row3}}\right\|_2} \end{aligned} \tag{5-32}$$

The scale factors are the reciprocals of these sensitivities.

$$\begin{aligned} SF_{\dot{p}} &= 1 \big/ \dot{p}_{1\%} \\ SF_{\dot{q}} &= 1 \big/ \dot{q}_{1\%} \\ SF_{\dot{r}} &= 1 \big/ \dot{r}_{1\%} \end{aligned} \tag{5-33}$$

Performance Weighting

The performance weighting was made to be a direct feed-through diagonal matrix having no dynamics. The performance weights are varied as part of the HOC tuning process.

$$z_{\mathrm{p}} = \underbrace{\begin{bmatrix} W_{\mathrm{p\_}p\mathrm{Err}} & & \\ & W_{\mathrm{p\_}q\mathrm{Err}} & \\ & & W_{\mathrm{p\_}r\mathrm{Err}} \end{bmatrix}}_{W_{\mathrm{P}}} \begin{Bmatrix} p_{\mathrm{err}} \\ q_{\mathrm{err}} \\ r_{\mathrm{err}} \end{Bmatrix} \tag{5-34}$$

In this work, the angular rate error unit was deg/sec.

Significance of Actuator and Performance Weightings

The actuator weighting applies cost to actuator activity, while the performance weighting applies cost to the tracking errors. The magnitude of the performance weighting relative to the actuator weighting determines the aggressiveness (gain) of the state-feedback portion of the HOC $\left(\upsilon_{HOC} = C_c x_c\right)$. Usually, increasing the performance weighting reduces stability margins.

5.2.4.6 Select HOC design weights by evaluating Attitude Mode as design weights are varied.

Now the Augmented Plant can be assembled, and the HOC designed according to the HOC Design Formulas Section. This design and evaluation phase should be conducted at a minimum of two airspeeds, one low and one high. The HOC is scheduled with airspeed, but in this research the weights are not, with the one exception being $W_{r\mathrm{Tgt}}$.

A range of compensators are designed for different performance and noise weights, while evaluating: (1) positive semi-definiteness of the Riccati equation solutions, (2) HOC poles, (3) Attitude Mode phase margins, (4) rate tracking errors due to air turbulence while in Attitude Mode, and (5) rate tracking errors due to pilot inceptor movement while in Attitude Mode. If the HOC has large negative poles, it causes issues with discrete time implementation. Assuming a 100 Hz update rate, if HOC poles are much over 50 rad/s, the noise weighting needs to increase. High performance weights produce high gain (aggressive) compensators, while as performance weights go to zero the performance of the augmented control approaches that of the Baseline Controller without HOC. Performance is evaluated in terms of RMS of the rate tracking error, under excitation from either air turbulence (all axes at the same time) or pilot inceptor movement in one axis at a time, versus phase margin. A judgment is then made as

to which combination of weights meets the pole magnitude and phase margin requirements while providing the best overall reduction in rate tracking errors.

Using the final choice for the design weights, HOCs are designed at all airspeed breakpoints and some checks are made: (1) positive semi-definiteness of the Riccati equation solutions, (2) HOC poles, (3) the Attitude Mode gain and phase margins.

All of this work has used linearized plants. Once the design looks good in that environment it needs to be checked in fully nonlinear simulation, initially using scripted batch simulation analysis and then in piloted simulations.

5.2.5 **Example HOC Weighting Selections**

HOC designs were performed for two HOC variants applied to the same plant – a stitched full flight envelope airframe (see Section Chapter 2) combined with the Baseline Controller in Rate Mode. The Baseline Rate Mode was tuned with speed-independent gains such that the minimum Attitude Mode phase margin is in the neighborhood of 50 degrees, and Attitude Mode gain margins are greater than 6 dB. The first HOC design variant is feedback only (angular rate errors) with air turbulence disturbance. The second HOC design variant is feedforward (angular rate targets) and feedback with disturbances being pilot inceptor movement and air turbulence. The first HOC variant is referred to as HOC_FB, and the second as HOC_FBFF.

The process for selecting noise and performance weights is as follows: 1) Start with an initial guess of equal weighting for all noise weights, and equal weighting for all performance weights. 2) Sweep noise and performance weighting factors (W_n and W_p) which scale, in unison, the associated axis-specific weights. 3) Evaluate the results in each axis in terms of Attitude Mode gain and phase margin, RMS rate errors while in Attitude Mode, largest pole magnitude of the HOC and of the Rate Mode with HOC. 4) Make note of the best weighting factor combination for each of the axes. 5) Apply axis-specific weighting adjustments. 6) Perform in-unison weighting factor sweeps again. This process repeats until RMS errors

begin to increase, or some limit is approached. The following limits were imposed for the designs in this paper: 43deg phase margin, 6dB gain margin, pole magnitudes less than 54 rad/s.

With HOC_FB, the performance objective was response to turbulence in terms of RMS rate error in Attitude Mode. With HOC_FBFF, the performance objectives were RMS rate errors due to random pilot input and due to turbulence. Final noise and performance weightings for both architectures are shown in Table 5-1.

Table 5-1. Final Noise and Performance Weightings

Weight Type	**Weight Term**	**HOC_FB**	**HOC_FBFF**
perform	$W_{\mathrm{p\_}p\mathrm{Err}}$	45.3	1
perform	$W_{\mathrm{p\_}q\mathrm{Err}}$	60.4	1.6
perform	$W_{\mathrm{p\_}r\mathrm{Err}}$	164.6	1.5
noise	$W_{n\_p\mathrm{Err}}$	0.72	0.24
noise	$W_{n\_q\mathrm{Err}}$	0.842	0.384
noise	$W_{n\_r\mathrm{Err}}$	0.88	0.9
noise	$W_{n\_p\mathrm{Tgt}}$	n/a	$6{*}W_{n\_p\mathrm{Err}}$
noise	$W_{n\_q\mathrm{Tgt}}$	n/a	$3{*}W_{n\_q\mathrm{Err}}$
noise	$W_{n\_r\mathrm{Tgt}}$	n/a	$1.9{*}W_{n\_r\mathrm{Err}}$, 10 kts $5{*}W_{n\_r\mathrm{Err}}$, 120 kts

5.3 Results

All results presented here were obtained using the full flight envelope flight dynamics model described in Chapter 2.

5.3.1 **Rate Errors from Turbulence and Random Pilot Inputs**

Figure 5-3 through Figure 5-14 show root-mean-square (RMS) rate error and gain margin versus phase margin with the two HOC variants and for the Baseline Controller alone. The HOC curves are formed by sweeping W_{p} for three values of W_n , where these weighting factors scale the final-design axis-specific weights in unison, as was done in the weighting selection procedure. The Baseline curves are formed by scaling-up the roll rate, pitch rate, and yaw rate feedback gains, by a common factor in unison.

To reduce clutter, the weighting and scale factors are not shown on the curves, but the final design points are marked. For HOCs the marked points are for $(W_p,W_n) = (1,1)$, and for Baseline alone the marked points are for scale factor 1. The Baseline design point, indicated by a black square, is the start of the solid black Baseline curve, and this curve proceeds outward with scale factors greater than 1. The HOC curves are closest to the nominal Baseline result when W_p is smallest. The HOC line colors correspond to values of W_n : 0.8 is blue, 1 is green, 1.2 is red. HOC_FB results are indicated by dotted lines, with a magenta cirle around the final design result. HOC_FBFF results are shown as solid colored lines, with a green diamond around the final design result.

These figures show that the HOC_FBFF controller provides the best overall improvement, relative to the Baseline, in terms of following pilot commands and turbulence rejection. The turbulence rejection was not quite as good as the HOC_FB controller, but still generally better than the Baseline Controller with increased rate gains. Both the HOC_FB and increased-gain Baseline improve upon turbulence rejection, but usually increase rate-errors during pilot inputs. As has already been implied, the HOC_FB shows the greatest improvement in turbulence rejection while remaining within design limits.

Figure 5-15 through Figure 5-20 show the rate error response versus time to random pilot input in one axis, for the HOC_FBFF final design and Baseline nominal design. These are the raw rate error results that were processed into the RMS of rate error results. The results show that the tracking errors are visibly reduced in both the on-axis and off-axis responses in most cases. In some cases, certain axes show virtually no change from the baseline case (no improvement or degradation).

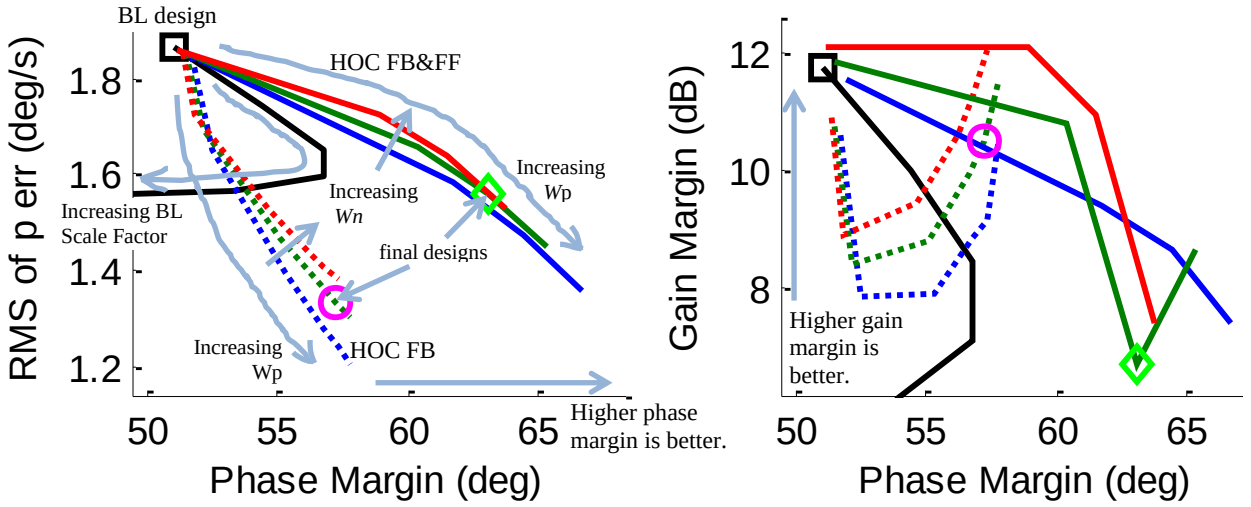

Figure 5-3. RMS Error from Turbulence, Gain and Phase Margins – Lateral Axis, 10 knots

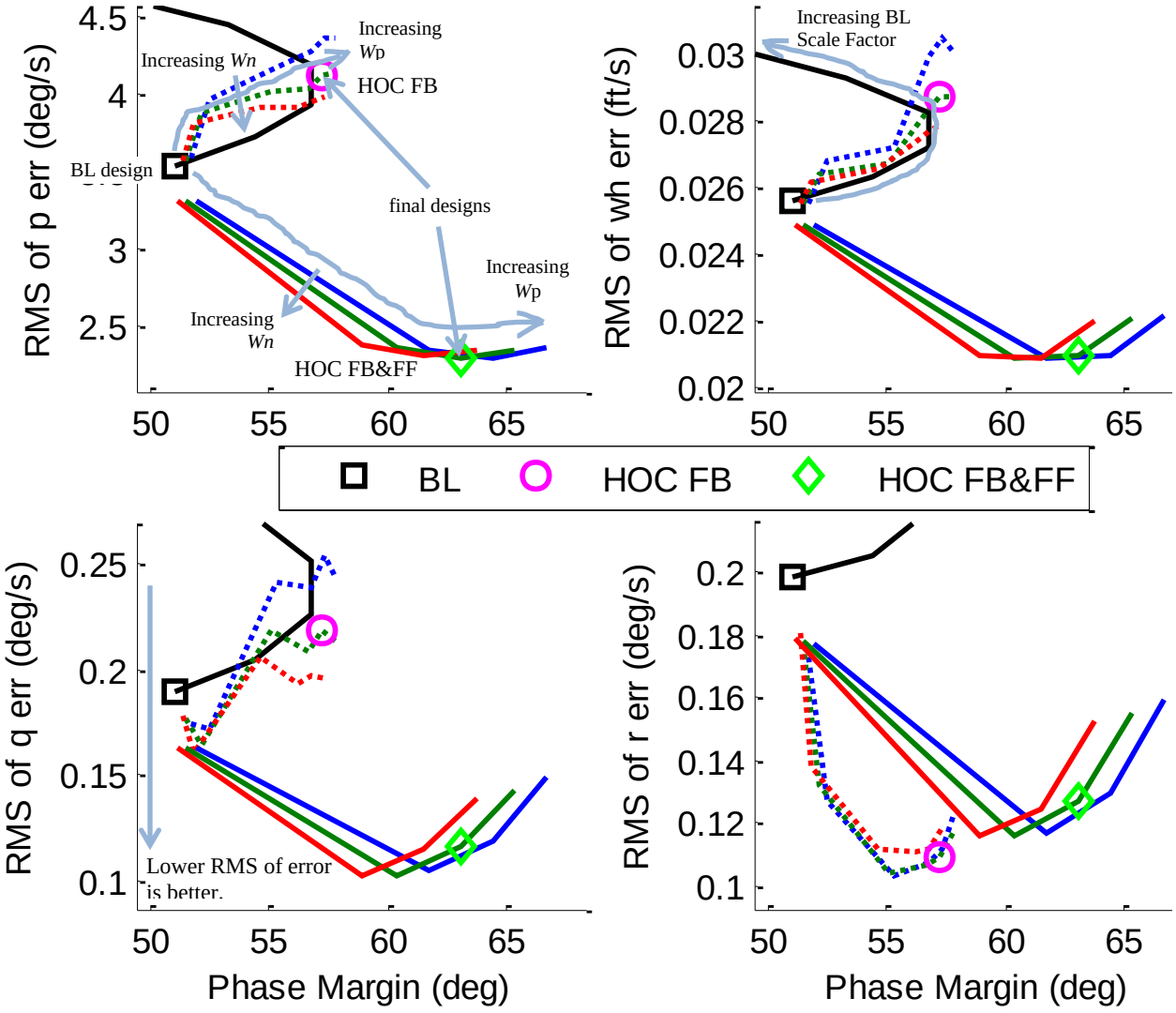

Figure 5-4. RMS Errors from Pilot Lateral – 10 knots

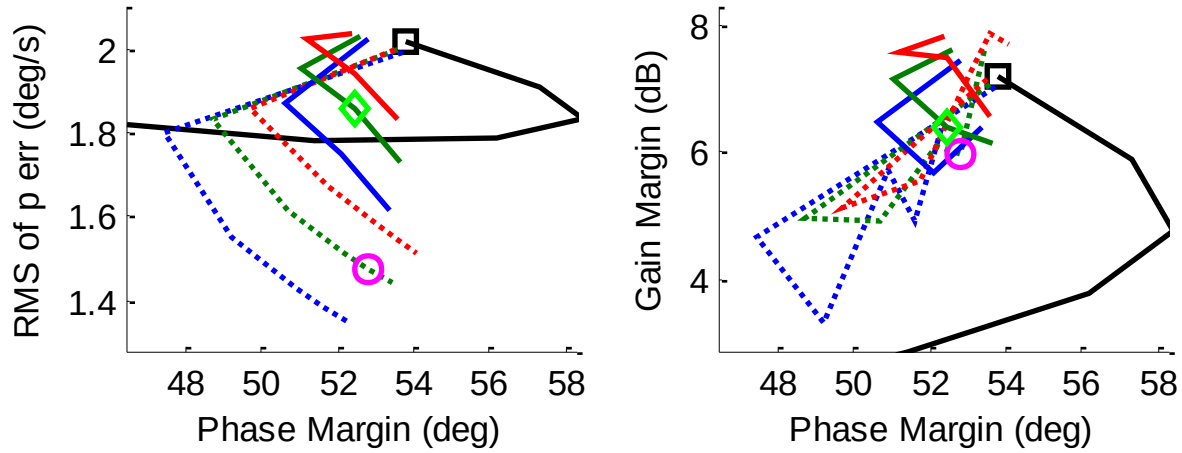

Figure 5-5. RMS Error from Turbulence, Gain and Phase Margins – Lateral Axis, 120 knots

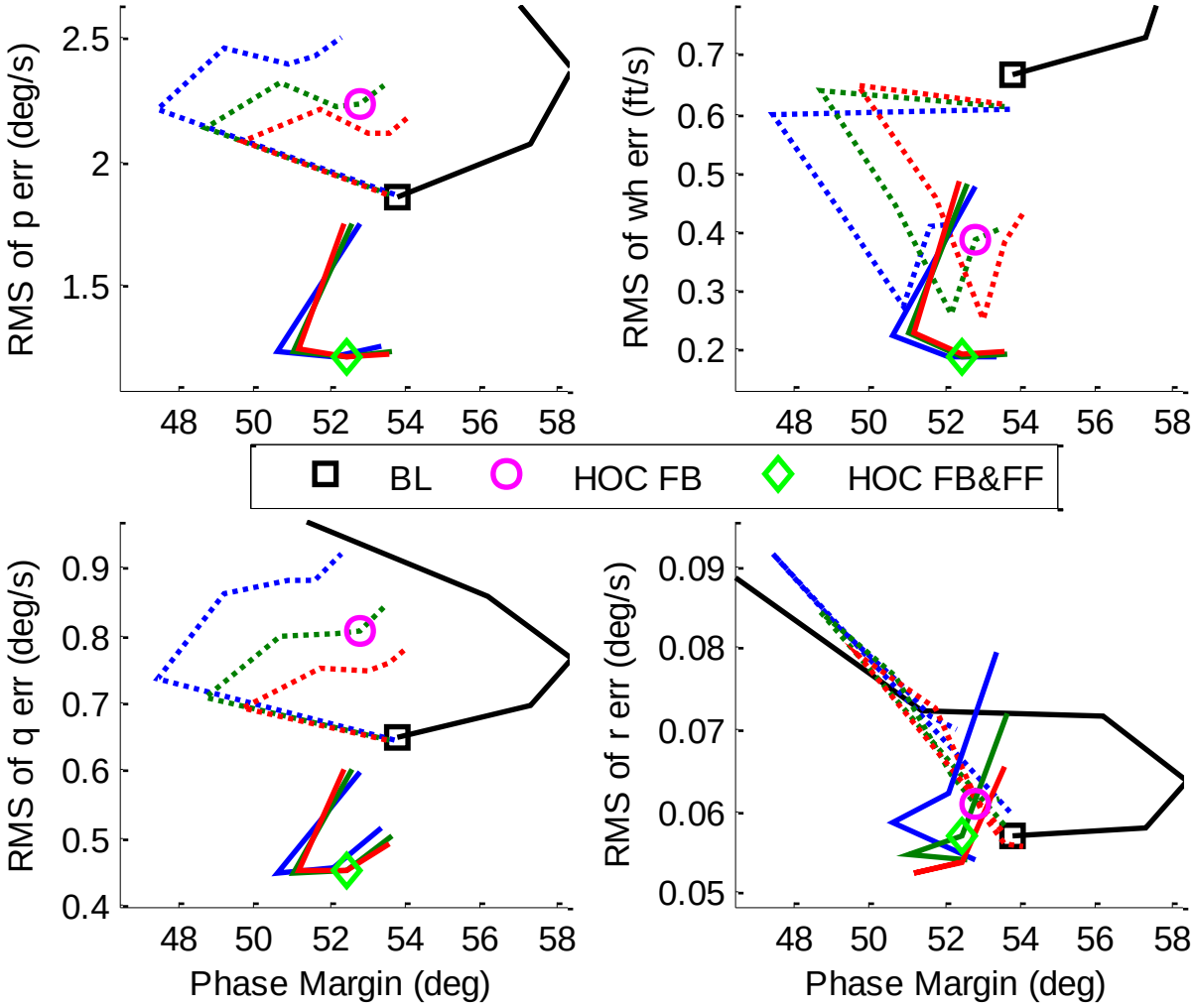

Figure 5-6. RMS Errors from Pilot Lateral – 120 knots

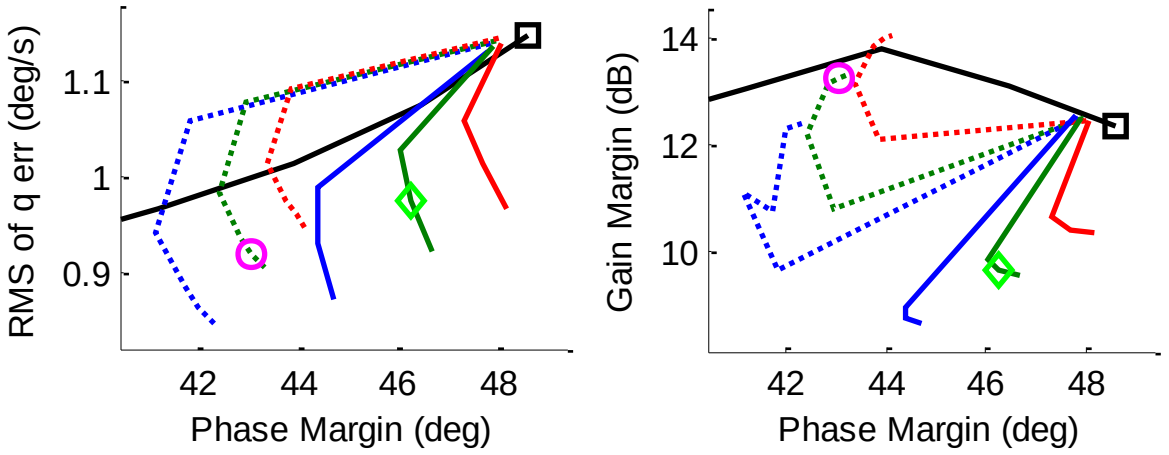

Figure 5-7. RMS Error from Turbulence, Gain and Phase Margins – Longitudinal Axis, 10 knots

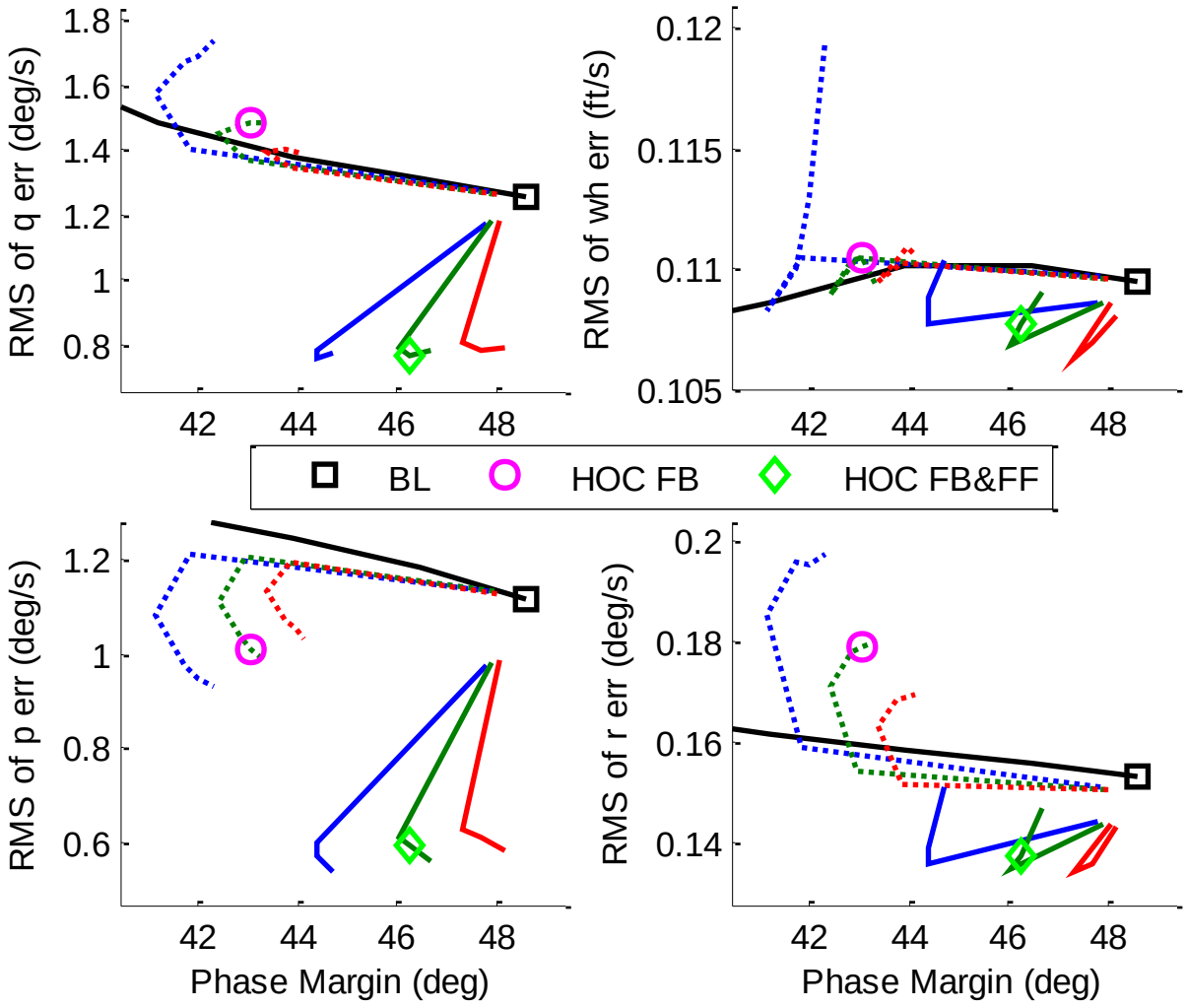

Figure 5-8. RMS Errors from Pilot Longitudinal – 10 knots

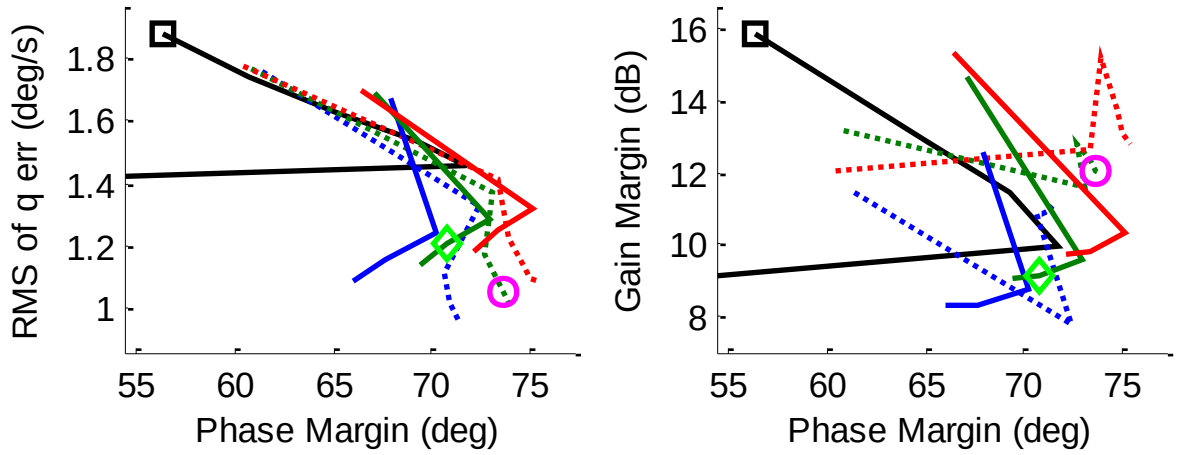

Figure 5-9. RMS Error from Turbulence, Gain and Phase Margins – Longitudinal Axis, 120 knots

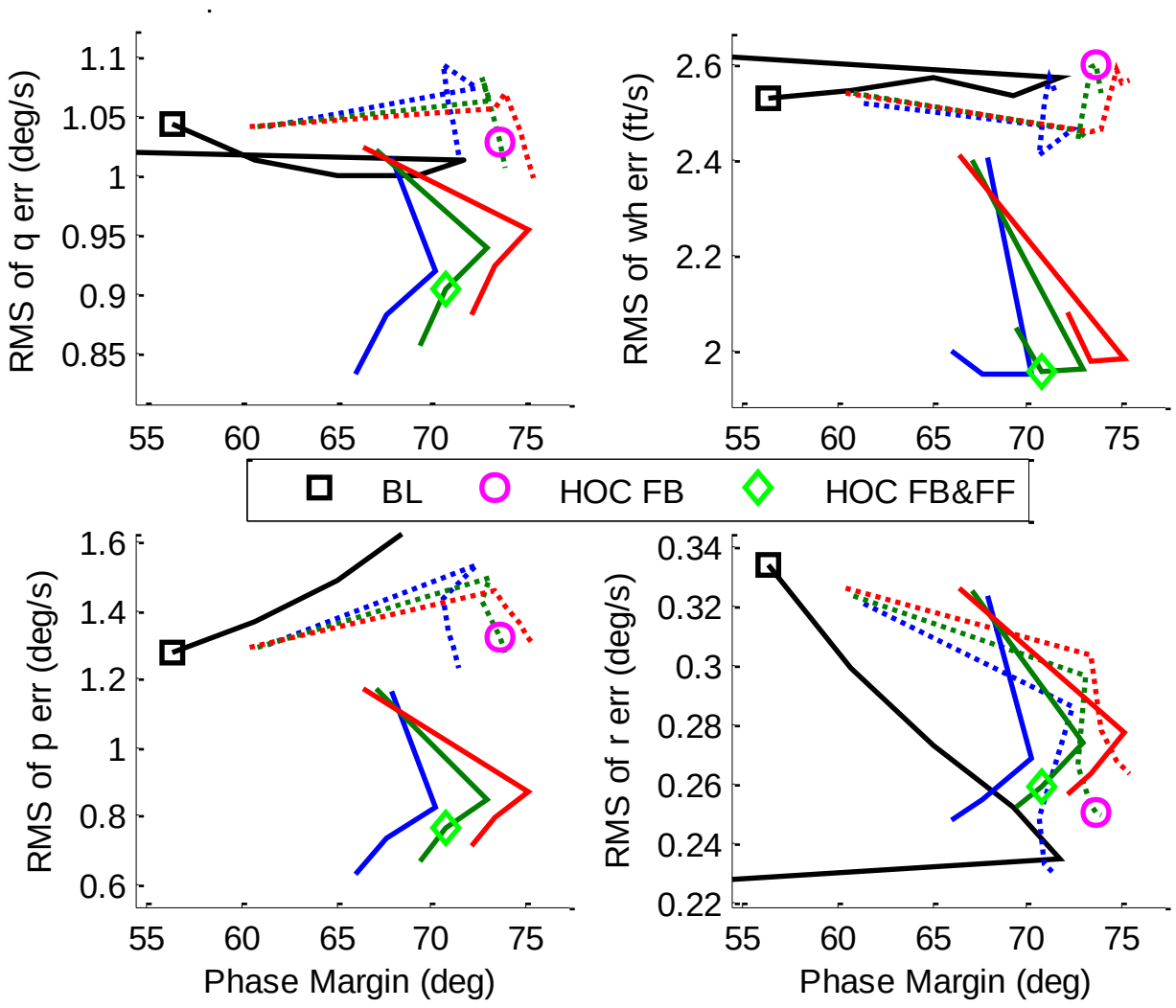

Figure 5-10. RMS Errors from Pilot Longitudinal – 120 knots

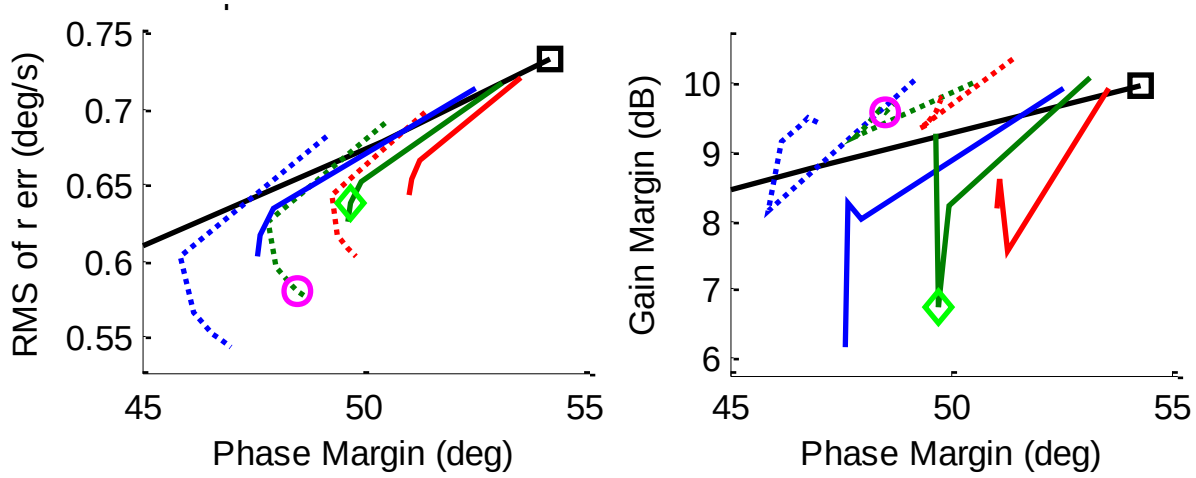

Figure 5-11. RMS Error from Turbulence, Gain and Phase Margins – Yaw Axis, 10 knots

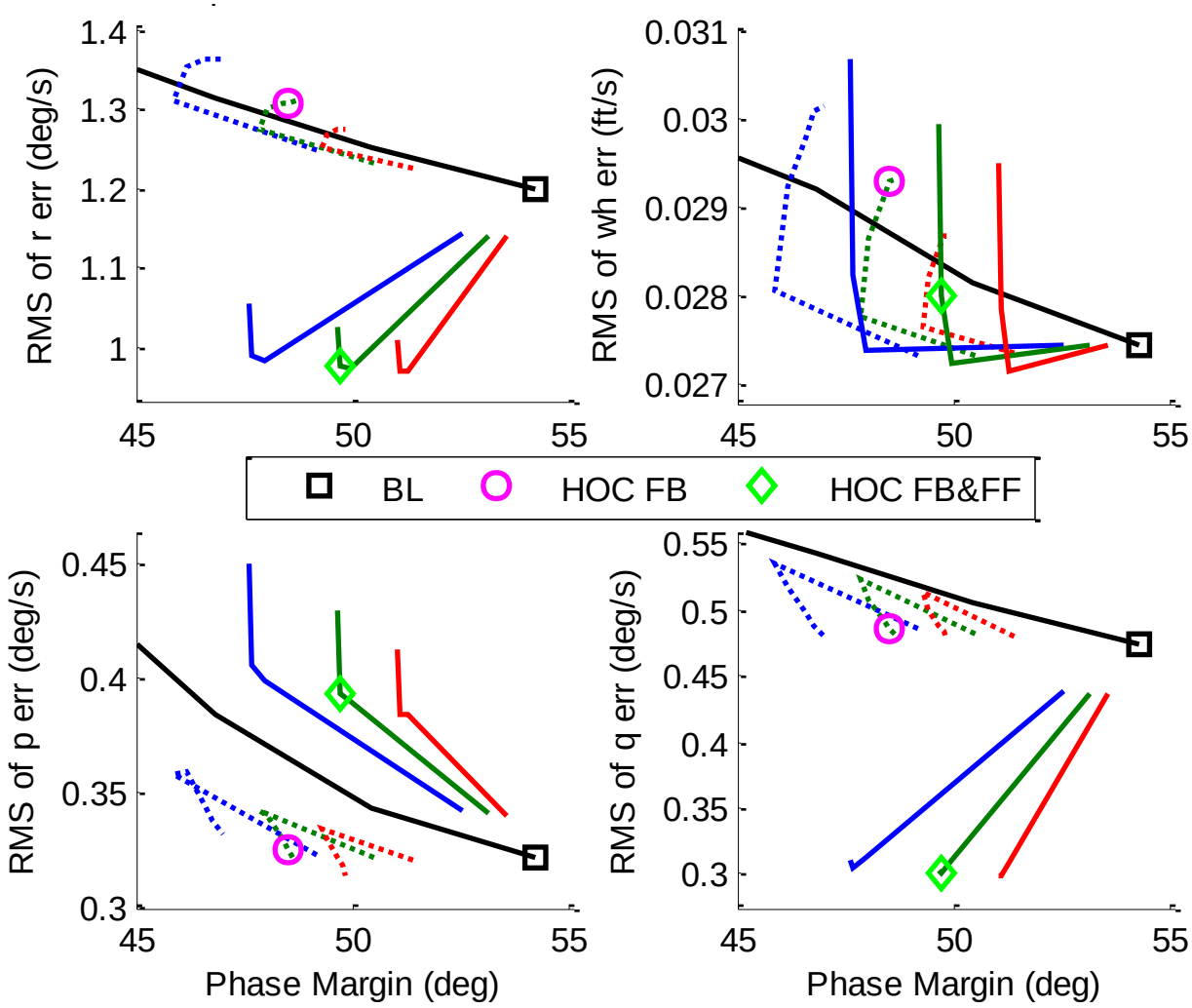

Figure 5-12. RMS Errors from Pilot Pedal – 10 knots

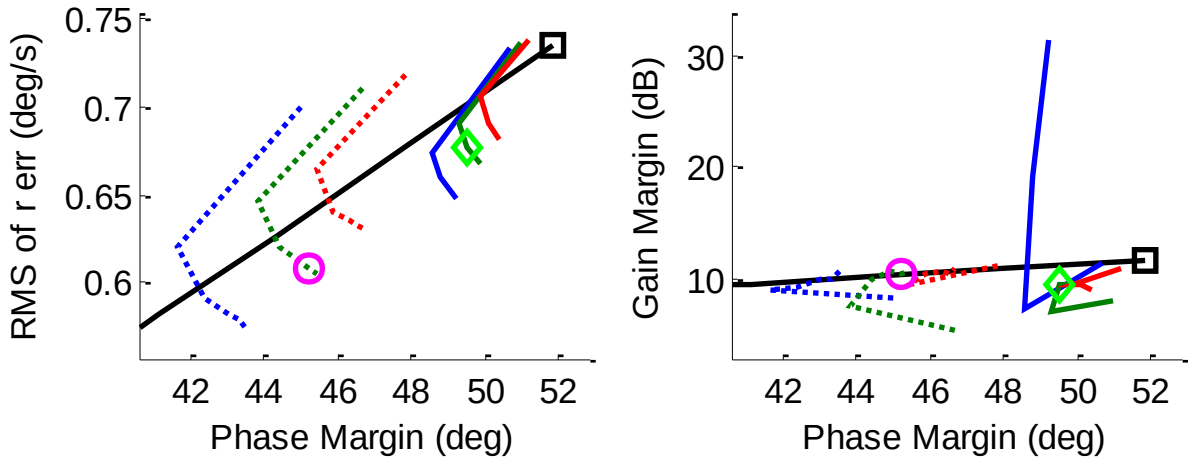

Figure 5-13. RMS Error from Turbulence, Gain and Phase Margins – Yaw Axis, 120 knots

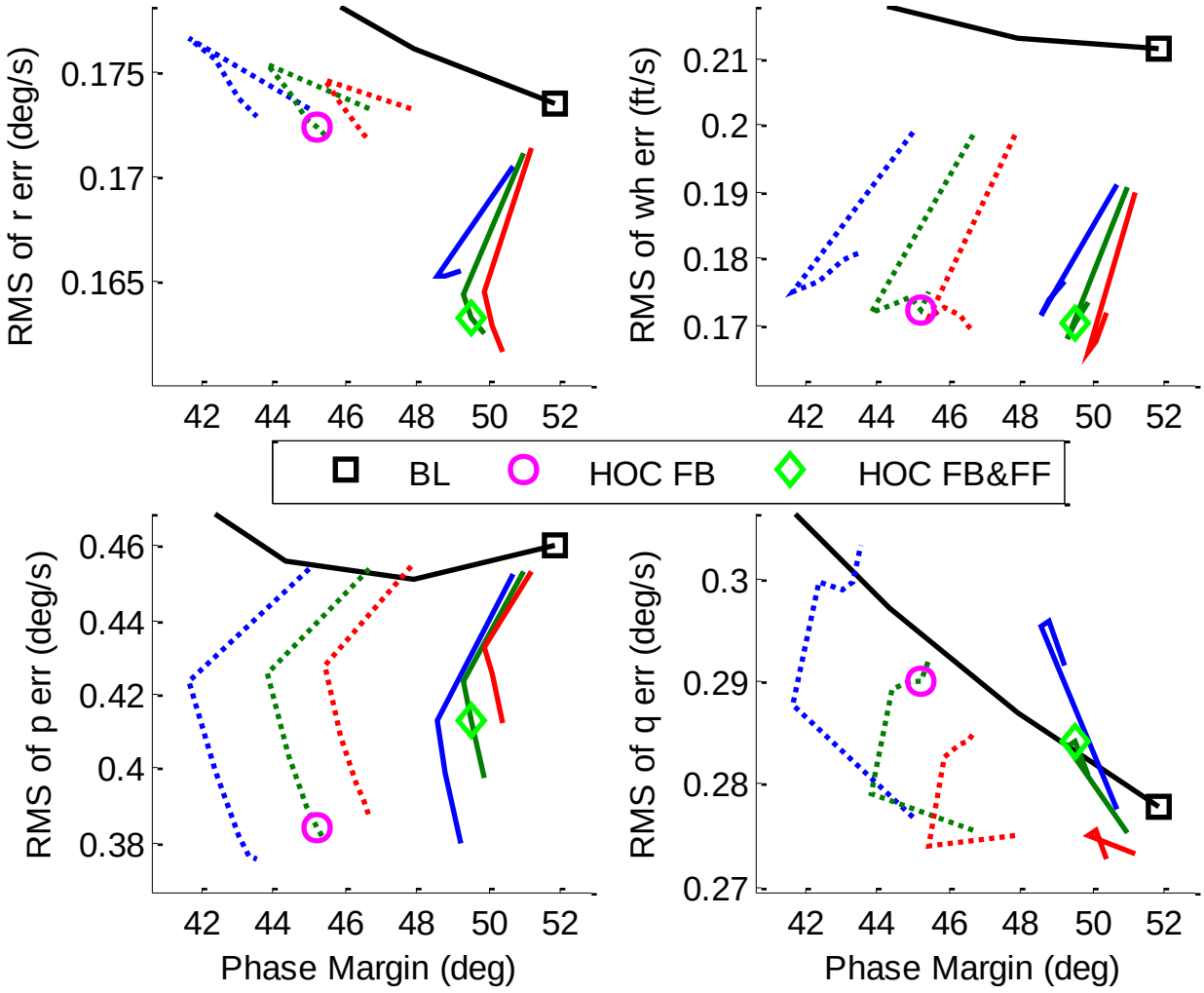

Figure 5-14. RMS Errors from Pilot Pedal – 120 knots

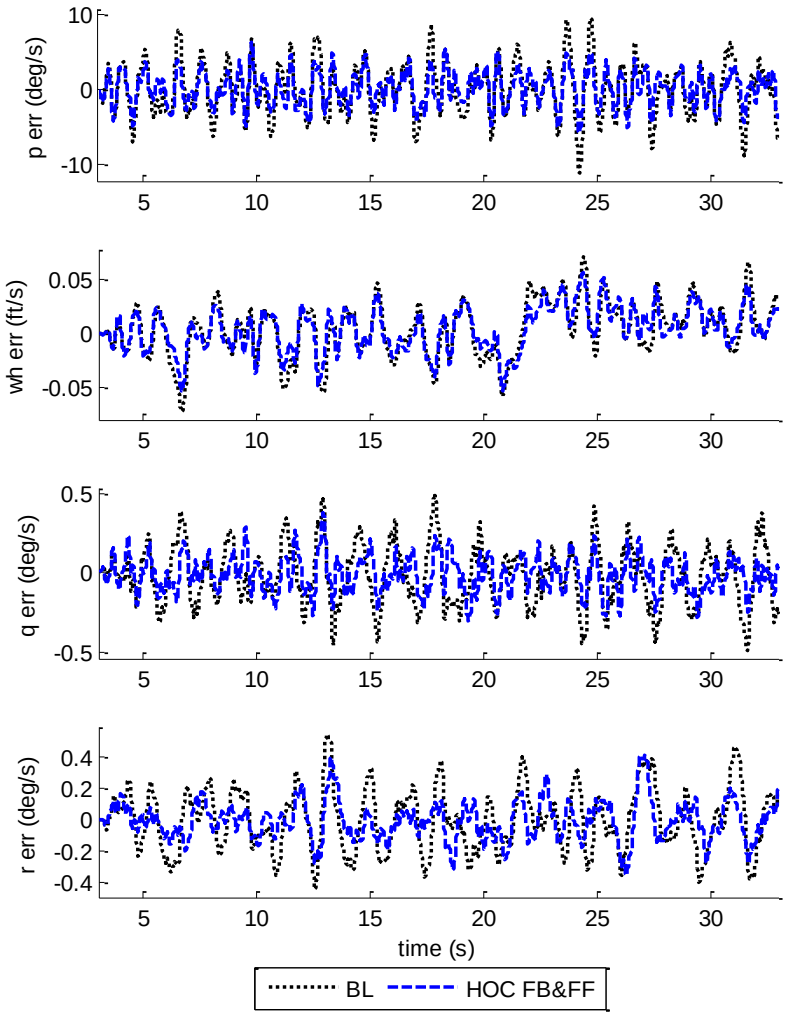

Figure 5-15. Rate Errors from Pilot Lateral – 10 knots

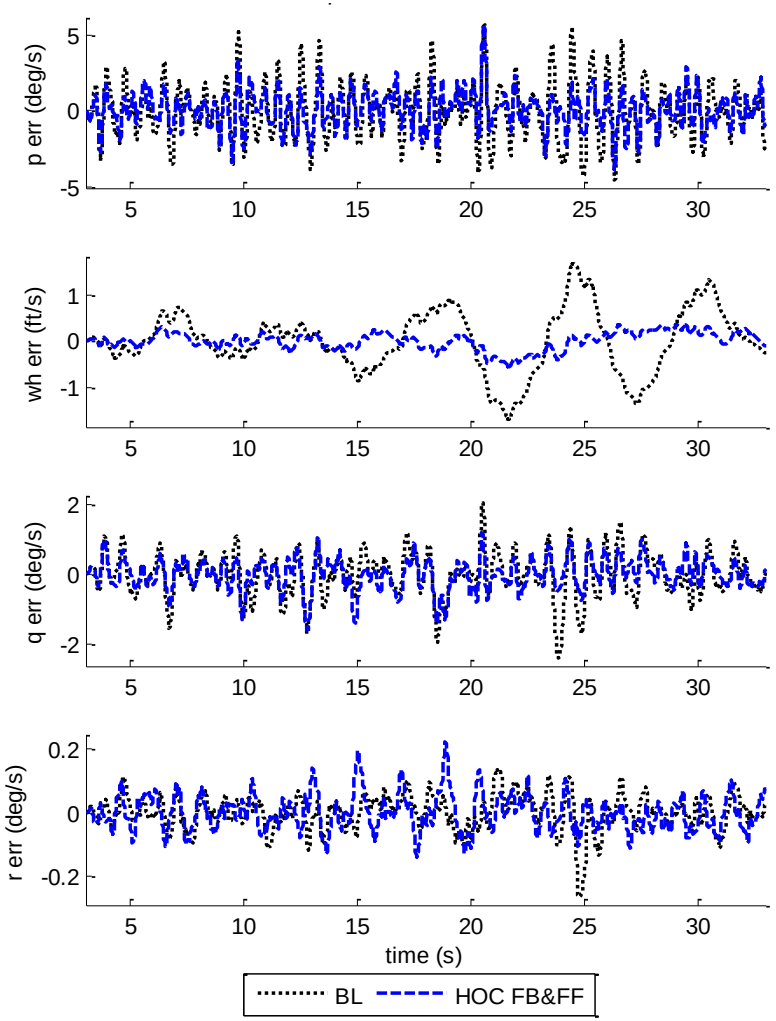

Figure 5-16. Rate Errors from Pilot Lateral – 120 knots

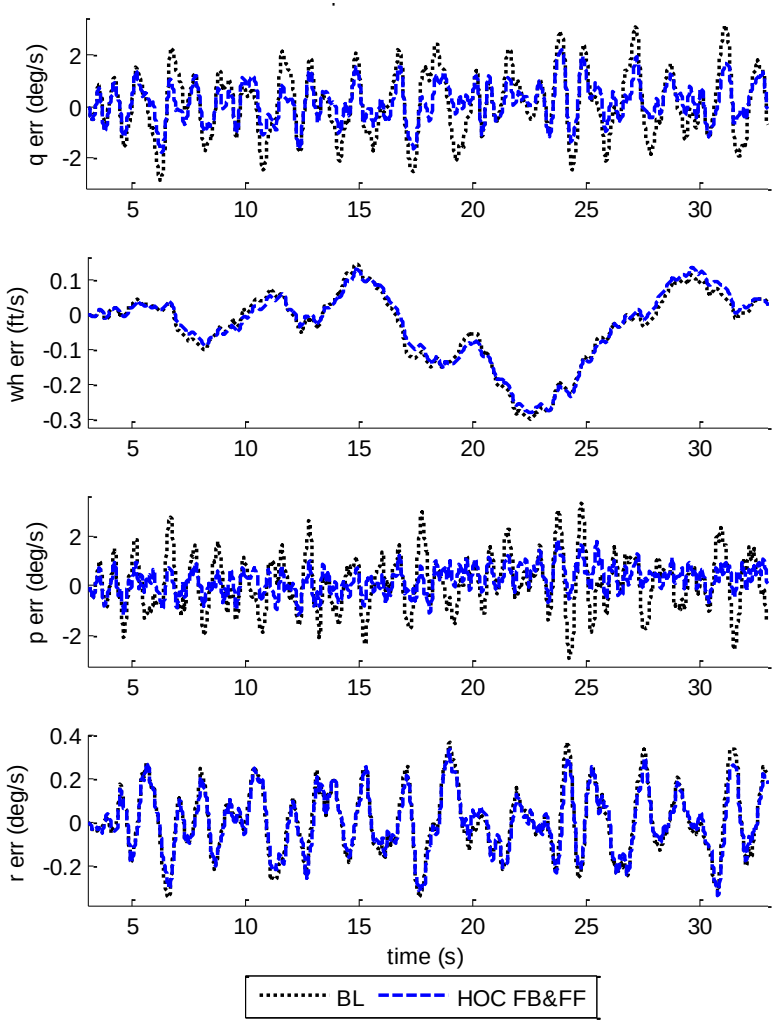

Figure 5-17. Rate Errors from Pilot Longitudinal – 10 knots

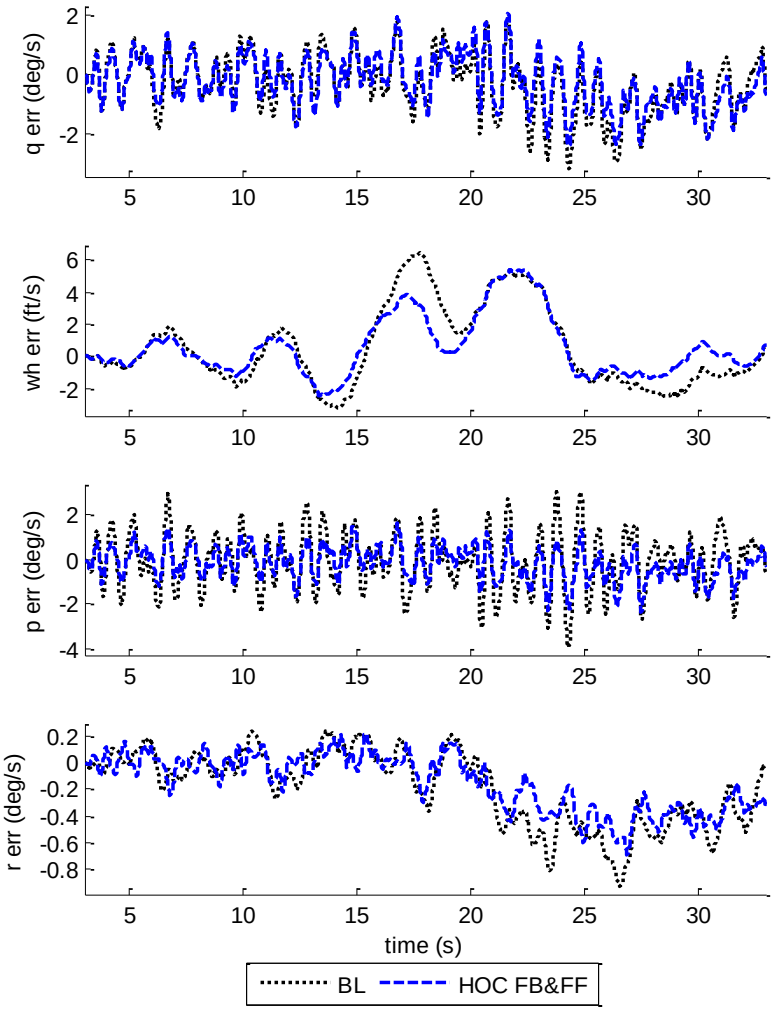

Figure 5-18. Rate Errors from Pilot Longitudinal – 120 knots

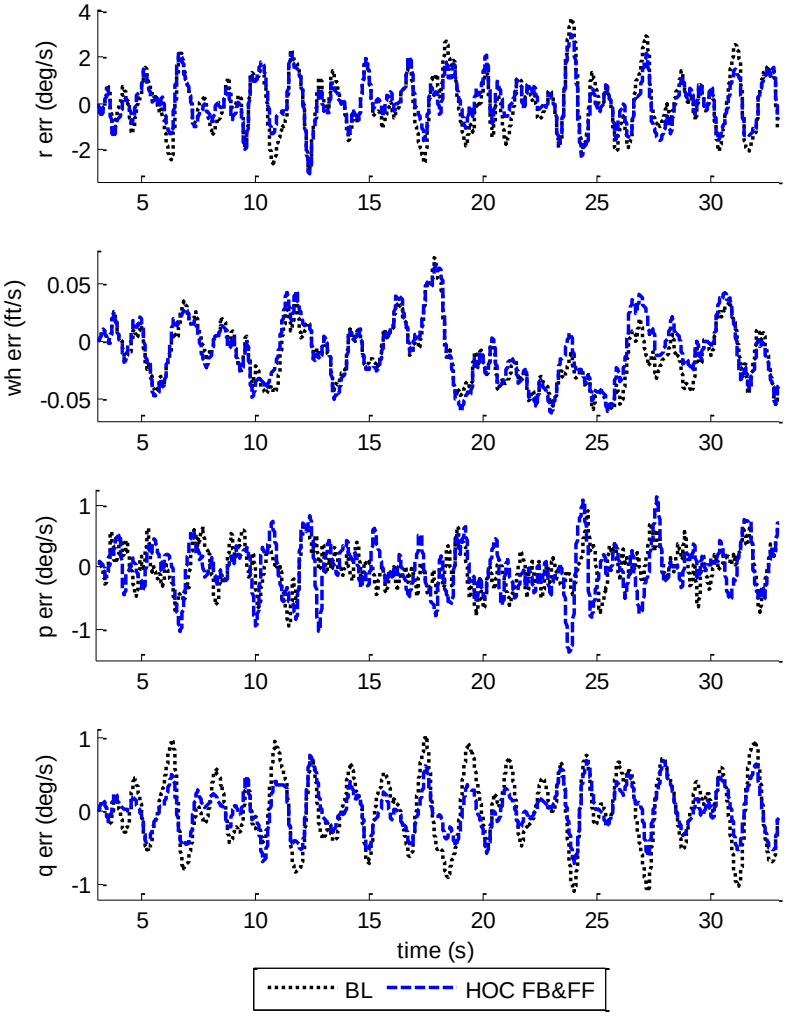

Figure 5-19. Rate Errors from Pilot Pedal – 10 knots

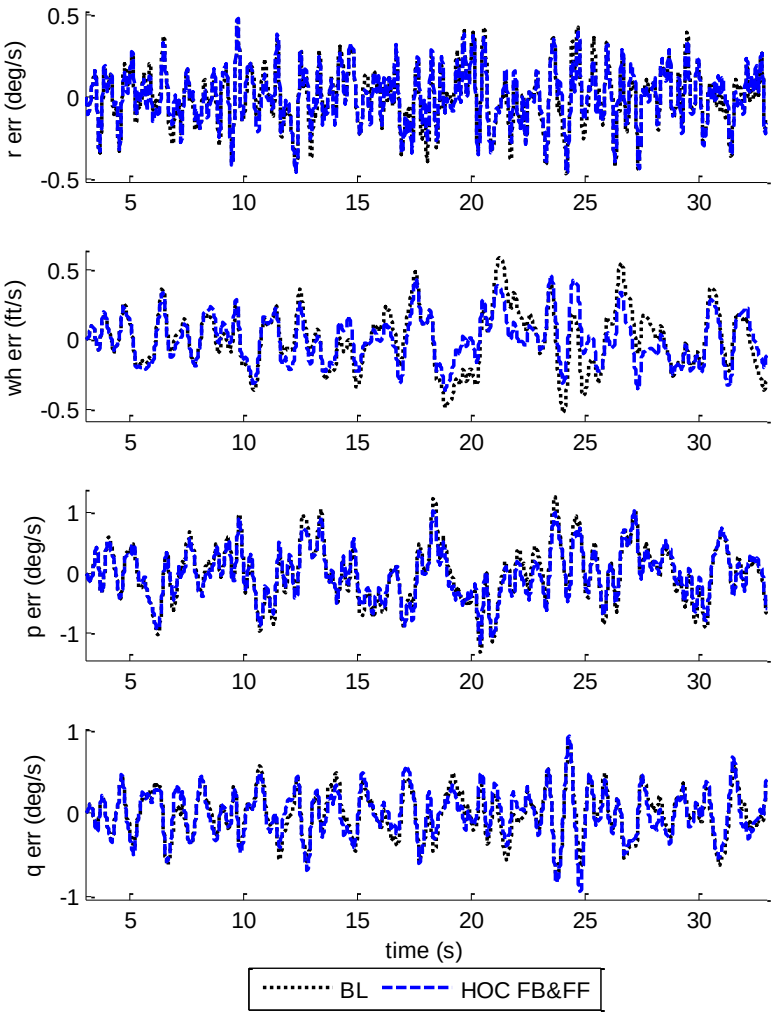

Figure 5-20. Rate Errors from Pilot Pedal – 120 knots

5.3.2 **Responses to Standard Pilot Test Inputs**

Figure 5-21 through Figure 5-33 show responses to pilot pulse, doublet, and step inputs in various modes, for the Baseline nominal design and HOC_FBFF final design. Where there are two lines of the same color on the same axes, the dashed-dot line is the command and the solid line is the response. Occasionally a single figure contains results for three runs with differing input magnitude. Note that in some of the large amplitude input cases there is SAS saturation as expected, but there does not appear to be much increased tendancy towards saturation with the HOC_FBFF design. A bit of increased saturation is seen in the Pedal Step at low speed (Figure 5-31).

Responses to the lateral inceptor are discussed next. At low speed, in Rate Mode, during a roll rate pulse (Figure 5-21), the HOC_FBFF augmentation causes the roll rate to stop somewhat short of the peak command, but reduces overshoot and oscillations upon the return to zero command. At low speed, during roll attitude steps (Figure 5-22), the HOC_FBFF augmentation slows the roll attitude response slightly, but significantly smooths the settling phase. At high speed, in Rate Mode, during a roll rate pulse (Figure 5-23), with HOC_FBFF augmentation the roll rate undershoots the peak command by about the same amount as the Baseline overshoots. Then the augmentation reduces the roll rate overshoot and oscillations upon the return to zero command. At high speed, in Roll Rate Command Attitude Hold mode, during roll rate pulses (Figure 5-24), HOC_FBFF augmentation significantly increases the damping of the roll rate response, but also causes the roll rate to stop short of the peak command. At high speed, in heading hold mode, a lateral doublet causes the roll attitude to deviate from trim then come back, which re-references the heading (Figure 5-25). HOC_FBFF augmentation improves the damping of high speed Heading Hold.

Now responses to longitudinal inceptor are discussed. At low speed, during a pitch rate pulse (Figure 5-26), HOC_FBFF augmentation modifies the response from overshoot to undershoot (slight in both cases) and increases the damping. Also, HOC_FBFF augmentation reduces the dynamic roll rate due to pitch rate. At low speed, during pitch attitude steps (Figure 5-27), HOC_FBFF augmentation slightly slows the pitch attitude rise and slightly increases the steady state error, but also improves settling,

especially in the case of the largest step. At high speed, during a pitch rate pulse (Figure 5-28), HOC_FBFF augmentation results in more undershoot, but also tighter following of the command during the return to zero, including less long-term drift. HOC_FBFF augmentation also improves suppression of the roll rate response during this maneuver. At high speed, during longitudinal inceptor steps (Figure 5-29), HOC_FBFF augmentation slightly slows the rise, but improves damping. The attitude commands are drifting because the airspeed is slowing which increases the pitch attitude trim, and the command is a constant bias off of trim attitude. At high speed, in Attitude Command Speed Hold mode, a longitudinal pulse causes the re-referencing of the speed command (Figure 5-30). HOC_FBFF augmentation reduces the damping of the speed-settling.

Finally, responses to pedal are discussed. At low speed, during yaw rate steps (Figure 5-31), HOC_FBFF augmentation causes the way rate to steady-out a little short of the command, and also causes the yaw SAS to remain saturated longer. At low speed, in Heading Hold mode, a pedal pulse results in a new heading reference (Figure 5-32). HOC_FBFF augmentation improves settling at the new heading. At high speed, during lateral acceleration steps (Figure 5-33), HOC augmentation only makes a noticeable difference in the largest step, and this difference is only a slight improvement. This improvement appears to be mostly in the off-axis response, judging by the activity of the collective, lateral SAS, and longitudinal SAS.

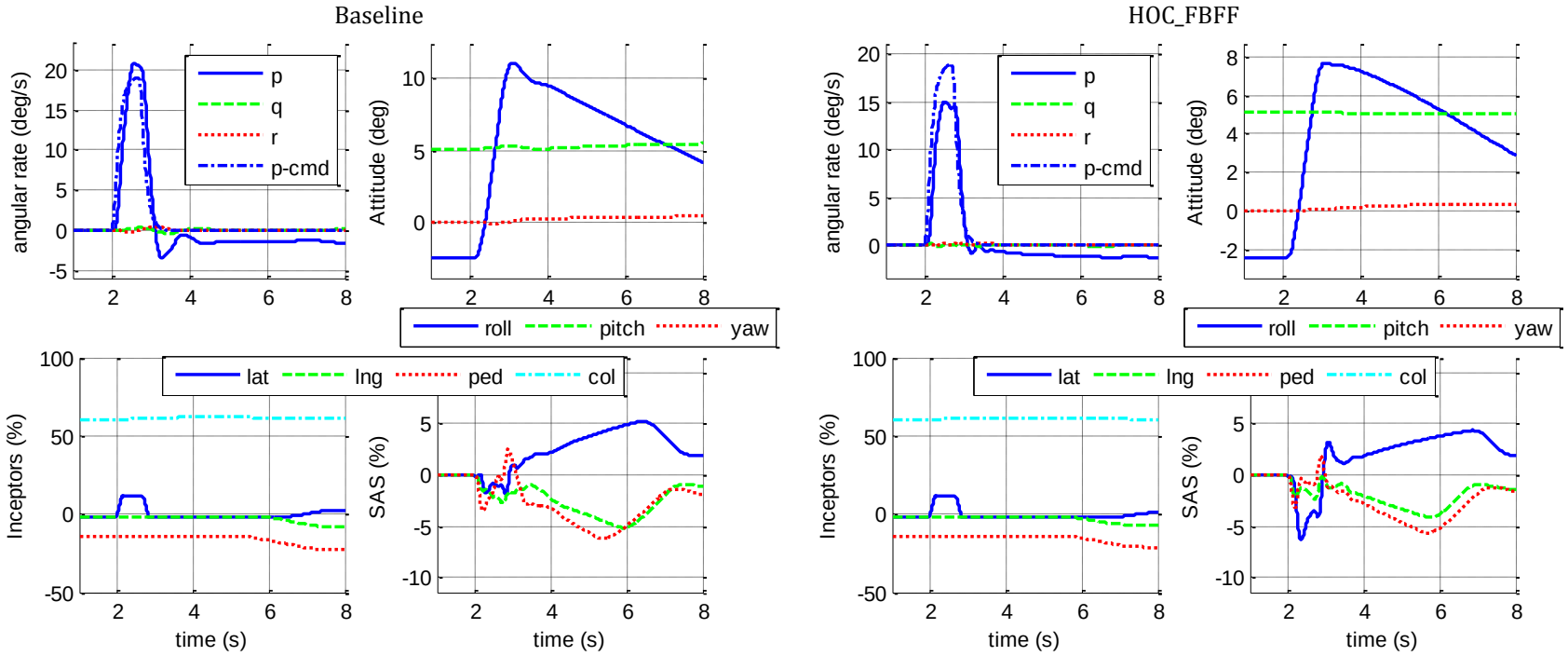

Figure 5-21. Pilot Lateral Pulse, Rate Mode – 10 knots

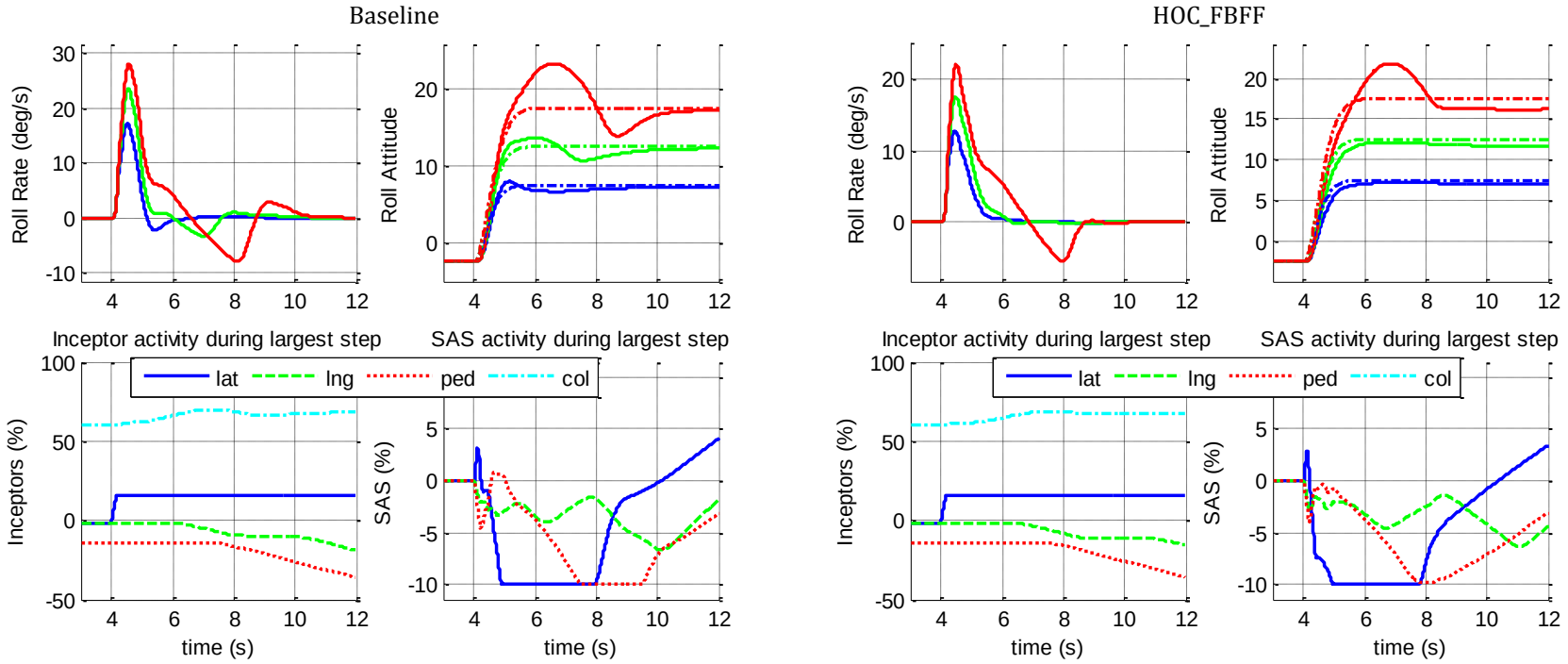

Figure 5-22. Pilot Lateral Step, Attitude Mode – 10 knots

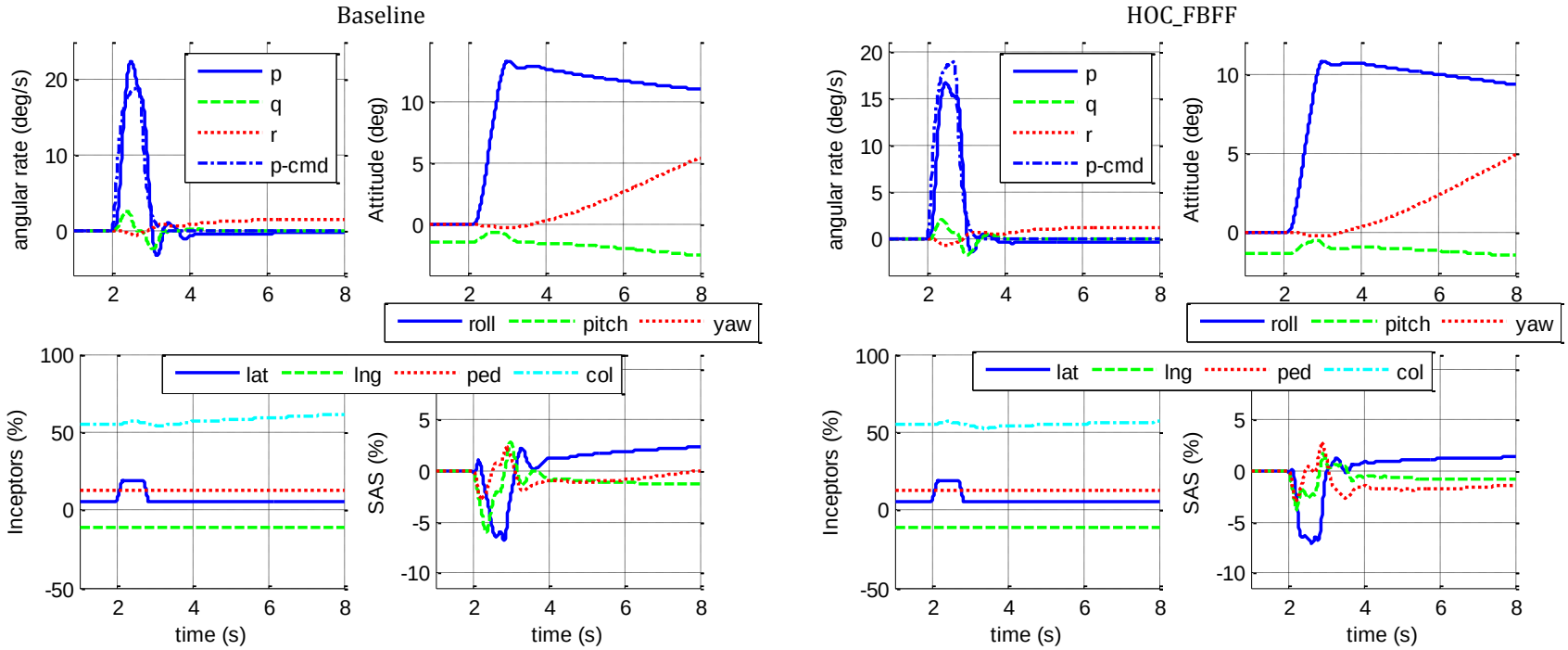

Figure 5-23. Pilot Lateral Pulse, Rate Mode – 120 knots

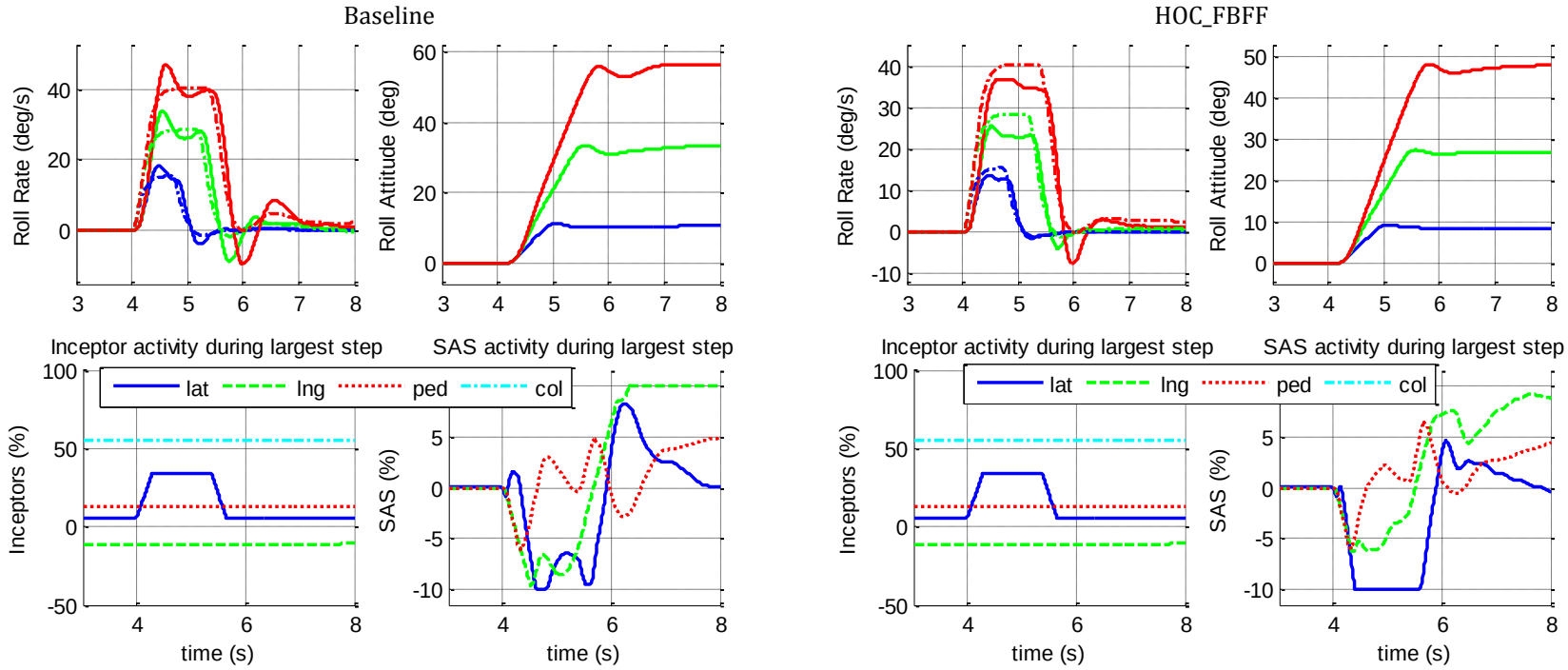

Figure 5-24. Pilot Lateral Pulse (RCAH), Attitude Mode – 120 knots

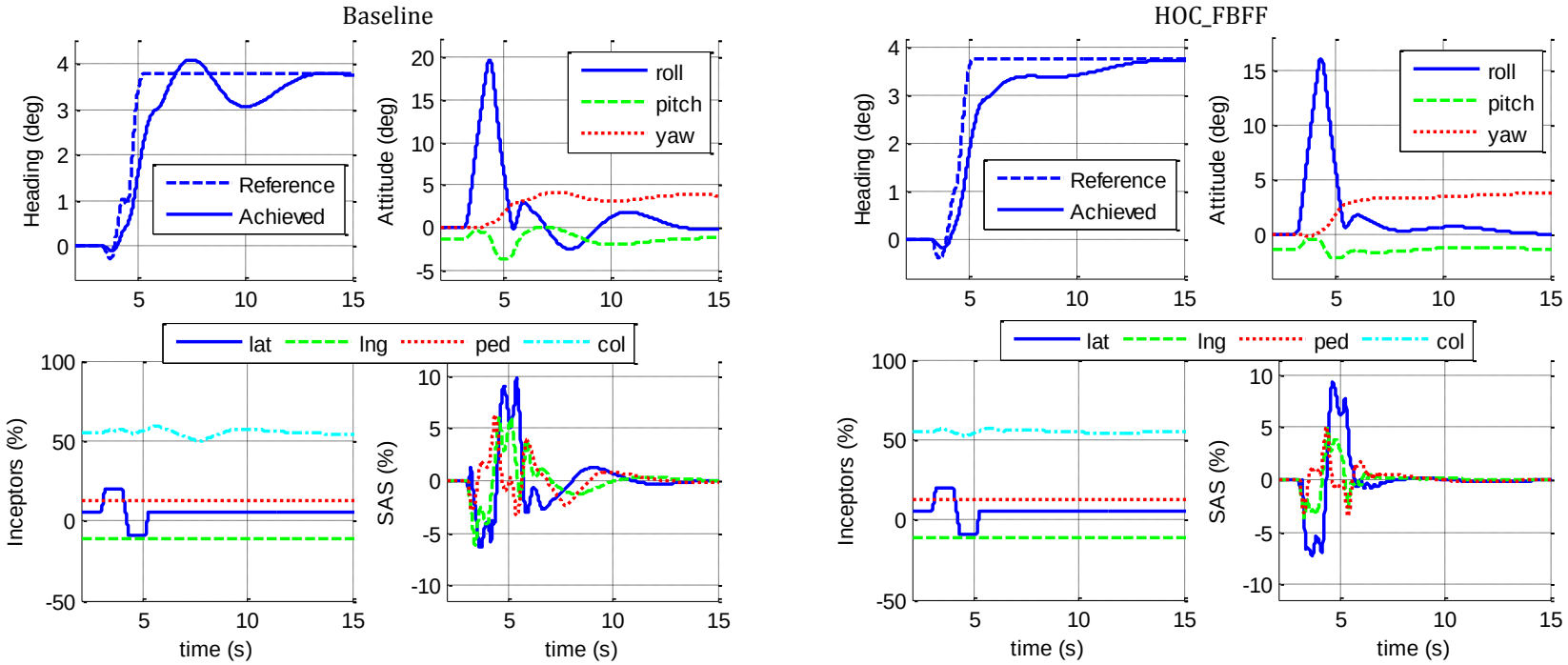

Figure 5-25. Pilot Lateral Doublet (RCHH), Attitude-HH Mode – 120 knots

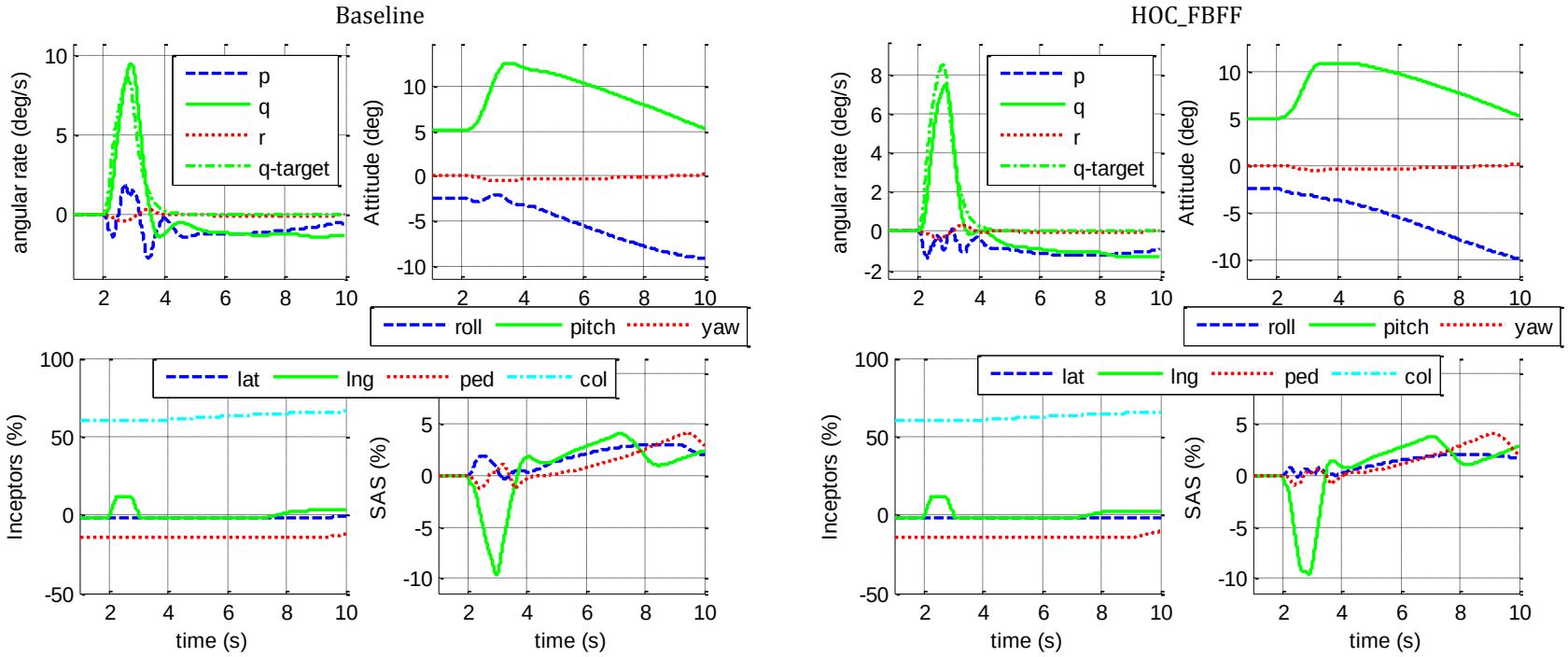

Figure 5-26. Pilot Longitudinal Pulse, Rate Mode – 10 knots

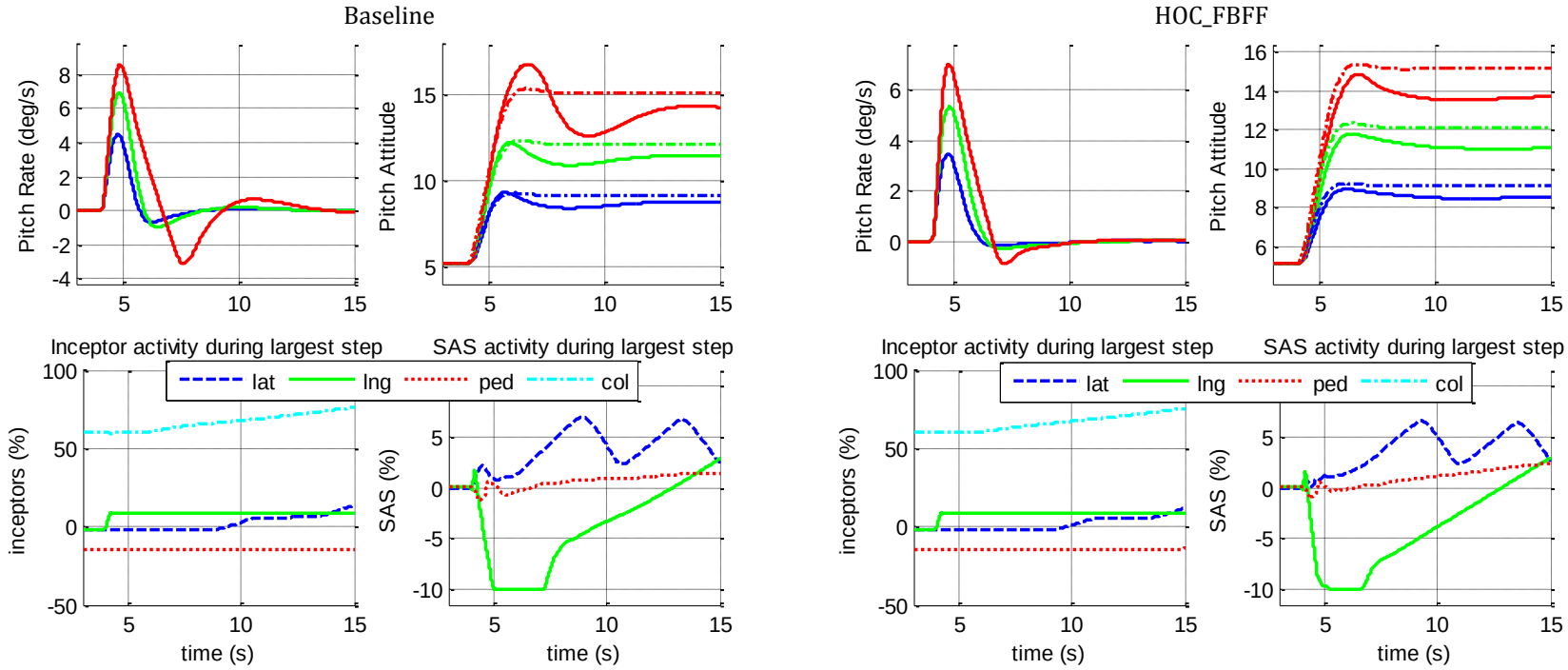

Figure 5-27. Pilot Longitudinal Step, Attitude Mode – 10 knots

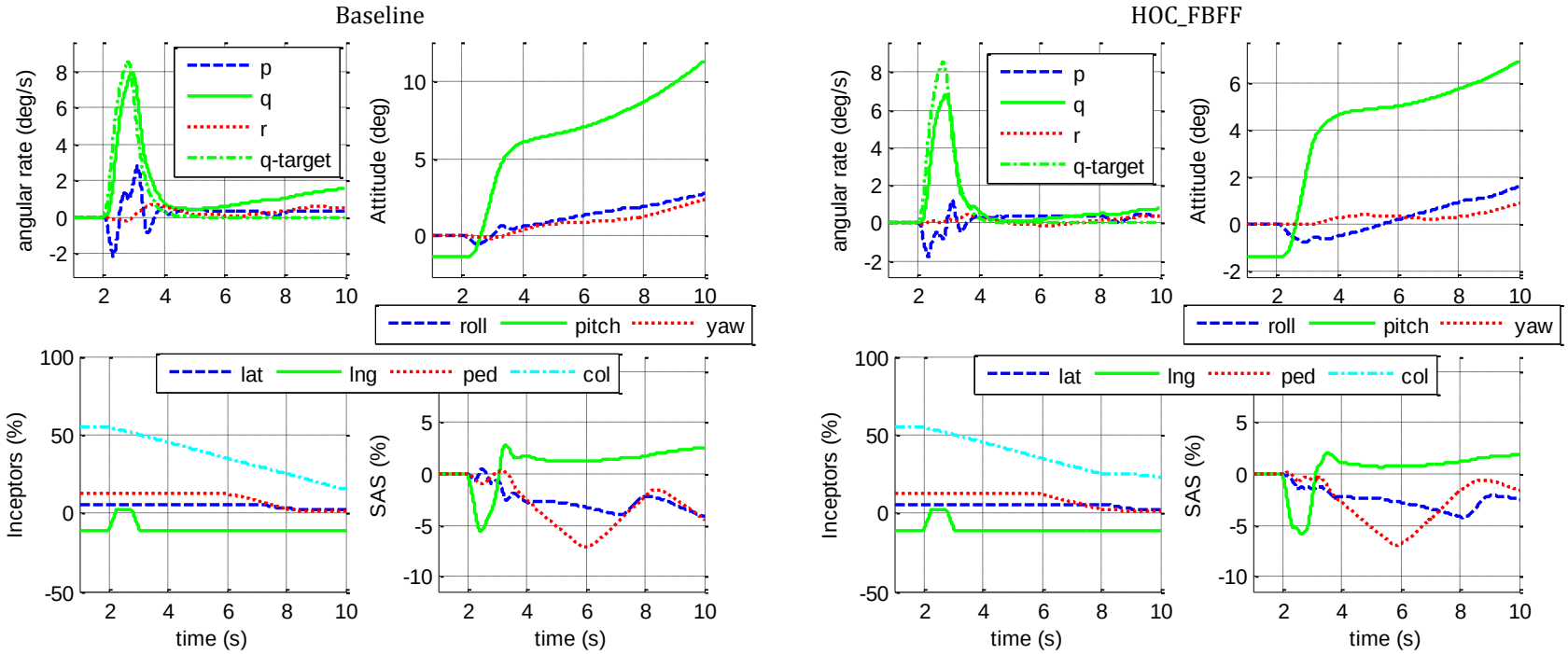

Figure 5-28. Pilot Longitudinal Pulse, Rate Mode – 120 knots

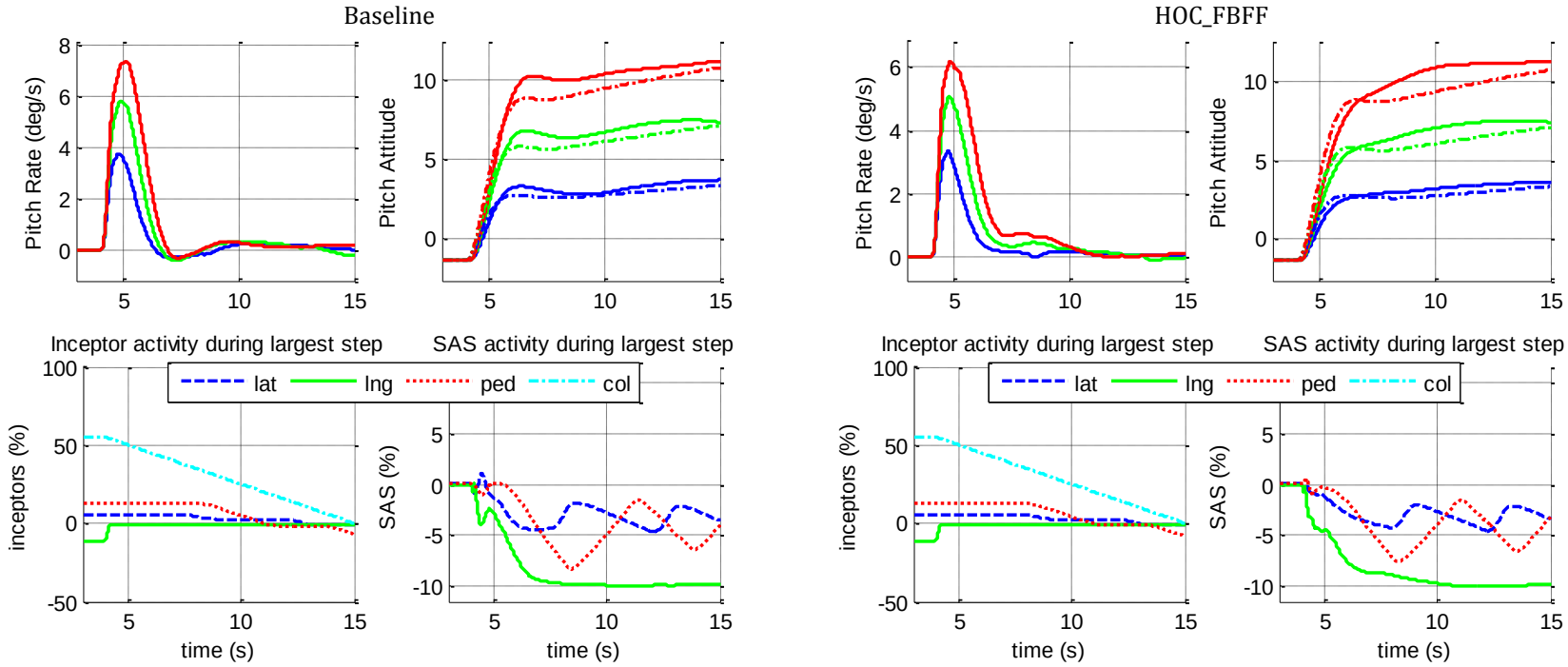

Figure 5-29. Pilot Longitudinal Step, Attitude Mode – 120 knots

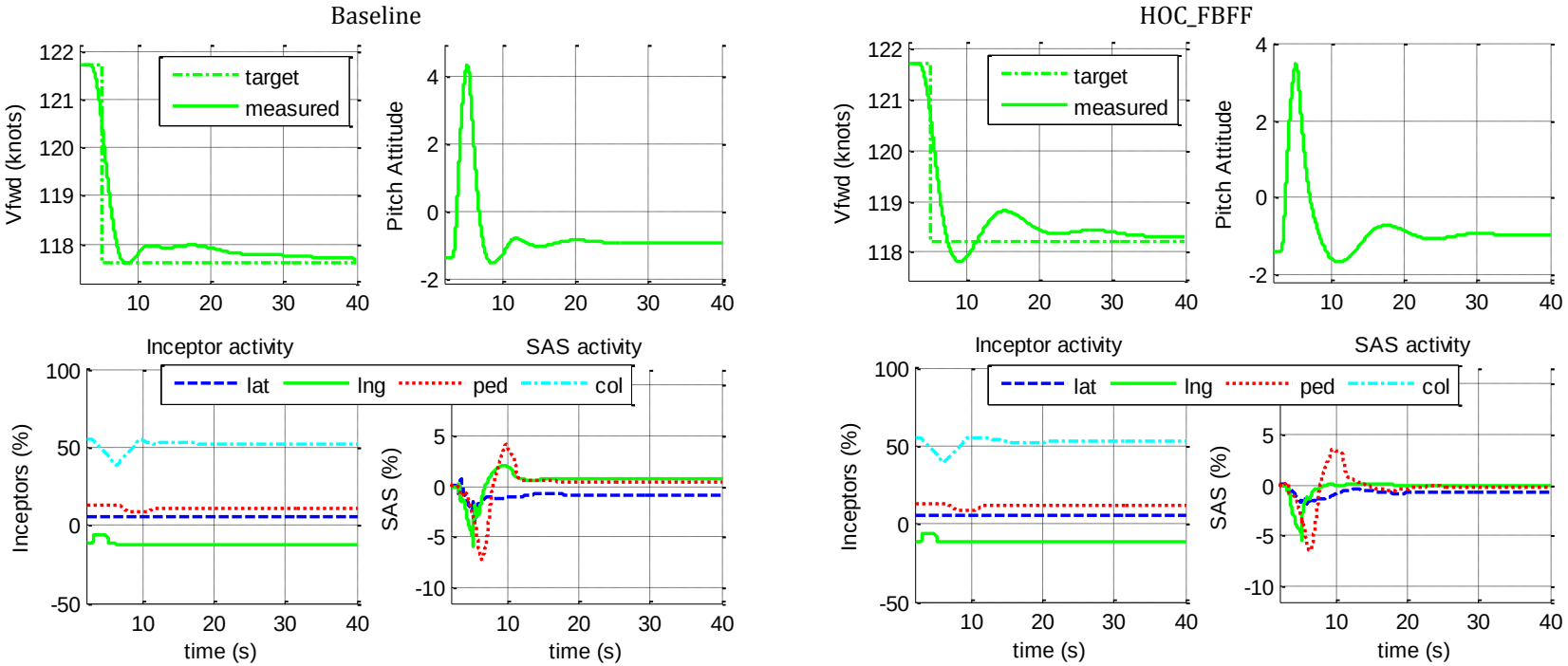

Figure 5-30. Pilot Longitudinal Pulse (ACSH), Attitude Mode – 120 knots

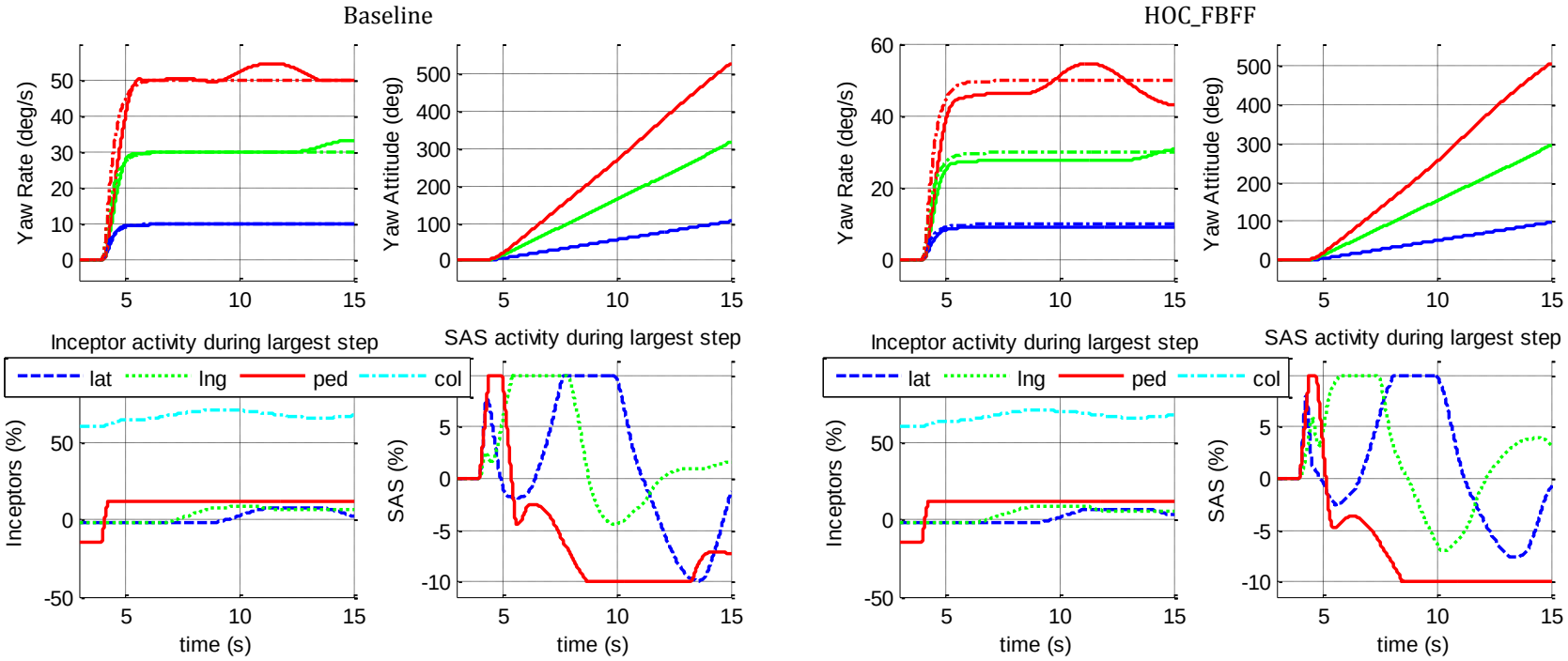

Figure 5-31. Pilot Pedal Step (RC), Attitude Mode – 10 knots

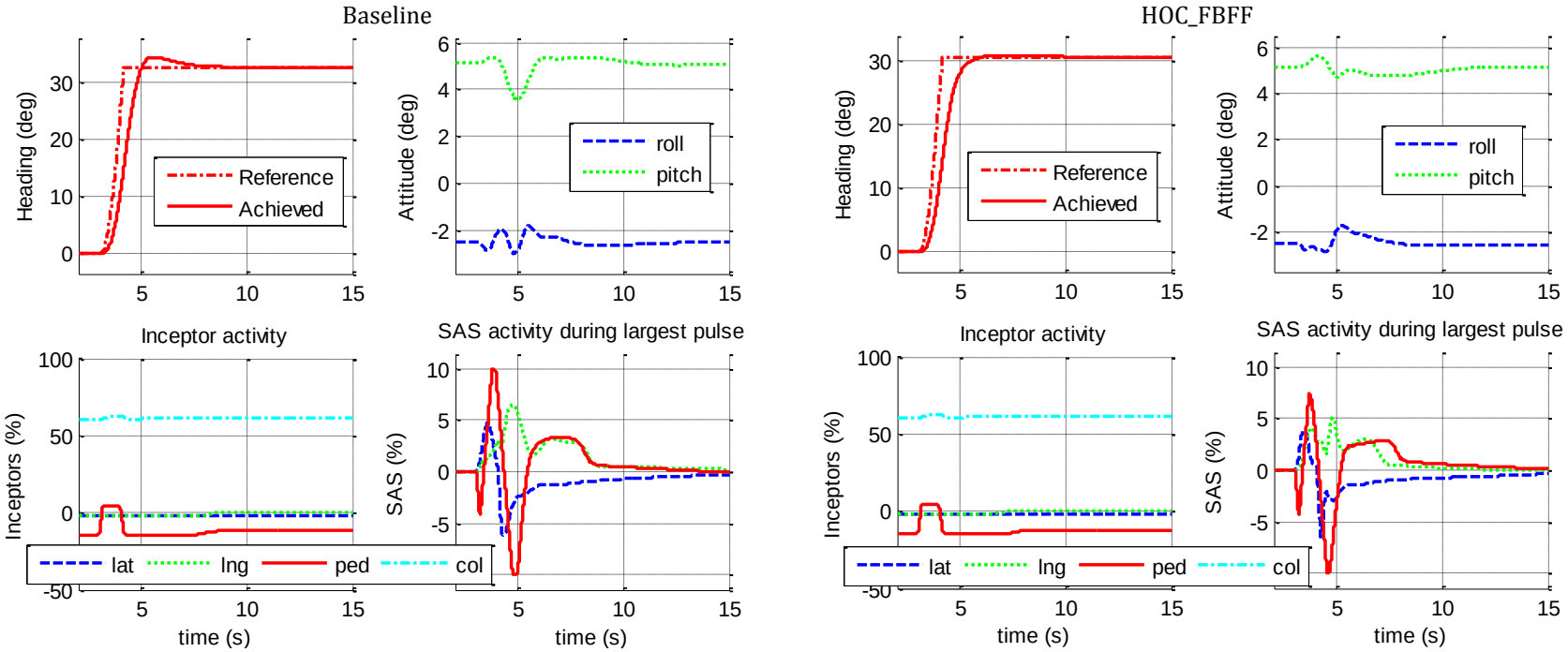

Figure 5-32. Pilot Pedal Pulse (RCHH), Attitude-HH Mode – 10 knots

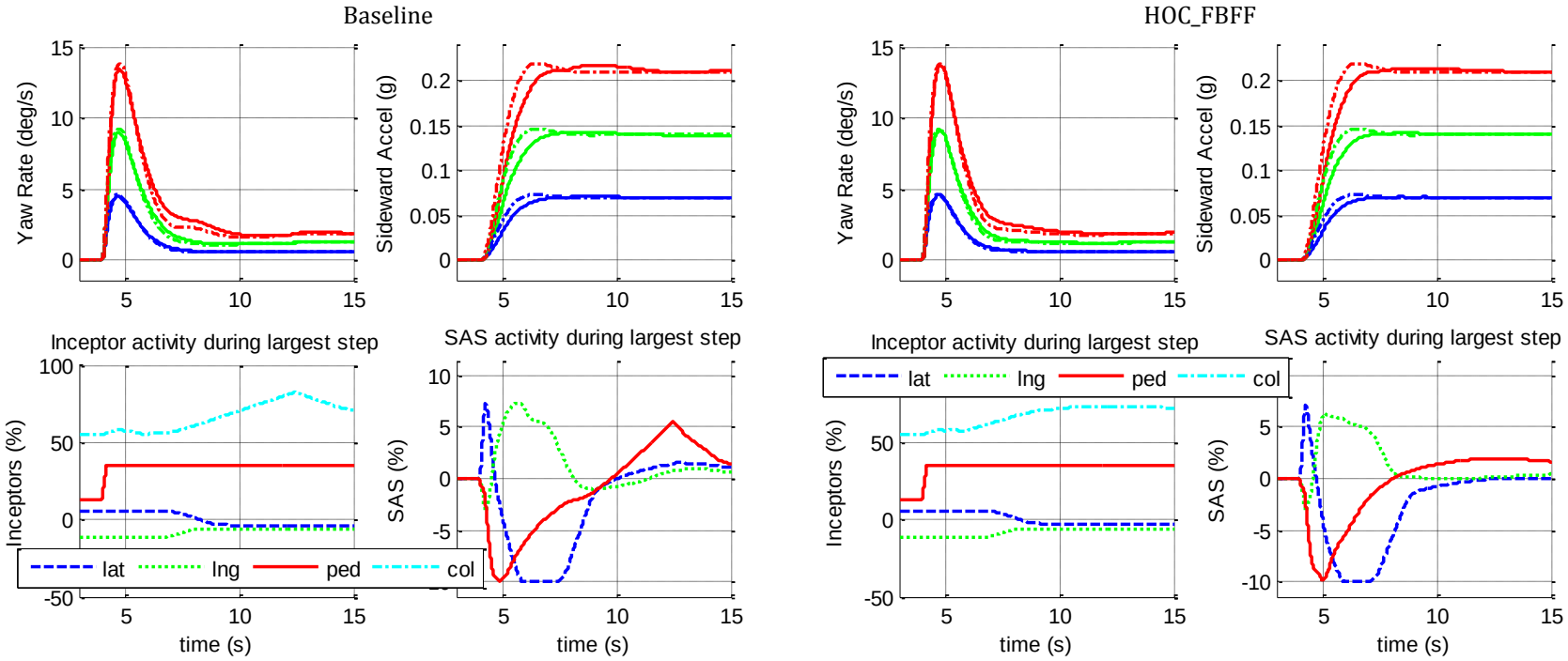

Figure 5-33. Pilot Pedal Step (LatAccel), Attitude Mode – 120 knots

5.3.3 **Robustness Analysis**

The following robustness analysis shows the effects of perturbing bare airframe parameters upon stability and performance of the Baseline-Control-only system versus the HOC_FBFF-augmented system. The control laws are in Attitude / Altitude mode, except longitudinal pilot input performance at high speed is assessed in Attitude / Climb Rate mode. The perturbed bare airframe parameters are: weight, fuselage station center of gravity (fscg, +aft), main rotor blade density (bld den), and lag damper effectiveness (lag damp). The magnitudes of the perturbations are

weight: 92% and 109% of design

fscg: 5 inches forward and aft of design

bld den: 90% and 110% of design

lag damp: 80% of design

Baseline controller results are in black. HOC_ FBFF augmentation results are in green. Baseline controller results with the design-plant are indicated by a black square, while HOC_ FBFF augmentation results with the design-plant are indicated by a green diamond. Perturbed plant results are indicated by triangles: left-pointing means the parameter is reduced, right-pointing means the parameter is increased.

Overall, HOC_ FBFF augmentation neither helps nor hurts robustness significantly. Specific robustness impacts, per axis, per perturbation, and per speed regime, are covered in the following sub-sections.

5.3.3.1 Stability Robustness

In this Chapter, stability robustness is assessed through the closed-loop poles of the linearized full simulation in Simulink. Gain and phase margins are not used because the increased number of states with HOC active makes the conversion from state-space to frequency-domain too numerically unreliable.

Stability robustness is measured in three ways. The first stability-robustness measure is the change in minimum damping ratio relative to the design-plant case. The second measure is the maximum fractional closure of a pole λ toward the imaginary axis.

$$\text{fractional closure} = \frac{\text{real}\left(\lambda_{\text{ptrb}}\right) - \text{real}\left(\lambda_{\text{dsgn}}\right)}{\text{-real}\left(\lambda_{\text{dsgn}}\right)} \tag{5-35}$$

A fractional closure of 0 means the real part of the pole ($-\tau_{decay}$) has not changed with the perturbation in bare airframe. A fractional closure of 1 means the real part of the perturbed pole is 0 (this pole has reached the boundary of stability). If a perturbation causes a pole to have a fractional closure of 0.5, then if the pole were to continue changing at that rate with increased magnitude of the perturbation, then stability would be lost with double the perturbation magnitude that was tested. The third stability-robustness measure is the same as the second, but only considering perturbed poles that are complex. This third robustness measure is probably better than the second because, with rotorcraft, poles are unlikely to cross the stability boundary along the real axis.

At low speed, stability robustness is very slightly lower with HOC active (Figure 5-34). At high speed, stability robustness is again very slightly lower with HOC active (Figure 5-35).

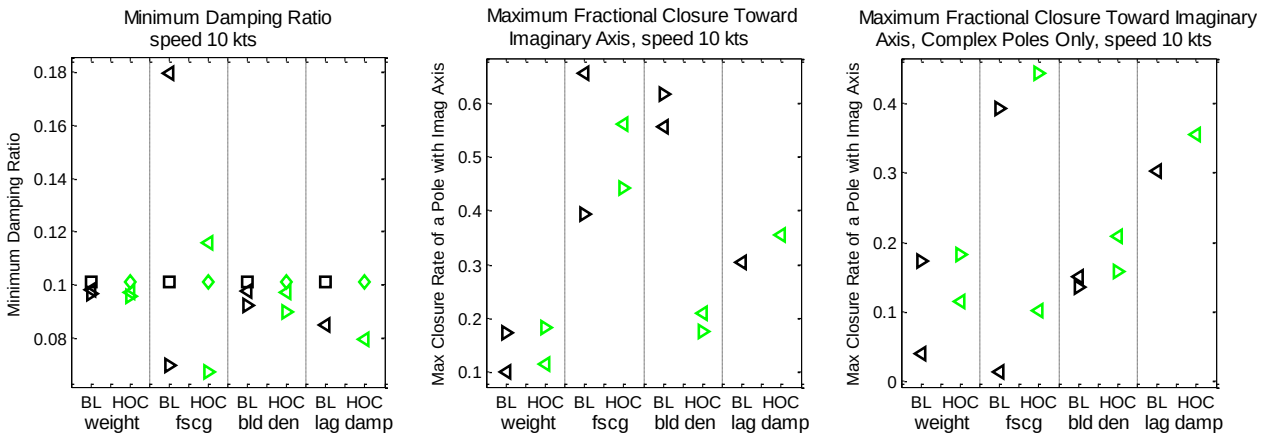

Figure 5-34. BL vs HOC, Stability Robustness – 10 knots

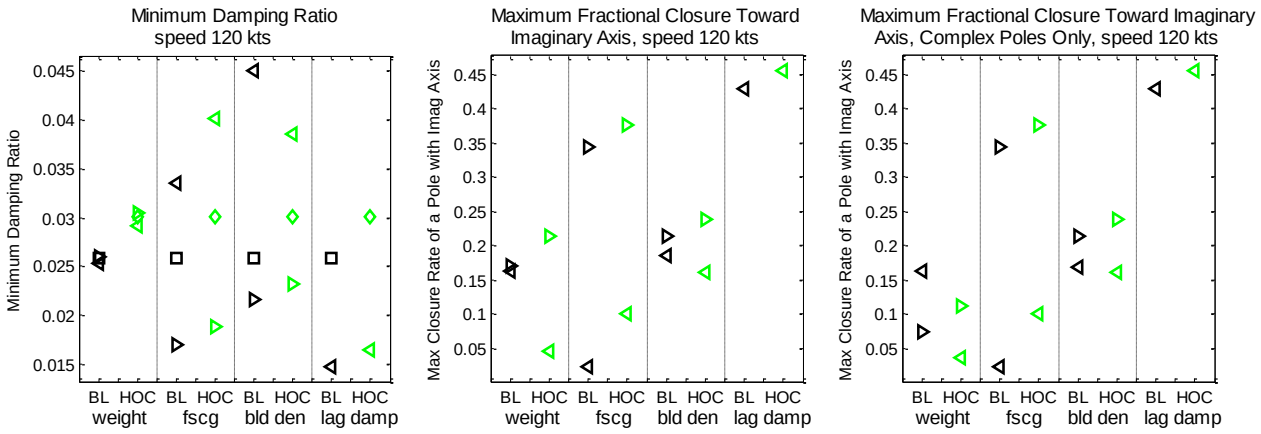

Figure 5-35. BL vs HOC, Stability Robustness – 120 knots

5.3.3.2 Performance Robustness

Turbulence performance robustness is assessed through changes in the root-mean-square of rates. At low speed, with HOC, turbulence performance is a little more robust to fscg and blade density (Figure 5-36). At high speed, with HOC, turbulence performance is more robust to fscg (Figure 5-37).

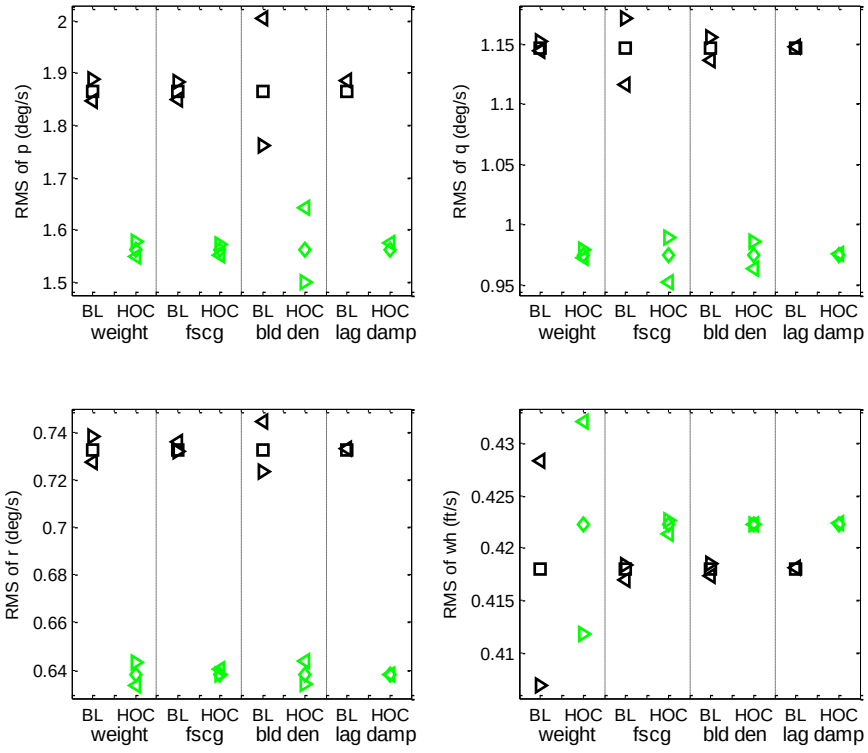

Figure 5-36. BL vs HOC, Performance Robustness, Turbulence – 10 knots

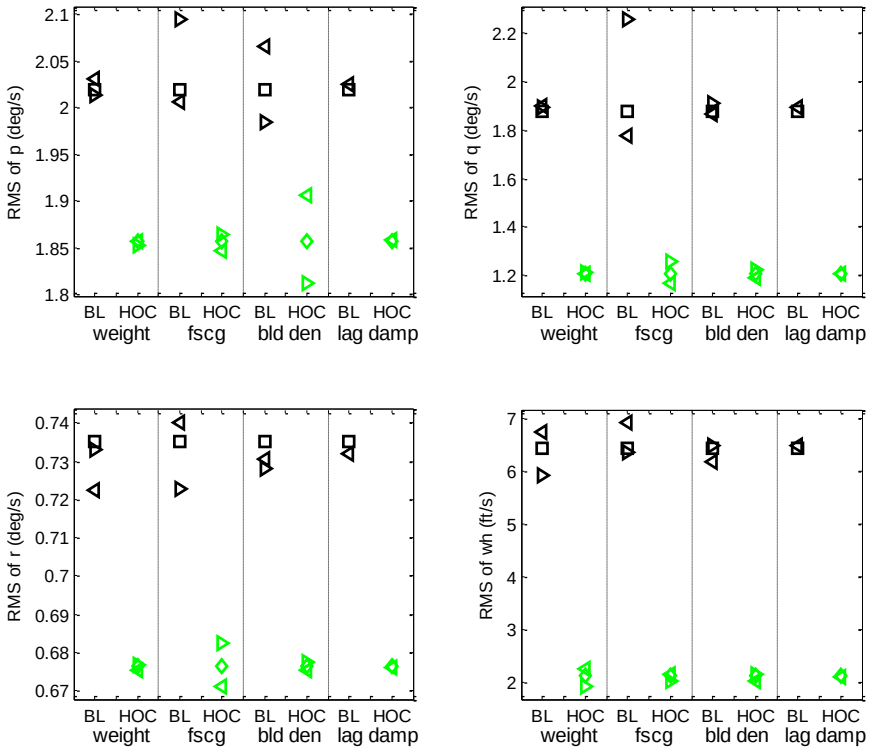

Figure 5-37. BL vs HOC, Performance Robustness, Turbulence – 120 knots

Command-following performance robustness is assessed through changes in the root-mean-square of rate errors during random band-limited (9 rad/s corner) pilot input, one inceptor at a time. These rate errors are the difference between lagged commands and measured response.

At low speed, with lateral input (Figure 5-38): HOC improves roll rate robustness to blade density. HOC improves pitch rate robustness. HOC improves yaw rate robustness to fscg and blade density, but reduces yaw rate robustness to weight. At high speed, with lateral input (Figure 5-39): HOC improves roll rate robustness to weight. HOC improves climb rate robustness to fscg and blade density, and improves pitch rate robustness to blade density.

At low speed, with longitudinal input (Figure 5-40): HOC improves pitch rate robustness to blade density. HOC improves roll rate robustness, and improves yaw rate robustness to weight and blade density. At high speed, with longitudinal input (Figure 5-41): HOC slightly reduces pitch rate robustness to fscg. HOC improves climb rate robustness.

At low speed, with pedal input (Figure 5-42): HOC improves yaw rate robustness to weight, and improves pitch rate robustness to weight and blade density. HOC reduces roll rate robustness. At high

speed, with pedal input (Figure 5-43): HOC improves yaw rate robustness to fscg, and improves climb rate robustness. HOC reduces pitch rate robustness to weight.

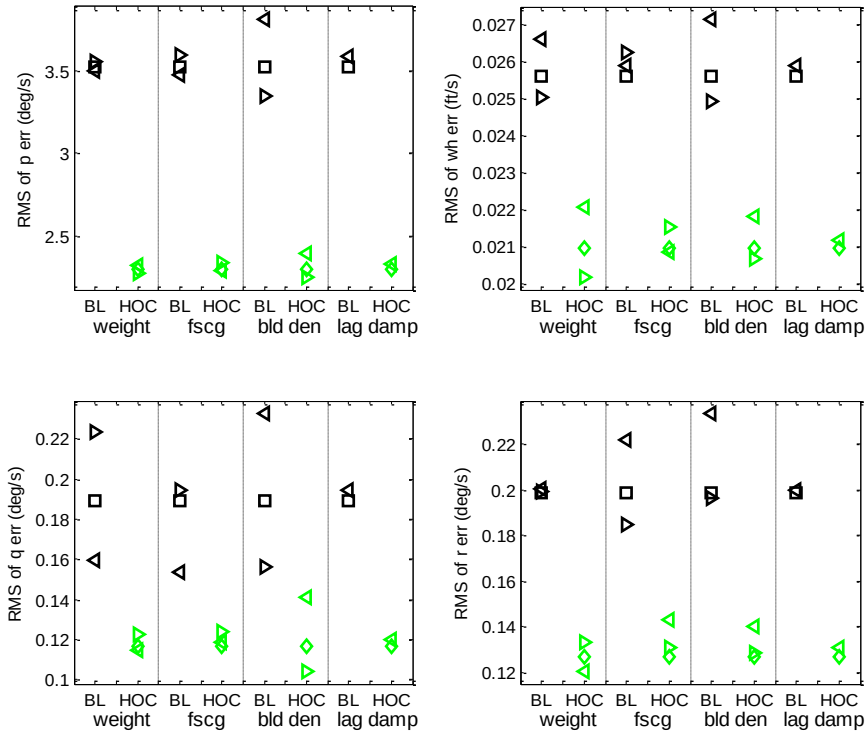

Figure 5-38. BL vs HOC, Performance Robustness, Pilot Lateral – 10 knots

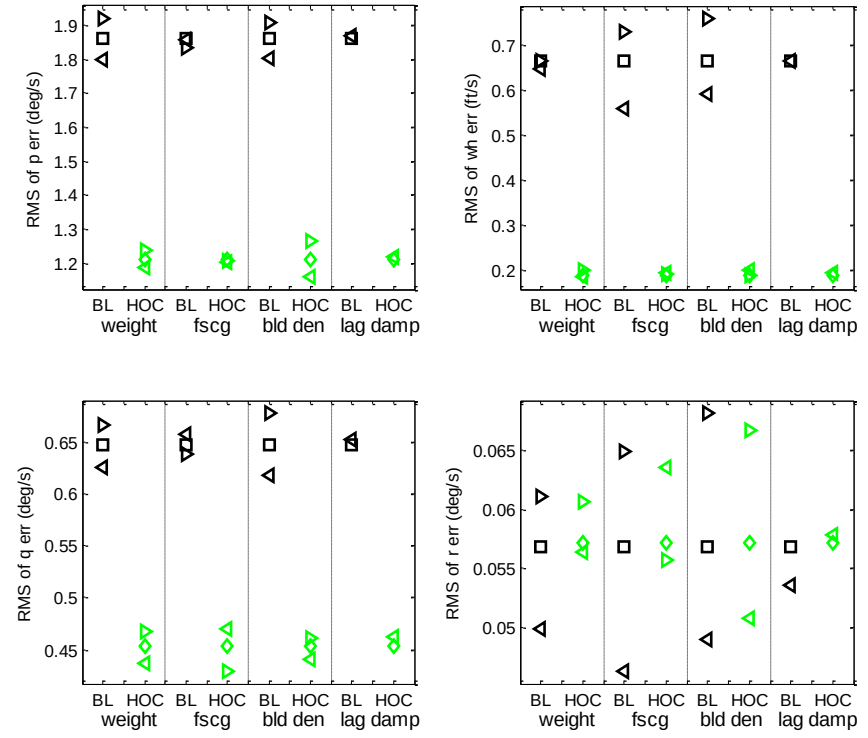

Figure 5-39. BL vs HOC, Performance Robustness, Pilot Lateral – 120 knots

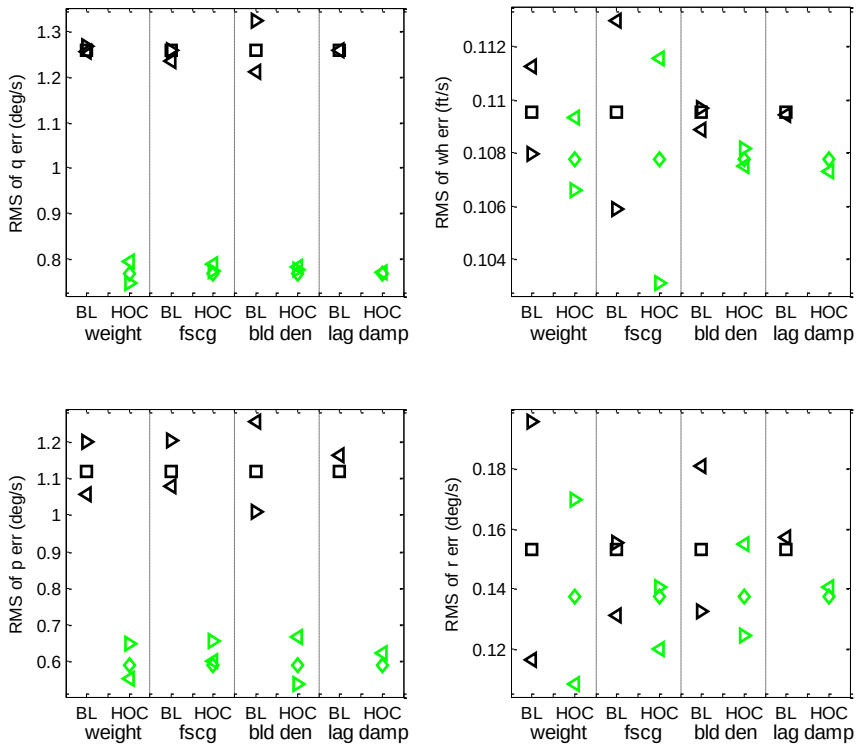

Figure 5-40. BL vs HOC, Performance Robustness, Pilot Longitudinal – 10 knots

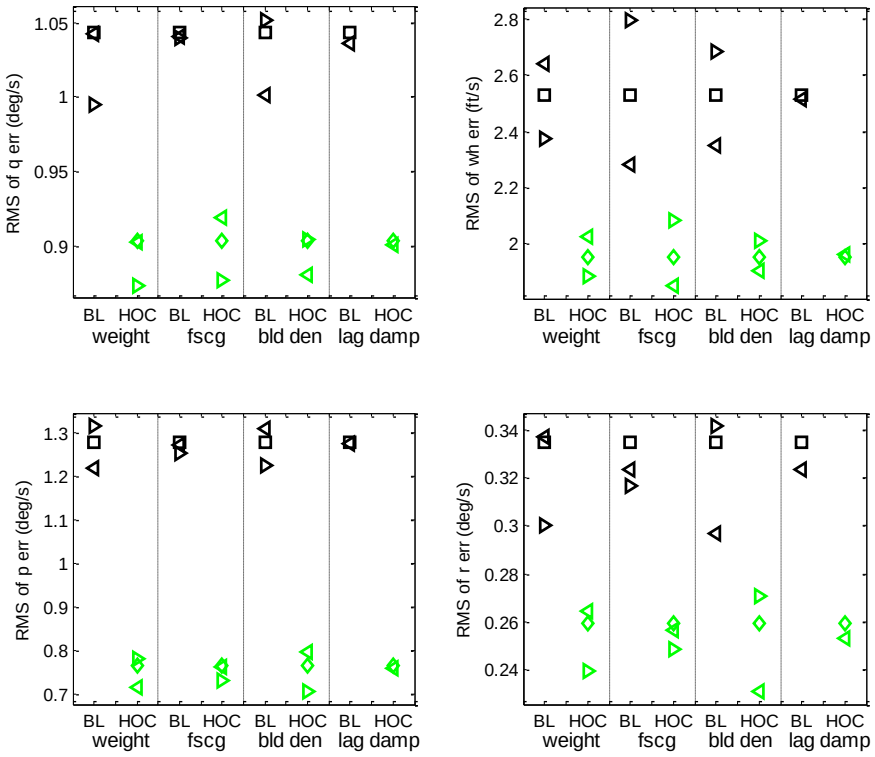

Figure 5-41. BL vs HOC, Performance Robustness, Pilot Longitudinal – 120 knots

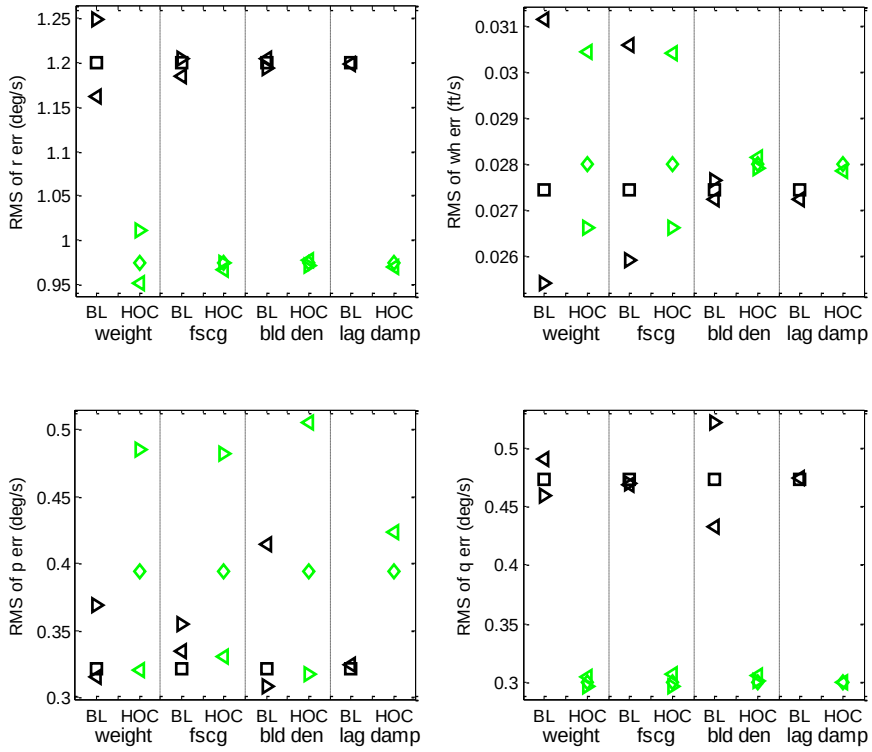

Figure 5-42. BL vs HOC, Performance Robustness, Pilot Pedal – 10 knots

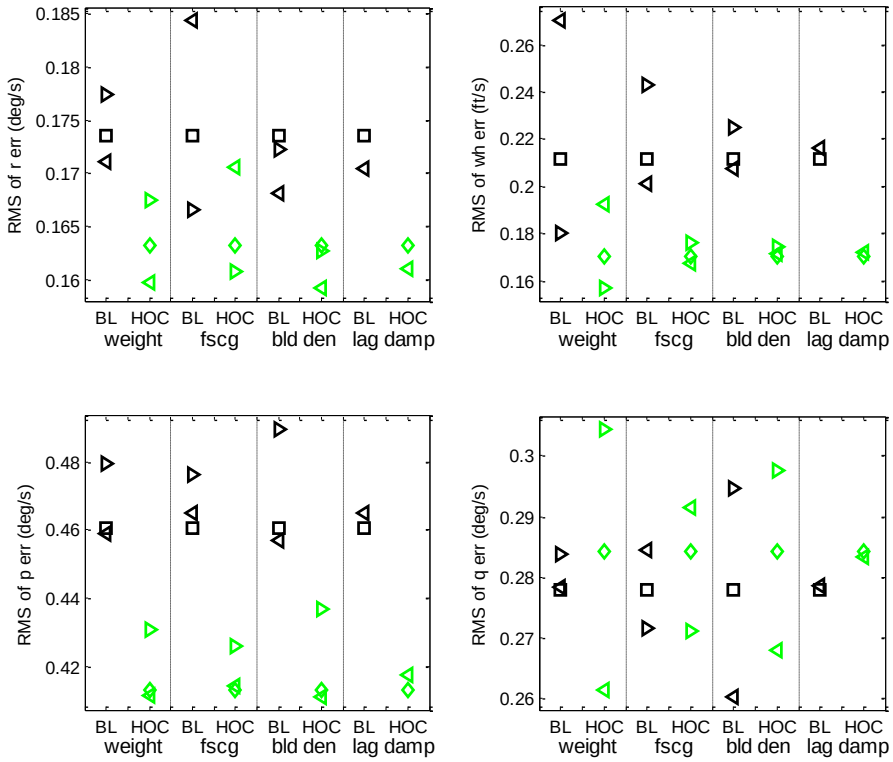

Figure 5-43. BL vs HOC, Performance Robustness, Pilot Pedal – 120 knots

5.4 Conclusions regarding High Order Compensator Augmentation

1) This Chapter presented an architecture and design methodology for H_2 MIMO augmentation of a multi-mode baseline controller. By designing the HOC_FBFF compensator to reduce the three angular rate errors in the presence of rate target input and turbulence disturbance, it also generally improves higher modes since they use rate control as an inner loop. Because the HOC acts to reduce response errors that are relative to a command model, it generally results in closer following of the command model, which should be designed according to handling qualities specifications.

2) Because the HOC is designed based on the dynamics of a rate-compensated rotorcraft, accurate system identification should be safely achievable from flight testing, which increases the likelihood that improvements from HOC that are seen in simulation will be realized.

3) The HOC is selectable (and de-selectable) and can easily be authority-limited, which might ease certification. A cockpit switch could allow the pilot to disable HOC, and automated monitoring could be developed to disable HOC if undesirable outputs are detected. The HOC authority was not limited in this work, but there were no significant issues with excessive HOC contribution when applied to a 10% authority control system.

4) The HOC_FBFF controller was generally found to provide the best overall improvement, relative to the Baseline, in terms of following pilot commands and turbulence rejection. The turbulence rejection was not quite as good as the HOC_FB controller, but still generally better than the Baseline control law with increased gain.

5) In some cases the HOC_FBFF compensator increased steady-state error somewhat. This is not a major concern, as the command is coming from a pilot inceptor, so the small steady-state errors seen are likely not noticeable. Still, it is preferable that the HOC not alter the steady-state characteristics of the Baseline; this could be accomplished by adding washout filters to the HOC feed forward inputs.

5.5 HOC Future Work – Adding H_∞ Constraint

As noted above, the HOC augmentation, designed to minimize the H_2 measure of the closed-loop system $\xi \to z$, was not found to provide general improvement to the robustness of the control system. The H_2 measure is generally viewed as a good measure of control performance, while the H_∞ measure relates to control robustness against uncertainty in the plant. With H_∞ design, the maximum gain from input to output, over all frequencies, is limited by a chosen scalar: γ. For H_∞ performance, the inputs ξ are taken to be deterministic sinusoids, and the performance measure is

$$\left\| G_{CL} \right\|_\infty = \max_{\omega \in \Re} \frac{\sqrt{z^*(j\omega) z(j\omega)}}{\sqrt{\xi^*(j\omega) \xi(j\omega)}} < \gamma \tag{5-36}$$

where $\xi(j\omega)$ is the complex vector describing the magnitude and phase of input sinusoids and $z(j\omega)$ is likewise for the output. The * operator indicates complex conjugate transpose.

The present work could be extended by researching whether designing the HOC to constrain the H_∞ measure of the closed loop can improve robustness while maintaining a performance advantage over the Baseline Control alone. That is, one could investigate the application of quasi-optimal-H_2 / H_∞-constrained (hereafter: H_2/H_∞) controller design. This controller constrains the H_∞ measure of the closed loop, while minimizing the *upper bound* on the H_2 measure rather than minimizing the H_2 measure itself. One would prefer design formulas that minimize the H_2 measure while also constraining the H_∞ measure, but such have not been reported. However, with all H_2/H_∞ design formulas, as the H_∞ constraint is increased toward infinity, the H_2/H_∞ formulas reduce to the standard optimal H_2 formulas. Riccati equation based formulas are available for the different-weighting H_2 / H_∞ controller (different outputs for each measure), but these take the form of three coupled Riccati equations that require a specialized solution technique that is not readily available (Ref. [7], Sections 4 and 8). Equal-weighting for H_2 and H_∞ results in design formulas involving two decoupled Riccati equations, which can be solved using standard math libraries. However, all such published design formulas are contingent upon assumptions that the

present problem can violate, most often: $B_1 D_{21}^T = 0$ and $C_1^T D_{12} = 0$. Therefore, design formulas that are applicable to the present problem are derived here.

Glover and Mustafa, Ref. [36], derive a solution to the H_2 / H_∞ control problem, with equalized weighting on H_2 and H_∞ performance, that involves two decoupled algebraic Riccati equations, without the common assumptions $B_1 D_{21}^T = 0$ and $C_1^T D_{12} = 0$. They pose the problem as finding the maximum entropy (at infinity) H_∞ controller, but this is shown by Mustafa, Ref. [37], to be equivalent to the H_2/H_∞ control problem. The Glover and Mustafa solution is nearly in the needed form, but it assumes $D_{12} = \begin{bmatrix} 0 \\ I \end{bmatrix}$ and $D_{21} = [0 \quad I]$. The following derivation relaxes these constraints on D_{12} and D_{21} to the requirement that they each have full rank, by following a procedure found in Safonov et al., Ref. [38].

5.5.1 **Equal-Weighting H_2/H_∞ Compensator with $B_1 D_{21}^T \neq 0$ and $C_1^T D_{12} \neq 0$**

The Two-Input Two-Output plant is

$$\begin{aligned} \dot{x} &= Ax + B_2 \upsilon + B_1 \xi \\ z &= C_1 x + D_{12} \upsilon \\ y &= C_2 x + D_{21} \xi \end{aligned} \tag{5-37}$$

The *D* matrices can be written in Singular Value Decomposition (SVD) form as

$$D_{12} = U_{D_{12}} \begin{bmatrix} 0 \\ \sum_{D_{12}} \end{bmatrix} V_{D_{12}}^T \quad , \quad D_{21} = U_{D_{21}} \begin{bmatrix} 0 & \sum_{D_{21}} \end{bmatrix} V_{D_{21}}^T \tag{5-38}$$

Note that the *U* and *V* matrices are unitary, so $U^T U = U U^T = I$ and $V^T V = V V^T = I$. Make the substitutions

$$\xi = V_{D_{21}} \xi^{(2)} \quad , \quad \upsilon = V_{D_{12}} \sum_{D_{12}}^{-1} \upsilon^{(2)} \tag{5-39}$$

into the plant equations.

$$\begin{aligned} \dot{x} &= Ax + B_1 V_{D_{21}} \xi^{(2)} + B_2 V_{D_{12}} \sum_{D_{12}}^{-1} \upsilon^{(2)} \\ z &= C_1 x + D_{12} V_{D_{12}} \sum_{D_{12}}^{-1} \upsilon^{(2)} = C_1 x + U_{D_{12}} \begin{bmatrix} 0 \\ I \end{bmatrix} \upsilon^{(2)} \\ y &= C_2 x + D_{21} V_{D_{21}} \xi^{(2)} = C_2 x + U_{D_{21}} \begin{bmatrix} 0 & \sum_{D_{21}} \end{bmatrix} \xi^{(2)} \end{aligned} \tag{5-40}$$

Now pre-multiply the *z* equation by $U_{D_{12}}^T$, and the *y* equation by $\sum_{D_{21}}^{-1} U_{D_{21}}^T$.

$$z^{(2)} = U_{D_{12}}^T z = U_{D_{12}}^T C_1 x + \begin{bmatrix} 0 \\ I \end{bmatrix} \upsilon^{(2)}$$
$$y^{(2)} = \Sigma_{D_{21}}^{-1} U_{D_{21}}^T y = \Sigma_{D_{21}}^{-1} U_{D_{21}}^T C_2 x + \begin{bmatrix} 0 & I \end{bmatrix} \xi^{(2)} \tag{5-41}$$

Because $V_{D_{21}}$ and $U_{D_{12}}^T$ are unitary, the measures of the closed loop system (both H_2 and H_∞) are unchanged by this transformation. That is, the measure of $\xi^{(2)} \to z^{(2)}$ is identical to the measure of $\xi \to z$. The system equations above are in the form assumed by Ref. [36] *Lemma 2* and *Remark 1*. The plant matrices corresponding to the Ref. [36] formulation are identified in the present derivation by a ~ cap, and the corresponding expressions from the present formulation are shown by Equation (5-42).

$$\begin{aligned} &\tilde{A} = A && \tilde{B}_1 = B_1 V_{D_{21}} && \tilde{B}_2 = B_2 V_{D_{12}} \Sigma_{D_{12}}^{-1} \\ &\tilde{C}_1 = U_{D_{12}}^T C_1 && && \tilde{D}_{12} = \begin{bmatrix} 0 \\ I \end{bmatrix} \\ &\tilde{C}_2 = \Sigma_{D_{21}}^{-1} U_{D_{21}}^T C_2 && \tilde{D}_{21} = \begin{bmatrix} 0 & I \end{bmatrix} \end{aligned} \tag{5-42}$$

The Ref. [36] solution also utilizes matrices defined as follows. Let $\tilde{D}_{12\perp}$ make $\begin{bmatrix} \tilde{D}_{12} & \tilde{D}_{12\perp} \end{bmatrix}$ square and orthogonal, and let $\tilde{D}_{21\perp}$ make $\begin{bmatrix} \tilde{D}_{21} \\ \tilde{D}_{21\perp} \end{bmatrix}$ square and orthogonal. This means

$$\tilde{D}_{12\perp} = \begin{bmatrix} I \\ 0 \end{bmatrix} \text{ and } \tilde{D}_{21\perp} = \begin{bmatrix} I & 0 \end{bmatrix} \tag{5-43}$$

The H_2/H_∞ compensator is given in terms of the matrices $\hat{P} \geq 0$ and $Q \geq 0$, which are the stabilizing solutions to the following two decoupled Riccati equations.

$$\begin{aligned} 0 &= \left[\tilde{A} - \tilde{B}_2 \tilde{D}_{12}^T \tilde{C}_1 \right]^T \hat{P} + \hat{P} \left[\tilde{A} - \tilde{B}_2 \tilde{D}_{12}^T \tilde{C}_1 \right] - \hat{P} \left[\tilde{B}_2 \tilde{B}_2^T - \gamma^{-2} \tilde{B}_1 \tilde{B}_1^T \right] \hat{P} + \tilde{C}_1^T \tilde{D}_{12\perp} \tilde{D}_{12\perp}^T \tilde{C}_1 \\ 0 &= \left[\tilde{A} - \tilde{B}_1 \tilde{D}_{21}^T \tilde{C}_2 \right] Q + Q \left[\tilde{A} - \tilde{B}_1 \tilde{D}_{21}^T \tilde{C}_2 \right]^T - Q \left[\tilde{C}_2^T \tilde{C}_2 - \gamma^{-2} \tilde{C}_1^T \tilde{C}_1 \right] Q + \tilde{B}_1 \tilde{D}_{21\perp}^T \tilde{D}_{21\perp} \tilde{B}_1^T \end{aligned} \tag{5-44}$$

The compensator is then given by

$$\dot{x}_c = \tilde{A}_c x_c + \tilde{B}_c y^{(2)} \quad , \quad \upsilon^{(2)} = \tilde{C}_c x_c \tag{5-45}$$

where the above state-space matrices are

$$\tilde{C}_c = -\left(\tilde{D}_{12}^T\tilde{C}_1 + \tilde{B}_2^T\hat{P}\right)\left(I - \gamma^{-2}Q\hat{P}\right)^{-1} \quad , \quad \tilde{B}_c = \tilde{B}_1\tilde{D}_{21}^T + Q\tilde{C}_2^T$$

$$\begin{aligned}\tilde{A}_c &= \tilde{A} - \tilde{B}_1\tilde{D}_{21}^T\tilde{C}_2 + Q\left(\gamma^{-2}\tilde{C}_1^T\tilde{C}_1 - \tilde{C}_2^T\tilde{C}_2\right) + \left(\tilde{B}_2 + \gamma^{-2}Q\tilde{C}_1^T\tilde{D}_{12}\right)\tilde{C}_c \\ &= \tilde{A} - \left(\tilde{B}_1\tilde{D}_{21}^T + Q\tilde{C}_2^T\right)\tilde{C}_2 + \gamma^{-2}Q\tilde{C}_1^T\left(\tilde{C}_1 + \tilde{D}_{12}\tilde{C}_c\right) + \tilde{B}_2\tilde{C}_c \\ &= \tilde{A} - \tilde{B}_c\tilde{C}_2 + \gamma^{-2}Q\tilde{C}_1^T\left(\tilde{C}_1 + \tilde{D}_{12}\tilde{C}_c\right) + \tilde{B}_2\tilde{C}_c\end{aligned} \tag{5-46}$$

In the terms of the present plant description, the Riccati equations are

$$\begin{aligned}0 &= \left[A - B_2V_{D_{12}}\Sigma_{D_{12}}^{-1}\begin{bmatrix}0 & I\end{bmatrix}U_{D_{12}}^TC_1\right]^T\hat{P} + \hat{P}\left[A - B_2V_{D_{12}}\Sigma_{D_{12}}^{-1}\begin{bmatrix}0 & I\end{bmatrix}U_{D_{12}}^TC_1\right] \\ &\quad -\hat{P}\left[B_2V_{D_{12}}\Sigma_{D_{12}}^{-2}V_{D_{12}}^TB_2^T - \gamma^{-2}B_1V_{D_{21}}V_{D_{21}}^TB_1^T\right]\hat{P} + C_1^TU_{D_{12}}\begin{bmatrix}I\\0\end{bmatrix}\begin{bmatrix}I & 0\end{bmatrix}U_{D_{12}}^TC_1 \\ 0 &= \left[A - B_1V_{D_{21}}\begin{bmatrix}0\\I\end{bmatrix}\Sigma_{D_{21}}^{-1}U_{D_{21}}^TC_2\right]Q + Q\left[A - B_1V_{D_{21}}\begin{bmatrix}0\\I\end{bmatrix}\Sigma_{D_{21}}^{-1}U_{D_{21}}^TC_2\right]^T \\ &\quad -Q\left[C_2^TU_{D_{21}}\Sigma_{D_{21}}^{-2}U_{D_{21}}^TC_2 - \gamma^{-2}C_1^TU_{D_{12}}U_{D_{12}}^TC_1\right]Q + B_1V_{D_{21}}\begin{bmatrix}I\\0\end{bmatrix}\begin{bmatrix}I & 0\end{bmatrix}V_{D_{21}}^TB_1^T\end{aligned} \tag{5-47}$$

the compensator definition is

$$\begin{aligned}\dot{x}_c &= \tilde{A}_cx_c + \tilde{B}_c\Sigma_{D_{21}}^{-1}U_{D_{21}}^Ty \\ &= A_cx_c + B_cy\end{aligned} \quad , \quad \begin{aligned}\upsilon &= V_{D_{12}}\Sigma_{D_{12}}^{-1}\upsilon^{(2)} = V_{D_{12}}\Sigma_{D_{12}}^{-1}\tilde{C}_cx_c \\ &= C_cx_c\end{aligned} \tag{5-48}$$

and the compensator state-space matrices are

$$\begin{aligned}C_c &= V_{D_{12}}\Sigma_{D_{12}}^{-1}\tilde{C}_c = -V_{D_{12}}\Sigma_{D_{12}}^{-1}\left(\tilde{D}_{12}^T\tilde{C}_1 + \tilde{B}_2^T\hat{P}\right)\left(I - \gamma^{-2}Q\hat{P}\right)^{-1} \\ &= -V_{D_{12}}\Sigma_{D_{12}}^{-1}\left(\begin{bmatrix}0 & I\end{bmatrix}U_{D_{12}}^TC_1 + \Sigma_{D_{12}}^{-1}V_{D_{12}}^TB_2^T\hat{P}\right)\left(I - \gamma^{-2}Q\hat{P}\right)^{-1} \\ &= -\left(V_{D_{12}}\Sigma_{D_{12}}^{-1}\begin{bmatrix}0 & I\end{bmatrix}U_{D_{12}}^TC_1 + V_{D_{12}}\Sigma_{D_{12}}^{-2}V_{D_{12}}^TB_2^T\hat{P}\right)\left(I - \gamma^{-2}Q\hat{P}\right)^{-1}\end{aligned}$$

$$\begin{aligned}B_c &= \tilde{B}_c\Sigma_{D_{21}}^{-1}U_{D_{21}}^T = \left(\tilde{B}_1\tilde{D}_{21}^T + Q\tilde{C}_2^T\right)\Sigma_{D_{21}}^{-1}U_{D_{21}}^T \\ &= \left(B_1V_{D_{21}}\begin{bmatrix}0\\I\end{bmatrix} + QC_2^TU_{D_{21}}\Sigma_{D_{21}}^{-1}\right)\Sigma_{D_{21}}^{-1}U_{D_{21}}^T = \left(B_1V_{D_{21}}\begin{bmatrix}0\\I\end{bmatrix}\Sigma_{D_{21}}^{-1}U_{D_{21}}^T + QC_2^TU_{D_{21}}\Sigma_{D_{21}}^{-2}U_{D_{21}}^T\right)\end{aligned} \tag{5-49}$$

$$\begin{aligned}A_c &= \tilde{A}_c = \tilde{A} - \tilde{B}_c\tilde{C}_2 + \tilde{B}_2\tilde{C}_c + \gamma^{-2}Q\tilde{C}_1^T\left(\tilde{C}_1 + \tilde{D}_{12}\tilde{C}_c\right) \\ &= A - \tilde{B}_c\Sigma_{D_{21}}^{-1}U_{D_{21}}^TC_2 + B_2V_{D_{12}}\Sigma_{D_{12}}^{-1}\tilde{C}_c + \gamma^{-2}QC_1^TU_{D_{12}}\left(U_{D_{12}}^TC_1 + \begin{bmatrix}0\\I\end{bmatrix}\Sigma_{D_{12}}V_{D_{12}}^TC_c\right) \\ &= A - B_cC_2 + B_2C_c + \gamma^{-2}QC_1^T\left(C_1 + D_{12}C_c\right)\end{aligned}$$

The next step is to express the final solution in terms of D_{12} and D_{21}, rather than their SVD's. Working backwards, some expressions involving these matrices are written in terms of their SVD's.

$$D_{12} = U_{D_{12}} \begin{bmatrix} 0 \\ \Sigma_{D_{12}} \end{bmatrix} V_{D_{12}}^T \quad , \quad D_{12}^T = V_{D_{12}} \begin{bmatrix} 0 & \Sigma_{D_{12}} \end{bmatrix} U_{D_{12}}^T$$

$$D_{12}^T D_{12} = V_{D_{12}} \Sigma_{D_{12}}^2 V_{D_{12}}^T \ , \ \left(D_{12}^T D_{12} \right)^{-1} = V_{D_{12}} \Sigma_{D_{12}}^{-2} V_{D_{12}}^T$$

$$\left(D_{12}^T D_{12} \right)^{-1} D_{12}^T = V_{D_{12}} \Sigma_{D_{12}}^{-2} V_{D_{12}}^T V_{D_{12}} \begin{bmatrix} 0 & \Sigma_{D_{12}} \end{bmatrix} U_{D_{12}}^T = V_{D_{12}} \Sigma_{D_{12}}^{-1} \begin{bmatrix} 0 & I \end{bmatrix} U_{D_{12}}^T$$

$$D_{12} \left(D_{12}^T D_{12} \right)^{-1} D_{12}^T = U_{D_{12}} \begin{bmatrix} 0 \\ \Sigma_{D_{12}} \end{bmatrix} V_{D_{12}}^T V_{D_{12}} \Sigma_{D_{12}}^{-1} \begin{bmatrix} 0 & I \end{bmatrix} U_{D_{12}}^T = U_{D_{12}} \begin{bmatrix} 0 \\ I \end{bmatrix} \begin{bmatrix} 0 & I \end{bmatrix} U_{D_{12}}^T$$

$$\begin{aligned} I - D_{12} \left(D_{12}^T D_{12} \right)^{-1} D_{12}^T &= U_{D_{12}} \begin{bmatrix} I & 0 \\ 0 & I \end{bmatrix} U_{D_{12}}^T - U_{D_{12}} \begin{bmatrix} 0 & 0 \\ 0 & I \end{bmatrix} U_{D_{12}}^T = U_{D_{12}} \begin{bmatrix} I & 0 \\ 0 & 0 \end{bmatrix} U_{D_{12}}^T \\ &= U_{D_{12}} \begin{bmatrix} I \\ 0 \end{bmatrix} \begin{bmatrix} I & 0 \end{bmatrix} U_{D_{12}}^T \end{aligned} \tag{5-50}$$

$$D_{21} = U_{D_{21}} \begin{bmatrix} 0 & \Sigma_{D_{21}} \end{bmatrix} V_{D_{21}}^T \ , \ D_{21}^T = V_{D_{21}} \begin{bmatrix} 0 \\ \Sigma_{D_{21}} \end{bmatrix} U_{D_{21}}^T \ ,$$

$$D_{21} D_{21}^T = U_{D_{21}} \Sigma_{D_{21}}^2 U_{D_{21}}^T \ , \ \left(D_{21} D_{21}^T \right)^{-1} = U_{D_{21}} \Sigma_{D_{21}}^{-2} U_{D_{21}}^T$$

$$D_{21}^T \left(D_{21} D_{21}^T \right)^{-1} = V_{D_{21}} \begin{bmatrix} 0 \\ \Sigma_{D_{21}} \end{bmatrix} U_{D_{21}}^T U_{D_{21}} \Sigma_{D_{21}}^{-2} U_{D_{21}}^T = V_{D_{21}} \begin{bmatrix} 0 \\ I \end{bmatrix} \Sigma_{D_{21}}^{-1} U_{D_{21}}^T$$

$$D_{21}^T \left(D_{21} D_{21}^T \right)^{-1} D_{21} = V_{D_{21}} \begin{bmatrix} 0 \\ I \end{bmatrix} \Sigma_{D_{21}}^{-1} U_{D_{21}}^T U_{D_{21}} \begin{bmatrix} 0 & \Sigma_{D_{21}} \end{bmatrix} V_{D_{21}}^T = V_{D_{21}} \begin{bmatrix} 0 \\ I \end{bmatrix} \begin{bmatrix} 0 & I \end{bmatrix} V_{D_{21}}^T$$

$$I - D_{21}^T \left(D_{21} D_{21}^T \right)^{-1} D_{21} = V_{D_{21}} \begin{bmatrix} I & 0 \\ 0 & I \end{bmatrix} V_{D_{21}}^T - V_{D_{21}} \begin{bmatrix} 0 & 0 \\ 0 & I \end{bmatrix} V_{D_{21}}^T = V_{D_{21}} \begin{bmatrix} I & 0 \\ 0 & 0 \end{bmatrix} V_{D_{21}}^T = V_{D_{21}} \begin{bmatrix} I \\ 0 \end{bmatrix} \begin{bmatrix} I & 0 \end{bmatrix} V_{D_{21}}^T$$

Utilizing these equivalencies, the equal-weighting H_2 / H_∞ compensator solution is:

Riccati equations

$$\begin{aligned} 0 &= \left[A - B_2 \left(D_{12}^T D_{12} \right)^{-1} D_{12}^T C_1 \right]^T \hat{P} + \hat{P} \left[A - B_2 \left(D_{12}^T D_{12} \right)^{-1} D_{12}^T C_1 \right] \\ &\quad - \hat{P} \left[B_2 \left(D_{12}^T D_{12} \right)^{-1} B_2^T - \gamma^{-2} B_1 B_1^T \right] \hat{P} + C_1^T \left[I - D_{12} \left(D_{12}^T D_{12} \right)^{-1} D_{12}^T \right] C_1 \end{aligned} \tag{5-51}$$

$$\begin{aligned} 0 &= \left[A - B_1 D_{21}^T \left(D_{21} D_{21}^T \right)^{-1} C_2 \right] Q + Q \left[A - B_1 D_{21}^T \left(D_{21} D_{21}^T \right)^{-1} C_2 \right]^T \\ &\quad - Q \left[C_2^T \left(D_{21} D_{21}^T \right)^{-1} C_2 - \gamma^{-2} C_1^T C_1 \right] Q + B_1 \left[I - D_{21}^T \left(D_{21} D_{21}^T \right)^{-1} D_{21} \right] B_1^T \end{aligned} \tag{5-52}$$

Compensator state-space matrices

$$\begin{aligned} C_c &= -\left(\left(D_{12}^T D_{12} \right)^{-1} D_{12}^T C_1 + \left(D_{12}^T D_{12} \right)^{-1} B_2^T \hat{P} \right) \left(I - \gamma^{-2} Q \hat{P} \right)^{-1} \\ &= -\left(D_{12}^T D_{12} \right)^{-1} \left(D_{12}^T C_1 + B_2^T \hat{P} \right) \left(I - \gamma^{-2} Q \hat{P} \right)^{-1} \end{aligned}$$

$$\begin{aligned} B_c &= \left(B_1 D_{21}^T \left(D_{21} D_{21}^T \right)^{-1} + Q C_2^T \left(D_{21} D_{21}^T \right)^{-1} \right) \\ &= \left(B_1 D_{21}^T + Q C_2^T \right) \left(D_{21} D_{21}^T \right)^{-1} \end{aligned} \tag{5-53}$$

$$A_c = A - B_c C_2 + B_2 C_c + \gamma^{-2} Q C_1^T \left(C_1 + D_{12} C_c \right)$$

Solve for $\hat{P}$ in the first Riccati equation (Equation (5-51)). Solve for Q in the second Riccati equation (Equation (5-52)). Then form the state space matrices (Equation (5-53)), which define the HOC (Equation (5-26)).

Curiously, this equal-weighting H_2/H_∞ controller solution matches the solution to "The pure H_∞ standard problem" given in Haddad and Bernstein, Ref. [7], Section 5, with D_{11}=0 (E_∞=0 in their notation). Glover and Mustafa, Ref. [36], show that a set of controllers satisfy a given H_∞ constraint (as long as that constraint is larger than the minimum achievable), and the central solution within that ball of controllers is the solution that minimizes the bound on H_2. So, the pure H_∞ solution derived by Haddad and Bernstein is the central H_∞ solution, at least for the strictly proper case (D_{11}=0).

Chapter 6

General Conclusions

MIMO explicit command model following architectures are attractive for baseline rotorcraft control design for the following reasons. They provide dynamic decoupling, so that feedback control is more channelized (SISO). Command models can be designed to meet handling qualities requirements. The feed forward path can provide response quickness without feedback control aggressiveness, which eases the task of meeting both stability margin and quickness specifications. Command models provide commands that actually represent the desired response, so that errors terms are a measure of deviation from desired behavior, which facilitates application of a high order regulator (the HOC) to draw the response closer to that which is desired. Further, the inputs to command models, the targets, can also be useful inputs to the HOC for the reduction of errors.

The two MIMO explicit command model following methods presented here, DI and EMF, were shown to provide similar performance. For both, angular rate model following was implemented, along with selectable vertical rate model following. For both, the vertical rate model following was derived in a novel way so that activation is accomplished via a single connection, rather than transitioning between 3x4 and 4x4 architectures. The advantages for DI are that it adds no states to the control system (other than those for state estimation, if required), it can be non-linear, and it is easily scheduled based on a parameter such as forward speed. For those reasons, DI was selected as the Baseline control architecture for the HOC study. Still, EMF seems to be a viable alternative. An advantage for EMF is that it does not use state feedback, so it can be based on a design model having states that are neither measured nor estimated. As explained in a future work section, EMF could actually bypass the reduced-order-model approach, and be derived from a full order model or from frequency-domain flight test data.

An architecture and design methodology for high order compensator (HOC) augmentation of a command-model-following Baseline controller was presented. With this architecture, the HOC compensator is selectable and can easily be authority-limited, which might ease certification. A cockpit

switch could allow the pilot to disable HOC, and automated monitoring could be developed to disable HOC if undesirable outputs are detected. Because the HOC is designed based on the dynamics of a rate-compensated rotorcraft, accurate system identification should be safely achievable from flight testing, which increases the likelihood that improvements from HOC that are seen in simulation will be realized.

The HOC design methodology was carried out twice on an example helicopter model, once with turbulence rejection as the objective, and once with the additional objective of closely following pilot commands. The turbulence rejection HOC is feedback only (HOC_FB, utilizing angular rate errors), while the combined objective HOC has both feedback and feedforward elements (HOC_FBFF, utilizing angular rate targets and errors). The HOC_FB was found to be better at improving turbulence rejection but generally degrades the following of pilot commands. The HOC_FBFF improves turbulence rejection relative to the Baseline controller, but not by as much as HOC_FB. However, HOC_FBFF also generally improves the following of pilot commands.

Combined application of the methods developed and investigated here were shown to improve model following control of manned rotorcraft. The usefulness of this dissertation to practicing control designers is enhanced through detailed design procedures and implementation tips. And, to facilitate improvement upon the present methods, ground work has been laid in areas of investigation that could be productive.

This dissertation presents advancements in control system design, which were motivated by the problem of manned helicopter control. Some of these techniques are specific to that application, such as selectable model following in the vertical axis. Others are more generally applicable to control design, such as HOC augmentation that includes feed-forward elements, and such as the effects of actuator and sensor dynamics on Dynamic Inversion. One result, the more-general equal-weighting H_2/H_∞ solution, is of mathematical interest in that it reveals an un-reported relationship to an H_∞ solution.

Bibliography

[1] Stevens, B. L., and Lewis, F. L., *Aircraft Control and Simulation, 2nd Edition*, John Wiley & Sons, Inc., Hoboken, New Jersey, 2003, Chapter 5, Section 8.

[2] Catapang, D. R., Tischler, M. B., and Biezad, D. J., "Robust Crossfeed Design for Hovering Rotorcraft," *International Journal of Robust and Nonlinear Control*, Vol. 4, pp. 161-180, 1994.

[3] Sahani, N. A., and Horn, J. F., "Adaptive Model Inversion Control of a Helicopter with Structural Load Limiting," *Journal of Guidance, Control, and Dynamics*, Vol. 29, No. 2, 2006.

[4] Horn, J. F.; and Bridges, D. O.; "A Model Following Controller Optimized for Gust Rejection during Shipboard Operations." Proceedings of the American Helicopter Society 63rd Annual Forum, Virginia Beach, VA, May 1-3, 2007.

[5] Doyle, J.C.; Glover, K.; Khargonekar, P.P.; and Francis, B.A.; "State-Space Solutions to Standard H_2 and H_∞ Control Problems," *IEEE Transactions on Automatic Control*, Vol. 34, No. 8, p. 831-847, August 1989.

[6] Boyd, S.; Balakrishnan, V.; Feron, E.; and ElGhaoui, L.; "Control System Analysis and Synthesis via Linear Matrix Inequalities", Proceedings of the American Control Conference, San Francisco, CA, June 2-4, 1993, p. 2147-2154.

[7] Haddad, W.M.; and Bernstein, D.S.; "Generalized Riccati Equations for the Full- and Reduced-Order Mixed-Norm H_2/H_∞ Standard Problem." *Systems and Control Letters*, Vol. 14, p. 185-197, 1990.

[8] Khargonekar, P. P.; and Rotea, M. A.; "Mixed H_2/H_∞ Control: A Convex Optimization Approach." *IEEE Transactions on Automatic Control*, Vol. 36, No. 7, p. 824-837, July 1991.

[9] Manness, M. A.; and Murray-Smith, D. J.; "Aspects of Multivariable Flight Control Law Design for Helicopters Using Eigenstructure Assignment." *Journal of the American Helicopter Society*, 37(3), p. 18-32, July 1992.

[10] Takahashi, M. D.; "Synthesis and Evaluation of an H2 Control Law for a Hovering Helicopter." *Journal of Guidance, Control, and Dynamics*, Vol 16, No. 3, p. 579-584, May-June 1993.

[11] Foster, N. P.; Spurgeon, S. K.; and Postlethwaite, I.; "Robust Model-Reference Tracking Control with a Sliding Mode applied to an ACT Rotorcraft." 19th European Rotorcraft Forum, Cernobbio, Italy, Sept. 14-16, 1993, ERF-1993-Vol2-H4.

[12] Spurgeon, S. K.; Edwards, C.; and Foster, N. P.; "Robust Model Reference Control Using a Sliding Mode Controller/Observer Scheme with application to a Helicopter Problem." IEEE Workshop on Variable Structure Systems, 1996, p. 36-41.

[13] Postlethwaite, I.; Smerlas, A.; Walker, D. J.; Gubbels, A. W.; Baillie, S. W.; Strange, M. E.; and Howitt, J.; "H-infinity control of the NRC bell 205 fly-by-wire helicopter." *Journal of the American Helicopter Society*, 44(4), p. 276-284, 1999.

[14] Postlethwaite, I.; Konstantopoulos, I. K.; Sun, X.-D.; Walker, D. J.; and Alford, A. G.; "Design, Flight Simulation, and Handling Qualities Evaluation of an LPV Gain-Scheduled Helicopter Flight Control System". *European Journal of Control* (2000)6:553-566.

[15] Wan, E. A.; and Bogdanov, A. A.; "Model predictive neural control with applications to a 6 DoF helicopter model." Proceedings of the American Control Conference, Arlington, VA, June 25-27, 2001, p. 488-493.

[16] Bogdanov, A. A.; Wan, E. A.; Carlsson, M.; Zhang, Y.; Kieburtz, R.; and Baptista, A.; "Model Predictive Neural Control of a High-Fidelity Helicopter Model." AIAA Guidance, Navigation, and Control Conference and Exhibit; Montreal, Canada, August 5-9, 2001, AIAA-2001-4164.

[17] Hovakimyan, N.; Kim, N.; Calise, A. J., Prasad, J. V. R., and Corban, E.; "Adaptive Output Feedback for High-Bandwidth Control of an Unmanned Helicopter." AIAA Guidance, Navigation, and Control Conference and Exhibit, Montreal, Canada, August 5-9, 2001, AIAA-2001-4181.

[18] Corban, J. E.; Calise, A. J., Prasad, J. V. R.; Hur, J.; and Kim, N.; "Flight Evaluation of Adaptive High-Bandwidth Control Methods for Unmanned Helicopters," AIAA Guidance, Navigation, and Control Conference and Exhibit, Monterey, CA, August 5-8, 2002, AIAA-2002-4441.

[19] Johnson, E. N.; and Kannan, S. K.; "Adaptive Flight Control for an Autonomous Unmanned Helicopter," AIAA Guidance, Navigation, and Control Conference and Exhibit, Monterey, CA, August 5-8, 2002, AIAA-2002-4439.

[20] Krupadanam, A. S.; Annaswamy, A. M.; and Mangoubi, R. S.; "Multivariable Adaptive Control Design with Applications to Autonomous Helicopters," *Journal of Guidance, Control, and Dynamics*; Vol. 25, No. 5, pp. 843-851, September 2002.

[21] Bichlmeier, M.; Holzapfel, F.; Xargay, E.; and Hovakimyan, N.; "L1 Adaptive Augmentation of a Helicopter Baseline Controller," AIAA Guidance, Navigation, and Control Conference; Boston, MA, August 19-22, 2013, AIAA 2013-4855.

[22] Hayes, P. M.; Grill, I.; and Horn, J. F.; "Gust Rejection Using Active Trailing Edge Flaps," Proceedings of the American Helicopter Society 68th Annual Forum, Fort Worth, Texas, May 1-3, 2012.

[23] Rigsby, J.; Hung, C.-H.; and Horn, J. F.; "Design and Evaluation of a Robust Feedback Controller for Helicopters Handling Externally Slung Loads," Proceedings of the American Helicopter Society 69th Annual Forum, Phoenix, AZ, May 21-23, 2013.

[24] Anon., *ADS-33E-PRF Aeronautical Design Standard – Performance Specifications – Handling Qualities Requirements for Military Rotorcraft*, U.S. Army Aviation and Missile Command – Aviation Engineering Directorate, Redstone Arsenal, AL, March 21st, 2000.

[25] Howlett, J. J., "UH-60A BLACK HAWK Engineering Simulation Program: Volume I – Mathematical Model", NASA CR 166309, Dec. 1981.

[26] Zivan, L., Tischler, M. B., "Development of a Full Flight Envelope Helicopter Simulation Using System Identification," *Journal of the American Helicopter Society*, Vol. 55, paper 022003, 2010.

[27] Harding, J. W., Moody, S. J., Jeram, G. J., Mansur, M. H., and Tischler, M. B., "Development of Modern Control Laws for the AH-64D in Hover/Low Speed Flight," Proceedings of the American Helicopter Society 62nd Annual Forum, Phoenix, AZ, May 9-11, 2006.

[28] Zanetti, F., Colautti, S., Saggiani, G. M., and Rossi, V., "Rotary Wing UAV: HIL Tests for a Model-Based Feedforward Controller," 34th European Rotorcraft Forum, ERF34, p.295-332, 2008.

[29] Michalek, M. M., "Simple causal fixed-structure feedforward control law for general continuous-time LTI SISO systems," 2014 European Control Conference, Strasbourg, France, June 24-27, 2014, p. 61-66.

[30] Xiaodong S. U., "A Novel Method of Dynamic Decoupling for Multi-axis Sensor," 2009 International Conference on Test and Measurement (ICTM 2009), p 137-40, 2009

[31] Horn, J. F., and Bridges, D. O., "A Model Following Controller Optimized for Gust Rejection during Shipboard Operations," Proceedings of the American Helicopter Society 63rd Annual Forum, Virginia Beach, VA, May 1-3, 2007.

[32] Guo, W., and Horn, J. F., "Rotor State Feedback Control for Rotorcraft with Variable Rotor Speed," Paper AIAA 2009-5797, AIAA Guidance, Navigation, and Control Conference 2009, Chicago, IL, August 10-13, 2009, AIAA 2009-5797.

[33] Horn, J. F., Guo, W., and Ozdemir, G. T., "Use of Rotor State Feedback to Improve Closed Loop Stability and Handling Qualities," *Journal of the American Helicopter Society*, Vol. 57, paper 022001, 2012.

[34] Lusardi, J. A., Tischler, M. B., Blanken, C. L., and Labows, S. J., "Empirically Derived Helicopter Response Model and Control System Requirements for Flight in Turbulence," *Journal of the American Helicopter Society*, Vol. 49(3), p.340-349, July 2004.

[35] Blankinship, K., "State-Space Formula for the Two-Input/Two-Output Coupling Numerator," *AIAA Journal of Guidance, Control, and Dynamics*, Vol. 28, No. 3, p. 546-547, May-June 2005.

[36] Glover, K.; and Mustafa, D.; "Derivation of the maximum entropy H_∞-controller and a state-space formula for its entropy", *International Journal of Control*, Vol. 50, No. 3, p. 899-916, 1989.

[37] Mustafa, D.; "Relations between maximum-entropy/ H_∞ control and combined H_∞/LQG control", *Systems & Control Letters*, Vol. 12, p. 193-203, 1989.

[38] Safonov, M.G.; Limebeer, D.J.N.; and Chiang, R.Y.; "Simplifying the H∞ Theory Via Loop Shifting, Matrix Pencil and Descriptor Concepts", *International Journal of Control*, Vol. 50, No. 6, p. 2467-2488, 1989.

Appendix A

Elements of the Decoupling Matrix $\mathbf{M}_{3x4}$

Formulas for the elements of the decoupling matrix $\mathbf{M}_{3x4}$ are derived. Multiply Equation (4-8) by the common denominator of the plant transfer functions to put the problem in terms of the plant transfer function matrix numerators.

$$\begin{bmatrix} N_{\text{lat}}^{p} & N_{\text{lng}}^{p} & N_{\text{ped}}^{p} & N_{\text{col}}^{p} \\ N_{\text{lat}}^{q} & N_{\text{lng}}^{q} & N_{\text{ped}}^{q} & N_{\text{col}}^{q} \\ N_{\text{lat}}^{r} & N_{\text{lng}}^{r} & N_{\text{ped}}^{r} & N_{\text{col}}^{r} \end{bmatrix} \begin{bmatrix} 1 & \frac{u_{\text{lat}}}{d_{\text{lng}}} & \frac{u_{\text{lat}}}{d_{\text{ped}}} & \frac{u_{\text{lat}}}{u_{\text{col}}} \\ \frac{u_{\text{lng}}}{d_{\text{lat}}} & 1 & \frac{u_{\text{lng}}}{d_{\text{ped}}} & \frac{u_{\text{lng}}}{u_{\text{col}}} \\ \frac{u_{\text{ped}}}{d_{\text{lat}}} & \frac{u_{\text{ped}}}{d_{\text{lng}}} & 1 & \frac{u_{\text{ped}}}{u_{\text{col}}} \\ 0 & 0 & 0 & 1 \end{bmatrix} \begin{Bmatrix} \Delta d_{\text{lat}} \\ \Delta d_{\text{lng}} \\ \Delta d_{\text{ped}} \\ \Delta u_{\text{col}} \end{Bmatrix} = \begin{bmatrix} \# & 0 & 0 & 0 \\ 0 & \# & 0 & 0 \\ 0 & 0 & \# & 0 \end{bmatrix} \begin{Bmatrix} \Delta d_{\text{lat}} \\ \Delta d_{\text{lng}} \\ \Delta d_{\text{ped}} \\ \Delta u_{\text{col}} \end{Bmatrix} \tag{A-1}$$

Solve for the elements of the dynamic decoupling matrix by considering one column at a time. Multiply that column with the rows of N that are required to be orthogonal (product is specified to be 0).

$$\begin{Bmatrix} N_{\text{lat}}^{q} \\ N_{\text{lat}}^{r} \end{Bmatrix} + \begin{bmatrix} N_{\text{lng}}^{q} & N_{\text{ped}}^{q} \\ N_{\text{lng}}^{r} & N_{\text{ped}}^{r} \end{bmatrix} \begin{Bmatrix} \frac{u_{\text{lng}}}{d_{\text{lat}}} \\ \frac{u_{\text{ped}}}{d_{\text{lat}}} \end{Bmatrix} = \begin{Bmatrix} 0 \\ 0 \end{Bmatrix} \quad , \quad \begin{bmatrix} N_{\text{lat}}^{p} & N_{\text{ped}}^{p} \\ N_{\text{lat}}^{r} & N_{\text{ped}}^{r} \end{bmatrix} \begin{Bmatrix} \frac{u_{\text{lat}}}{d_{\text{lng}}} \\ \frac{u_{\text{ped}}}{d_{\text{lng}}} \end{Bmatrix} + \begin{Bmatrix} N_{\text{lng}}^{p} \\ N_{\text{lng}}^{r} \end{Bmatrix} = \begin{Bmatrix} 0 \\ 0 \end{Bmatrix} ,$$

$$\begin{bmatrix} N_{\text{lat}}^{p} & N_{\text{lng}}^{p} \\ N_{\text{lat}}^{q} & N_{\text{lng}}^{q} \end{bmatrix} \begin{Bmatrix} \frac{u_{\text{lat}}}{d_{\text{ped}}} \\ \frac{u_{\text{lng}}}{d_{\text{ped}}} \end{Bmatrix} + \begin{Bmatrix} N_{\text{ped}}^{p} \\ N_{\text{ped}}^{q} \end{Bmatrix} = \begin{Bmatrix} 0 \\ 0 \end{Bmatrix} \quad , \quad \begin{bmatrix} N_{\text{lat}}^{p} & N_{\text{lng}}^{p} & N_{\text{ped}}^{p} \\ N_{\text{lat}}^{q} & N_{\text{lng}}^{q} & N_{\text{ped}}^{q} \\ N_{\text{lat}}^{r} & N_{\text{lng}}^{r} & N_{\text{ped}}^{r} \end{bmatrix} \begin{Bmatrix} \frac{u_{\text{lat}}}{u_{\text{col}}} \\ \frac{u_{\text{lng}}}{u_{\text{col}}} \\ \frac{u_{\text{ped}}}{u_{\text{col}}} \end{Bmatrix} + \begin{Bmatrix} N_{\text{col}}^{p} \\ N_{\text{col}}^{q} \\ N_{\text{col}}^{r} \end{Bmatrix} = \begin{Bmatrix} 0 \\ 0 \\ 0 \end{Bmatrix} \tag{A-2}$$

Now solve for the elements of the dynamic decoupling matrix.

$$\begin{Bmatrix} \frac{u_{\text{lng}}}{d_{\text{lat}}} \\ \frac{u_{\text{ped}}}{d_{\text{lat}}} \end{Bmatrix} = -\begin{bmatrix} N_{\text{lng}}^{q} & N_{\text{ped}}^{q} \\ N_{\text{lng}}^{r} & N_{\text{ped}}^{r} \end{bmatrix}^{-1} \begin{Bmatrix} N_{\text{lat}}^{q} \\ N_{\text{lat}}^{r} \end{Bmatrix} = -\frac{\begin{bmatrix} N_{\text{ped}}^{r} & -N_{\text{ped}}^{q} \\ -N_{\text{lng}}^{r} & N_{\text{lng}}^{q} \end{bmatrix}}{N_{\text{lng}}^{q} N_{\text{ped}}^{r} - N_{\text{lng}}^{r} N_{\text{ped}}^{q}} \begin{Bmatrix} N_{\text{lat}}^{q} \\ N_{\text{lat}}^{r} \end{Bmatrix} \tag{A-3}$$

$$\begin{Bmatrix} \dfrac{u_{\text{lat}}}{d_{\text{lng}}} \\ \dfrac{u_{\text{ped}}}{d_{\text{lng}}} \end{Bmatrix} = -\begin{bmatrix} N_{\text{lat}}^{p} & N_{\text{ped}}^{p} \\ N_{\text{lat}}^{r} & N_{\text{ped}}^{r} \end{bmatrix}^{-1} \begin{Bmatrix} N_{\text{lng}}^{p} \\ N_{\text{lng}}^{r} \end{Bmatrix} = -\frac{\begin{bmatrix} N_{\text{ped}}^{r} & -N_{\text{ped}}^{p} \\ -N_{\text{lat}}^{r} & N_{\text{lat}}^{p} \end{bmatrix}}{N_{\text{lat}}^{p} N_{\text{ped}}^{r} - N_{\text{lat}}^{r} N_{\text{ped}}^{p}} \begin{Bmatrix} N_{\text{lng}}^{p} \\ N_{\text{lng}}^{r} \end{Bmatrix} \tag{A-4}$$

$$\begin{Bmatrix} \dfrac{u_{\text{lat}}}{d_{\text{ped}}} \\ \dfrac{u_{\text{lng}}}{d_{\text{ped}}} \end{Bmatrix} = -\begin{bmatrix} N_{\text{lat}}^{p} & N_{\text{lng}}^{p} \\ N_{\text{lat}}^{q} & N_{\text{lng}}^{q} \end{bmatrix}^{-1} \begin{Bmatrix} N_{\text{ped}}^{p} \\ N_{\text{ped}}^{q} \end{Bmatrix} = -\frac{\begin{bmatrix} N_{\text{lng}}^{q} & -N_{\text{lng}}^{p} \\ -N_{\text{lat}}^{q} & N_{\text{lat}}^{p} \end{bmatrix}}{N_{\text{lat}}^{p} N_{\text{lng}}^{q} - N_{\text{lat}}^{q} N_{\text{lng}}^{p}} \begin{Bmatrix} N_{\text{ped}}^{p} \\ N_{\text{ped}}^{q} \end{Bmatrix} \tag{A-5}$$

$$\begin{Bmatrix} \dfrac{u_{\text{lat}}}{u_{\text{col}}} \\ \dfrac{u_{\text{lng}}}{u_{\text{col}}} \\ \dfrac{u_{\text{ped}}}{u_{\text{col}}} \end{Bmatrix} = -\begin{bmatrix} N_{\text{lat}}^{p} & N_{\text{lng}}^{p} & N_{\text{ped}}^{p} \\ N_{\text{lat}}^{q} & N_{\text{lng}}^{q} & N_{\text{ped}}^{q} \\ N_{\text{lat}}^{r} & N_{\text{lng}}^{r} & N_{\text{ped}}^{r} \end{bmatrix}^{-1} \begin{Bmatrix} N_{\text{col}}^{p} \\ N_{\text{col}}^{q} \\ N_{\text{col}}^{r} \end{Bmatrix}$$

$$= -\frac{\begin{bmatrix} N_{\text{lng}}^{q} N_{\text{ped}}^{r} - N_{\text{lng}}^{r} N_{\text{ped}}^{q} & N_{\text{lng}}^{r} N_{\text{ped}}^{p} - N_{\text{lng}}^{p} N_{\text{ped}}^{r} & N_{\text{lng}}^{p} N_{\text{ped}}^{q} - N_{\text{lng}}^{q} N_{\text{ped}}^{p} \\ N_{\text{lat}}^{r} N_{\text{ped}}^{q} - N_{\text{lat}}^{q} N_{\text{ped}}^{r} & N_{\text{lat}}^{p} N_{\text{ped}}^{r} - N_{\text{lat}}^{r} N_{\text{ped}}^{p} & N_{\text{lat}}^{q} N_{\text{ped}}^{p} - N_{\text{lat}}^{p} N_{\text{ped}}^{q} \\ N_{\text{lat}}^{q} N_{\text{lng}}^{r} - N_{\text{lat}}^{r} N_{\text{lng}}^{q} & N_{\text{lat}}^{r} N_{\text{lng}}^{p} - N_{\text{lat}}^{p} N_{\text{lng}}^{r} & N_{\text{lat}}^{p} N_{\text{lng}}^{q} - N_{\text{lat}}^{q} N_{\text{lng}}^{p} \end{bmatrix}}{\begin{array}{c} N_{\text{lat}}^{p} N_{\text{lng}}^{q} N_{\text{ped}}^{r} + N_{\text{lng}}^{p} N_{\text{ped}}^{q} N_{\text{lat}}^{r} + N_{\text{ped}}^{p} N_{\text{lat}}^{q} N_{\text{lng}}^{r} \\ -N_{\text{lat}}^{r} N_{\text{lng}}^{q} N_{\text{ped}}^{p} - N_{\text{lng}}^{r} N_{\text{ped}}^{q} N_{\text{lat}}^{p} - N_{\text{ped}}^{r} N_{\text{lat}}^{q} N_{\text{lng}}^{p} \end{array}} \begin{Bmatrix} N_{\text{col}}^{p} \\ N_{\text{col}}^{q} \\ N_{\text{col}}^{r} \end{Bmatrix} \tag{A-6}$$

Given a 5-state plant, the results above appear to be 8th order or 12th order. For the cases considered, the actual highest order was 3rd after pole-zero cancellations with tolerance 0.01 rad/s. For implementation, these "exact" transfer functions were replaced with stable 2nd order approximations through frequency-domain fitting over the range $1 \text{ rad/sec} \leq \omega \leq 10 \text{ rad/sec}$.

Appendix B

Elements of the Decoupling Matrix $\mathbf{M}_{1x3}$

Formulas for the elements of the mixing matrix $\mathbf{M}_{1x3}$ are derived. Start with the angular rate mixing, and replace Δu_{col} with the expression involving the decoupled inputs, Equation (4-12).

$$\begin{Bmatrix} \Delta u_{\text{lat}} \\ \Delta u_{\text{lng}} \\ \Delta u_{\text{ped}} \end{Bmatrix} = \mathbf{M}_{3x4} \begin{Bmatrix} \Delta d_{\text{lat}} \\ \Delta d_{\text{lng}} \\ \Delta d_{\text{ped}} \\ \Delta u_{\text{col}} \end{Bmatrix} = \begin{bmatrix} 1 & \frac{u_{\text{lat}}}{d_{\text{lng}}} & \frac{u_{\text{lat}}}{d_{\text{ped}}} & \frac{u_{\text{lat}}}{u_{\text{col}}} \\ \frac{u_{\text{lng}}}{d_{\text{lat}}} & 1 & \frac{u_{\text{lng}}}{d_{\text{ped}}} & \frac{u_{\text{lng}}}{u_{\text{col}}} \\ \frac{u_{\text{ped}}}{d_{\text{lat}}} & \frac{u_{\text{ped}}}{d_{\text{lng}}} & 1 & \frac{u_{\text{ped}}}{u_{\text{col}}} \end{bmatrix} \left\{ \begin{bmatrix} \Delta d_{\text{lat}} \\ \Delta d_{\text{lng}} \\ \Delta d_{\text{ped}} \\ \underbrace{\begin{matrix} \frac{u_{\text{col}}}{d_{\text{lat}}} & \frac{u_{\text{col}}}{d_{\text{lng}}} & \frac{u_{\text{col}}}{d_{\text{ped}}} \end{matrix}}_{\mathbf{M}_{1x3}} & 1 \end{bmatrix} \begin{Bmatrix} \Delta d_{\text{lat}} \\ \Delta d_{\text{lng}} \\ \Delta d_{\text{ped}} \\ \Delta d_{\text{col}} \end{Bmatrix} \right\} \tag{B-1}$$

$$= \begin{bmatrix} 1+\frac{u_{\text{lat}}}{u_{\text{col}}}\frac{u_{\text{col}}}{d_{\text{lat}}} & \frac{u_{\text{lat}}}{d_{\text{lng}}}+\frac{u_{\text{lat}}}{u_{\text{col}}}\frac{u_{\text{col}}}{d_{\text{lng}}} & \frac{u_{\text{lat}}}{d_{\text{ped}}}+\frac{u_{\text{lat}}}{u_{\text{col}}}\frac{u_{\text{col}}}{d_{\text{ped}}} & \frac{u_{\text{lat}}}{u_{\text{col}}} \\ \frac{u_{\text{lng}}}{d_{\text{lat}}}+\frac{u_{\text{lng}}}{u_{\text{col}}}\frac{u_{\text{col}}}{d_{\text{lat}}} & 1+\frac{u_{\text{lng}}}{u_{\text{col}}}\frac{u_{\text{col}}}{d_{\text{lng}}} & \frac{u_{\text{lng}}}{d_{\text{ped}}}+\frac{u_{\text{lng}}}{u_{\text{col}}}\frac{u_{\text{col}}}{d_{\text{ped}}} & \frac{u_{\text{lng}}}{u_{\text{col}}} \\ \frac{u_{\text{ped}}}{d_{\text{lat}}}+\frac{u_{\text{ped}}}{u_{\text{col}}}\frac{u_{\text{col}}}{d_{\text{lat}}} & \frac{u_{\text{ped}}}{d_{\text{lng}}}+\frac{u_{\text{ped}}}{u_{\text{col}}}\frac{u_{\text{col}}}{d_{\text{lng}}} & 1+\frac{u_{\text{ped}}}{u_{\text{col}}}\frac{u_{\text{col}}}{d_{\text{ped}}} & \frac{u_{\text{ped}}}{u_{\text{col}}} \end{bmatrix} \begin{Bmatrix} \Delta d_{\text{lat}} \\ \Delta d_{\text{lng}} \\ \Delta d_{\text{ped}} \\ \Delta d_{\text{col}} \end{Bmatrix}$$

Combine the expression above with the expression for Δu_{col} (Equation (4-12)) to get an expression for the complete $\Delta\mathbf{u}$ vector in terms of the $\Delta\mathbf{d}$ vector,

$$\begin{Bmatrix} \Delta u_{\text{lat}} \\ \Delta u_{\text{lng}} \\ \Delta u_{\text{ped}} \\ \Delta u_{\text{col}} \end{Bmatrix} = \begin{bmatrix} 1+\frac{u_{\text{lat}}}{u_{\text{col}}}\frac{u_{\text{col}}}{d_{\text{lat}}} & \frac{u_{\text{lat}}}{d_{\text{lng}}}+\frac{u_{\text{lat}}}{u_{\text{col}}}\frac{u_{\text{col}}}{d_{\text{lng}}} & \frac{u_{\text{lat}}}{d_{\text{ped}}}+\frac{u_{\text{lat}}}{u_{\text{col}}}\frac{u_{\text{col}}}{d_{\text{ped}}} & \frac{u_{\text{lat}}}{u_{\text{col}}} \\ \frac{u_{\text{lng}}}{d_{\text{lat}}}+\frac{u_{\text{lng}}}{u_{\text{col}}}\frac{u_{\text{col}}}{d_{\text{lat}}} & 1+\frac{u_{\text{lng}}}{u_{\text{col}}}\frac{u_{\text{col}}}{d_{\text{lng}}} & \frac{u_{\text{lng}}}{d_{\text{ped}}}+\frac{u_{\text{lng}}}{u_{\text{col}}}\frac{u_{\text{col}}}{d_{\text{ped}}} & \frac{u_{\text{lng}}}{u_{\text{col}}} \\ \frac{u_{\text{ped}}}{d_{\text{lat}}}+\frac{u_{\text{ped}}}{u_{\text{col}}}\frac{u_{\text{col}}}{d_{\text{lat}}} & \frac{u_{\text{ped}}}{d_{\text{lng}}}+\frac{u_{\text{ped}}}{u_{\text{col}}}\frac{u_{\text{col}}}{d_{\text{lng}}} & 1+\frac{u_{\text{ped}}}{u_{\text{col}}}\frac{u_{\text{col}}}{d_{\text{ped}}} & \frac{u_{\text{ped}}}{u_{\text{col}}} \\ \frac{u_{\text{col}}}{d_{\text{lat}}} & \frac{u_{\text{col}}}{d_{\text{lng}}} & \frac{u_{\text{col}}}{d_{\text{ped}}} & 1 \end{bmatrix} \begin{Bmatrix} \Delta d_{\text{lat}} \\ \Delta d_{\text{lng}} \\ \Delta d_{\text{ped}} \\ \Delta d_{\text{col}} \end{Bmatrix} \tag{B-2}$$

and apply this input expression to the plant transfer function matrix for the plant that includes vertical rate as an output (the 6-state plant version of the example rotorcraft).

$$\Delta\mathbf{x} = \begin{bmatrix} \Delta v & \Delta w & p & q & r & \Delta\theta \end{bmatrix}^T, \quad \mathbf{y} = \begin{bmatrix} p & q & r & w^{\text{ned}} \end{bmatrix}^{\text{T}}$$

$$\Delta\dot{\mathbf{x}} = \mathbf{A}\Delta\mathbf{x} + \mathbf{B}\Delta\mathbf{u}, \quad \mathbf{y} = \mathbf{C}\Delta\mathbf{x}, \quad \text{where } w^{\text{ned}} = \Delta w - u_{\text{trm}}\Delta\theta \tag{B-3}$$

$$\mathbf{P}(s) = \frac{\mathbf{y}}{\mathbf{u}}(s) = \mathbf{C}\left[s\mathbf{I} - \mathbf{A}\right]^{-1}\mathbf{B} = \mathbf{C}\frac{\text{Adj}\left(s\mathbf{I} - \mathbf{A}\right)}{\left|s\mathbf{I} - \mathbf{A}\right|}\mathbf{B}, \quad \mathbf{N}(s) = \mathbf{C}\left[\text{Adj}\left(s\mathbf{I} - \mathbf{A}\right)\right]\mathbf{B}$$

The plant response to the $\Delta\mathbf{d}$ input is specified to be decoupled.

$$\begin{Bmatrix} p \\ q \\ r \\ w^{\text{ned}} \end{Bmatrix} = \overbrace{\begin{bmatrix} \frac{p}{u_{\text{lat}}} & \frac{p}{u_{\text{lng}}} & \frac{p}{u_{\text{ped}}} & \frac{p}{u_{\text{col}}} \\ \frac{q}{u_{\text{lat}}} & \frac{q}{u_{\text{lng}}} & \frac{q}{u_{\text{ped}}} & \frac{q}{u_{\text{col}}} \\ \frac{r}{u_{\text{lat}}} & \frac{r}{u_{\text{lng}}} & \frac{r}{u_{\text{ped}}} & \frac{r}{u_{\text{col}}} \\ \frac{w^{\text{ned}}}{u_{\text{lat}}} & \frac{w^{\text{ned}}}{u_{\text{lng}}} & \frac{w^{\text{ned}}}{u_{\text{ped}}} & \frac{w^{\text{ned}}}{u_{\text{col}}} \end{bmatrix}}^{\mathbf{P}(s)} \begin{bmatrix} 1 + \frac{u_{\text{lat}}}{u_{\text{col}}}\frac{u_{\text{col}}}{d_{\text{lat}}} & \frac{u_{\text{lat}}}{d_{\text{lng}}} + \frac{u_{\text{lat}}}{u_{\text{col}}}\frac{u_{\text{col}}}{d_{\text{lng}}} & \frac{u_{\text{lat}}}{d_{\text{ped}}} + \frac{u_{\text{lat}}}{u_{\text{col}}}\frac{u_{\text{col}}}{d_{\text{ped}}} & \frac{u_{\text{lat}}}{u_{\text{col}}} \\ \frac{u_{\text{lng}}}{d_{\text{lat}}} + \frac{u_{\text{lng}}}{u_{\text{col}}}\frac{u_{\text{col}}}{d_{\text{lat}}} & 1 + \frac{u_{\text{lng}}}{u_{\text{col}}}\frac{u_{\text{col}}}{d_{\text{lng}}} & \frac{u_{\text{lng}}}{d_{\text{ped}}} + \frac{u_{\text{lng}}}{u_{\text{col}}}\frac{u_{\text{col}}}{d_{\text{ped}}} & \frac{u_{\text{lng}}}{u_{\text{col}}} \\ \frac{u_{\text{ped}}}{d_{\text{lat}}} + \frac{u_{\text{ped}}}{u_{\text{col}}}\frac{u_{\text{col}}}{d_{\text{lat}}} & \frac{u_{\text{ped}}}{d_{\text{lng}}} + \frac{u_{\text{ped}}}{u_{\text{col}}}\frac{u_{\text{col}}}{d_{\text{lng}}} & 1 + \frac{u_{\text{ped}}}{u_{\text{col}}}\frac{u_{\text{col}}}{d_{\text{ped}}} & \frac{u_{\text{ped}}}{u_{\text{col}}} \\ \frac{u_{\text{col}}}{d_{\text{lat}}} & \frac{u_{\text{col}}}{d_{\text{lng}}} & \frac{u_{\text{col}}}{d_{\text{ped}}} & 1 \end{bmatrix} \begin{Bmatrix} \Delta d_{\text{lat}} \\ \Delta d_{\text{lng}} \\ \Delta d_{\text{ped}} \\ \Delta d_{\text{col}} \end{Bmatrix}$$

$$= \begin{bmatrix} \frac{p}{d_{\text{lat}}} & 0 & 0 & 0 \\ 0 & \frac{q}{d_{\text{lng}}} & 0 & 0 \\ 0 & 0 & \frac{r}{d_{\text{ped}}} & 0 \\ 0 & 0 & 0 & \frac{w^{\text{ned}}}{d_{\text{col}}} \end{bmatrix} \begin{Bmatrix} \Delta d_{\text{lat}} \\ \Delta d_{\text{lng}} \\ \Delta d_{\text{ped}} \\ \Delta d_{\text{col}} \end{Bmatrix} \tag{B-4}$$

As seen in the equation above, the plant vertical rate response is specified to be zero for arbitrary d_{lat}, d_{lng}, and d_{ped}. That is, the w^{ned} row of the plant, times the d_{lat}, d_{lng}, and d_{ped} columns of the second matrix, must be zero. In equation form,

$$\begin{bmatrix} N_{\text{lat}}^{w^{\text{ned}}} & N_{\text{lng}}^{w^{\text{ned}}} & N_{\text{ped}}^{w^{\text{ned}}} & N_{\text{col}}^{w^{\text{ned}}} \end{bmatrix} \begin{bmatrix} 1 + \frac{u_{\text{lat}}}{u_{\text{col}}}\frac{u_{\text{col}}}{d_{\text{lat}}} & \frac{u_{\text{lat}}}{d_{\text{lng}}} + \frac{u_{\text{lat}}}{u_{\text{col}}}\frac{u_{\text{col}}}{d_{\text{lng}}} & \frac{u_{\text{lat}}}{d_{\text{ped}}} + \frac{u_{\text{lat}}}{u_{\text{col}}}\frac{u_{\text{col}}}{d_{\text{ped}}} \\ \frac{u_{\text{lng}}}{d_{\text{lat}}} + \frac{u_{\text{lng}}}{u_{\text{col}}}\frac{u_{\text{col}}}{d_{\text{lat}}} & 1 + \frac{u_{\text{lng}}}{u_{\text{col}}}\frac{u_{\text{col}}}{d_{\text{lng}}} & \frac{u_{\text{lng}}}{d_{\text{ped}}} + \frac{u_{\text{lng}}}{u_{\text{col}}}\frac{u_{\text{col}}}{d_{\text{ped}}} \\ \frac{u_{\text{ped}}}{d_{\text{lat}}} + \frac{u_{\text{ped}}}{u_{\text{col}}}\frac{u_{\text{col}}}{d_{\text{lat}}} & \frac{u_{\text{ped}}}{d_{\text{lng}}} + \frac{u_{\text{ped}}}{u_{\text{col}}}\frac{u_{\text{col}}}{d_{\text{lng}}} & 1 + \frac{u_{\text{ped}}}{u_{\text{col}}}\frac{u_{\text{col}}}{d_{\text{ped}}} \\ \frac{u_{\text{col}}}{d_{\text{lat}}} & \frac{u_{\text{col}}}{d_{\text{lng}}} & \frac{u_{\text{col}}}{d_{\text{ped}}} \end{bmatrix} = \begin{bmatrix} 0 & 0 & 0 \end{bmatrix} \tag{B-5}$$

where the plant vertical rate transfer functions were converted to numerator polynomials by multiplying through by the plant common denominator. Perform the matrix multiplication, collect like terms, and move the non-$\mathbf{M}_{1x3}$ terms to the right.

$$\begin{aligned}
\left(N_{\text{lat}}^{w^{\text{ned}}} \frac{u_{\text{lat}}}{u_{\text{col}}} + N_{\text{lng}}^{w^{\text{ned}}} \frac{u_{\text{lng}}}{u_{\text{col}}} + N_{\text{ped}}^{w^{\text{ned}}} \frac{u_{\text{ped}}}{u_{\text{col}}} + N_{\text{col}}^{w^{\text{ned}}} \right) \frac{u_{\text{col}}}{d_{\text{lat}}} &= -N_{\text{lat}}^{w^{\text{ned}}} - N_{\text{lng}}^{w^{\text{ned}}} \frac{u_{\text{lng}}}{d_{\text{lat}}} - N_{\text{ped}}^{w^{\text{ned}}} \frac{u_{\text{ped}}}{d_{\text{lat}}} \\
\left(N_{\text{lat}}^{w^{\text{ned}}} \frac{u_{\text{lat}}}{u_{\text{col}}} + N_{\text{lng}}^{w^{\text{ned}}} \frac{u_{\text{lng}}}{u_{\text{col}}} + N_{\text{ped}}^{w^{\text{ned}}} \frac{u_{\text{ped}}}{u_{\text{col}}} + N_{\text{col}}^{w^{\text{ned}}} \right) \frac{u_{\text{col}}}{d_{\text{lng}}} &= -N_{\text{lat}}^{w^{\text{ned}}} \frac{u_{\text{lat}}}{d_{\text{lng}}} - N_{\text{lng}}^{w^{\text{ned}}} - N_{\text{ped}}^{w^{\text{ned}}} \frac{u_{\text{ped}}}{d_{\text{lng}}} \\
\left(N_{\text{lat}}^{w^{\text{ned}}} \frac{u_{\text{lat}}}{u_{\text{col}}} + N_{\text{lng}}^{w^{\text{ned}}} \frac{u_{\text{lng}}}{u_{\text{col}}} + N_{\text{ped}}^{w^{\text{ned}}} \frac{u_{\text{ped}}}{u_{\text{col}}} + N_{\text{col}}^{w^{\text{ned}}} \right) \frac{u_{\text{col}}}{d_{\text{ped}}} &= -N_{\text{lat}}^{w^{\text{ned}}} \frac{u_{\text{lat}}}{d_{\text{ped}}} - N_{\text{lng}}^{w^{\text{ned}}} \frac{u_{\text{lng}}}{d_{\text{ped}}} - N_{\text{ped}}^{w^{\text{ned}}}
\end{aligned} \tag{B-6}$$

Each equation above involves only one $\mathbf{M}_{1x3}$ term, so the solution is simple.

$$\begin{aligned}
\frac{u_{\text{col}}}{d_{\text{lat}}} &= \left(N_{\text{lat}}^{w^{\text{ned}}} \frac{u_{\text{lat}}}{u_{\text{col}}} + N_{\text{lng}}^{w^{\text{ned}}} \frac{u_{\text{lng}}}{u_{\text{col}}} + N_{\text{ped}}^{w^{\text{ned}}} \frac{u_{\text{ped}}}{u_{\text{col}}} + N_{\text{col}}^{w^{\text{ned}}} \right)^{-1} \left(-N_{\text{lat}}^{w^{\text{ned}}} - N_{\text{lng}}^{w^{\text{ned}}} \frac{u_{\text{lng}}}{d_{\text{lat}}} - N_{\text{ped}}^{w^{\text{ned}}} \frac{u_{\text{ped}}}{d_{\text{lat}}} \right) \\
\frac{u_{\text{col}}}{d_{\text{lng}}} &= \left(N_{\text{lat}}^{w^{\text{ned}}} \frac{u_{\text{lat}}}{u_{\text{col}}} + N_{\text{lng}}^{w^{\text{ned}}} \frac{u_{\text{lng}}}{u_{\text{col}}} + N_{\text{ped}}^{w^{\text{ned}}} \frac{u_{\text{ped}}}{u_{\text{col}}} + N_{\text{col}}^{w^{\text{ned}}} \right)^{-1} \left(-N_{\text{lat}}^{w^{\text{ned}}} \frac{u_{\text{lat}}}{d_{\text{lng}}} - N_{\text{lng}}^{w^{\text{ned}}} - N_{\text{ped}}^{w^{\text{ned}}} \frac{u_{\text{ped}}}{d_{\text{lng}}} \right) \\
\frac{u_{\text{col}}}{d_{\text{ped}}} &= \left(N_{\text{lat}}^{w^{\text{ned}}} \frac{u_{\text{lat}}}{u_{\text{col}}} + N_{\text{lng}}^{w^{\text{ned}}} \frac{u_{\text{lng}}}{u_{\text{col}}} + N_{\text{ped}}^{w^{\text{ned}}} \frac{u_{\text{ped}}}{u_{\text{col}}} + N_{\text{col}}^{w^{\text{ned}}} \right)^{-1} \left(-N_{\text{lat}}^{w^{\text{ned}}} \frac{u_{\text{lat}}}{d_{\text{ped}}} - N_{\text{lng}}^{w^{\text{ned}}} \frac{u_{\text{lng}}}{d_{\text{ped}}} - N_{\text{ped}}^{w^{\text{ned}}} \right)
\end{aligned} \tag{B-7}$$

With a 6-state angular-vertical rate plant, the results above appear to be 25$^{\text{th}}$ order. For the cases considered, the actual highest order was 5$^{\text{th}}$ after pole-zero cancellations with tolerance 0.01 rad/s. For implementation, these "exact" transfer functions were replaced with stable 2$^{\text{nd}}$ order approximations through frequency-domain fitting, as mentioned before.

Appendix C

Body Side and Down Velocity (*v* & *w*) Estimation

The Dynamic Inversion formulas in this paper require body side and down velocity states for feedback. This section presents methods for estimating those states.

Body-Side Velocity Estimation

Starting with an identified linear eight state model $(\Delta u, \Delta v, \Delta w, p, q, r, \Delta\phi, \Delta\theta)$, the inertial acceleration in the lateral (body-right) axis is approximately

$$\begin{aligned} a^{\mathrm{b}}_{\mathrm{i},y} \approx\ & g\sin\phi\cos\theta - g\sin\phi_{\mathrm{trm}}\cos\theta_{\mathrm{trm}} + A_{\dot{v},v}\left(v - v_{\mathrm{trm}}\right) + \left(A_{\dot{v},\mathrm{p}} - w_{\mathrm{trm}}\right)p + \left(A_{\dot{v},\mathrm{r}} + u_{\mathrm{trm}}\right)r \\ & + B_{\dot{v},\mathrm{lat}}\left(u_{\mathrm{lat}} - u_{\mathrm{lat,trm}}\right) + B_{\dot{v},\mathrm{ped}}\left(u_{\mathrm{ped}} - u_{\mathrm{ped,trm}}\right) + B_{\dot{v},\mathrm{col}}\left(u_{\mathrm{col}} - u_{\mathrm{col,trm}}\right) \end{aligned} \tag{C-1}$$

The measured lateral acceleration is

$$\begin{aligned} a^{\mathrm{b}}_{\mathrm{meas},y} = a^{\mathrm{b}}_{\mathrm{i},y} - g\sin\phi\cos\theta \approx\ & -g\sin\phi_{\mathrm{trim}}\cos\theta_{\mathrm{trim}} + A_{\dot{v},v}\left(v - v_{\mathrm{trm}}\right) + \left(A_{\dot{v},\mathrm{p}} - w_{\mathrm{trm}}\right)p + \left(A_{\dot{v},\mathrm{r}} + u_{\mathrm{trm}}\right)r \\ & + B_{\dot{v},\mathrm{lat}}\left(u_{\mathrm{lat}} - u_{\mathrm{lat,trm}}\right) + B_{\dot{v},\mathrm{ped}}\left(u_{\mathrm{ped}} - u_{\mathrm{ped,trm}}\right) + B_{\dot{v},\mathrm{col}}\left(u_{\mathrm{col}} - u_{\mathrm{col,trm}}\right) \end{aligned} \tag{C-2}$$

where *A*'s are stability derivatives and *B*'s are control derivatives. From this the body-right velocity deviation from trim, Δv, a state of the linearized model, can be estimated.

$$\Delta v_{\mathrm{est}} = v_{\mathrm{est}} - v_{\mathrm{trm}} = \frac{\begin{pmatrix} a^{\mathrm{b}}_{\mathrm{meas},y} + g\sin\phi_{\mathrm{trm}}\cos\theta_{\mathrm{trm}} - \left(A_{\dot{v},\mathrm{p}} - w_{\mathrm{trm}}\right)p - \left(A_{\dot{v},\mathrm{r}} + u_{\mathrm{trm}}\right)r \\ -B_{\dot{v},\mathrm{lat}}\left(u_{\mathrm{lat}} - u_{\mathrm{lat,trm}}\right) - B_{\dot{v},\mathrm{ped}}\left(u_{\mathrm{ped}} - u_{\mathrm{ped,trm}}\right) - B_{\dot{v},\mathrm{col}}\left(u_{\mathrm{col}} - u_{\mathrm{col,trm}}\right) \end{pmatrix}}{A_{\dot{v},v}} \tag{C-3}$$

This estimate relies heavily upon the relationship between inputs **u** and the resulting acceleration. To account for actuation and measurement dynamics, the effective **u** associated with the measured acceleration (the **u** to be used in equation (C-3)) is computed by passing the commanded **u** through a filter consisting of the actuation and measurement dynamics in series.

Body-Down Velocity Estimation

The transformation between body and heading frame is

$$\begin{Bmatrix} u^{\mathrm{h}} \\ v^{\mathrm{h}} \\ w^{\mathrm{h}} \end{Bmatrix} = {}^{\mathrm{h}}T^{\mathrm{b}} \begin{Bmatrix} u \\ v \\ w \end{Bmatrix} = \begin{bmatrix} \cos\theta & \sin\theta\ \sin\phi & \sin\theta\ \cos\phi \\ 0 & \cos\phi & -\sin\phi \\ -\sin\theta & \cos\theta\ \sin\phi & \cos\theta\ \cos\phi \end{bmatrix} \begin{Bmatrix} u \\ v \\ w \end{Bmatrix} \tag{C-4}$$

In Equation (C-4), all speed variables are relative to the air. The present work uses descent rate as an approximate measure of w^{h}. Unfortunately, because descent rate is not relative to the air, the effect of vertical wind is not captured. Body-forward velocity (u) is obtained from a forward-pointing pitot-static probe. Body-right velocity (v) is estimated as shown above.

$$v_{\mathrm{est}} = \Delta v_{\mathrm{est}} + v_{\mathrm{trm}} \tag{C-5}$$

Assume that roll (ϕ) and pitch (θ) attitudes are measured. To get the estimate for w, start with the formula for w^{h} in Equation (C-4).

$$w^{\mathrm{h}} = (-\sin\theta)u + (\cos\theta\ \sin\phi)v + (\cos\theta\ \cos\phi)w \tag{C-6}$$

Solving for w gives

$$w_{\mathrm{est}} = \frac{w^{\mathrm{h}} + (\sin\theta)u - (\cos\theta\ \sin\phi)v_{\mathrm{est}}}{\cos\theta\ \cos\phi} \tag{C-7}$$

The deviation from trim, a state of the linearized model, is

$$\Delta w_{\mathrm{est}} = w_{\mathrm{est}} - w_{\mathrm{trm}} \tag{C-8}$$

If roll and pitch measurements are not available, estimates must be generated.

Appendix D

Descent Acceleration from Measured States and Inputs

Let roll and pitch attitudes be (ϕ,θ), respectively. Descent rate is

$$w^{\mathrm{h}} = (-\sin\theta)u + (\cos\theta\sin\phi)v + (\cos\theta\cos\phi)w \tag{D-1}$$

Taking the derivative, and keeping only the more significant terms that are linear in the states,

$$\dot{w}^{\mathrm{h}} \approx -(\cos\theta)\dot{\theta}u_{\mathrm{trm}} + (\cos\theta\cos\phi)\dot{\phi}v_{\mathrm{trm}} + (\cos\theta\sin\phi)\dot{v} - (\cos\theta\sin\phi)\dot{\phi}w_{\mathrm{trm}} + (\cos\theta\cos\phi)\dot{w} \tag{D-2}$$

where

$$\dot{\theta} = q\cos\phi - r\sin\phi \quad , \quad \dot{\phi} \approx p \tag{D-3}$$

Making these substitutions, and collecting the factors on each state or state derivative,

$$\begin{aligned}
\dot{w}^{\mathrm{h}} &\approx -(\cos\theta)(q\cos\phi - r\sin\phi)u_{\mathrm{trm}} + (\cos\theta\cos\phi)\,pv_{\mathrm{trm}} \\
&\quad + (\cos\theta\sin\phi)\dot{v} - (\cos\theta\sin\phi)\,pw_{\mathrm{trm}} + (\cos\theta\cos\phi)\dot{w} \\
&\approx (v_{\mathrm{trm}}\cos\theta\cos\phi - w_{\mathrm{trm}}\cos\theta\sin\phi)\,p - (\cos\theta\cos\phi)u_{\mathrm{trm}}q \\
&\quad + (\cos\theta\sin\phi)u_{\mathrm{trm}}r + (\cos\theta\sin\phi)\dot{v} + (\cos\theta\cos\phi)\dot{w}
\end{aligned} \tag{D-4}$$

Now the state derivatives are replaced by states and control inputs, using the system equations.

$$\begin{aligned}
\frac{\dot{w}^{\mathrm{h}}}{\cos\theta} &\approx \sin\phi\left\{\begin{matrix}(A_{1,1}\Delta v + A_{1,2}\Delta w + A_{1,3}p + A_{1,4}q + A_{1,5}r) + \\ (B_{1,1}\Delta u_{\mathrm{lat}} + B_{1,2}\Delta u_{\mathrm{lng}} + B_{1,3}\Delta u_{\mathrm{ped}} + B_{1,4}\Delta u_{\mathrm{col}})\end{matrix}\right\} \\
&\quad + \cos\phi\left\{\begin{matrix}(A_{2,1}\Delta v + A_{2,2}\Delta w + A_{2,3}p + A_{2,4}q + A_{2,5}r) + \\ (B_{2,1}\Delta u_{\mathrm{lat}} + B_{2,2}\Delta u_{\mathrm{lng}} + B_{2,3}\Delta u_{\mathrm{ped}} + B_{2,4}\Delta u_{\mathrm{col}})\end{matrix}\right\} \\
&\quad + (v_{\mathrm{trm}}\cos\phi - w_{\mathrm{trm}}\sin\phi)\,p - u_{\mathrm{trm}}q\cos\phi + u_{\mathrm{trm}}r\sin\phi
\end{aligned} \tag{D-5}$$

Finally, the derivative of descent rate is written compactly in terms of the state and control input vectors.

$$\begin{aligned}
\dot{w}^{\mathrm{ned}} = \dot{w}^{\mathrm{h}} &\approx \cos\theta\begin{bmatrix}\sin\phi & \cos\phi\end{bmatrix}\begin{bmatrix} A_{1,1} & A_{1,2} & (A_{1,3} - w_{\mathrm{trm}}) & A_{1,4} & (A_{1,5} + u_{\mathrm{trm}}) \\ A_{2,1} & A_{2,2} & (A_{2,3} + v_{\mathrm{trm}}) & (A_{2,4} - u_{\mathrm{trm}}) & A_{2,5}\end{bmatrix}\Delta\mathbf{x} \\
&\quad + \cos\theta\begin{bmatrix}\sin\phi & \cos\phi\end{bmatrix}\begin{bmatrix} B_{1,1} & B_{1,2} & B_{1,3} & B_{1,4} \\ B_{2,1} & B_{2,2} & B_{2,3} & B_{2,4}\end{bmatrix}\Delta\mathbf{u} \\
&= [\mathbf{CA}]_{\dot{w}^{\mathrm{ned}},\phi\theta}\,\Delta\mathbf{x} + [\mathbf{CB}]_{\dot{w}^{\mathrm{ned}},\phi\theta}\,\Delta\mathbf{u}
\end{aligned} \tag{D-6}$$

Appendix E

Computation of $[\mathbf{CA}]_{\varphi\theta}$ and $[\mathbf{CB}]^{-1}_{\varphi\theta}$

$[\mathbf{CA}]_{\phi\theta}$ is constructed as:

$$[\mathbf{CA}]_{\phi\theta} = \begin{bmatrix} \cos\theta \lfloor \sin\phi \quad \cos\phi \rfloor \begin{bmatrix} [\mathbf{CA}]_{\phi\theta,\,\text{row1sin}} \\ [\mathbf{CA}]_{\phi\theta,\,\text{row1cos}} \end{bmatrix} \\ A_{3,1} \quad A_{3,2} \quad A_{3,3} \quad A_{3,4} \quad A_{3,5} \\ A_{4,1} \quad A_{4,2} \quad A_{4,3} \quad A_{4,4} \quad A_{4,5} \\ A_{5,1} \quad A_{5,2} \quad A_{5,3} \quad A_{5,4} \quad A_{5,5} \end{bmatrix} = \begin{bmatrix} [\mathbf{CA}]_{\dot{w}^{\text{ned}},\,\phi\theta} \\ C_{pqr}A \end{bmatrix} \tag{E-1}$$

where

$$\begin{aligned} [\mathbf{CA}]_{\phi\theta,\,\text{row1sin}} &= \begin{bmatrix} A_{1,1} & A_{1,2} & (A_{1,3} - w_{\text{trim}}) & A_{1,4} & (A_{1,5} + u_{\text{trim}}) \end{bmatrix} \\ [\mathbf{CA}]_{\phi\theta,\,\text{row1cos}} &= \begin{bmatrix} A_{2,1} & A_{2,2} & (A_{2,3} + v_{\text{trim}}) & (A_{2,4} - u_{\text{trim}}) & A_{2,5} \end{bmatrix} \end{aligned} \tag{E-2}$$

$[\mathbf{CA}]_{\phi\theta,\,\text{row1sin}}$ and $[\mathbf{CA}]_{\phi\theta,\,\text{row1cos}}$ are constants at a given forward speed trim, so they can be precomputed and scheduled.

$[\mathbf{CB}]_{\phi\theta}$ is constructed as:

$$[\mathbf{CB}]_{\phi\theta} = \begin{bmatrix} [\mathbf{CB}]_{\dot{w}^{\text{ned}},\,\phi\theta} \\ \mathbf{C}_{pqr}\mathbf{B} \end{bmatrix} = \begin{bmatrix} \cos\theta \lfloor \sin\phi \quad \cos\phi \rfloor \begin{bmatrix} B_{1,1} & B_{1,2} & B_{1,3} & B_{1,4} \\ B_{2,1} & B_{2,2} & B_{2,3} & B_{2,4} \end{bmatrix} \\ B_{3,1} \quad B_{3,2} \quad B_{3,3} \quad B_{3,4} \\ B_{4,1} \quad B_{4,2} \quad B_{4,3} \quad B_{4,4} \\ B_{5,1} \quad B_{5,2} \quad B_{5,3} \quad B_{5,4} \end{bmatrix} \tag{E-3}$$

$[\mathbf{CB}]^{-1}_{\phi\theta}$ is constructed using the following formula for analytic inversion of a matrix:

$$[\mathbf{CB}]^{-1}_{\phi\theta} = \frac{\left[\text{cof}\left([\mathbf{CB}]_{\phi\theta}\right)\right]^{\text{T}}}{\left|[\mathbf{CB}]_{\phi\theta}\right|} \tag{E-4}$$

The determinant term is formulated as follows.

$$\frac{\left|\left[\mathbf{CB}\right]_{\phi\theta}\right|}{\cos\theta} =$$

$$\left[\begin{vmatrix} B_{3,2} & B_{3,3} & B_{3,4} \\ B_{4,2} & B_{4,3} & B_{4,4} \\ B_{5,2} & B_{5,3} & B_{5,4} \end{vmatrix} - \begin{vmatrix} B_{3,1} & B_{3,3} & B_{3,4} \\ B_{4,1} & B_{4,3} & B_{4,4} \\ B_{5,1} & B_{5,3} & B_{5,4} \end{vmatrix} \begin{vmatrix} B_{3,1} & B_{3,2} & B_{3,4} \\ B_{4,1} & B_{4,2} & B_{4,4} \\ B_{5,1} & B_{5,2} & B_{5,4} \end{vmatrix} - \begin{vmatrix} B_{3,1} & B_{3,2} & B_{3,3} \\ B_{4,1} & B_{4,2} & B_{4,3} \\ B_{5,1} & B_{5,2} & B_{5,3} \end{vmatrix}\right] \begin{bmatrix} B_{1,1} & B_{2,1} \\ B_{1,2} & B_{2,2} \\ B_{1,3} & B_{2,3} \\ B_{1,4} & B_{2,4} \end{bmatrix} \begin{Bmatrix} \sin\phi \\ \cos\phi \end{Bmatrix} \qquad \text{(E-5)}$$

$$= \begin{bmatrix} \left|\left[\mathbf{CB}\right]_{\phi\theta}\right|_{\sin} & \left|\left[\mathbf{CB}\right]_{\phi\theta}\right|_{\cos} \end{bmatrix} \begin{Bmatrix} \sin\phi \\ \cos\phi \end{Bmatrix}$$

Now the cofactor term is formulated one row at a time.

$$\begin{aligned} &\operatorname{cof}\left(\left[\mathbf{CB}\right]_{\phi\theta}\right)_{\text{row 1}} \\ &= \begin{bmatrix} \begin{vmatrix} B_{3,2} & B_{3,3} & B_{3,4} \\ B_{4,2} & B_{4,3} & B_{4,4} \\ B_{5,2} & B_{5,3} & B_{5,4} \end{vmatrix} & - \begin{vmatrix} B_{3,1} & B_{3,3} & B_{3,4} \\ B_{4,1} & B_{4,3} & B_{4,4} \\ B_{5,1} & B_{5,3} & B_{5,4} \end{vmatrix} & \begin{vmatrix} B_{3,1} & B_{3,2} & B_{3,4} \\ B_{4,1} & B_{4,2} & B_{4,4} \\ B_{5,1} & B_{5,2} & B_{5,4} \end{vmatrix} & - \begin{vmatrix} B_{3,1} & B_{3,2} & B_{3,3} \\ B_{4,1} & B_{4,2} & B_{4,3} \\ B_{5,1} & B_{5,2} & B_{5,3} \end{vmatrix} \end{bmatrix} \end{aligned} \qquad \text{(E-6)}$$

$$\frac{\operatorname{cof}\left(\left[\mathbf{CB}\right]_{\phi\theta}\right)_{\text{row 2}}}{\cos\theta}$$

$$= \begin{bmatrix} \sin\phi & \cos\phi \end{bmatrix} \begin{bmatrix} B_{1,1} & B_{1,2} & B_{1,3} & B_{1,4} \\ B_{2,1} & B_{2,2} & B_{2,3} & B_{2,4} \end{bmatrix} \begin{bmatrix} 0 & \begin{vmatrix} B_{4,3} & B_{4,4} \\ B_{5,3} & B_{5,4} \end{vmatrix} & - \begin{vmatrix} B_{4,2} & B_{4,4} \\ B_{5,2} & B_{5,4} \end{vmatrix} & \begin{vmatrix} B_{4,2} & B_{4,3} \\ B_{5,2} & B_{5,3} \end{vmatrix} \\ - \begin{vmatrix} B_{4,3} & B_{4,4} \\ B_{5,3} & B_{5,4} \end{vmatrix} & 0 & \begin{vmatrix} B_{4,1} & B_{4,4} \\ B_{5,1} & B_{5,4} \end{vmatrix} & - \begin{vmatrix} B_{4,1} & B_{4,3} \\ B_{5,1} & B_{5,3} \end{vmatrix} \\ \begin{vmatrix} B_{4,2} & B_{4,4} \\ B_{5,2} & B_{5,4} \end{vmatrix} & - \begin{vmatrix} B_{4,1} & B_{4,4} \\ B_{5,1} & B_{5,4} \end{vmatrix} & 0 & \begin{vmatrix} B_{4,1} & B_{4,2} \\ B_{5,1} & B_{5,2} \end{vmatrix} \\ - \begin{vmatrix} B_{4,2} & B_{4,3} \\ B_{5,2} & B_{5,3} \end{vmatrix} & \begin{vmatrix} B_{4,1} & B_{4,3} \\ B_{5,1} & B_{5,3} \end{vmatrix} & - \begin{vmatrix} B_{4,1} & B_{4,2} \\ B_{5,1} & B_{5,2} \end{vmatrix} & 0 \end{bmatrix} \qquad \text{(E-7)}$$

$$= \begin{bmatrix} \sin\phi & \cos\phi \end{bmatrix} \begin{bmatrix} \operatorname{cof}\left(\left[\mathbf{CB}\right]_{\phi\theta}\right)_{\text{row 2 sin}} \\ \operatorname{cof}\left(\left[\mathbf{CB}\right]_{\phi\theta}\right)_{\text{row 2 cos}} \end{bmatrix}$$

$$\frac{\operatorname{cof}\left(\left[\mathbf{CB}\right]_{\phi\theta}\right)_{\text{row 3}}}{\cos\theta}$$

$$= \begin{bmatrix} \sin\phi & \cos\phi \end{bmatrix} \begin{bmatrix} B_{1,1} & B_{1,2} & B_{1,3} & B_{1,4} \\ B_{2,1} & B_{2,2} & B_{2,3} & B_{2,4} \end{bmatrix} \begin{bmatrix} 0 & - \begin{vmatrix} B_{3,3} & B_{3,4} \\ B_{5,3} & B_{5,4} \end{vmatrix} & \begin{vmatrix} B_{3,2} & B_{3,4} \\ B_{5,2} & B_{5,4} \end{vmatrix} & - \begin{vmatrix} B_{3,2} & B_{3,3} \\ B_{5,2} & B_{5,3} \end{vmatrix} \\ \begin{vmatrix} B_{3,3} & B_{3,4} \\ B_{5,3} & B_{5,4} \end{vmatrix} & 0 & - \begin{vmatrix} B_{3,1} & B_{3,4} \\ B_{5,1} & B_{5,4} \end{vmatrix} & \begin{vmatrix} B_{3,1} & B_{3,3} \\ B_{5,1} & B_{5,3} \end{vmatrix} \\ - \begin{vmatrix} B_{3,2} & B_{3,4} \\ B_{5,2} & B_{5,4} \end{vmatrix} & \begin{vmatrix} B_{3,1} & B_{3,4} \\ B_{5,1} & B_{5,4} \end{vmatrix} & 0 & - \begin{vmatrix} B_{3,1} & B_{3,2} \\ B_{5,1} & B_{5,2} \end{vmatrix} \\ \begin{vmatrix} B_{3,2} & B_{3,3} \\ B_{5,2} & B_{5,3} \end{vmatrix} & - \begin{vmatrix} B_{3,1} & B_{3,3} \\ B_{5,1} & B_{5,3} \end{vmatrix} & \begin{vmatrix} B_{3,1} & B_{3,2} \\ B_{5,1} & B_{5,2} \end{vmatrix} & 0 \end{bmatrix} \qquad \text{(E-8)}$$

$$= \begin{bmatrix} \sin\phi & \cos\phi \end{bmatrix} \begin{bmatrix} \operatorname{cof}\left(\left[\mathbf{CB}\right]_{\phi\theta}\right)_{\text{row 3 sin}} \\ \operatorname{cof}\left(\left[\mathbf{CB}\right]_{\phi\theta}\right)_{\text{row 3 cos}} \end{bmatrix}$$

$$
\begin{aligned}
&\frac{\operatorname{cof}\left(\left[\mathbf{CB}\right]_{\phi\theta}\right)_{\text{row 4}}}{\cos\theta} \\
&= \begin{bmatrix} \sin\phi & \cos\phi \end{bmatrix} \begin{bmatrix} B_{1,1} & B_{1,2} & B_{1,3} & B_{1,4} \\ B_{2,1} & B_{2,2} & B_{2,3} & B_{2,4} \end{bmatrix} \begin{bmatrix} 0 & \begin{vmatrix} B_{3,3} & B_{3,4} \\ B_{4,3} & B_{4,4} \end{vmatrix} & -\begin{vmatrix} B_{3,2} & B_{3,4} \\ B_{4,2} & B_{4,4} \end{vmatrix} & \begin{vmatrix} B_{3,2} & B_{3,3} \\ B_{4,2} & B_{4,3} \end{vmatrix} \\ -\begin{vmatrix} B_{3,3} & B_{3,4} \\ B_{4,3} & B_{4,4} \end{vmatrix} & 0 & \begin{vmatrix} B_{3,1} & B_{3,4} \\ B_{4,1} & B_{4,4} \end{vmatrix} & -\begin{vmatrix} B_{3,1} & B_{3,3} \\ B_{4,1} & B_{4,3} \end{vmatrix} \\ \begin{vmatrix} B_{3,2} & B_{3,4} \\ B_{4,2} & B_{4,4} \end{vmatrix} & -\begin{vmatrix} B_{3,1} & B_{3,4} \\ B_{4,1} & B_{4,4} \end{vmatrix} & 0 & \begin{vmatrix} B_{3,1} & B_{3,2} \\ B_{4,1} & B_{4,2} \end{vmatrix} \\ -\begin{vmatrix} B_{3,2} & B_{3,3} \\ B_{4,2} & B_{4,3} \end{vmatrix} & \begin{vmatrix} B_{3,1} & B_{3,3} \\ B_{4,1} & B_{4,3} \end{vmatrix} & -\begin{vmatrix} B_{3,1} & B_{3,2} \\ B_{4,1} & B_{4,2} \end{vmatrix} & 0 \end{bmatrix} \\
&= \begin{bmatrix} \sin\phi & \cos\phi \end{bmatrix} \begin{bmatrix} \operatorname{cof}\left(\left[\mathbf{CB}\right]_{\phi\theta}\right)_{\text{row 4 sin}} \\ \operatorname{cof}\left(\left[\mathbf{CB}\right]_{\phi\theta}\right)_{\text{row 4 cos}} \end{bmatrix}
\end{aligned}
\tag{E-9}
$$

$$
\left[\mathbf{CB}\right]_{\phi\theta}^{-1} = \frac{\left[\operatorname{cof}\left(\left[\mathbf{CB}\right]_{\phi\theta}\right)\right]^{\mathrm{T}}}{\left|\left[\mathbf{CB}\right]_{\phi\theta}\right|} = \frac{\begin{bmatrix} \dfrac{\operatorname{cof}\left(\left[\mathbf{CB}\right]_{\phi\theta}\right)_{\text{row1}}}{\cos\theta} \\ \begin{bmatrix} \sin\phi & \cos\phi \end{bmatrix} \begin{bmatrix} \operatorname{cof}\left(\left[\mathbf{CB}\right]_{\phi\theta}\right)_{\text{row 2 sin}} \\ \operatorname{cof}\left(\left[\mathbf{CB}\right]_{\phi\theta}\right)_{\text{row 2 cos}} \end{bmatrix} \\ \begin{bmatrix} \sin\phi & \cos\phi \end{bmatrix} \begin{bmatrix} \operatorname{cof}\left(\left[\mathbf{CB}\right]_{\phi\theta}\right)_{\text{row 3 sin}} \\ \operatorname{cof}\left(\left[\mathbf{CB}\right]_{\phi\theta}\right)_{\text{row 3 cos}} \end{bmatrix} \\ \begin{bmatrix} \sin\phi & \cos\phi \end{bmatrix} \begin{bmatrix} \operatorname{cof}\left(\left[\mathbf{CB}\right]_{\phi\theta}\right)_{\text{row 4 sin}} \\ \operatorname{cof}\left(\left[\mathbf{CB}\right]_{\phi\theta}\right)_{\text{row 4 cos}} \end{bmatrix} \end{bmatrix}^{\mathrm{T}}}{\begin{bmatrix} \left|\left[\mathbf{CB}\right]_{\phi\theta}\right|_{\sin} & \left|\left[\mathbf{CB}\right]_{\phi\theta}\right|_{\cos} \end{bmatrix} \begin{Bmatrix} \sin\phi \\ \cos\phi \end{Bmatrix}}
\tag{E-10}
$$

In the final formula above, except for the trig functions, all elements are constants at a given forward speed trim, so they can be precomputed and scheduled.

VITA

James Michael Spires

James Michael Spires was born on April 1, 1971, in Jackson, Mississippi, USA. After earning the Advanced Diploma with Honors from Mary G. Montgomery High School in Semmes, Alabama, he entered Auburn University in the Fall of 1989. He graduated from Auburn University in 1993 with a Bachelor of Mechanical Engineering degree, and in 1995 with a Master of Science degree in Mechanical Engineering. During his time at Auburn, Mr. Spires was inducted into Pi Tau Sigma (Mechanical Engineering honor society) and Tau Beta Pi (Engineering honor society), and earned the Private Pilot license with Single Engine Land and Instrument ratings. He then entered industry, working for sixteen years as an engineer dealing with jet engines, missiles, UAV's, and helicopters, while also advancing his piloting credentials to Commercial Pilot, Single Engine Land and Sea, Multi-Engine Land. Mr. Spires joined The Pennsylvania State University (Penn State) in Spring 2012 to pursue his doctoral studies in Aerospace Engineering, under the guidance of Dr. Joseph F. Horn. This dissertation is a product of his research at Penn State in rotorcraft dynamics and control.